Modification of the Metal Lattice in Transition Metals by Light Elements: Synthesis, Characterisations and Catalytic Applications



Tianyi Chen

Oriel College

University of Oxford

A thesis submitted for the degree of

Doctor of Philosophy

Michaelmas 2020

Dedication

To my families and friends.

Declaration

I hereby declare that the work presented in this thesis is my own and the use of all materials from other sources has been properly and fully acknowledged.

Part of this thesis is presented in the following journal:

- 1st Author

*"*Interstitial Boron Atoms in Palladium Lattice of Industrial Type of Nano-catalyst: Properties and Structural Modifications*"*, Tianyi Chen, Ieuan Ellis, Thomas Hooper, Emanuela Liberti, Lin Ye, Benedict T.W. Lo, Colum O'Leary, Alex A Sheader, Gerardo Martinez, Lewys Jones, Ping-luen Ho, Pu Zhao, James Cookson, Peter Bishop, Philip Chater, John Hanna, Peter Nellist, Shik Chi Edman Tsang. *J. Am. Chem. Soc.* 2019, 141, 50, 19616-19624

*"*Interstitial and Substitutional Light Elements in Transition metals for Heterogeneous Catalysis*",* Tianyi Chen, Christopher Foo, Shik Chi Edman Tsang, *Chem. Sci.* 2021, 12, 517-532

*"*Direct Evidence of Substitution of Pt Atoms by Li as Pt_7Li in Lithiated Supported Pt Nanoparticle and Ultraselective Catalytic Hydrogenation*",* Tianyi Chen, Christopher Foo, Jianwei Zheng, Huihuang Fang, Peter Nellist and Shik Chi Edman Tsang. *Adv. Mater.* (under review)

Tianyi Chen

Acknowledgement

First and foremost, I would like to thank Professor Edman Tsang and Professor Peter Nellist for giving me the chance to join their research groups, offering essential help and guidance along the progress of the research.

I really appreciate that I received valuable assistance and support from the following individuals within Edman, Peter and other research groups.

Edman Tsang Group:

Thanks for Dr. Lin Ye and Mr. Chris Foo for their synchrotron analysis.

Thanks for Dr. Ben Lo for his support about *in-situ* PDF and refinement.

Thanks for Mr. Huihuang Fang for mailing my samples to Xiamen university for XPS characterisation and providing valuable advice.

Peter Nellist Group:

Thanks for Dr. Gerardo Martinez for his support and training on JEOL 3000 (TEM mode), JEOL ARM200F and ptychography processing.

Thanks for Dr. Aakash Varambhia for his support and training on JEOL 3000 (STEM mode), alignment of EELS upon JEOL ARM200F.

Thanks for Dr. Colum O'Leary for his support and training on ptychography processing, JEOL ARM200F and ARM slots in Year 2.

Thanks for Miss Alex Sheader for her support and training on JEOL ARM200F(EELS).

Thanks for Mr. James Sode for his teaching on implementation of open source python coding, Hyperspy.

Thanks for Dr. Zezhong Zhang for his teaching about STEM simulations.

Outside the research group:

Thanks for Dr. Emanuela Liberti for her quantitative simulated ADF and phase images of Pd-^{int}B, teaching of simulations, training on JEOL ARM300F (Harwell).

Thanks for Dr. Ian Griffith for his training on JEOL ARM200F (Oxford Materials).

Thanks for Dr. Thomas Hooper for his work about ^{105}Pd VOC ssNMR of Pd-^{int}Li/C and Pd-^{int}B/C (Warwick University).

During the writing up stage, I would like to thank my colleagues for proofreading my thesis and giving me timely feedback: Mr. Huihuang Fang, Mr. Guangchao Li, Dr. Jianwei Zheng, Dr. Pu Zhao, Dr. Tugce Ayvali, Miss. Emma Hedley, Mr. Christopher Foo, Mr. William Vickery, Miss. Yue Wang, Dr. Colum O'Leary and Mr. James Sode. Also, I want to thank my friends Miss. Ally King, Miss. Jiabei Bao, Miss. Kailing Ng, Dr. James Hogg, Dr. Shababa Selim and Dr. Jiaqi Bai, for although they were not in the research group, they never hesitated to take time on proofreading and giving constructive suggestions.

I would like to express my great gratitude to all of my friends, in particular Miss Jiabei Bao, Miss. Yiyan Chen, Miss. Jacqueline Chen, Miss. Xiaowen Dong, Miss Yingjun Huang, Miss. Xingchen Li, Miss. Kailing Ng, Miss Yunqing Wang and Mr. ZhenXuan Zhou…..(so many

name). Whether in London, UK, Europe, Asia or North American, they have always been my support, giving me mental/psychological support and helping me to sort out a problem one after another. Herein, I want to thank them, for I know without them, I wouldn't be able to overcome the difficulties on my journey to DPhil.

Finally, I want to express my great gratitude to my families, especially my parents, for supporting me physically and mentally (yet they never ask for return). Without them, studying in Oxford University would have been just a dream.

Abstract

Heterogeneous catalysis plays an important role in the pharmaceutical and petrochemical industries. Due to the poor chemical selectivity in many processes, it is essential to design novel catalysts to resolve this problem. Recently, interstitially modifying transition metal NPs with light elements has become a potential strategy for adjusting surface energy and tuning catalytic activity. However, this new class of catalysts remains relatively unexplored due to a lack of adequate characterisation evidence.

Herein, the work presented in this thesis continues the structural characterisation of the Pd-^{int}B/C and Pd-^{int}Li/C, reported from previous work, by using a novel combination of analytical techniques that span from the atomic to the macro level. Initially, these characterisations showed that after B and Li incorporation the Pd lattice maintains a face-centred cubic structure, but tolerates structural distortion. These structural distortions can further result in the local formation of the HCP structure. Additionally, the combination of STEM-EELS and ptychography was attempted to directly observe the presence of B and Li at the atomic level.

Meanwhile, in order to broaden the scope of the light element modified catalyst family, attempts were made to alloy Li into the Pt host metal system. It was found that the unit cell of the Pt contracts after thermal treatment at elevated temperature, indicating the formation of the Pt-^{sub}Li nano bimetallic alloy. The combination of XPS and ssNMR confirms the presence of Li in the metal framework, in addition to the SXRD. The STEM-ADF imaging reveals the presence of the Pt_7Li. Seemingly, this is the first report of Pt-Li based NPs synthesis to date. This catalyst displays premium 2,5-bis(hydroxymethyl)furan (BHMF) selectivity when catalysing HMF hydrogenation; this is due to the Li blocking specific, undesired reaction pathways. It is anticipated that such an in-depth investigation will help influence the future design and characterisation of novel, light element alloyed systems.

Keywords: Heterogeneous catalysis, catalysis modification, characterisation, catalytic hydrogenation.

Abbreviations

SXRD	Synchrotron X-Ray Diffraction
XRD	X-Ray (Powder) diffraction
IPO	Isopropanol
NPs	Nanoparticles
GC	Gas Chromatography
GC/MS	Gas Chromatography Mass Spectrometry
MAS ssNMR	Magic Angle Spinning Solid-State Nuclear Magnetic Resonance
EELS	Electron Energy Loss Spectroscopy
XPS	X-Ray Photoelectron Spectroscopy
(X)PDF	X-Ray Pair Distribution Function
STEM-ADF	Scanning Transmission Electron Microscope-Annular Dark Field Imaging
TEM-BF	Transmission Electron Microscope-Bright Field Imaging
Pd/C	Palladium Nanoparticles on Carbon Support
Pt/C	Platinum Nanoparticles on Carbon Support
Pt-Li/C	Lithium Doped Platinum Nanoparticles on Carbon Support
Pd-^{int}Li/C NPs	Interstitially Lithium Doped Palladium Nanoparticles on Carbon Support
Pd-^{int}B/C NPs	Interstitially Boron Doped Palladium Nanoparticles on Carbon Support
TGA	Thermogravimetric Analyser
HMF	5-(Hydroxymethyl)furfural
DMTHF	2,5-Dimethyltetrahydrofuran
MFA	5-Methyl Furfuryl Alcohol
FA	Furfuryl Alcohol

MEFA	5-[(1-methylethoxy) methyl]-2-furanmethanol
BHMF	2,5-Bis(hydroxymethyl)furan
MF	5-Methyl Furfural
ZLP	Zero Loss Peak

List of Tables

Table 1.1. Major features, advantages, and disadvantages of homogeneous, heterogeneous and enzymatic catalysts. 5
Table 1.2. Analytical techniques used in the characterisation of light-element modification of transition-metal NPs.[60] 28
Table 1.3. Catalytic performance of Pt-based catalysts for hydrogenation of HMF to BHMF.[132] 31
Table 3.1. The summary of reaction temperature and time used in hydrogenation of HMF reaction. 87
Table 3.2. Parameters of ADF imaging simulation. 88
Table 3.3. Parameters of ADF imaging simulation. 89
Table 3.4. Parameters of ADF imaging simulation. 90
Table 3.5. Parameters of phase imaging simulation. 91
Table 3.6. Parameters of phase imaging simulation at the 60, 80 and 200 kV. 92
Table 4.1. Catalytic performance of Pd-based catalysts for hydrogenation of acetylene to ethylene. 96
Table 4.2. Data of XRD patterns of Pd before/after B doping. 100
Table 4.3. R-factors of 5 wt% Pd-^{int}B/C samples by Le Bail fitting. 102
Table 4.4. Summary of Space group and lattice parameters for the structure of 5 wt% Pd-^{int}B/C retrieved by TOPAS refinement. 102
Table 4.5. The list of the maximum radius of a dopant that may be accommodated in an tetrahedral or octahedral hole in a close-packed solid composed of spheres of radius r. 105
Table 4.6. Lattice parameter and occupancy versus temperature of 50 wt% Pd-^{int}B/C. 106
Table 4.7. EELS quantification analysis results of four 5 wt% Pd-^{int}B/C NPs. 110
Table 5.1. Data of XRD patterns of Pd before/after Li doping. 124
Table 5.2. R-factors of 5 wt% Pd-^{int}Li/C samples by Le Bail. 128
Table 5.3. Summary of the space group and lattice parameters for the structure of 5 wt% Pd-^{int}Li/C retrieved by TOPAS refinement. 128
Table 5.4. Summary of GOF for the structure of 5 wt% Pd-^{int}Li/C retrieved by TOPAS refinement. 129
Table 5.5. Microstrain measurement of the 5 wt% Pd/C and 5 wt% Pd-^{int}Li/C. 129
Table 5.6. The relationship between radius ratio and coordination number. 134
Table 5.7. Lattice parameter and occupancy versus temperature of 50 wt% Pd-^{int}Li/C. 135
Table 6.1. Measurement of weight loss during the TGA of Li(OAc)·2H_2O, Pt/C and Li(OAc)·2H_2O and 20 wt% Pt/C. 157
Table 6.2. Data of XRD patterns of Pt before/after thermal calcination at 650 °C after 2 hours, in the presence of the Li(OAc)·2H_2O. 160
Table 6.3. R-factors of Pt/C sample by Rietveld method. 163
Table 6.4. Summary of space group and lattice parameters for the structure of the 20 wt% Pt/C retrieved by TOPAS refinement. 163
Table 6.5. R-factors of 20 wt% Pt-Li/C sample by Rietveld method. 165
Table 6.6. Summary of space group and lattice parameters for the structure of the 20 wt% Pt-Li/C retrieved by TOPAS refinement. 166
Table 6.7. Curve-fitting results of 20 wt% Pt/C and 20 wt% Pt-Li/C. 171
Table 6.8. ^{7}Li MAS ssNMR of conventional lithium species. 172
Table 6.9. Catalytic performances of 20 wt% Pt/C and 20 wt% Pt-^{sub}Li/C in the hydrogenation of HMF in IPA. Reaction conditions: [HMF] =0.126 g, T =120 °C; P = 30 bar; t = 2 hours. 179
Table 6.10. Time-course of hydrogenation HMF with 20 wt% Pt/C and 20 wt% Pt-^{sub}Li/C with regards to the conversion and the selectivity toward BHMF in IPA. 180
Table 8.1. Catalytic performances of 5 wt% Pd/C, 5 wt% Pd-^{int}B/C and 5 wt% Pd-^{int}Li/C in the hydrogenation of HMF in IPA. Reactions: HMF = 0.126 g, T = 120 °C; P = 30 bar; t = 2 hour. 211

List of Figures

Figure 1.1. Examples of the most important catalytic reactions. The figure is drawn on basis of ref. 45 and ref. 46. 6
Figure 1.2. Volcano plot: the reaction temperature, for a set reaction rate of formic acid decomposition, plotted against the enthalpy of formation of the transition metal formate. This figure has been reproduced from ref. 49 with permission from Royal Society of Chemistry, copyright 2014..... 7
Figure 1.3. Schematic representation of the size regime of NPs related to general "micro" scale objects, cell, virus and the wavelength of the ultraviolet wave. This figure has been reproduced from ref. 51 with permission from Royal Society of Chemistry, copyright 2009. 8
Figure 1.4. An example of the relationship between melting point and particle size. This figure has been reproduced from ref. 63 with permission from American Physical Society, copyright 1976..... 10
Figure 1.5. An example of how the coordination number of the surface atoms varies with the particle size. This figure has been reproduced from ref. 65 with permission from Royal Society of Chemistry, copyright 2014. 11
Figure 1.6. Geometric and electronic structures of the particles with different sizes (single atom, cluster and nanoparticle). This figure has been reproduced from ref. 66 with permission from American Chemical Society, copyright 2018. 11
Figure 1.7. Schematics representations of metal NPs in different shapes. From left to right: cube, tetrahedron, octahedron, bar, and sphere-like shape..... 12
Figure 1.8. The example of different surfaces of FCC metal Platinum (Pt) NPs. (a) (100) of FCC. (b) (111) of FCC (c) (110) of FCC. This figure has been reproduced from ref. 65 with permission from Royal Society of Chemistry, copyright 2014. 12
Figure 1.9. The conventional SMSI formation process. This figure has been reproduced from ref. 78 with permission from Springer Nature, copyright 2020. Reducible oxides are characteristic of formation of oxygen vacancy or donation of oxygen to an adsorbed species easily in comparison with nonreducible oxides. The formation of oxygen vacancy or donation of oxygen to an adsorbed species can result in change of surface composition, from M_nO_m to M_nO_{m-x}. The removal of oxygen can lead to excess electrons that are redistributed on the cation empty levels, and hence changing their oxidation state. Conventional reducible oxides are TiO_2, WO_3, NiO, Fe_2O_3, CeO_2, etc..[79] 14
Figure 1.10. Schematic illustration of three main patterns. (a) core-shell. (b) heterostructure. (c) Mix-alloy. This figure has been reproduced from ref. 89 with permission from WILEY-VCH, copyright 2011. 16
Figure 1.11. Schematic representation of intermetallic compound (Left) and solid solution alloy (Right). This figure has been reproduced from ref. 58 with permission from American Chemical Society, copyright 2008. 17
Figure 1.12. A schematic of substitutional and interstitial solid solution alloys. (a) Substitutional solid solution alloy, atoms of the host metal systems are annotated with green dots; atoms of the foreign atoms are annotated with blue dots. (b) Interstitial solid solution alloy, atoms of the host metal systems are annotated with green dots; atoms of the foreign atoms are annotated with yellow dots. 19
Figure 1.13. Pressure-concentration-temperature phase diagram of the Pd-H. This figure has been reproduced from ref. 138 with permission from Wiley-VCH, copyright 2019..... 24
Figure 1.14. An example of the chemical production of building block chemicals and liquid fuels from biomass-derived HMF.[174] This figure has been reproduced from ref. 174 with permission from Royal Society of Chemistry, copyright 2014. 30
Figure 2.1. A typical Bragg Brentano geometry configuration of lab-source X-ray diffractometer. This figure was drawn on basis of ref. 4..... 49
Figure 2.2. A typical configuration of SR-XRD beamline. This figure was drawn on basis of ref. 5. 50
Figure 2.3. Scattering of X-rays from the 1st and 2nd rows of atoms in a crystal lattice. This figure was drawn on basis of ref. 6..... 50

Figure 2.4. A schematic of a neutron diffraction experiment. This figure was drawn on basis of ref. 10. 52
Figure 2.5. A schematic representation of the process for collecting PDF scattering information. This figure was drawn on basis of ref. 14..... 54
Figure 2.6. A schematic of ICP-MS configuration. This figure was drawn on basis of ref. 22. 56
Figure 2.7. The schematic of XPS instrumental configuration. This figure was drawn on basis of ref. 23..... 57
Figure 2.8. Energy level diagram for a sample in good electrical contact. This figure has been reproduced from ref. 24 with permission from Elsevier, copyright 2020..... 58
Figure 2.9. The energy difference between the α and β spin state is dependent on the applied magnetic field B_0. This figure was drawn on basis of ref. 6. 60
Figure 2.10. In magic angle spinning, the sample rotates at 54.74º with respect to the external magnetic field. This figure was drawn on basis of ref. 27..... 61
Figure 2.11. (a) Ray schematic without aberration corrector. (b) Ray schematic with an aberration corrector. (c) Ray schematic of chromatic aberration. (d) Ray schematic after correction of chromatic aberration. This figure was drawn on basis of ref. 31, 32..... 64
Figure 2.12. (a) The schematic optical configuration of TEM imaging mode. (b) The type of signals generated when electron beam interacts with a specimen. (c) The Schematic optical configuration of STEM imaging mode. This figure was drawn on basis of ref. 37..... 65
Figure 2.13. Schematic of EELS configuration in STEM mode. This figure was drawn on basis of ref. 42..... 67
Figure 2.14. (a) A typical example of Pd-^{int}Li/C EELS spectrum. (b) A typical example of Pd-^{int}B/C EELS spectrum..... 68
Figure 2.15. (a) An instrumental configuration of STEM ptychography. When the probe is scanned across the specimen, the intensity of the electrons scattered to high angles is collected by the ADF detector, while the pixelated detector records a 2D diffraction pattern. (b) An schematic representation of 4-dimentional dataset G(K_f, Qp) for a typical Q_p (spatial frequency), where two diffracted beams ($\pm Q_p$) overlap with the direct beam. This figure was drawn on basis of ref. 49..... 70
Figure 2.16. A schematic diagram of the GC-MS/GC set-up used in this work. This figure is drawn on the basis of ref. 56. 71
Figure 4.1. Lab source XRD patterns of 5 wt% Pd/C (red), 5 wt% Pd-^{int}B/C (orange). The peaks labelled with dash lines corresponding to Pd (111), (200), (220), (311) and (222) are characteristic of the Pd face-centred cubic (FCC) structure.[18] 99
Figure 4.2. SXRD diffraction patterns of the 5 wt% Pd/C and 5 wt% Pd-^{int}B/C. 101
Figure 4.3. (a) A typical example of 5 wt% Pd-^{int}B/C NP contains FCC and HCP phase, which are demonstrated in inset (b). FCC (ABCA) and HCP (ABA) stacking have been annotated by red, blue and green dots. These dots represent different atomic layers. 103
Figure 4.4. Probe average structural distortion by using *in-situ* XPDF and PDFgui. (a) XPDF profile of 50 wt% Pd/C and 50 wt% Pd-^{int}B/C at room temperature provides information on Pd−Pd bond distance at the range of 2 to 6 Å. (b) *in-situ* XPDF of Pd-^{int}B/C. The temperature is rising up from room temperature to the elevated temperature, at the range of 2 to 6 Å. (c) The relationship between the Pd–Pd lattice parameter and corresponding B occupancy possibility in the octahedral sites under different temperature. (d) A typical fit – fitting range = 1.5 – 15 Å. R_w = 12.5%; other fittings parameters can be found in Table 4.6. 104
Figure 4.5. ^{105}Pd VOCS static NMR comparing 50 wt% Pd-^{int}B/C to Pd metal, PVP stabilised NPs and the 50 wt% Pd/C precursor labelled with their respective particle size distributions.[30] 108
Figure 4.6. Typical EELS elemental analysis of the 5 wt% Pd-^{int}B NP on the carbon support. (a) EELS spectrum extracted from the EELS spectrum image recorded from a Pd-^{int}B NP. The three edges are starting at 188 eV, 284 eV and 334 eV. (b) and (e) are the spectrum images of Pd-^{int}B NPs. Elemental maps of the Pd-^{int}B NPs are presented in the (c), (d), (f) and (g), where the Pd-$M_{4,5}$ is annotated with

blue and the B-K edge is annotated with red, respectively. The B elemental distribution in (d) is different from that in (g), highlighting that the B doping source distributes inhomogeneously for each NP. .. 109
Figure 4.7. Simultaneously acquired Z-contrast STEM-ADF and phases images (reconstructed by Wigner Distribution Deconvolution (WDD)) of a 5 wt% Pd-^{int}B dispersed on the carbon support, where is oriented in the [110] zone axis. (a) ADF-image of Pd-^{int}B NP. Inset (b) from (a) highlights an enlarged area. Inset (d) from (c) phase image reconstructed by using a WDD method. New atomic columns arise after aberration correction between the Pd atomic columns, which matches well with the general crystal model proposed by XPDF. This experiment was performed at an emission current of 6.0 μA, pixel dwell time of 0.25 ms and a total dose of 0.9×10^6 $e^-Å^{-2}$. 112
Figure 4.8. Simulated ADF images of $PdB_{0.2}$ single crystal and Pd over different thicknesses. The simulated ADF images have the same number of repeating unit cells. Owing to the difference in the Pd−Pd lattice parameter for Pd and Pd-^{int}B specimen, the thickness is slightly different. B atomic columns are not visible in the ADF image because of the Z-contrast rule. 113
Figure 4.9. Simulated phase image of Pd and $PdB_{0.2}$ over different thickness. Multislice frozen phonon methods implemented in the MULTEM was used for the simulation. B atoms can be observed at the interstitial sites. Pd atomic columns demonstrate phase contrast reversal and wrapping, which is attributed to the dynamical scattering of electrons, so that affects the multiplicative approximation. This phenomenon partially leads to the well-known contrast mismatch between experimental phase images and simulations, named as the Stobbs factor.[43] 114
Figure 5.1. Particle size analysis by STEM-ADF imaging. (a) Overview STEM-ADF image of 5 wt% Pd-^{int}Li/C NPs. (b) Histogram from size analysis of catalyst particles. Average particle size 5.77 nm. 123
Figure 5.2. XRD patterns of 5 wt% Pd/C (blue), 5 wt% Pd-^{int}Li/C (green). The peaks labelled with dash lines corresponding to the Pd (111), (200), (220), (311) and (222) are characteristics of the Pd face-centred cubic (FCC) structure. 124
Figure 5.3. The ^{105}Pd static VOCS NMR of 50 wt% Pd/C, 50 wt% Pd-^{int}Li/C at 14.1 T.[9] 125
Figure 5.4. SXRD patterns of the 5 wt% Pd/C and 5 wt% Pd-^{int}Li/C samples. Diffraction patterns of Pd/C are annotated with blue and diffraction patterns of the Pd-^{int}Li/C are annotated with green. The peaks labelled with dash lines corresponding to the Pd (111), (200), (220), (311) and (222) were characteristics of the Pd face-centred cubic (FCC) structure. 127
Figure 5.5. Neutron diffraction for the time-of-flight neutron profiles measured for 50 wt% Pd/C and 50 wt% Pd-^{int}Li/C. The Pd phases corresponding to the individual spacing are annotated with black. * means unknown phases. The peaks at 2.1390 and 1.5108 Å are anticipated as the phase of BCT carbon, based on ref. 16. 131
Figure 5.6. Local structural distortion probed by using in-situ XPDF and PDFgui. (a) XPDF analysis of 50 wt% Pd/C and 50 wt% Pd-^{int}Li/C at room temperature providing data on Pd−Pd bond distance at the range of 2 to 6 Å. (b) in-situ XPDF of 50 wt% Pd-^{int}Li/C from room temperature to the elevated temperature at the range of 2 to 6 Å. (c) The Pd–Pd lattice parameter and corresponding Li occupancy in the octahedral sites against temperature. (d) A typical fit – fitting range = 1.5 – 15 Å. R_w = 20.6%; other fittings parameters can be found in Table 5.6. 133
Figure 5.7. EELS of 5 wt% Pd-^{int}Li/C and 5 wt% Pd/C at 200 kV. (a) and (e) are SI survey images of Pd/C and Pd-^{int}Li/C, respectively, which indicate the locations of the NPs to be characterised. (b) and (f) are spectrum images of Pd/C and Pd-^{int}Li/C, where EELS spectra were taken along each pixel of the selected red square. (c) is the EELS spectrum of Pd/C and (g) is the EELS spectrum of Pd-^{int}Li/C. (d) is the inset of EELS spectrum (c), which shows the Pd-$N_{2,3}$ edge starting from the 51 eV. (h) is the inset of EELS spectrum (g), which shows the Pd-$N_{2,3}$ edge starting from 51 eV. Additionally, the Li-K edge is absent in the spectrum. The literature location of the Pd-$N_{2,3}$ edge and Li-K edge are annotated with black dotted lines respectively. The resolution of the EELS is 0.8 eV in accordance with the full width at half maximum (FWHM) of the ZLP (see Appendix Figure 8.11). 136
Figure 5.8. EELS of 5 wt% Pd-^{int}Li/C and 5 wt% Pd/C at 80 kV. (a) and (e) are SI survey images of Pd/C and Pd-^{int}Li/C, respectively, which indicate the location of the NPs to be characterised. (b) and (f)

are spectrum images of Pd/C and Pd-^{int}Li/C, where EELS spectra were taken along each pixel of the selected red square. (c) is the EELS spectrum of Pd/C and (g) is the EELS spectrum of Pd-^{int}Li/C. (d) is the inset of EELS spectrum (c), which shows the Pd $N_{2,3}$ edge starting from 51 eV. (h) is the inset of EELS spectrum (g), which shows the Pd-$N_{2,3}$ edge starting from 51 eV. Additionally, the Li-K edge is absent in the spectrum. The literature location of the Pd-$N_{2,3}$ edge and the Li-K edge are annotated with black dotted lines respectively. The resolution of the EELS is 0.8 eV in accordance with the full width at half maximum (FWHM) of the ZLP (see Appendix Figure 8.12)..... 137
Figure 5.9. EELS of 5 wt% Pd-^{int}Li/C and 5 wt% Pd/C at 60 kV. (a) and (e) are SI survey images of Pd/C and Pd-^{int}Li/C, respectively, which indicate the location of the NPs to be characterised. (b) and (f) are spectrum images of Pd/C and Pd-^{int}Li/C, where EELS spectra were taken along each pixel of the selected red square. (c) is the EELS spectrum of Pd/C and (g) is the EELS spectrum of Pd-^{int}Li/C. (d) is the inset of EELS spectrum (c), which shows the Pd $N_{2,3}$ edge starting from 51 eV. (h) is the inset of EELS spectrum (g), which shows the Pd-$N_{2,3}$ edge starting from 51 eV. Additionally, the Li-K edge is absent in the spectrum. The literature location of the Pd-$N_{2,3}$ edge and the Li-K edge are annotated with black dotted lines respectively. The resolution of EELS is 0.2 eV in accordance with full width at half maximum (FWHM) of the ZLP (see Appendix Figure 8.13). 138
Figure 5.10. Z-contrast STEM-ADF imaging of 5 wt% Pd-^{int}Li/C NP. (a) is a typical Z-contrast STEM-ADF of a 5 wt% Pd-^{int}Li/C NP, which is well-orientated in the zone axis <110> direction. Two phases are found in (a) and has been further demonstrated in (b). Region annotated with green shows FCC structure; region annotated with orange shows HCP structure. FCC (ABCA) and HCP (ABA) stacking have been annotated by red, blue and green dots. These dots represent different atomic layers. 140
Figure 5.11. Simulated Z-contrast ADF-STEM image of Pd-^{int}Li/C and Pd/C over the different thickness of 2 nm, 4 nm and 6 nm respectively. 142
Figure 5.12. Simultaneous Z-contrast ADF-STEM image and phase image of 5 wt% Pd-^{int}Li/C. (a) is the ADF imaging of the NP. The inset (b) shows enlarged images with an atomic configuration orientated in <110> direction. The Li atomic columns are invisible because of low atomic number. (c) is the phase image reconstructed via the WDD method. (d) is the inset of phase image (c), which shows that contrast resolves and new atomic columns labelled with blue arrows emerge at octahedral sites. 143
Figure 5.13. Ptychographic imaging simulation of Pd-^{int}Li over different thicknesses and Li octahedral site occupancy (occ) at 200 kV (semi-convergence angle: 22.3 mrad). 144
Figure 5.14. Simultaneous Z-contrast ADF-STEM image and phase image of 5 wt% Pd-^{int}Li/C at 80 kV. (a) is the ADF imaging of the NP. The inset (b) shows enlarged images with an atomic configuration orientated in <110> direction. The Li atomic columns are invisible because of low atomic number. (c) is the phase images reconstructed via WDD method. (d) is the inset of phase image (c). 145
Figure 5.15. Ptychographic imaging simulation of Pd-^{int}Li over different thickness at 80 kV (semi-convergence angle: 24.8 mrad). Image contrast was compared at Li octahedral site occupancy occ = 0 and occ = 1, respectively. These results reveal that residue intensity can be found in the interstitial sites, but the aperture is not big enough to fully resolve the Li atomic columns. 146
Figure 5.16. Ptychographic imaging simulation of Pd-^{int}Li with the thickness of 2 nm at 80 kV (semi-convergence angle 31.74 mrad). Image contrast was compared at octahedral site occupancies (occ) of 0 and 1, respectively. 146
Figure 5.17. Ptychographic imaging simulation of Pd-^{int}Li over the different thicknesses at 60 kV (semi-convergence angle: 30.6 mrad). Image contrast was compared at Li site occupancies of (occ = 0) and (occ = 1), respectively. These results reveal that residue intensity can be found in the interstitial sites, but the aperture is not big enough to fully resolve the Li atomic columns. 147
Figure 5.18. Ptychographic imaging simulation of Pd-^{int}Li with a thickness of 2 nm at 60 kV (semi-convergence angle 39.1 mrad). Image contrast was compared at Li site occupancies of occ = 0 and occ = 1, respectively. 148
Figure 6.1. Suggested partial phase diagram of Pt-Li based on differential thermal analysis. This figure has been reproduced from ref. [4] with permission from Springer Nature, copyright 1991. 154

Figure 6.2. TGA of 20 wt% Pt/C, Li(OAc)·2H_2O and the mixture of Li(OAc)·2H_2O with 20 wt% Pt/C from 0 to 1000 ℃. The weight loss in each stage is further displayed in Table 6.1. 157
Figure 6.3. Ex-situ XRD profiles of heating 20 wt% Pt/C + Li (OAc)·2H_2O at different temperatures for two hours under a N_2 atmosphere. Mixtures were characterised with XRD after heating at 350, 400, 450, 500, 550, 600, 650, 700, 750 ℃, without vacuum filtration treatment. The inset shows an example that diffraction peaks of Pt shift to a higher angle when the temperature is at 650 ℃. The peaks labelled with dash lines corresponding to the Pt (111), (200), (220), (311) and (222) are characteristics of the Pt face-centred cubic (FCC) structure. 159
Figure 6.4. Ex-situ XRD profiles of 20 wt% Pt/C and 20 wt% Pt/C + Li(OAc)·2H_2O after thermal treatment at 650 ℃ for 2 hours under a N_2 environment. The collected sample was characterised by XRD without vacuum filtration treatment. The peaks labelled with dash lines corresponding to the Pt (111), (200), (220), (311) and (222) are characteristic of the Pt face-centred cubic (FCC) structure. 161
Figure 6.5. (a) SXRD profiles of 20 wt% Pt/C and 20 wt% Pt-Li/C. (b) shows the enlarged diffraction patterns at the range of 8 to 32° enlarged from the inset annotated with blue square. * is used to label the peaks locating at 10.5º, 12.2°, 17. 2°, 20.23°, 26.7° and 27.3°, which are corresponding to the index of (111), (002), (022), (113), (133), (024) of the Pt_7Li, respectively. 162
Figure 6.6. (a) Structure of Pt_7Li in which the atomic arrangement of Pt is (0, 0, 0) and (0, 0.25, 0.25), and the atomic arrangement of Li is (0.5, 0.5, 0.5).[3,4] (b) Simulated SXRD of Pt_7Li based on the experimental setting in the Diamond Light Source I11 beamline with the incident wavelength of 0.825300 Å..... 164
Figure 6.7. A schematic shows the Pt/C is substituted by foreign Li dopants to generate Pt_7Li, despite this is an interstitial intermetallic compound on the basis of the Li location. 166
Figure 6.8. Neutron diffraction for the TOF neutron profiles over the 20 wt% Pt/C (red) and 20 wt% Pt-Li/C (blue). The Pt phases corresponding to the individual spacing are annotated in black. * means unknown diffraction phases. The peaks at 2.1390, 1.5108 and 1.2190 Å area anticipated as the phases of the BCT carbon, based on ref. 23. 167
Figure 6.9. XPS profile of 20 wt% Pt/C and 20 wt% Pt-Li/C. (a) A survey spectrum from the surface of the 20 wt% Pt/C and 20 wt% Pt-Li/C. (b) inset from (a) shows the enlarged spectrum at the range of 45 to 67 eV (annotated with green square). Peaks have been corrected based on the measurement of C1s..... 169
Figure 6.10. Pt 4f XPS profiles for (a) 20 wt% Pt-Li/C and (b) 20 wt% Pt/C. 170
Figure 6.11. ^{7}Li MAS ssNMR chemical shifts of 20 wt% Pt/C and Li(OAc)·2H_2O before and after thermal treatment. (a) 20 wt% Pt/C and Li(OAc)·2H_2O before thermal treatment. The peak located at -1.39 ppm is attributed to the Li(OAc)·2H_2O. (b) 20 wt% Pt/C and Li(OAc)·2H_2O after thermal treatment. The obtained sample was washed with EtOH and water to remove the unreacted Li species and Li based side products before measurement. The signal can be deconvoluted into two peaks. One is located at -0.1 ppm, and the other is located at -9.9 ppm. 172
Figure 6.12. EELS study of 20 wt% Pt/C and 20 wt% Pt-Li/C. (a) ADF image of 20 wt% Pt-Li/C NP, where EELS spectra were taken along each pixel of the selected area. (b) EELS spectra image of the 20 wt% Pt-Li/C NP. (c) EELS spectra of the selected square in EELS spectra image (b). (d) ADF image of 20 wt% Pt/C NP, where EELS spectra were taken along each pixel of the selected area. (e) EELS spectra of the 20 wt% Pt/C. (f) EELS spectra of the selected square. The locations of the Pt low loss edge, $O_{2,3}$ and $N_{6,7}$, are annotated with the red dash line.[33] 173
Figure 6.13. Simultaneously acquired Z-contrast STEM-ADF, ptychographic phase images of 20 wt% Pt-Li/C NPs without miss-tilt. (a) Z-contrast STEM-ADF image of 20 wt% Pt-Li/C NP orientated in the <110> zone axis. (b) Inset from (a) highlights an enlarged area of the NP. Pt_7Li orientated in the <110> direction is superimposed with the inset, demonstrating a good match between the Pt_7Li model and the NP structure. Mixed Pt and Li atoms are annotated with blue dots and Pt atoms are annotated with gray dots. (c) ADF intensity line profile taken along the line is indicated in (a). (d) Ptychographic phase image was reconstructed by using a Wigner Distribution Deconvolution (WDD) method.[39] (e) Inset from (d) does not show any new contrast between the Pt atomic columns. (f) Ptychography phase

image intensity line profile taken along the line is indicated in (e). (h), (i) and (j) are the ADF image simulations of the Pt_7Li over different thicknesses. Pt columns are annotated with red and Pt-Li columns are annotated with blue. 174
Figure 6.14. Proposed catalytic reaction pathway of HMF reaction. 181
Figure 8.1. Particle size of the 5 wt% Pd-^{int}B/C NPs. (a) ADF-STEM image of 5 wt% Pd-^{int}B NPs dispersed on the carbon support. The average particle size is 6.69 nm, which is obtained from manual particle size analysis depicted in the histogram (b). 192
Figure 8.2. Lab source XRD patterns of 50 wt% Pd/C (black), 50 wt% Pd-^{int}B/C (red) and 50 wt% Pd-^{int}Li/C (blue). 193
Figure 8.3. A schematic representation of the derivation for the min. and max radius ratio for tetrahedral (a) and octahedral interstitial sites of FCC (b), and cubic interstitial site. The dot line in (a) represents ¼ unit cell edge. The figure is drawn on basis of ref. 1. 194
Figure 8.4. Example of a Pd-^{int}B/C intrinsic stacking fault model. Blue dots represent Pd atoms; red dots represent octahedral sites; grey dots represent tetrahedral sites. (a) Pd atomic configuration oriented in a <110> direction. (b) demonstrates an example of Pd atomic configuration projected along a [-1 1 0] direction if an intrinsic stacking fault happens. (c) Pd atomic configuration oriented in a <110> with octahedral sites and tetrahedral sites shown. (d) partially demonstrates the positions where Pd atoms may emerge if an intrinsic stacking fault happens. These models show no atomic occupancy at the observed octahedral site columns, but rather atomic occupancy appearing close to tetrahedral sites.196
Figure 8.5. Example of a Pd-^{int}B/C extrinsic stacking fault model. Blue dots represent Pd atoms; red dots represent octahedral sites; grey dots represent tetrahedral sites. (a) Pd atomic configuration oriented in a <110> direction. (b) demonstrates an example of Pd atomic configuration projected along a [-1 1 0] direction if an extrinsic stacking fault happens. (c) Pd atomic configuration oriented in a <110> with octahedral sites and tetrahedral sites shown. (d) partially demonstrates the positions where Pd atoms may emerge if an extrinsic stacking fault happens. These models show no atomic occupancy at the observed octahedral site columns, but rather atomic occupancy appearing close to tetrahedral sites.197
Figure 8.6. Example of a Pd-^{int}B/C twinning fault model, where plane A is a twinning line. Blue dots represent Pd atoms; red dots represent octahedral sites; grey dots represent tetrahedral sites. (a) Pd atomic configuration oriented in a <110> direction. (b) demonstrates an example of Pd atomic configuration projected along a [-1 1 0] direction if a twinning fault happens. (c) Pd atomic configuration oriented in a <110> with octahedral sites and tetrahedral sites shown. (d) partially demonstrates the positions where Pd atoms may emerge if a twinning fault happens. These models show no atomic occupancy at the observed octahedral site columns, but rather atomic occupancy appearing close to tetrahedral sites. 198
Figure 8.7. Example of a Pd-^{int}B/C twinning fault model, where plane B is a twinning line. Blue dots represent Pd atoms; red dots represent octahedral sites; grey dot represent tetrahedral sites. (a) Pd atomic configuration oriented in a <110> direction. (b) demonstrates an example of Pd atomic configuration projected along a [-1 1 0] direction if a twinning fault happens. (c) Pd atomic configuration oriented in a <110> with octahedral sites and tetrahedral sites shown. (d) partially demonstrates the positions where Pd atoms may emerge if a twinning fault happens. These models show no atomic occupancy at the observed octahedral site columns, but rather atomic occupancy appearing close to tetrahedral sites.199
Figure 8.8. Example of a Pd-^{int}B/C twinning fault model, where plane C is a twinning line. Blue dots represent Pd atoms; red dots represent octahedral sites; grey dots represent tetrahedral site. (a) Pd atomic configuration oriented in a <110> direction. (b) demonstrates an example of Pd atomic configuration projected along a [-1 1 0] direction if a twinning fault happens. (c) Pd atomic configuration oriented in a <110> with octahedral sites and tetrahedral sites shown. (d) partially demonstrates the positions where Pd atoms may emerge if a twinning fault happens. These models show no atomic occupancy at the observed octahedral site columns, but rather atomic occupancy appearing close to tetrahedral sites.200
Figure 8.9. Simultaneously acquired Z-contrast STEM-ADF and ptychographic phase image of a 5 wt% Pd-^{int}B/C NP oriented in the relatively defect free [211] zone axis. (a) Z-contrast STEM-ADF image of a Pd-^{int}B/C NP. (b) inset from (a) shows an enlarged area of the NP. (c) Ptychographic phase

image reconstructed using the Wigner Distribution Deconvolution (WDD) method. (d) inset from (c) shows an enlarged area of the NP. The enlarged ptychography phase image shows intensity in some, but not all, of the octahedral sites suggesting that these are not artefacts due to aberrations. The ADF image does not show corresponding intensity suggesting the presence of B in the octahedral site. This matches well with the model predicted by XPDF (overlaid). 201
Figure 8.10. Examples of the polycrystalline 5 wt% Pd-^{int}Li/C NPs, which are demonstrated in (a) and (b). 202
Figure 8.11. ZLP of EELS at 200 kV. The full width at half maximum (FWHM) of the ZLP is 0.8 eV. 203
Figure 8.12. ZLP of EELS at 80 kV. The full width at half maximum (FWHM) of the ZLP is 0.8 eV. 204
Figure 8.13. ZLP of EELS at 80 kV. The full width at half maximum (FWHM) of the ZLP is 0.15 eV. 205
Figure 8.14. Strain variation relative to the centre of a Pd-^{int}Li/C NP, computed by StatSTEM[7]. (a) The reference position for the straining mapping. (b) ε_{xx} strain map of the Pd-^{int}Li NP. (c) ε_{yy} strain map of the Pd-^{int}Li NP. (d) ε_{xy} strain map of the Pd-^{int}Li NP. The intensity scale shows relative deformation. To clarify the nomenclature, terms "compressive strain" ($\varepsilon < 0$) and "tensile strain" ($\varepsilon > 0$) refer to the contracted and expanded lattice parameters measured with respect to the reference region (a).[32] With regards to the type of the strain, εxx and εyy are the normal strain, and the εxy is the shear strain. HCP and left lateral FCC facet were excluded for strain mapping computation to improve the accuracy of the result. 206
Figure 8.15. Thickness of the NP acquired at 200 kV. Line profile (a) was taken across the NP, the thickness of the NP is about 5.6 nm in accordance with (b). 207
Figure 8.16. Thickness of the NP acquired at 80 kV. Line profile (a) was taken across the NP, the thickness of the NP is about 4.5 nm in accordance with (b). 207
Figure 8.17. BF-TEM of 20 wt% Pt-Li/C NPs. 208
Figure 8.18. ZLP of EELS at 200 kV. The full width at half maximum (FWHM) of the ZLP is 0.95 eV. 209
Figure 8.19. Line profile (b) indicates the thickness of the NP in (a) is 5.822 nm. 210

Contents

Dedication i
Declaration ii
Acknowledgement iii
Abstract v
Abbreviations vi
List of Tables viii
List of Figures ix
Thesis Overview 1
Chapter 1 Introduction 3
1.1 Overview of Catalysts 3
1.2 Heterogeneous Catalysts 5
1.2.1 Categories of Heterogeneous Catalysts 5
1.2.2 Chemisorption of the Heterogeneous Catalyst 7
1.3 Nanoparticles for Heterogeneous Catalysis 7
1.4 Chemical and Structural Tuning of the Catalytic Activity 8
1.4.1 Structural Tuning 9
1.4.2 Chemical Tuning 13
1.5 Classification and Thermodynamics of Nanoalloys 16
1.5.1 The Structure of Nanoalloys 16
1.5.2 Categories and Thermodynamics of the Mixed-Nanoalloy 17
1.6 Categories of the Solid Solution Alloy 19
1.6.1 Substitutional Alloy 20
1.6.2 Interstitial Alloy 20
1.7 The Interstitial Alloys of Pd and Pt 22
1.7.1 Background of Pd and Pt metals 22
1.7.2 Palladium Based Interstitial Alloy 23
1.7.3 Platinum Based Interstitial Alloy 26
1.8 Characterisation of Light Element Modified Nanoparticles. 27
1.9 Hydrogenation of HMF to Value-Added Chemicals 29
1.9.1 Importance of BHMF 30
1.9.2 Literature Work of Pt Catalysed Hydrogenation of HMF to BHMF 31
1.10 Objectives 32
1.11 References 34

Chapter 2 Principle of Analytical Techniques 47
2.1 Introduction 47
2.2 Thermogravimetric Analysis (TGA) 48
2.3 X-Ray Diffraction (XRD) 48
2.4 Neutron Diffraction 51
2.5 Pair Distribution Function (PDF) 53
2.6 Inductively Coupled Plasma Mass Spectroscopy (ICP-MS) 55
2.7 X-Ray Photoelectron Spectroscopy (XPS) 56
2.8 Solid State Nuclear Magnetic Resonance (ssNMR) 59
2.9 Electron Microscopy 62
2.10 Electron Energy Loss Spectroscopy (EELS) 67
2.11 Electron Ptychography 69
2.12 Gas Chromatography-Mass Spectroscopy (GC-MS) 71
2.13 References 74
Chapter 3 Experimental Procedures 79
3.1 General information 79
3.2 Materials and Methods 79
3.2.1 X-Ray Diffraction (XRD) 79
3.2.2 X-Ray Photoelectron Spectroscopy (XPS) 79
3.2.3 Thermogravimetric Analysis (TGA) 80
3.2.4 Transmission Electron Microscopy-Bright Field Imaging (TEM-BF) 80
3.2.5 Scanning Transmission Electron Microscopy-Annular Dark Field Imaging (STEM-ADF) 80
3.2.6 Electron Energy Loss Spectroscopy (EELS) 80
3.2.7 Ptychography 82
3.2.8 Synchrotron X-Ray Diffraction (SXRD) 82
3.2.9 in-situ X-Ray Pair Distribution Function (XPDF) 83
3.2.10 Solid State Nuclear Magnetic Resonance (ssNMR) 83
3.2.11 Neutron Diffraction 84
3.2.12 Analysis of Product Distribution 84
3.3 Experimental Procedures 85
3.3.1 5 wt% Pd/C Synthesis 85
3.3.2 Pd-^{int}B/C Synthesis 85
3.3.3 Pd-^{nt}Li/C Synthesis 86
3.3.4 Pt-^{sub}Li/C Synthesis 86

3.3.5 Hydrogenation of 5-(hydroxymethyl)furfural (HMF) 86
3.4 Computational Programme 87
3.4.1 ADF Imaging Simulation 87
3.4.2 Ptychographic Imaging Simulation 90
3.4.2.1 Pd-^{int}B/C 90
3.4.2.2 Pd-^{int}Li/C 91
3.5 References 93
Chapter 4 In-Depth Characterisation of Pd-^{int}B/C NPs 95
4.1 Introduction 95
4.2 Objectives and Methodology 98
4.3 X-Ray Diffraction (XRD) 99
4.4 Synchrotron X-Ray Diffraction (SXRD) 101
4.5 In-situ X-Ray Pair Distribution Function (XPDF) 103
4.6 ^{105}Pd VOCS Static Solid State Nuclear Magnetic Resonance (ssNMR) 107
4.7 Electron Energy Loss Spectroscopy (EELS) 109
4.8 Annular Dark Field (ADF)-Ptychography Imaging 111
4.9 Conclusion 115
4.10 References 116
Chapter 5 In-Depth Characterisation of Pd-^{int}Li/C NPs 120
5.1 Introduction 120
5.2 Objectives and Methodology 122
5.3 Initial Characterisation with ICP, XRD and STEM-ADF 123
5.4 ^{105}Pd Static VOC Solid State Nuclear Magnetic Resonance (ssNMR) 125
5.5 Synchrotron X-Ray Diffraction (SXRD) 126
5.6 Neutron Diffraction 130
5.7 In-situ X-Ray Pair Distribution Function (XPDF) 132
5.8 Electron Energy Loss Spectroscopy (EELS) 135
5.8.1 200 kV 136
5.8.2 80 kV 136
5.8.3 60 kV 137
5.9 Annular Dark Field (ADF) Imaging 139
5.10 Ptychographic Imaging at 200 kV 142
5.11 Ptychographic Investigation at Low Voltage 144
5.11.1 Ptychographic Imaging at 80 kV 144
5.11.2 Ptychographic Imaging at 60 kV 147

5.12 Conclusion 148
5.13 References 150
Chapter 6 Design of Platinum Lithium Binary NPs 153
6.1 Introduction 153
6.2 Objectives and Methodology 156
6.3 Thermogravimetric Analysis (TGA) 157
6.4 X-Ray Diffraction (XRD) 159
6.5 Synchrotron X-Ray Diffraction (SXRD) 162
6.6 Neutron Diffraction 167
6.7 X-Ray Photoelectron Spectroscopy (XPS) 168
6.8 ^{7}Li MAS Solid State Nuclear Magnetic Resonance (ssNMR) 171
6.9 Electron Energy Loss Spectroscopy (EELS) 172
6.10 Simultaneous Annular Dark Field (ADF) and Ptychographic Imaging 174
6.11 Catalytic Testing in the Hydrogenation of HMF 176
6.12 Conclusion 182
6.13 References 183
Chapter 7 Conclusion & Future Work 187
7.1 Conclusion 187
7.2 Future Work 188
7.2.1 Pd-^{int}B/C Project 188
7.2.2 Pd-^{int}Li/C Project 189
7.2.3 Pt-^{sub}Li/C Project 189
7.3 References 191
Chapter 8 Appendix 192
8.1 Supporting information of Chapter 4 192
8.1.1 Particle Size Analysis 192
8.1.2 Lab-Source XRD of 50 wt% Pd/C, Pd-^{int}B/C and Pd-^{int}Li/C 193
8.1.3 The derivation for the minimum and maximum radius ratio for tetrahedral and octahedral interstitial sites. 194
8.1.4 Typical Examples of Intrinsic Stacking Faults, Extrinsic Stacking Faults and Twinning Models 196
8.1.5 Additional Ptychographic Dataset of Pd-^{int}B/C NP 201
8.2 Supporting information of Chapter 5 202
8.2.1 Polycrystalline NPs 202
8.2.2 ZLP of EELS 203

8.2.3 Strain Mapping 206
8.2.4 Thickness of the NPs 207
8.3 Supporting information of Chapter 6 208
8.3.1 Particle Distribution of the Pt-^{sub}Li/C NPs 208
8.3.2 ZLP of EELS at 200 kV 209
8.3.3 Thickness of the NPs 210
8.3.4 Hydrogenation of HMF via 5 wt% Pd/C, 5 wt% Pd-^{int}B/C and 5 wt% Pd-^{int}Li/C 211
8.4 References 212

Thesis Overview

This thesis consists of eight chapters, with three chapters summarising the research over three and a half years of DPhil study.

Chapter One– Introduces the basic concept and background knowledge of NPs. The effects that influence the catalytic properties of NPs are summarised in terms of size, shape, support and additives. The characterisation techniques for NPs are summarised in terms of the different incident sources. Target products and employment of metal catalysts for HMF have also been outlined.

Chapter Two– Introduces the background and principle of analytical techniques used for Chapter Four to Six.

Chapter Three– Experimental procedures for synthesis, characterisations, imaging simulation and catalytic testing of the NPs.

Chapter Four– In-depth investigation of Pd-^{int}B/C. Multi-analytical techniques characterise the Pd NPs interstitially modified with B additives. The macro-analytical techniques establish an average crystal model. Additionally, a micro-analytical technique is used to probe the local B concentration via EELS, in an attempt to visualise the B atomic columns directly.

Chapter Five– In-depth investigation of Pd-^{int}Li/C. Similar to Chapter 4. Multi-analytical techniques characterise the Pd NPs interstitially modified with Li additives. The macro-analytical techniques establish an average crystal model. Also, micro-analytical techniques are used to probe the presence of Li by EELS at different accelerating voltages. Due to the knock-on damage issue, it was also attempted to visualise the Li atomic columns at the interstitial sites at lower accelerating voltages, in addition to the conventional 200 kV.

Chapter Six– Synthesis of Pt-Li/C. Synthesis of Pt-Li binary alloy NPs was first to be reported. The materials were characterised via conventional and advanced techniques. Additionally, the catalysts were tested in the selective hydrogenation of HMF to BHMF reaction.

Chapter Seven– Conclusion and future work.

Chapter Eight– Appendix

Chapter 1 Introduction

Catalysts play a vital role in the field of chemistry. A catalyst is needed for at least one step in 90% of chemical processes. Currently due to environmental issues, the world seeks sustainable alternatives to traditional chemical processes; therefore, the societal role of catalysis is becoming increasingly important. According to a survey of U.S. industries, catalysis has been involved in over 60% of the 63 product manufacturing advances and 90% of the 34 process innovations spanning from 1930 to 1980, which reveals its essential role in the field of chemical industries.[1]

1.1 Overview of Catalysts

The definition of a catalyst is a material which can accelerate reaction rate by lowering the activation energy barrier, but is not consumed during the reaction.[2] Catalysts can be enzymatic, homogeneous or heterogeneous.[3] Each catalysts type has its own advantages and limitations, which can be demonstrated in Table 1.1.

Enzymatic catalysis uses enzyme which accelerate a typical life-essential chemical reaction; usually by orders of magnitudes, typically improving the rate of reaction by orders of 10^6 to 10^{20}.[4,5] Enzymes can provide reaction pathways with high selectivity and efficiency, and enable reaction processes under mild conditions. Besides this, the mechanism of enzymatic catalysis is reasonably understood.[4] There is increased interest in enzymatic catalysis due to growing demand for enantiopure pharmaceuticals.[6,7] Additionally, as enzymes are derived from living systems, utilisation of enzymatic catalysts typically bypasses toxicological concerns which arise when using chemical catalysts.[8] Despite the many advantages of enzymatic catalysis, its use in industry is limited due to the stability of the enzyme, which can be denatured at high temperature or high/low pH.[9,10,11,12] Current research related to enzymatic

catalysis is ongoing to enhance stability and increase reaction scope via rational design,[14] directed evolution,[14] chemical modification[13] and immobilisation.[14]

In homogeneous catalysis both the catalyst and the reagents are found in the same phase, typically both are in a liquid phase. Normally, a homogeneous catalyst consists of metal ions surrounded by ligands. Homogeneous catalysis has several distinct advantages that range from understanding of reaction mechanisms,[15] to their exceptional product selectivity and reaction activity.[16,17] The ligand can influence solubility and stability of the metal complex, and also tune the selectivity of a given catalyst towards the synthesis of the target compounds.[18] Homogeneous catalysts can be utilised in the pharmaceutical field,[19] Monsanto process,[20] Wacker process,[21] hydroformylation[22] and polymerisation.[23] The main drawback of homogeneous catalysis is the difficulty in separating the product from the catalyst, and hence in industry, heterogeneous catalysis is preferable.

In heterogeneous catalysis, the phase of catalyst differs from that of the reagents. For instance, the hydrogenation of alkene to alkane is accelerated by the presence of a solid transition metal catalyst.[24] In contrast to homogeneous catalysis, only the surface atoms are available for reaction in heterogeneous catalysts, which means that utilisation of metal atoms is much lower in comparison with the homogeneous catalysts. Except for this, understanding mechanism for a heterogeneous catalytic reaction is often a hurdle because the intermediates are challenging to identify using conventional methods.[25] The use of heterogeneous catalysts is still preferred in industry because they are often stable to harsh reaction conditions (elevated temperatures and/or pressures),[18] and allow easier recycling of the catalyst from the products due to differences in phases.[26] Moreover, heterogeneous catalysts are involved in 90% of chemical production and play an essential role in the production of fine chemicals,[27] crude oil processing and the synthesis of other petrochemicals.[28,29] Furthermore, heterogeneous catalysts

are becoming more prominent in the fields of fuel cells,[30] green chemistry[31] and nanotechnology.[32]

Table 1.1. Major features, advantages, and disadvantages of homogeneous, heterogeneous and enzymatic catalysts.

Type of Catalyst	Advantages	Limitation
Enzymatic	High stereoselectivity and efficiency under mild conditions[4,5]	Temperature and pH sensitive;[33] sometimes are insufficiently stable under operating conditions[12]
	Lower environmental and physiological toxicity[8]	
	Mechanism reasonably understood	
Homogeneous	Mechanism reasonably understood	Difficult separation[33,34]
	High activity and selectivity[34]	
Heterogeneous	Ease of separation	Low metal atom utilisation[33]
	Stable under relatively harsh conditions	Mechanism relatively poorly understand

1.2 Heterogeneous Catalysts

1.2.1 Categories of Heterogeneous Catalysts

The scope of the heterogeneous catalysts is broad, including metals and metal oxides, metal sulfides,[35] nitrides,[36] carbides,[37] phosphates,[38] phosphides,[39] zeolites,[40] ion-exchange resins[41] and clays.[42] In general, the main composition of the catalyst formulations come from metal and metal oxides, particularly from the group of transition metals, because they are more reactive owing to their unfilled d-bands.[43] They have proven their importance in industrial catalysis, since these transition metal-based heterogeneous catalysts have the ability to activate small molecules, such as H_2, O_2, N_2, as well as the C−H, C−O, C−N and C−O bonds.[44] Precious metals, for example Pt or Pd, are particularly important in the field of heterogeneous catalysis, and their most important catalytic processes are summarised in Figure 1.1.[45]

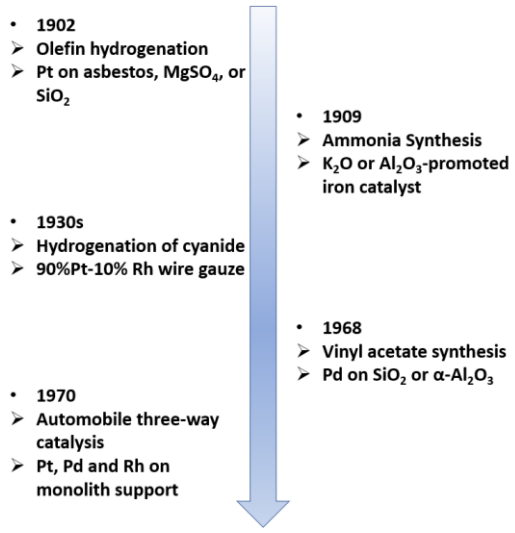


Figure 1.1. Examples of the most important catalytic reactions. The figure is drawn on basis of ref. 45 and ref. 46.

Regarding the number of phases, the type of the heterogeneous catalyst can be classified as uniform and multiphasic catalysts, respectively.[47] If the solid is monophasic and atoms in the bulk of the high-surface-area solid either participate directly or are implicated indirectly in the catalytic reactions,[48] such material is defined as a uniform catalyst, such as skeletal Nickel. Another prominent example is ZSM-5, which the channels and pores allow for the diffusion of molecules, exposing a high internal surface area for the reaction. Metal catalysts dispersed on a high surface area material (serving as a support) are classified as multiphasic catalysts.[47] Moreover, heterogeneous catalysts can fall into one of two categories in terms of the location of their active sites. In the case of zeolites and SBA-15 based mesoporous materials, the active sites are the internal surfaces, such as pores and cavities. On the other hand, metal or metal oxide species typically have active sites located on the particle surface.

1.2.2 Chemisorption of the Heterogeneous Catalyst

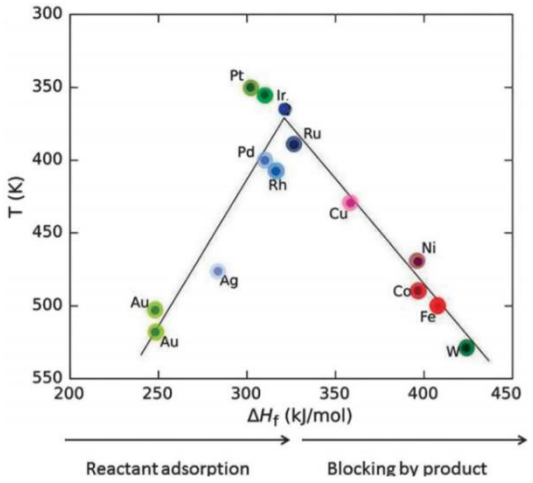


Figure 1.2. Volcano plot: the reaction temperature, for a set reaction rate of formic acid decomposition, plotted against the enthalpy of formation of the transition metal formate. This figure has been reproduced from ref. 49 with permission from Royal Society of Chemistry, copyright 2014.

A typical heterogeneous catalytic reaction involves molecular adsorption of the reactants from liquid/gas phases onto a solid surface, chemical reaction of the adsorbed species, and subsequent desorption of the products away from the solid phase. Optimisation of catalytic adsorption is important for heterogeneous catalysis, which was demonstrated by French chemist Paul Sabatier.[49] It can be illustrated by the volcano plot (see Figure 1.2) which expresses the reaction temperature, for a set reaction rate of formic acid decomposition, plotted against the enthalpy of formation of the transition metal formate. [49,50] Later transition metals, such as Ag and Au, have low adsorption energy which limits adsorption to the surface and thus requires higher temperatures to raise the reaction rate. Whereas, the early transition metals, such as Ni, Co and Fe, have a high enthalpy of adsorption, so the product cannot desorb from the metal surface easily, resulting in catalyst poisoning. Therefore, it is highly important to govern the adsorption properties to ensure the substrate bonding is not too weak or too strong.

1.3 Nanoparticles for Heterogeneous Catalysis

Substances that have at least one dimension (length, width or thickness) in the range of 1 to 100 nm (Figure 1.3), are often classified as nanoparticles (NPs).[51] They can be synthesised

by either a top-down or a bottom-up approach.[52] The top-down approach is to break up a bulk material into small particles while the bottom-up method is to assemble basic units (atoms or molecule) into bigger particles.[53] When viewed in more detail, NPs contain quantitative percentages of coordinatively unsaturated atoms dispersed at the particle surface, edges and corners. Partly unsaturated atoms like adatoms on surfaces, or atoms at kinks, edges and corners, normally have a high tendency to coordinate with substrates owing to their low coordination number.

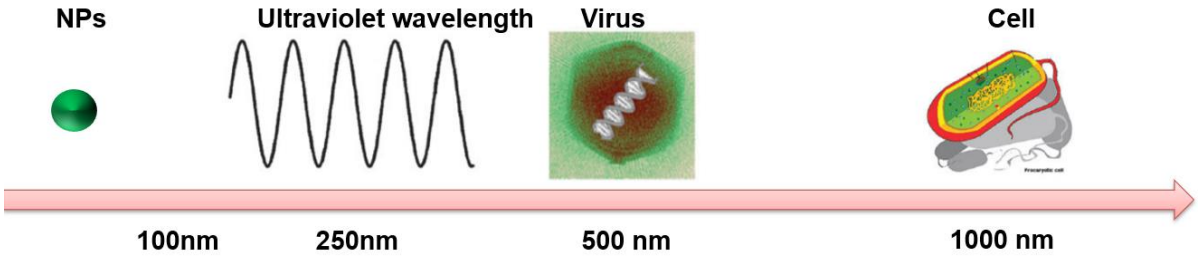


Figure 1.3. Schematic representation of the size regime of NPs related to general "micro" scale objects, cell, virus and the wavelength of the ultraviolet wave. This figure has been reproduced from ref. 51 with permission from Royal Society of Chemistry, copyright 2009.

Additionally, owing to the presence of the unsaturated atoms, they possess physical and chemical properties that are intermediate between the single atom, nanocluster and those of the bulk materials.[54] Significant research in the past 20 years has pushed the field of nanotechnology forward. However, it remains challenging to design and synthesise novel catalysts with desired active sites and to understand and rationalise the mechanisms at the molecular level.

1.4 Chemical and Structural Tuning of the Catalytic Activity

According to literature, a good catalyst should feature the following key properties:

1). The catalyst should provide good selectivity for the production of the target products and avoid the formation of undesirable side-products.

2). The catalyst should perform at an adequate reaction rate for a given set of reaction conditions.

3). The catalyst should be stable for a long enough reaction time or be able to be regenerated after appropriate treatments if the catalyst is deactivated.

4). The accessibility for the reactants and products to the active sites needs to be good so that high reaction rates can be maintained.

From literature it is evident, the overall catalytic performance is a sum of the contribution of individual NPs with various chemical and physical effects. Therefore, it is important to design NPs catalyst by optimisation of the particle size,[55] shape,[56] support selections[57] and alloying of specific dopants or additives[58].

1.4.1 Structural Tuning

1.4.1.1 Particle Size

Early investigations into the particle size effect can be dated back to the 19th century.[59] Taking the example of the hydrogenation of ethylene, in the absence of a catalyst ethane is not produced at room temperature at any appreciable rate despite this reaction being thermodynamically favourable.[60] In 1897, Paul Sabatier reported that the hydrogenation of ethylene can be greatly accelerated in the presence of finely divided nickel.[60,61] To date, intense research has been accumulated to establish the correlation between the particle size and surface area of the metal catalyst.

The properties of a material can change significantly when reducing the size of its particles. The surface-to-volume ratio (the ratio between surface atoms to the total atoms within one particle), increases dramatically as the particle sizes are scaled down to <10 nm.[62] In NPs, surface atoms have a lower coordination number and hence are less stable; as a result, the

melting point of the nanoscale material is much lower compared to the bulk form of the same material (as shown in Figure 1.4). [63]

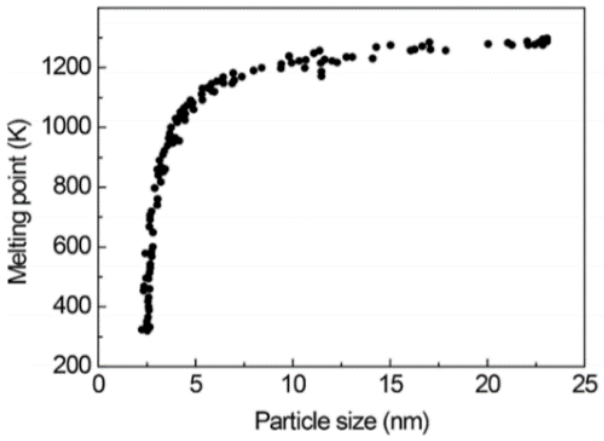


Figure 1.4. An example of the relationship between melting point and particle size. This figure has been reproduced from ref. 63 with permission from American Physical Society, copyright 1976.

The coordination environment of surface atoms varies with particle size, which can be seen in Figure 1.5. The fraction of surface atoms with coordination number (CN) 9, 7 and 4 of a cuboctahedral NPs changes dramatically with the particle size. Moreover, when the particle size scales down, the effect of under-coordinated atoms at the corners and edges becomes dominant. In the case of the activity of CO oxidation on Pt NPs, it was found that highly under-coordinated Pt atoms (CN=7) at the edge were active for CO oxidation; whereas, Pt atoms with CN of 9 on the terrace were inactive. This phenomenon revealed the strong correlation between particle size and catalytic activity. Also, the location of the d-band centre is dependent on the particle size. In the case of a Pt catalyst in the ORR reaction, DFT calculations have highlighted the adsorption energies of oxygen-containing species upon NPs differs to bulk Pt.[64]

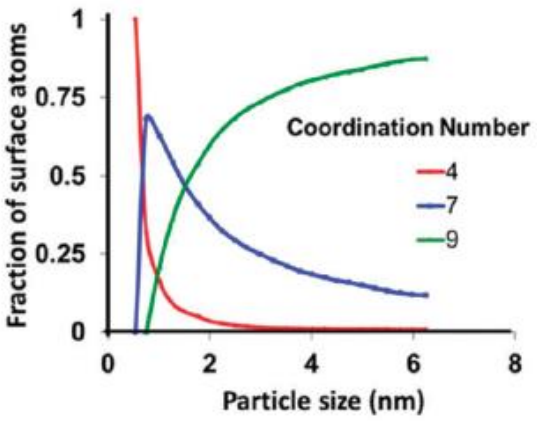


Figure 1.5. An example of how the coordination number of the surface atoms varies with the particle size. This figure has been reproduced from ref. 65 with permission from Royal Society of Chemistry, copyright 2014.

Furthermore, another consequence of the particle-size effect is the variation of the electronic structure, as illustrated in Figure 1.6. The electronic structure of the NPs is often treated as the metal energy band. Nevertheless, when the particle size is scaled down to approximately 1 nm, an ultra-small NP, often called a metal cluster, has a discrete d-electron DOS instead. Recently, with the development of synthesis strategies, ultrasmall particles or even single atoms can disperse on specific supports, with the corresponding d-electron density of states (DOS) existing in the form of atomic orbitals.[66] Such research on how to accurately control particle size is bridging the gap between heterogeneous and homogeneous catalysts.

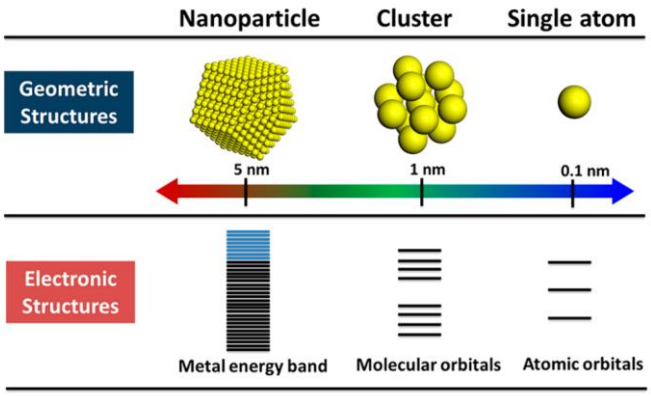


Figure 1.6. Geometric and electronic structures of the particles with different sizes (single atom, cluster and nanoparticle). This figure has been reproduced from ref. 66 with permission from American Chemical Society, copyright 2018.

1.4.1.2 Shape

With regards to metal NPs (particle size > 1nm), their geometric structures are relatively stable in comparison to metal clusters. Different crystallographic surfaces of a NP can display unique geometric structures and electronic states, leading to high activities and/or selectivities.[67,68] By constraining the nanocrystal into a single shape, a uniform metal surface of NPs can be exposed to the external environment.

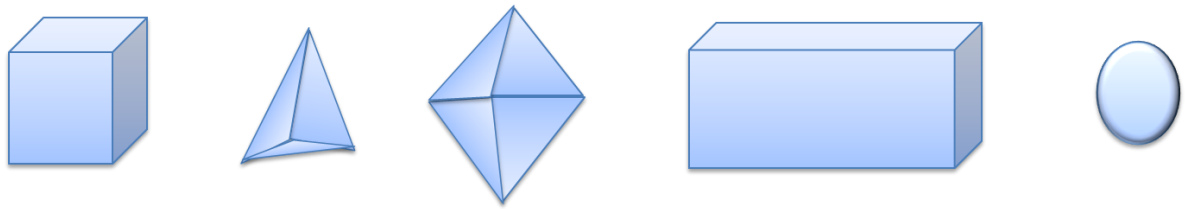


Figure 1.7. Schematics representations of metal NPs in different shapes. From left to right: cube, tetrahedron, octahedron, bar, and sphere-like shape.

Decades of research has brought huge contributions to the synthesis of NPs with well-controlled shape (outlined in Figure 1.7).[69,70] In general, the major exposed metal surfaces of FCC packed metal NPs with single shape are (100), (111) and (110), as demonstrated in Figure 1.8. A review has concluded that each miller index surface is different in aspects of electron density, coordination number (CN), distance between neighbouring atoms, surface occupancy and adsorption energy of reactants or intermediate molecules.[65]

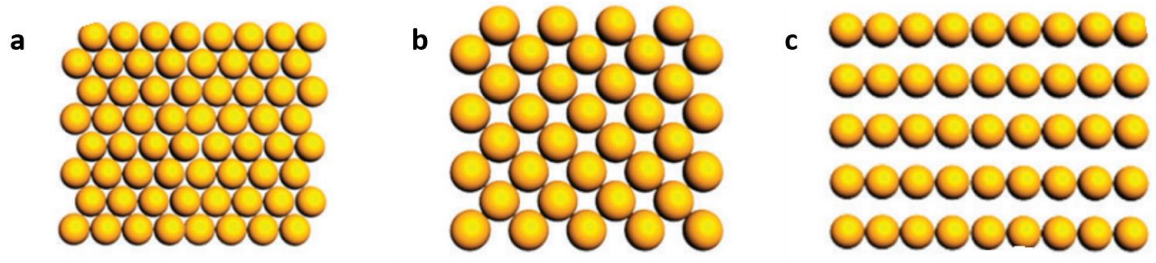


Figure 1.8. The example of different surfaces of FCC metal Platinum (Pt) NPs. (a) (100) of FCC. (b) (111) of FCC (c) (110) of FCC. This figure has been reproduced from ref. 65 with permission from Royal Society of Chemistry, copyright 2014.

Both the metal surface occupancy and the coordination environment for FCC packed crystallographic structures conform to the trend: (111) > (100) > (110). The difference in the

surface occupancy can lead to a big difference in adsorption energy or activation barrier of reactant molecules at the dissociation step. This is due to the repulsion of adjacent adsorbates and the coverage of adsorbates, whilst the variation in coordination number can result in the electronic state variation of the surface atoms, leading to a difference in catalytic performance. Furthermore, as suggested by DFT calculations, d-band centres are also dependent on the crystallographic surface, which manifests as a difference in adsorption energy.[71,72] The change in adsorption energy of a molecule is heavily dependent on the coupling between the valence state of an adsorbate and the d-band centre of the metal.[73] The bond strength is governed by the electronic occupancy of the anti-bonding state. At the metal surface, the occupancy is dependent on the energy of the anti-bonding state relative to the Fermi level. Hence, a metal with a higher energy state with respect to the Fermi level can form stronger bonds. For example, metal atoms located at the (110) face have a lower coordination number but have a higher energy state; allowing them to form a stronger adsorption with the reactant molecules.

1.4.2 Chemical Tuning

1.4.2.1 Support

As mentioned above, the particle size can influence the stability of the NPs. NPs have a tendency to aggregate giving rise to bulk-like characteristics when operating at elevated temperatures over prolonged periods of time. However, this can be circumvented in the presence of supports which allows particle size to be maintained. Supports also have a synergistic role with NPs at the surface to activate the substrate; it is equivalent to the synergy of alloying additives to the NPs, in addition to providing NPs stabilisation.[74]

Metal support interactions have been frequently investigated to improve catalytic performance of transition metals by engineering geometric and/or electronic structures of these metal sites. The term “strong metal-support interactions” (SMSI) was introduced by Tauster *et al*. in 1978 to describe the significant changes in the chemisorption properties of Group (8-10)

metals deposited on TiO_2 in a reducing atmosphere.[75] A consensus has now been reached that the origin of the SMSI effect is ascribed to the metal NPs encapsulation by oxide layers (Figure 1.9), which is driven by minimisation of the high surface energy of the metal NPs by mobile support suboxide species. In the case of TiO_2 supported catalysts, suboxide species are TiO_x ($x<2$).[76,77]

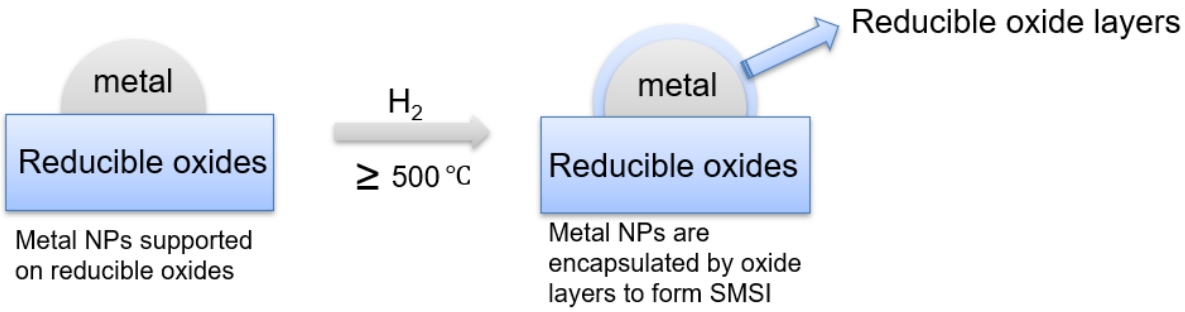


Figure 1.9. The conventional SMSI formation process. This figure has been reproduced from ref. 78 with permission from Springer Nature, copyright 2020. Reducible oxides are characteristic of formation of oxygen vacancy or donation of oxygen to an adsorbed species easily in comparison with nonreducible oxides. The formation of oxygen vacancy or donation of oxygen to an adsorbed species can result in change of surface composition, from M_nO_m to M_nO_{m-x}. The removal of oxygen can lead to excess electrons that are redistributed on the cation empty levels, and hence changing their oxidation state. Conventional reducible oxides are TiO_2, WO_3, NiO, Fe_2O_3, CeO_2, *etc.*.[79]

To be specific, the adsorption of CO on Pd was drastically suppressed because of SMSI. The coverage of the metal sites by reducible oxides can alter the geometric ensembles and so maintain the thermal stability of the Pd catalysts. On the other hand, an enhanced chemisorption of CO has been observed when Au was incorporated onto the surface of reduced TiO_2. Reduced TiO_2 contains sub-stoichiometric oxygen, leading to the presence of suboxides ($Ti^{3+}O_x$), which can tune the local electronic structure of the Au metal surface and allow electron transfer from $Ti^{3+}O_x$. This results in an electron-rich Au that enhances CO adsorption/binding.[80] In parallel to the SMSI effect, the combination of metal and support can also result in charge redistribution between the interface of the metal and support (the typical region is constrained to several layers of the metal surface at the interface),[81] which is called electronic metal-support interactions (EMSI). The charge transfer from NPs surface to support or from support to NPs

surface can lead to electron-deficient or electron-rich configurations at active sites. The movement direction and magnitude of the charge transfer is dependent on the differences in Fermi level of the metal NPs and the support. Iwasawa and co-workers are the pioneering investigators of EMSI with their studies on Pt/Y_2O_3 and Pt/ZrO_2 systems.[82] X-ray absorption near-edge structure (XANES) spectroscopy, revealed that ZrO_2 and Y_2O_3 donate electrons to Pt, increasing the electron density at Pt. Due to the presence of the interactions mentioned above, supports and metal NPs can work cooperatively during the reaction, inducing a synergistic effect to the catalytic activity and selectivity.

1.4.2.2 Promoter and Additives

Since the very first discovery of ‘‘impurities’’ accidentally optimising the reaction conversion and product selectivity,[83] promoters and additives have been used in the main metal framework or metal supports, and continue to emerge as a conventional strategy to tune the electronic structure and adsorption properties of the catalyst.

Functionalisation of the supports with different elements can adjust the electronic structure of supports, which can be typically found in the field of carbon-based materials[84] and/or the metal oxides.[83] Nitrogen (N) is one of the most investigated elements as dopant for carbon-based supports. It has been reported that the presence of N doping can enhance the support-metal NP binding strength, resulting in smaller NPs with better stability.[85] Moreover, the electronic structure is dependent on the carbon matrix position of the N doping, which can be found in the case of the functionalisation of metal oxides, such as the N doped TiO_2 system. In comparison with the pure TiO_2, the energy gap between the conduction band to the valence band of the substitutional N-doped TiO_2 was lowered from ~3.2 eV to ~3.06 eV, whereas the energy gap of the interstitial N-doped TiO_2 decreased to ~2.46 eV.[86,87] Moreover, introducing cationic or anionic dopants to reducible supports can enhance their conductivity, making them more suitable supports for electrocatalysis. However, for this conventional strategy, the effect

of additives or promoters is only significant at the metal-support interface. If the metal active site is distant from the metal-support interface, the presence of the additives cannot significantly impact upon the catalytic properties.[88] Hence, doping should be done selectively at the metal active sites rather than the support.

Foreign elements can also be doped into the metal NPs directly, which can demonstrate unusual electronic and chemical properties that are distinct from those of their metal system.[89] This can be reflected in the presence of the foreign element diluting the active metal sites, or adjusting the electronic structure of the parent metal system directly.[90]

1.5 Classification and Thermodynamics of Nanoalloys

1.5.1 The Structure of Nanoalloys

In the case of bulk metals, the alloy is the combination of more than one component, at least one of which is a metallic element. There are binary, ternary and quaternary alloys, which consist of two, three and four components respectively (containing at least one metallic element). In the case of the NPs, the three-dimensional crystallographic structure might be similar to the that of the bulk material, however, in some cases, the crystal structure of the alloy may differ from the bulk material and be of different crystal structure or even an amorphous structure under a given condition.[91]

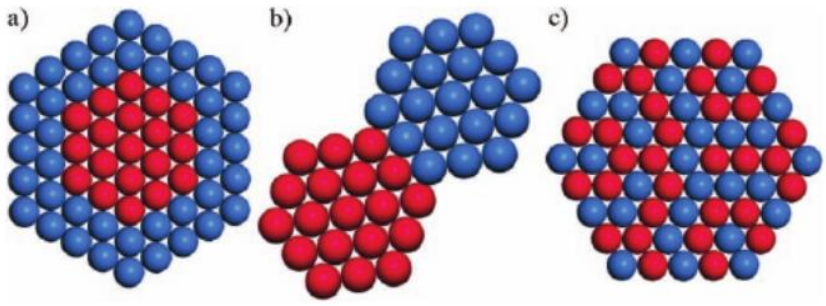


Figure 1.10. Schematic illustration of three main patterns. (a) core-shell. (b) heterostructure. (c) Mix-alloy. This figure has been reproduced from ref. 89 with permission from WILEY-VCH, copyright 2011.

In general, the structure can be mainly classified as core/shell,[92] heterostructure or mixed nanoalloy structure as shown below (Figure 1.10).[58,89] Core-shell based nanoalloys (Figure 1.10a) consist of a core of atoms of one type (A), surrounded by a shell of atoms of another type (B). Alternatively, individual nucleation and growth of two different types of elements can take place and share a mixed interface during the process, giving heterostructure forms (Figure 1.10b). The third possible alloy is a mixed-nanoalloy form (Figure 1.10c). It is well known that the architecture of the nanocrystal, after alloying with the foreign atoms or additives, is modified in terms of atomic ordering, crystal structure (space group), the internal structure (with different types of defects or stacking faults) and morphology, including the configuration.

1.5.2 Categories and Thermodynamics of the Mixed-Nanoalloy

With regards to the atomic ordering, mixed nanoalloys can further fall into the categories of intermetallic compounds and random alloys (solid solution alloys) (Figure 1.11).[93] The term solid solution alloy is used to describe two components distributed non-homogeneously and are randomly mixed. In contrast, an intermetallic compound is reserved for a system that has long-range atomic order and well-defined stoichiometry. The space group and atomic arrangements of the intermetallic phase are different to that of the parent pure metals, whereas the solid solution alloy remains the same.

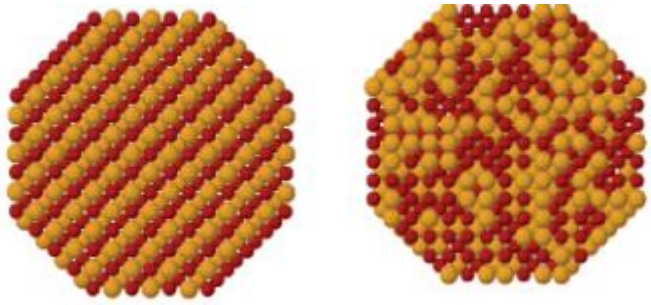


Figure 1.11. Schematic representation of intermetallic compound (Left) and solid solution alloy (Right). This figure has been reproduced from ref. 58 with permission from American Chemical Society, copyright 2008.

The formation of solid solution alloys or intermetallic compounds can be explained from a thermodynamic perspective:[94]

$$\Delta G_f = \Delta H_f - T\Delta S_f \qquad \text{(Equation 1.1)}$$

Where ΔH_f and ΔS_f are the formation enthalpy and entropy for alloying using pure metals, respectively, and T is the absolute temperature. When the properties of the constituent elements are very close, ΔH_f is close to zero or slightly negative. Therefore, the disordered structure ($\Delta S_f > 0$) is favourable, and hence a negative ΔG_f is obtained, but the ordered structure cannot be explained in terms of entropy. Nevertheless, if the electronic properties of the elemental constituents are particularly different, a high negative ΔH_f is sufficient to compensate for the entropy loss, leading to a negative ΔG_f. Furthermore, transformation from an ordered structure (known as Kurnakov-type intermetallic compound) to a disordered structure can be driven by enhancing the contribution of $-T\Delta S_f$.[90,94] Thus, the driving force for formation of solid-solution alloys (entropy-driven) and intermetallic compounds (enthalpy-driven) are different. However, it is worth noting that this equation fails to provide an accurate guide when considering the factors of strain, defects etc.[94] Overall, this classification is essential because solid solution alloys and interatomic compounds behave differently even if the elemental composition and atomic ratios are same.

In literature, the term ‘doping’ is used most frequently to describe the addition of small quantities of a foreign element as a promoter or additive to a catalyst or semiconductor. This type of ‘doping’ is usually described in a general, non-specific way. This term will also be used to describe large concentrations of additive; for example in Y-doped ZrO_2, in which the Y content is above 10%. As admitted by literature,[95] as long as the modification is mild and the parent structure remains approximately unchanged, this term is still applicable. Therefore, it is more suitable to use the term ‘doping’ when describing solid-solution alloys and use other words when describing intermetallic compounds.

1.6 Categories of the Solid Solution Alloy

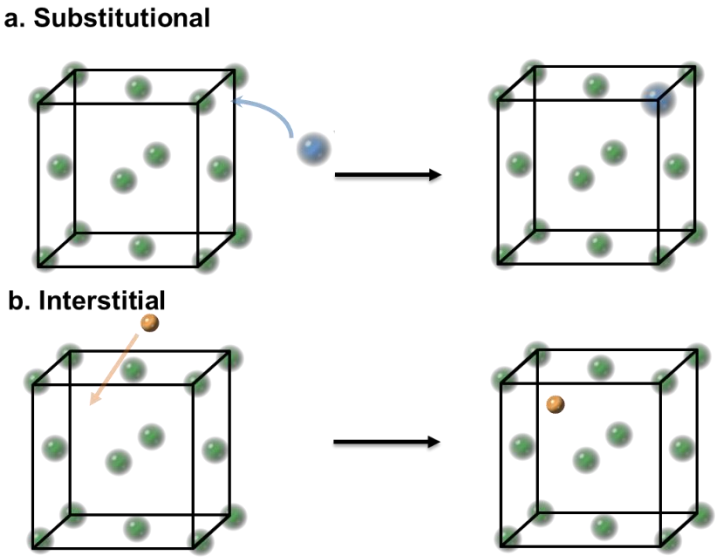


Figure 1.12. A schematic of substitutional and interstitial solid solution alloys. (a) Substitutional solid solution alloy, atoms of the host metal systems are annotated with green dots; atoms of the foreign atoms are annotated with blue dots. (b) Interstitial solid solution alloy, atoms of the host metal systems are annotated with green dots; atoms of the foreign atoms are annotated with yellow dots.

Chemical doping is one of the processes that can synthesise a solid solution alloy. Depending on the site modification of the host metal system, the solid solution alloy can be further classified into two subcategories− substitution alloy and interstitial alloy. For clarity, the binary combination will be denoted in this thesis by the host metal system (M) and the counterpart element (N), from here on. Specific substitutional or interstitial solid solution alloy/doping phases are assigned as M−^{sub}N and M−^{int}N, respectively. Solid-solution phases that are reported as a specified composition are expressed as M_mN_n. When not describing a specific phase, the binary designation combined with a dash (M−N) will be used. This designation represents a composition of various phases, a generic term for a binary system, and/or a simple combination of two elements with an uncertainty of their chemical states. In substitutional alloys, the atoms of the host unit cell are replaced by foreign atoms (illustrated in Figure 1.12a). In contrast to substitutional alloys, an interstitial alloy has foreign atoms,[96] usually light elements, taking residence at interstitial sites of the host metal unit cell (displayed in Figure 1.12b).

1.6.1 Substitutional Alloy

For typical substitutional solid-solution alloys, the atomic size and electronic properties of the foreign element are similar to that of the parent metal. Normally, the difference in atomic diameters should be less than 15%, in light of the Hume-Rothery rule, which is expressed in Equation 1.2.[97]

$$\left(\frac{r_{solute}-r_{solvent}}{r_{solvent}}\right)\times 100 \leq 15\% \qquad \text{(Equation 1.2)}$$

The substitutional alloy formation can finetune the electronic structure by changing the number of electrons per atom in the unit cell; modifying the chemisorption properties of the metal surface.[98] It can happen to both individual constituent metal and metal oxide systems. For example, Cu can be alloyed into Ni, leading to the formation of a substitutional alloy.[99] The presence of Cu in the substitutional alloy system is anticipated to fill the d-band vacancies of Ni and suppress the formation of γ-NiOOH, a low-activity species formed during electrocatalytic oxidation of methanol. In the case of the metal oxide based substitutional alloy system formation, a small fraction of the cations of a ‘‘host oxide’’ can be substituted with different cations.[83] Alternatively, foreign anions, such as halogen group elements, can replace the anion in the metal oxide system.[100]

Nevertheless, as reported in literature, the stability of substitutional alloys might be a problem since the foreign atoms may not have strong location preferences in the substitutional alloys, leading to diffusion at elevated temperature. This can result in segregation, thus the chemisorption properties of the segregated alloy system are restored to the catalytic properties of the segregated element.[101]

1.6.2 Interstitial Alloy

Unlike the substitutional alloys, interstitial alloy formation requires the foreign atom to be sufficiently small to diffuse into the interstitial sites of the host metal system. The conventional

interstitial alloys are metal carbides[37], nitrides[102] and borides[103]. The foreign element often takes residence at the largest available interstitial site: octahedral in face-centre-cubic (FCC) and hexagonal-close-packed (HCP) structures, and trigonal prismatic in hexagonal (Hex) structure.

The crystal structure is governed by geometric and electronic factors. The geometric factor is based on Hägg's rule,[104] which dictates the ratio (0.59) of non-metal atomic radius (r_x) to that of the metal atomic radius (r_M) for the interstitial alloy formation.[105] When the ratio of the (r_X/r_M) is less than 0.59, the structure of the interstitial alloy will be simple, such as the aforementioned simple structures, FCC, HCP and Hex. When the ratio of the (r_X/r_M) is greater than 0.59, an interstitial alloy with a more complicated structure will be obtained, for instance, Cr_3C_2.[106] Though exceptions to the rules have been reported, for example, the carbides of Fe,[107] this rule is generally still valid and can be found in literature frequently.[108,109]

The second factor that governs crystal structure is the electronic effect. The nature of the metallic bond of interstitial solid solution alloys is slightly different because of the orbital mixing of foreign elements and host metal systems, such as the s-p orbital of the non-metal element and the s-p-d orbital of the metal elements. In light of the Engel-Brewer theory of metals, [96,110] it was suggested that the structure adopted by a metal or interstitial solid solution alloy is dependent on the s-p counts (electron configuration or the total number of (s+p) electron per atom) as follows:[111,112]

- BCC: $sp^{0.5}$
- HCP: $sp^{0.7\text{-}1.1}$
- FCC: $sp^{1.5\text{-}2}$

It can be found that the increments in this count can promote the structural transformation from BCC to HCP to FCC. Additionally, foreign elements taking residence in a metal structure can

result in lattice expansion of the host system, which is indicative of interstitial solid solution alloy formation.

The history of interstitial alloys as catalysts can be dated back to the utilisation of tungsten carbide for the isomerisation of neo-pentane to isopentane,[113] which has similar catalytic behaviour to Pt. It was suggested that after alloying with the foreign element, carbon, the addition of the valence electron to the tungsten can enhance the reactivity of the tungsten. By comparison of the valence band x-ray photoelectron spectrum of tungsten carbide, tungsten and platinum, it was found that the electronic density of states near the Fermi level of tungsten carbide is closer to that of platinum than the pure tungsten metal.[114] This result reveals that this strategy can enhance the reactivity of the elements to the right of the periodic table, which paves a possible path for the design of novel catalysts in the future.[113]

1.7 The Interstitial Alloys of Pd and Pt

1.7.1 Background of Pd and Pt metals

Platinum-group metals, including Ru, Ir, Rh, Pd, Pt and Os,[115] serve an important role in catalysis, energy/storage transfer, inert chemical coatings *etc.*.[116,117] For example, Pd plays a critical role in the catalysis of cross-coupling reactions,[118] hydrogenation reactions,[119] and hydrogen evolution reactions,[120] whilst Pt is widely utilised in oxygen reduction reactions,[121] hydrogen oxidation reactions,[121] and cross-coupling reactions.[122] In daily life, Pd and Pt are two of the major catalytic components for automotive catalytic converters for the oxidation of CO into CO_2.[123] The recently tightened emission regulations in the EU and US have led to extensive usage of Pd in automotive catalytic converters that accounts of approximately 80% of the total Pd demand.[124,125] The rapid depletion of Pd has caused the cost of Pd to increase so that it is more expensive than Pt and Au.[126] The automotive catalytic converter is normally operated at the temperature range of 150-600 °C, but the temperature can suddenly increase to

1000 °C.[127] Under such operating conditions, this will cause the sintering effect that increases the particle size of the catalyst and decreases the catalytic activity per unit mass of the catalyst. Moreover, if the automotive catalytic convertor is at a lower temperature than 200 °C, these metals are unavoidably poisoned by CO.[128] To lower the probability of sintering, particles of Pd and Pt are usually dispersed on high surface area supports (e.g cordierite, alumina, titanium dioxide and silica).[129] Additionally, noble metals such as Pd and Pt are often alloyed with other elements over a broad compositional range for the synthesis of novel catalysts. This helps to reduce the amount of the noble catalyst needed as well as to fine tune the chemisorption energy of reactants to reduce the surface poisoning effect.

Generally speaking, Pd and Pt are alloyed with neighbouring late or early transition metals to form substitutional solid solution alloys or intermetallic compounds.[130,131] Recently, in the field of the interstitial solid solution alloys for catalyst applications, Pd has become the focus for more research.[132] The addition of foreign light elements to the precious metal interstitial site can tune the electronic nature of the metal surface, therefore avoiding the formation of side products.[132] The very rich chemistry of these interstitial alloys offers a chance for the development of new catalysts; in particular, for the synthesis of Pt and Pd materials, as well dispersed NPs.

1.7.2 Palladium Based Interstitial Alloy

1.7.2.1 Palladium Hydride

When a Pd metal surface is in contact with hydrogen, molecular H_2 will readily dissociate into atomic hydrogen on the surface of Pd; which can further diffuse and dissolve in the octahedral sites of Pd,[133] leading to the formation of Pd hydride. These metal hydrides have potential applications in hydrogen storage and heterogeneous catalysis.[134,135] Depending on the fraction of hydrogen, Pd hydride has two phases, which can be demonstrated in Figure 1.13. *At* the condition of a low hydrogen gas pressure and room temperature, hydrogen is slightly

dissolved in the Pd, leading to the formation of solid-solution phase. This phase is termed α-PdH_x (where x is $0 \leq x \leq 0.03$). The lattice parameter of the Pd slightly increases from 0.3887 nm to 0.3895 nm. As hydrogen gas pressure increases, β-PdH_x phase (where $x \geq 0.58$) forms after adsorption of a large amount of hydrogen and the Pd lattice expands from 0.3887 nm to 0.4025 nm.[136,137] A mixture of α-PdH_x and β-PdH_x (where x is $0.03 \leq x \leq 0.58$) can co-exist.

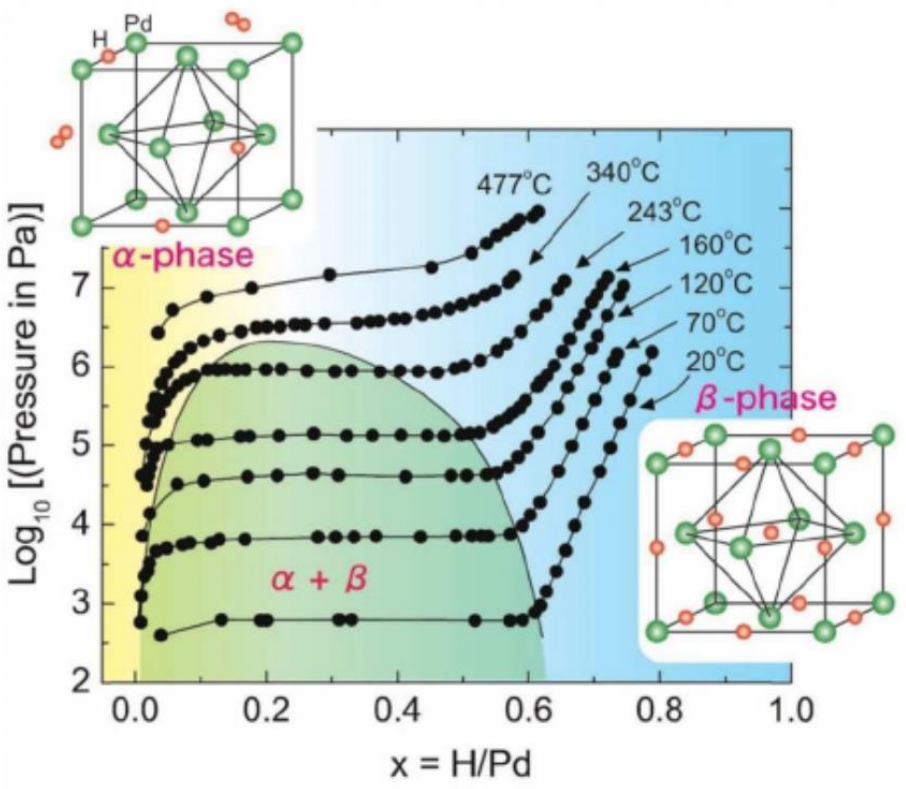


Figure 1.13. Pressure-concentration-temperature phase diagram of the Pd-H. This figure has been reproduced from ref. 138 with permission from Wiley-VCH, copyright 2019.

Both the α-phase and β-phase play a key role in heterogeneous catalysis, especially for selective hydrogenation of ethyne to ethene, because the conversion and selectivity of the target products are highly dependent on the ratio of these two phases.[139] The presence of β-PdH_x can accelerate the conversion rate but also leads to over-hydrogenation. In contrast, α-PdH_x is less active but is more selective to the formation of ethene. In parallel to the hydrogenation reaction, carburisation of the palladium can also take place, leading to the formation of PdC_x phase, which will be introduced in next section.[139]

1.7.2.2 Palladium Carbide

Since the pioneering work of Graham, where it was observed that hydrogen is able to dissolve in the Pd metal interstitially,[140] the family of Pd interstitial solid solution alloys has expanded to include Palladium carbide.[141] Palladium carbide (Pd-^{int}C) can be formed when Pd serves as catalyst for hydrogenation reactions or other reactions in hydrocarbon environments.[142,143] C atoms form from acetylene decomposition on the Pd surface and can diffuse into the lattice to form Pd carbide. When C resides at octahedral sites (where the molar fraction is 0.13), the structure is similar to the β-PdH_x.[139] In-situ X-ray photoelectron spectroscopic measurements and in-situ prompt gamma activation analysis indicated an increase of C content in the Pd can inhibit the formation of β-PdH_x, reducing the tendency for over-hydrogenation.[144] Hence, doping/alloying light elements into the heavy metal systems could yield potential catalysts for selective hydrogenation reactions.

1.7.2.3 Palladium Boride

As mentioned, modification of the Pd interstitial sites with C can inhibit the formation of β-PdH_x. This can also be achieved by doping the Pd with another light element, boron (B).[145] It is also anticipated that B can reside at the octahedral sites of Pd, but Hägg's rule fails to explain this because B is theoretically too large to incorporate into Palladium interstitial sites ($\frac{R_M}{R_I} = 0.67$). The molar fraction of B can be up to maximum 0.18 and the structure of Pd metal system retains FCC packing. Moreover, the presence of B at the interstitial sites can make a contribution to the Pd lattice parameter expansion, from 3.89 Å to maximum 4.03 Å.[146] Except for the utilisation of the Pd-^{int}B based catalyst in the selective hydrogenation reaction,[147] it has been employed for formic acid decomposition[148] and oxygen reduction reaction;[149] for which it showed premium activity and selectivity. This can be attributed to the downshift of the d-band centre of this metal, resulting from the movement of electrons from the p orbital to

the d orbital.[150] These results suggest that the Pd metal, after being alloyed with B, can open a new window for novel catalyst design.

1.7.2.4 Palladium Lithium Alloy

Compared with the former two interstitial systems, Pd-Li binary systems have had less attention. The detailed study of bulky ordered alloy binary palladium-lithium systems was conducted by J. Sangster and A. D. Pelton.[151] Depending on the molar fraction between Pd and Li, the structure definitions can be divided into Li-rich and Li-deficient species. The solubility of Li in Pd is dependent on the magnetic susceptibly, which is affected by the temperature. For example, the solubility of Li in Pd is 6% at the room temperature, whilst the solubility of Li in Pd is approximately 9 % and 11 % at 900 and 1100 °C , respectively.[151] The theoretical study of Pd-Li systems was later investigated by the Gelatt;[152] where it was revealed that there is a small interaction between the s orbital of Li and d orbital of the Pd. Ellis reported a solid synthesis method that can alloy Li into the interstitial sites of a Pd host system under relatively mild conditions. The work of Ellis and its complementary refinements suggested that Li is able to reside at the octahedral sites of Pd, with a crystallographic structure that is similar to β-PdH_x and $PdB_{0.18}$.[145] Additionally, it was also found that Pd catalysts, after Li modification, can have enhanced selectivity for converting acetylene to ethene. This was attributed to Li blocking the formation of β-PdH_x.

1.7.3 Platinum Based Interstitial Alloy

In comparison with the Pd based binary system, the field of Pt-based binary systems has not attracted as much interest and limited studies have been reported in the literature. As emphasised in the foregoing description, light elements such as C, B and Li can diffuse into the interstitial sites of the parent metal system, leading to the formation of the interstitial alloy. For the synthesis of Pt-Li alloy system, the initial study can be dated back to 1948, when interatomic $PtLi_2$ alloy was synthesised from molten Li and metallic Pt under an argon

atmosphere.[153] Pt_7Li interstitial alloy was first reported in 1962,[154] and the structure was explored by neutron diffraction and X-ray powder diffraction.[155] B can be adapted to alloy into the Pt metal framework by hot-stage microscopy.[156] A Pt-B binary system can also be prepared by equilibrating Pt with B_2O_3 in the temperature range of 1200 - 1300 K. Direct density measurements, lattice contraction and the temperature coefficients, suggest that B can be randomly distributed in the Pt metal system both interstitially and substitutionally.[157] Also, the incorporation of C into Pt metal system was explored in 1970 by quenching a mixture of C and Pt over a broad range of temperatures. It was found that the lattice parameter of Pt increased slightly after quenching the mixture at 1400 °C which could be attributed to the presence of C occupying interstitial sites.[158] Such an interstitial compound can also be prepared by DC reactive sputtering using a low percentage of CH_4 in Ar, where XPS measurements indicated that the amount of carbon can be up to 17 at%.[159] With the exception of the electro-deposition of Li into Pt electrodes for formic acid oxidation, to the best of my knowledge, catalytic applications of Pt interstitial alloys have not yet been reported. Therefore, more research is required to explore this field.

1.8 Characterisation of Light Element Modified Nanoparticles.

As discussed previously, both substitution of atoms within the metal framework with foreign elements, and the occupation of interstitial sites of the host metal systems with foreign atoms, can have profound effects upon the properties of the host metal system, even at very low concentrations. Foreign atoms can induce changes in the electronic and transport properties, lattice parameters, and cause phase transitions. However, regardless of the chosen synthetic method and subsequent adaptations to prepare a solid catalyst with dopants, it is difficult to predict whether the foreign elements will be located at the surface, interstitial sites or vertices of the host metal system. Therefore, if the catalytic performance is promoted after addition of the foreign additives, it is expected that confirming the location of the foreign

elements will establish an in-depth understanding of the relationship between the dopant-host metal system and catalytic performance.

Table 1.2. Analytical techniques used in the characterisation of light-element modification of transition-metal NPs.[60]

Incident source	Analytical technique	Main information	Ref
Photons	XRD	Atomic positions and occupancies of crystalline structures	160
	EXAFS/XANES	Interatomic distances, chemical environments / oxidation states	161
	XPS	Electronic structure, oxidation states	149
	XPDF	Amorphous local structure	162
	FTIR	Vibrational frequency of intermediates on metallic surface	163
Electron	S/TEM	Crystal structure of nanoparticles	164,165
	EELS/EDX	Chemical composition/ oxidation states	166,147
	Ptychography, Differential Phase Contrast (DPC)	Imaging of light elements	167,168
Other	ssNMR	Chemical environment of light elements	162
	TPR	Oxidation states, oxidative and thermal stability	160
	DSC/TGA	Thermal stability	160
	ICP/MS	Elemental composition	149

A constant topic of discussion in literature,[83] is whether the employment of characterisation techniques can help answer the following questions:

1) Where are the foreign elements located?
2) Is the foreign element homogeneously distributed throughout a particle, i.e. surface/bulk distribution?

3) What is the chemical state of the foreign elements?

4) Is it possible to identify the potential phase caused by additives?

5) Is the surface composition the same or different from that of the bulk?

6) Can dopants be visualised directly?

With the advent and development in electronic devices and digital processing, more advanced characterisation techniques have emerged, in addition to the conventional techniques displayed in Table 1.2. Moreover, *in-situ* measurements allow the analysis of actual structural behaviour during reactions. Chapter 2 gives a brief overview and background introduction of analytical techniques utilised in Chapters 4 to 6.

1.9 Hydrogenation of HMF to Value-Added Chemicals

Since the last century, the demand for oil, petrochemicals and energy has increased dramatically. Limited reserves combined with the growth in demand have already pushed scientists to seek new, sustainable alternatives for fuels and chemical feedstocks. Biomass, especially waste plant carbohydrates, has become one of the most attractive and wide-spread alternative feedstocks but also contains an abundantly available carbon source.[169] This is because carbohydrates are the main structural components of the cell walls of plants, in which the carbohydrate polymers, termed cellulose and hemicellulose, are tightly bound to the lignin.[170] In general, any materials rich in cellulose, hemicelluloses, and lignin are termed lignocellulosic biomass.[171] Lignocellulosic biomass-derived 5-hydroxymethylfurfural (HMF) is considered a versatile resource for the production of chemicals and fuels.[172] This is primarily due to two main reasons: it contains six carbon atoms that exist in the hexoses, and the selectivity when converting fructose to HMF is higher in comparison with other platform chemicals, such as levulinic acid (LA).[173]

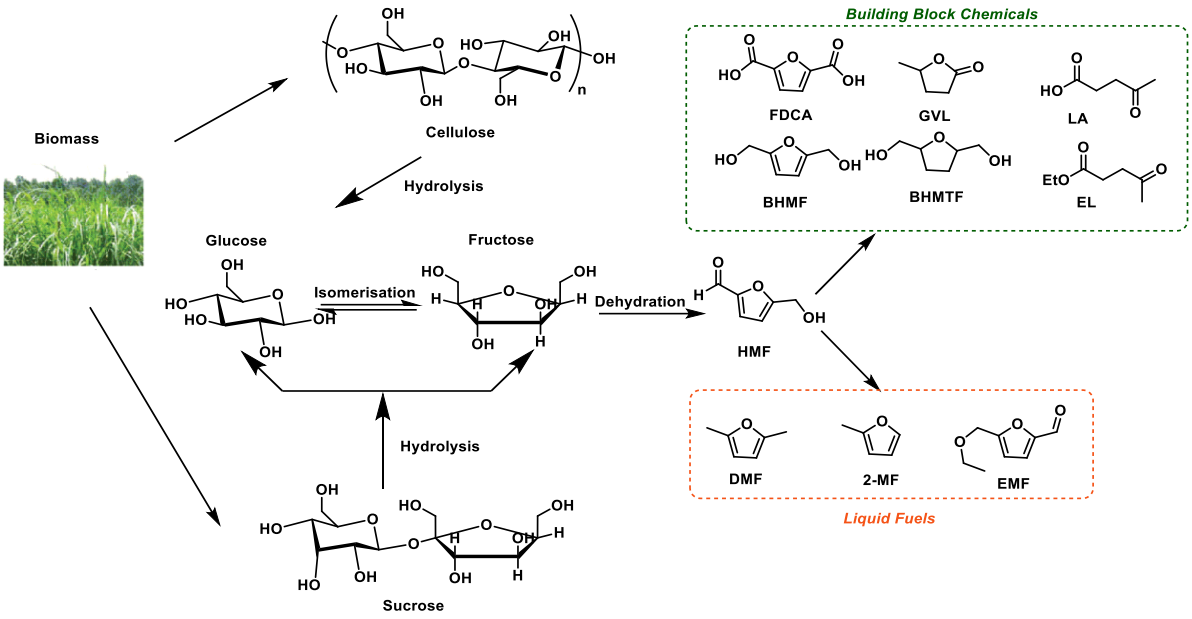


Figure 1.14. An example of the chemical production of building block chemicals and liquid fuels from biomass-derived HMF.[174] This figure has been reproduced from ref. 174 with permission from Royal Society of Chemistry, copyright 2014.

As seen in Figure 1.14 after extraction of cellulose or sucrose form biomass, they are depolymerised into glucose via hydrolysis. The glucose after isomerisation converts into fructose, which is further converted into HMF *via* a dehydration process. A number of C-5 or C-6 compounds can be formed from HMF, such as 2,5-furandicarboxylic acid (FDCA), gamma-valerolactone (GVL), levulinic acid (LA), 2,5-bishydroxymethylfuran (BHMF), (tetrahydrofuran-2,5-diyl)dimethanol (BHMTF), ethyl levulinate (EL), 2,5-dimethylfuran (DMF), 2-methylfuran (2-MF) and 5-ethoxymethylfurfural (EMF). These can serve as resources for applications in either fuel or polymer industries.

1.9.1 Importance of BHMF

Among the potential upgrade products, the selective hydrogenation of the carbonyl group in HMF to BHMF is particularly important, as it can be utilised for the preparation of resins, polymers and artificial fibres.[175,176] Additionally, it can also serve as an intermediate in the synthesis of drugs[177] and crown ethers.[178] Furthermore, hydrogenation of the BHMF can generate 2,5-bis-(hydroxymethyl)-tetrahydrofuran (BHMTHF), which can have applications

as a solvent,[175] monomer[179] and as a precursor in chemical synthesis e.g. for 1,6-hexanediol.[180] However, increasing selectivity towards isolated chemicals still remains a considerable challenge.[181] In addition, the cost price of HMF is also relatively high.[182] Thus, HMF and its products, without further research, are yet to become a commercially available chemical platform.

1.9.2 Literature Work of Pt Catalysed Hydrogenation of HMF to BHMF

Both noble metals (Ru, Pd, Pt, Au and etc.) and non-precious metals (Fe, Co, Ni and etc.) have been employed in tests for catalysing the production of BHMF. In comparison with other noble catalysts, fewer examples are related to the use of Pt catalysts for hydrogenation of HMF to BHMF (Table 1.3).[183] This is because Pt-based materials favour hydrodeoxygenation.[184]

Table 1.3. Catalytic performance of Pt-based catalysts for hydrogenation of HMF to BHMF.[132]

Entry	Catalyst	Reaction system	*T* (°C)	*P* (Bar)	*t* (h)	Conv %	Selec %	Ref
1	Pt/C	HMF (1 mmol); Catalyst (0.02 mmol); EMIMCI (20 mmol)	120	62	1	11	18%	[185]
2	Pt/MCM-41	HMF (4 mmol); Catalyst (0.1g); Water (2 mL)	35	8	2	96.6	99.2	[175]
3	$Pt_3Sn/SnO_2/rGo$	HMF (8 mmol); HMF/Pt = 654;EtOH (20 mL)	70	20	0.5	>99	>99	[186]
4	Pt/CeO_2-ZrO_2	HMF (0.3 mmol); catalyst (50 mg); EtOH (1.5 mL)	20	1	3	97	100	[187]

Chatterjee and co-workers reported that Pt NPs decorated on Si MCM-41, had much higher BHMF selectivity in comparison to other transition metals (Ni, Pd, Au, Ru and Ir). The achieved selectivity of BHMF can be up to 99.2% in aqueous solution after 2 hours under 62 bar of H_2 (Table 1.3, entry 2).[175] In this reaction, water serves as the optimised solvent and can be ascribed to promote the dispersion of Pt/MCM-41 because of the formation of hydrogen bonds to the surface MCM-41 hydroxyl groups. An ionic liquid, EMICI, was also used as a solvent and reaction medium for the production of BHMF, also reported by Chatterjee, but

resulted in a poor conversion and selectivity. Only 11% conversion over Pt/C in EMIMCI at 62 bar and 120 °C was achieved and its corresponding selectivity was only 18%. This can be partially explained by the low solubility of H_2 in the ionic liquid (Table 1.3, entry 1).[185] Shi and co-workers also tested the catalytic performance of bimetallic Pt-base catalysts. SnO_2 NPs were initially coated onto reduced graphene oxide (rGO), and then Pt_3Sn NPs were deposited to the former solid material. This catalytic system favoured hydrogenation of the C=O bond in HMF under mild conditions. The use of SnO_2 not only can promote the dispersion and stability of Pt_3Sn NPs, but also cause a synergistic effect with Pt_3Sn (Table 1.3, entry 3).[186] Kustov and co-workers recently showed that Pt NPs dispersed on a CeO_2-ZrO_2 support are efficient and active for selective hydrogenation of HMF to BHMF at room-temperature andambient H_2 pressure (Table 1.3, entry 4).[187] The interaction between Pt NPs with CeO_2 can result in partial oxide reduction with the formation of a new actives sites, which are highly selective for carbonyl group activation. The presence of ZrO_2 was used to enhance the reducibility of CeO_2. Such catalytic systems were able to initiate hydrogen spillover reactions over a temperature range of 223 – 298 K,confirmed by the TPR-H_2 result. All literature Pt-based catalytic systems are shown in Table 1.3. Further research is still required for the investigation of new Pt-based catalytic systems for the hydrogenation of HMF to BHMF.

1.10 Objectives

Catalytic adsorption properties of substrates can be modified by incorporating foreign species onto the surface of NPs. The utilisation of small elements, such as Li and B, can occupy the interstitial lattice sites or replace vertices of NPs in catalysis. Consequently, electronic charge transfer and lattice expansion/contraction within subsurface layers can contribute to unusual catalytic performance.

- It is well known that catalytic properties and reaction mechanisms have strong relationships with the structure of NPs. The promising developments in various types of equipment can offer opportunities to understand the structure of the NPs in more detail.
- Pd-^{int}B/C and Pd-^{int}Li/C are two novel NPs that have been reported by Tsang and co-workers.[97] The NPs were characterised by advanced techniques, namely SXRD, XPDF, neutron diffraction, STEM-ADF, EELS and ptychography.
- In parallel to the in-depth investigation of the Pd-^{int}B/C and Pd-^{int}Li/C systems, and the accessibility of novel interstitial NP system design was also explored. Pt has similar physical and chemical characteristics to Pd, so it is expected that Li can be alloyed and reside at the interstitial sites of the Pt. In addition, to evaluate its catalytic property, this catalyst is utilised in the hydrogenation of the HMF to BHMF and its properties examined.

1.11 References

1 I. Fechete, Y. Wang and J. C. Védrine, *Catal. Today*, 2012, **189**, 2–27.

2 G. Ertl, H. Knözinger, F. Schüth, and J. Weitkamp, *Handbook of Heterogeneous Catalysis*, Wiley-VCH Verlag GmbH & Co. KGaA, Weinheim, Germany, 2008.

3 Q. Zhang and Y. Yin, *Pure Appl. Chem.*, 2014, **86**, 53–69.

4 R. Callender and R. B. Dyer, *Acc. Chem. Res.*, 2015, **48**, 407–413.

5 S. Martí, M. Roca, J. Andrés, V. Moliner, E. Silla, I. Tuñón and J. Bertrán, *Chem. Soc. Rev.*, 2004, **33**, 98–107.

6 A. M. Klibanov, *Nature*, 2001, **409**, 241–246.

7 S. Sen and J. Puskas, *Molecules*, 2015, **20**, 9358–9379.

8 J. Chapman, A. Ismail and C. Dinu, *Catalysts*, 2018, **8**, 238.

9 P. K. Robinson, *Essays Biochem.*, 2015, **59**, 1–41.

10 V. Leskovac, in *Comprehensive Enzyme Kinetics*, Springer, Boston, MA, 2003, pp. 283–315.

11 M. T. Reetz, *Chem. Rec.*, 2016, **16**, 2449–2459.

12 M. T. Reetz, *J. Am. Chem. Soc.*, 2013, **135**, 12480–12496.

13 A. P. S. Brogan, K. P. Sharma, A. W. Perriman and S. Mann, *Nat. Commun.*, 2014, **5**, 5058.

14 S. Wu, R. Snajdrova, J. C. Moore, K. Baldenius and U. T. Bornscheuer, *Angew. Chem. Int. Ed.*, 2021, **60**, 88–119.

15 P. W. N. M. Van Leeuwen, *Homogeneous Catalysis : Understanding the Art*, Springer Netherlands, Dordrecht, 2004, vol. 13.

16 A. Nakamura, in *Fundamental Research in Homogeneous Catalysis*, Springer US, Boston, MA, 1979, pp. 41–54.

17 A. Corma and H. Garcia, *Top. Catal.*, 2008, **48**, 8–31.

18 D. J. Cole-Hamilton and R. P. Tooze, in *Catalyst Separation, Recovery and Recycling*, ed. David J. Cole-HamiltonRobert P. Tooze, 2006, pp. 1–8.

19 C. Barnard, *Platin. Met. Rev.*, 2008, **52**, 110–113.

20 F. E. Paulik and J. F. Roth, *Chem. Commun.*, 1968, **11**, 1578a.

21 S. A. Beyramabadi, H. Eshtiagh-Hosseini, M. R. Housaindokht and A. Morsali, *Organometallics*, 2008, **27**, 72–79.

22 D. M. Hood, R. A. Johnson, A. E. Carpenter, J. M. Younker, D. J. Vinyard and G. G. Stanley, *Science.*, 2020, **367**, 542–548.

23 R. A. Collins, A. F. Russell and P. Mountford, *Appl. Petrochemical Res.*, 2015, **5**, 153–171.

24 R. A. W. Johnstone, A. H. Wilby and I. D. Entwistle, *Chem. Rev.*, 1985, **85**, 129–170.

25 J. A. Dumesic, G. W. Huber and M. Boudart, in *Handbook of Heterogeneous Catalysis*, Wiley-VCH Verlag GmbH & Co. KGaA, Weinheim, Germany, 2008, pp. 1–15.

26 J. M. Thomas, *Proc. R. Soc. A Math. Phys. Eng. Sci.*, 2012, **468**, 1884–1903.

27 C. Copéret, M. Chabanas, R. Petroff Saint-Arroman and J.-M. Basset, *Angew. Chem. Int. Ed.*, 2003, **42**, 156–181.

28 J. J. Bravo-Suárez, R. V. Chaudhari and B. Subramaniam, in *ACS Symposium Series*, 2013, vol. 1132, pp. 3–68.

29 S. M. George, *Chem. Rev.*, 1995, **95**, 475–476.

30 J. Gallagher, *Nat. Rev. Chem.*, 2018, **2**, 0139.

31 Y. Liu, G. Zhao, D. Wang and Y. Li, *Natl. Sci. Rev.*, 2015, **2**, 150–166.

32 H. H. Kung and M. C. Kung, in *Nanotechnology in Catalysis*, Springer New York, pp.

1–11.

33 A. Wang, J. Li and T. Zhang, *Nat. Rev. Chem.*, 2018, **2**, 65–81.

34 M. E. Ali, M. M. Rahman, S. M. Sarkar and S. B. A. Hamid, *J. Nanomater.*, DOI:10.1155/2014/192038.

35 G. Wang, C. Li and H. Shan, *ACS Catal.*, 2014, **4**, 1139–1143.

36 A. Salamat, A. L. Hector, P. Kroll and P. F. McMillan, *Coord. Chem. Rev.*, 2013, **257**, 2063–2072.

37 Y. Xiao, J. Y. Hwang and Y. K. Sun, *J. Mater. Chem. A*, 2016, **4**, 10379–10393.

38 S. Kanai, I. Nagahara, Y. Kita, K. Kamata and M. Hara, *Chem. Sci.*, 2017, **8**, 3146–3153.

39 R. Prins and M. E. Bussell, *Catal. Letters*, 2012, **142**, 1413–1436.

40 J. Liang, Z. Liang, R. Zou and Y. Zhao, *Adv. Mater.*, 2017, **29**, 1701139.

41 N. Shibasaki-Kitakawa, H. Honda, H. Kuribayashi, T. Toda, T. Fukumura and T. Yonemoto, *Bioresour. Technol.*, 2007, **98**, 416–421.

42 J. Baloyi, T. Ntho and J. Moma, *RSC Adv.*, 2018, **8**, 5197–5211.

43 G. C.Bond, *Heterogeneous catalysis: principles and applications*, Oxford :Clarendon Press, Oxford, 1987, vol. 27.

44 G. C. Bond, *Catalysis by Metals*, London, New York, Academic press, London, First edn, 1962.

45 C. Satterfield, *Heterogeneous catalysis in industrial practice*, McGraw-Hill, New York, 2nd edn., 1991.

46 M.-H. Vu, M. Sakar and T.-O. Do, *Catalysts*, 2018, **8**, 621.

47 F. A. Peter Atkins, Tina Overton , Jonathan Rourke , Mark Weller, *Shriver and Atkins' Inorganic Chemistry*, OUP Oxford, 5th edn., 2009.

48 J. M. Thomas, *Angew. Chem. Int. Ed.*, 1988, **27**, 1673–1691.

49 E. Roduner, *Chem. Soc. Rev.*, 2014, **43**, 8226–8239.

50 W. J. M. Rootsaert and W. M. H. Sachtler, *Zeitschrift für Phys. Chemie*, 1960, **26**, 16–26.

51 R. J. White, R. Luque, V. L. Budarin, J. H. Clark and D. J. Macquarrie, *Chem. Soc. Rev.*, 2009, **38**, 481–494.

52 I. Ijaz, E. Gilani, A. Nazir and A. Bukhari, *Green Chem. Lett. Rev.*, 2020, **13**, 223–245.

53 P. Iqbal, J. A. Preece and P. M. Mendes, in *Supramolecular Chemistry*, John Wiley & Sons, Ltd, Chichester, UK, 2012.

54 A. T. Bell, *Science.*, 2003, **299**, 1688–1691.

55 X. Fang, B. Liu, K. Cao, P. Yang, Q. Zhao, F. Jiang, Y. Xu, R. Chen and X. Liu, *ACS Catal.*, 2020, **10**, 2799–2816.

56 I. Lee and F. Zaera, *Top. Catal.*, 2013, **56**, 1284–1298.

57 S. Bagheri, N. Muhd Julkapli and S. Bee Abd Hamid, *Sci. World J.*, 2014, **2014**, 1–21.

58 R. Ferrando, J. Jellinek and R. L. Johnston, *Chem. Rev.*, 2008, **108**, 845–910.

59 H. Davy, *Philos. Trans. R. Soc. London*, 1817, **107**, 77–85.

60 J. Heveling, *J. Chem. Educ.*, 2012, **89**, 1530–1536.

61 P. and J. B. C. R. S. Sabatier, *.Acad.Sci.*, 1897, **124**, 1358–1361.

62 P. van Helden, I. M. Ciobîcă and R. L. J. Coetzer, *Catal. Today*, 2016, **261**, 48–59.

63 P. Buffat and J.-P. Borel, *Phys. Rev. A*, 1976, **13**, 2287–2298.

64 H. Wang, Y. Wang, Z. Zhu, A. Sapi, K. An, G. Kennedy, W. D. Michalak and G. A. Somorjai, *Nano Lett.*, 2013, **13**, 2976–2979.

65 S. Cao, F. F. Tao, Y. Tang, Y. Li and J. Yu, *Chem. Soc. Rev.*, 2016, **45**, 4747–4765.

66 L. Liu and A. Corma, *Chem. Rev.*, 2018, **118**, 4981–5079.

67 H. M. Lu and X. K. Meng, *J. Phys. Chem. C*, 2010, **114**, 1534–1538.

68 H. Zhang, M. Jin, Y. Xiong, B. Lim and Y. Xia, *Acc. Chem. Res.*, 2013, **46**, 1783–1794.

69 M. Jin, G. He, H. Zhang, J. Zeng, Z. Xie and Y. Xia, *Angew. Chem. Int. Ed.*, 2011, **50**, 10560–10564.

70 Z. Wu, S. Yang and W. Wu, *Nanoscale*, 2016, **8**, 1237–1259.

71 J. K. Nørskov, T. Bligaard, B. Hvolbæk, F. Abild-Pedersen, I. Chorkendorff and C. H. Christensen, *Chem. Soc. Rev.*, 2008, **37**, 2163.

72 J. K. Nørskov, T. Bligaard, J. Rossmeisl and C. H. Christensen, *Nat. Chem.*, 2009, **1**, 37–46.

73 J. K. Norskov, F. Abild-Pedersen, F. Studt and T. Bligaard, *Proc. Natl. Acad. Sci.*, 2011, **108**, 937–943.

74 M. Sankar, N. Dimitratos, P. J. Miedziak, P. P. Wells, C. J. Kiely and G. J. Hutchings, *Chem. Soc. Rev.*, 2012, **41**, 8099.

75 S. J. Tauster, S. C. Fung and R. L. Garten, *J. Am. Chem. Soc.*, 1978, **100**, 170–175.

76 T. W. Van Deelen, C. Hernández Mejía and K. P. de Jong, *Nat. Catal.*, 2019, **2**, 955–970.

77 C. J. Pan, M. C. Tsai, W. N. Su, J. Rick, N. G. Akalework, A. K. Agegnehu, S. Y. Cheng and B. J. Hwang, *J. Taiwan Inst. Chem. Eng.*, 2017, **74**, 154–186.

78 P. Wu, S. Tan, J. Moon, Z. Yan, V. Fung, N. Li, S. Z. Yang, Y. Cheng, C. W. Abney, Z. Wu, A. Savara, A. M. Momen, D. Jiang, D. Su, H. Li, W. Zhu, S. Dai and H. Zhu, *Nat. Commun.*, 2020, **11**, 3042.

79 A. Ruiz Puigdollers, P. Schlexer, S. Tosoni and G. Pacchioni, *ACS Catal.*, 2017, **7**, 6493–6513.

80 M. S. Chen and D. W. Goodman, *Top. Catal.*, 2007, **44**, 41–47.

81 M. S. Chen, *Science*, 2004, **306**, 252–255.

82 H. Yoshitake and Y. Iwasawa, *J. Phys. Chem.*, 1992, **96**, 1329–1334.

83 E. W. McFarland and H. Metiu, *Chem. Rev.*, 2013, **113**, 4391–4427.

84 I. C. Gerber and P. Serp, *Chem. Rev.*, 2020, **120**, 1250–1349.

85 X. Ning, Y. Li, B. Dong, H. Wang, H. Yu, F. Peng and Y. Yang, *J. Catal.*, 2017, **348**, 100–109.

86 S. A. Ansari, M. M. Khan, M. O. Ansari and M. H. Cho, *New J. Chem.*, 2016, **40**, 3000–3009.

87 A. E. Giannakas, M. Antonopoulou, J. Papavasiliou, Y. Deligiannakis and I. Konstantinou, *J. Photochem. Photobiol. A Chem.*, 2017, **349**, 25–35.

88 T. Mitsudome, Y. Mikami, M. Matoba, T. Mizugaki, K. Jitsukawa and K. Kaneda, *Angew. Chem. Int. Ed.*, 2012, **51**, 136–139.

89 D. Wang and Y. Li, *Adv. Mater.*, 2011, **23**, 1044–1060.

90 S. Furukawa and T. Komatsu, *ACS Catal.*, 2017, **7**, 735–765.

91 N. Toshima and T. Yonezawa, *New J. Chem.*, 1998, **22**, 1179–1201.

92 R. Ghosh Chaudhuri and S. Paria, *Chem. Rev.*, 2012, **112**, 2373–2433.

93 K. D. Gilroy, A. Ruditskiy, H.-C. Peng, D. Qin and Y. Xia, *Chem. Rev.*, 2016, **116**, 10414–10472.

94 S. Furukawa, T. Komatsu and K. Shimizu, *J. Mater. Chem. A*, 2020, **8**, 15620–15645.

95 J. Maier, *Zeitschrift für Anorg. und Allg. Chemie*, 2017, **643**, 2083–2087.

96 S. T. Oyama, *Catal. Today*, 1992, **15**, 179–200.

97 Y. M. Zhang, J. R. G. Evans and S. Yang, *J. Cryst. Phys. Chem.*, 2010, **1**, 103–119.

98 M. Armbrüster, in *Encyclopedia of Catalysis*, John Wiley & Sons, Inc., Hoboken, NJ,

USA, 2011.

99 Y. An, H. Ijaz, M. Huang, J. Qu and S. Hu, *Dalt. Trans.*, 2020, **49**, 1646–1651.

100 A. Machocki and R. Jezior, *Chem. Eng. J.*, 2008, **137**, 643–652.

101 M. Armbrüster, R. Schlögl and Y. Grin, *Sci. Technol. Adv. Mater.*, 2014, **15**, 034803.

102 A. B. Dongil, *Nanomaterials*, 2019, **9**, 1111.

103 S. Carenco, D. Portehault, C. Boissière, N. Mézailles and C. Sanchez, *Chem. Rev.*, 2013, **113**, 7981–8065.

104 G.Hägg, *Phys. Chem.B*, 1931, **12**, 33.

105 H. Blank, *Philos. Mag. B*, 1996, **73**, 833–844.

106 L. H. Bennett, A. J. McAlister and R. E. Watson, *Phys. Today*, 1977, **30**, 34–41.

107 L. Toth, *Transiton Metal Carbides and Nitrides*, Academic press, First edn, 1971.

108 Y. Zhong, X. Xia, F. Shi, J. Zhan, J. Tu and H. J. Fan, *Adv. Sci.*, 2016, **3**, 1500286.

109 A. C. Lausche, J. A. Schaidle, N. Schweitzer and L. T. Thompson, in *Comprehensive Inorganic Chemistry II*, Elsevier, 2013, pp. 371–404.

110 L. Brewer, *Science.*, 1968, **161**, 115–122.

111 J. G. Chen, *Chem. Rev.*, 1996, **96**, 1477–1498.

112 N. A. Gokcen, in *Statistical Thermodynamics of Alloys*, Springer US, Boston, MA, 1986, pp. 237–326.

113 R. B. Levy and M. Boudart, *Science.*, 1973, **181**, 547–549.

114 L. H. Bennett, J. R. Cuthill, A. J. McAlister, N. E. Erickson and R. E. Watson, *Science.*, 1974, **184**, 563–565.

115 H. Renner, G. Schlamp, I. Kleinwächter, E. Drost, H. M. Lüschow, P. Tews, P. Panster, M. Diehl, J. Lang, T. Kreuzer, A. Knödler, K. A. Starz, K. Dermann, J. Rothaut, R. Drieselmann, C. Peter and R. Schiele, in *Ullmann's Encyclopedia of*

Industrial Chemistry, Wiley-VCH Verlag GmbH & Co. KGaA, Weinheim, Germany, 2001.

116 G. J. K. Acres, *Mater. Des.*, 1987, **8**, 258–262.

117 H. Dong, J. Zhao, J. Chen, Y. Wu and B. Li, *Int. J. Miner. Process.*, 2015, **145**, 108–113.

118 P. Devendar, R.-Y. Qu, W.-M. Kang, B. He and G.-F. Yang, *J. Agric. Food Chem.*, 2018, **66**, 8914–8934.

119 L. ĈERVENÝ, *Chem. Eng. Commun.*, 1989, **83**, 31–63.

120 S. Sarkar and S. C. Peter, *Inorg. Chem. Front.*, 2018, **5**, 2060–2080.

121 O. T. Holton and J. W. Stevenson, *Platin. Met. Rev.*, 2013, **57**, 259–271.

122 V. Lillo, J. A. Mata, A. M. Segarra, E. Peris and E. Fernandez, *Chem. Commun.*, 2007, 2184–2186.

123 R. J. F. and S. T. G. R.M. Heck, *Catalytic Air Pollution Control: Commercial Technology*, John Wiley & Sons, Inc., Hoboken, New Jersey, USA, 3rd edn., 2009.

124 D. M. Aruguete, M. Murayama, T. Blakney and C. Winkler, *Environ. Sci. Process. Impacts*, 2019, **21**, 133–144.

125 K. A. Jantan, C. Y. Kwok, K. W. Chan, L. Marchiò, A. J. P. White, P. Deplano, A. Serpe and J. D. E. T. Wilton-Ely, *Green Chem.*, 2017, **19**, 5846–5853.

126 BASF, Engelhard Industrial Bullion (EIB) Prices, https://apps.catalysts.basf.com/apps/eibprices/mp/, (accessed 27 January 2021).

127 The three-way catalytic converter, https://www.open.edu/openlearn/science-maths-technology/science/chemistry/the-three-way-catalytic-converter/content-section-1.5.2#:~:text=Exhaust catalysts usually operate in,catalyst) and high driving speeds., (accessed 28 January 2021).

128 E. J. Peterson, A. T. DeLaRiva, S. Lin, R. S. Johnson, H. Guo, J. T. Miller, J. Hun Kwak, C. H. F. Peden, B. Kiefer, L. F. Allard, F. H. Ribeiro and A. K. Datye, *Nat. Commun.*, 2014, **5**, 4885.

129 E. Prasetyo and C. Anderson, *Metals (Basel).*, 2020, **10**, 485.

130 X. Wang, N. Li, L. D. Pfefferle and G. L. Haller, *Catal. Today*, 2009, **146**, 160–165.

131 K. Kusada, H. Kobayashi, R. Ikeda, Y. Kubota, M. Takata, S. Toh, T. Yamamoto, S. Matsumura, N. Sumi, K. Sato, K. Nagaoka and H. Kitagawa, *J. Am. Chem. Soc.*, 2014, **136**, 1864–1871.

132 T. Chen, C. Foo and S. C. Edman Tsang, *Chem. Sci.*, 2021, **12**, 517–532.

133 T. B. Flanagan, *Annu.Rev.Mater.Sci.*, 1991, 269–304.

134 G. Li, H. Kobayashi, J. M. Taylor, R. Ikeda, Y. Kubota, K. Kato, M. Takata, T. Yamamoto, S. Toh, S. Matsumura and H. Kitagawa, *Nat. Mater.*, 2014, **13**, 802–806.

135 Z. Zhao, X. Huang, M. Li, G. Wang, C. Lee, E. Zhu, X. Duan and Y. Huang, *J. Am. Chem. Soc.*, 2015, **137**, 15672–15675.

136 B. D. Adams and A. Chen, *Mater. Today*, 2011, **14**, 282–289.

137 Y. Fukai, *The Metal-Hydrogen System*, Springer Berlin Heidelberg, Berlin, Heidelberg, 1993, vol. 21.

138 S. Dekura, H. Kobayashi, K. Kusada and H. Kitagawa, *ChemPhysChem*, 2019, **20**, 1158–1176.

139 A. Borodziński and G. C. Bond, *Catal. Rev.*, 2006, **48**, 91–144.

140 T. Graham, *Proc. R. Soc. London*, 1868, **16**, 422–427.

141 A. L. Bugaev, O. A. Usoltsev, A. A. Guda, K. A. Lomachenko, I. A. Pankin, Y. V. Rusalev, H. Emerich, E. Groppo, R. Pellegrini, A. V. Soldatov, J. A. van Bokhoven and C. Lamberti, *J. Phys. Chem. C*, 2018, **122**, 12029–12037.

142 J. Stachurski and A. Frąckiewicz, *J. Less Common Met.*, 1985, **108**, 249–256.

143 S. B. Ziemecki, G. A. Jones, D. G. Swartzfager, R. L. Harlow and J. Faber, *J. Am. Chem. Soc.*, 1985, **107**, 4547–4548.

144 D. Teschner, J. Borsodi, A. Wootsch, Z. Revay, M. Havecker, A. Knop-Gericke, S. D. Jackson and R. Schlogl, *Science.*, 2008, **320**, 86–89.

145 I. T. Ellis, E. H. Wolf, G. Jones, B. Lo, M. Meng-Jung Li, A. P. E. York and S. C. Edman Tsang, *Chem. Commun.*, 2017, **53**, 601–604.

146 M. Beck, M. Ellner and E. J. Mittemeijer, *Mater. Sci. Forum*, 2000, **321**–**324**, 604–609.

147 C. W. A. Chan, A. H. Mahadi, M. M. J. Li, E. C. Corbos, C. Tang, G. Jones, W. C. H. Kuo, J. Cookson, C. M. Brown, P. T. Bishop and S. C. E. Tsang, *Nat. Commun.*, 2014, **5**, 5787.

148 K. Jiang, K. Xu, S. Zou and W.-B. Cai, *J. Am. Chem. Soc.*, 2014, **136**, 4861–4864.

149 T. T. Vo Doan, J. Wang, K. C. Poon, D. C. L. Tan, B. Khezri, R. D. Webster, H. Su and H. Sato, *Angew. Chem. Int. Ed.*, 2016, **55**, 6842–6847.

150 B. Hammer and J. K. Norskov, *Nature*, 1995, **376**, 238–240.

151 J. Sangster and A. . Pelton, *J. Phase Equilibria*, 1992, **13**, 63–66.

152 C. D. Gelatt, A. R. Williams and V. L. Moruzzi, *Phys. Rev. B*, 1983, **27**, 2005–2013.

153 C. P. Nash, F. M. Boyden and L. D. Whittig, *J. Am. Chem. Soc.*, 1960, **82**, 6203–6204.

154 W.Bronger and W. Klemm, , *Z. Anorg. Allg. Chem.*, 1962, **74**, 58–81.

155 W. Bronger, G. Klessen and P. Müller, *J. Less Common Met.*, 1985, **109**, L1–L2.

156 Gerhard Reinacher, *Platin. Met. Rev.*, 1957, 136–137.

157 H. Brodowsky and H. Sagunski, *Berichte der Bunsengesellschaft für Phys. Chemie*, 1983, **87**, 803–805.

158 G. L. Selman, P. J. Ellison and a. S. Darling, *Platin. Met. Rev.*, 1970, **14**, 14–20.

159 A. Hecq, T. Robert, M. Hecq, J. . Delrue, J. . Pireaux and R. Caudano, *J. Less Common Met.*, 1981, **80**, P83–P89.

160 C. W. A. Chan, K. Y. Tam, J. Cookson, P. Bishop and S. C. Tsang, *Catal. Sci. Technol.*, 2011, **1**, 1584.

161 A. L. Bugaev, A. A. Guda, I. A. Pankin, E. Groppo, R. Pellegrini, A. Longo, A. V. Soldatov and C. Lamberti, *Catal. Today*, 2019, **336**, 40–44.

162 T. Chen, I. Ellis, T. J. N. Hooper, E. Liberti, L. Ye, B. T. W. Lo, C. O'Leary, A. A. Sheader, G. T. Martinez, L. Jones, P.-L. Ho, P. Zhao, J. Cookson, P. T. Bishop, P. Chater, J. V. Hanna, P. Nellist and S. C. E. Tsang, *J. Am. Chem. Soc.*, 2019, **141**, 19616–19624.

163 M. Nesselberger and M. Arenz, *ChemCatChem*, 2016, **8**, 1125–1131.

164 P. D. Nellist, in *Science of Microscopy*, Springer New York, New York, NY, pp. 65–132.

165 Z. Wang, D. Santhanagopalan, W. Zhang, F. Wang, H. L. Xin, K. He, J. Li, N. Dudney and Y. S. Meng, *Nano Lett.*, 2016, **16**, 3760–3767.

166 K. Kobayashi, H. Kobayashi, M. Maesato, M. Hayashi, T. Yamamoto, S. Yoshioka, S. Matsumura, T. Sugiyama, S. Kawaguchi, Y. Kubota, H. Nakanishi and H. Kitagawa, *Angew. Chem. Int. Ed.*, 2017, **56**, 6578–6582.

167 H. Yang, R. N. Rutte, L. Jones, M. Simson, R. Sagawa, H. Ryll, M. Huth, T. J. Pennycook, M. L. H. Green, H. Soltau, Y. Kondo, B. G. Davis and P. D. Nellist, *Nat. Commun.*, 2016, **7**, 12532.

168 B. Lin, X. Wu, L. Xie, Y. Kang, H. Du, F. Kang, J. Li and L. Gan, *Angew. Chem. Int. Ed.*, 2020, **59**, 20348–20352.

169 C.-H. (Clayton) Zhou, J. N. Beltramini, Y.-X. Fan and G. Q. (Max) Lu, *Chem. Soc. Rev.*, 2008, **37**, 527–549.

170 C. Somerville, *Science.*, 2004, **306**, 2206–2211.

171 M. Carrier, A. Loppinet-Serani, D. Denux, J.-M. Lasnier, F. Ham-Pichavant, F. Cansell and C. Aymonier, *Biomass and Bioenergy*, 2011, **35**, 298–307.

172 S. G. Wettstein, D. M. Alonso, E. I. Gürbüz and J. A. Dumesic, *Curr. Opin. Chem. Eng.*, 2012, **1**, 218–224.

173 R.-J. van Putten, J. C. van der Waal, E. de Jong, C. B. Rasrendra, H. J. Heeres and J. G. de Vries, *Chem. Rev.*, 2013, **113**, 1499–1597.

174 B. Saha and M. M. Abu-Omar, *Green Chem.*, 2014, **16**, 24–38.

175 M. Chatterjee, T. Ishizaka and H. Kawanami, *Green Chem.*, 2014, **16**, 4734–4739.

176 A. Corma, S. Iborra and A. Velty, *Chem. Rev.*, 2007, **107**, 2411–2502.

177 K. N. and K. horiuch. I.Matsumoto, *Jpn. Kokai*, 1973, **73**, 763.

178 J. M. Timko and D. J. Cram, *J. Am. Chem. Soc.*, 1974, **96**, 7159–7160.

179 C. Moreau, M. N. Belgacem and A. Gandini, *Top. Catal.*, 2004, **27**, 11–30.

180 T. Buntara, S. Noel, P. H. Phua, I. Melián-Cabrera, J. G. de Vries and H. J. Heeres, *Angew. Chem. Int. Ed.*, 2011, **50**, 7083–7087.

181 W. Hao, W. Li, X. Tang, X. Zeng, Y. Sun, S. Liu and L. Lin, *Green Chem.*, 2016, **18**, 1080–1088.

182 A. D. Patel, J. C. Serrano-Ruiz, J. A. Dumesic and R. P. Anex, *Chem. Eng. J.*, 2010, **160**, 311–321.

183 S. Chen, R. Wojcieszak, F. Dumeignil, E. Marceau and S. Royer, *Chem. Rev.*, 2018, **118**, 11023–11117.

184 M. Saidi, F. Samimi, D. Karimipourfard, T. Nimmanwudipong, B. C. Gates and M. R.

Rahimpour, *Energy Environ. Sci.*, 2014, **7**, 103–129.

185 M. Chidambaram and A. T. Bell, *Green Chem.*, 2010, **12**, 1253.

186 J. Shi, M. Zhang, W. Du, W. Ning and Z. Hou, *Catal. Sci. Technol.*, 2015, **5**, 3108–3112.

187 E. A. Redina, K. V. Vikanova, G. I. Kapustin, I. V. Mishin, O. P. Tkachenko and L. M. Kustov, *European J. Org. Chem.*, 2019, **2019**, 4159–4170.

Chapter 2 Principle of Analytical Techniques

2.1 Introduction

As emphasised by investigators in the heterogeneous catalysis field, understanding of structure-performance relationship, rationalisation of the catalytic mechanism and design of novel catalysis synthesis each rely upon a combination of different characterisation techniques from macro- to micro-scale, which is an interdisciplinary course in nature. It requires cooperation between scientists with different backgrounds, such as chemists, material scientists and theorists.[1]

This chapter provides an introduction to the analytical methods that were employed to characterise the physicochemical structure of Pd-^{int}B/C (Chapter 4), Pd-^{int}Li/C (Chapter 5) and Pt-^{sub}Li/C (Chapter 6) in this work. The conventional characterisation techniques, for example, thermogravimetric analysis (TGA), X-ray diffraction (XRD), X-ray photoelectron spectroscopy (XPS), scanning transmission electron microscopy ((S)TEM), inductively coupled plasma mass spectroscopy (ICP-MS) can each provide generic structural and chemical composition information. Although these traditional characterisation methods provide basic information about the modification of light elements in heavy metal frameworks, in depth understanding requires advanced techniques to address issues, such as

1. How the local modification influences the main metal framework?
2. Is it possible to prove the light dopant across the volume of the heavy metal NPs at the atomic level?

Thus, synchrotron X-ray powder diffraction (SXRD), neutron diffraction, *in-situ* X-ray pair distribution function (XPDF), solid state nuclear magnetic resonance (ssNMR), electron energy loss spectroscopy (EELS) and electron ptychography were employed to address these problems.

2.2 Thermogravimetric Analysis (TGA)

TGA is a conventional technique to study the change in mass as the temperature is increased. The key components of TGA apparatus are a balance and a furnace. Both solids and low volatility liquids are appropriate for TGA investigation. Typically, the amount of sample required to carry out the TGA measurements is within the range of 1 – 100 mg. Inert gases (N_2, Ar) or reactive gases (O_2, H_2, air supply) can be used for the gas supply. In general, the temperature range of the TGA is from room temperature to approximately 1000 – 1600 °C with an adjustable heating rate. When the sample is heated or cooled, the mass of the material either increases or decreases. Mass increase can be observed when the solid reacts with reactive gases such as O_2, H_2. In contrast, mass reduction is usually accompanied by thermal decomposition, vaporization of the bulk solids, vaporization of liquids adsorbed by solids, sublimation, desorption of gases, etc.[2]

The result of TGA measurements is presented in the form of a thermogravimetric curve that can be displayed in terms of integral (TG curve, mass loss in % or absolute in gram) or differential form (DTG curve, a derivative of the TG curve to time that is plotted against temperature). For the DTG curve, downward peaks mean mass loss phases while upward peaks mean mass gain phases. The resolution of the TGA measurements is dependent on the heating rate and the programme selections. In general, slower heating rates result in a TG curve with a higher resolution but the measurement takes longer to complete. In this thesis, TGA was tested as a preliminary analytical technique to predict the feasibility of the Pt-Li binary NPs formation.

2.3 X-Ray Diffraction (XRD)

XRD is one of the most conventional analytical techniques which can provide information on crystal structures, such as lattice parameters for phase identification.[3] In general, for the laboratory source XRD, incident X-rays are produced in a cathode X-ray tube. A filament is

heated to generate hot electrons which are accelerated to bombard a target metal material under a certain voltage. When the hot electrons have enough energy, they can knock out core electrons from the metal, and electrons in the outer shells relax and fill the vacancies, generating X-rays.[4] The X-rays are filtered with either foils or crystal monochromator which yields monochromatic X-rays for diffraction experiments. Copper metal is often utilised as the X-ray source for the lab-source XRD, and the typical wavelength is either $K_{\alpha 1}$ = (λ = 1.5406 Å) or $K_{\alpha 2}$ = (λ = 1.5416 Å). When these X-rays are collimated and irradiated onto the sample at angle θ, the X-ray detector counts the intensity of the scattered X-ray at an angle of 2θ, as presented in Figure 2.1.

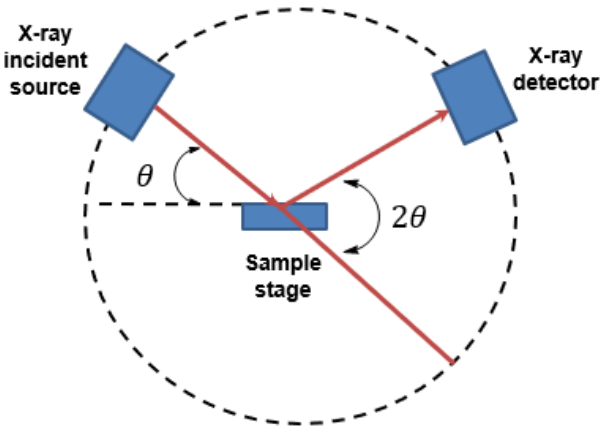


Figure 2.1. A typical Bragg Brentano geometry configuration of lab-source X-ray diffractometer. This figure was drawn on basis of ref. 4.

Synchrotron radiation has played a vital role for structural investigation. At a synchrotron radiation facility, electrons are generated in an electron gun, and subsequently accelerated to an energy of 3−8 billion electron-volts (6 GeV) in the booster ring. The electrons are then directed into a several-km circumference ultra-high vacuum storage ring. Electrons within the storage ring are moving at high speed and compelled to change their pathway under a magnetic field, emitting electromagnetic radiation in a narrow cone tangential to the ring. As shown in Figure 2.2, the electromagnetic radiation in a vertical direction is collimated by a collimating mirror into a parallel beam. A double crystal monochromator is used to filter electromagnetic radiation to yield monochromatic X-rays, and also confine the beam in the horizontal direction.

The focusing mirror is employed to further focus the beam in a vertical direction on the sample point.[5] The advent of the synchrotron X-rays allows the collection of data with high resolution, high intensity, high collimation and broad energy spectrum.

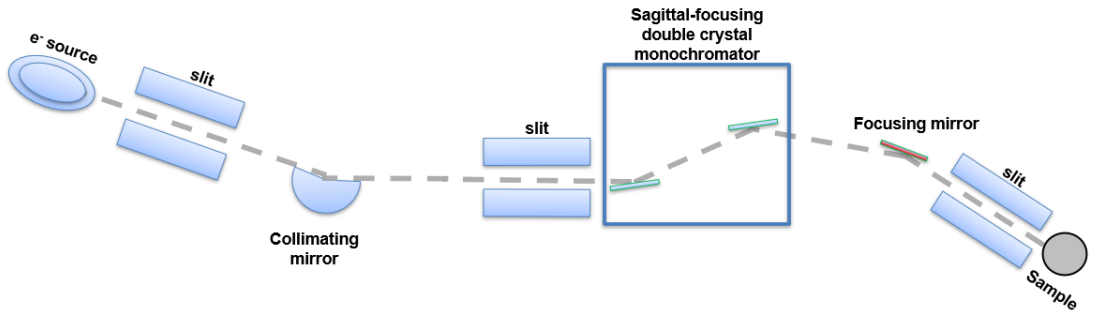


Figure 2.2. A typical configuration of SR-XRD beamline. This figure was drawn on basis of ref. 5.

When either incident lab-source or synchrotron X-ray shine to the crystalline sample at an angle θ, constructive interference will happen if satisfying two conditions as below (Figure 2.3):

1) the angle of the incident ray is equal to the angle of x-ray scattered,
2) the path difference is equal to an integer, n, of wavelength.

The Bragg's equation (Equation 2.1) below is utilised to predict the angle that a reflected beam will be observed

$$\sin\theta = \frac{n\lambda}{2d} \qquad \text{(Equation 2.1)}$$

Where λ is the wavelength of the incident source; n is an integer, referred to the order of diffraction; d is the lattice spacing, and the θ is the diffraction angle.

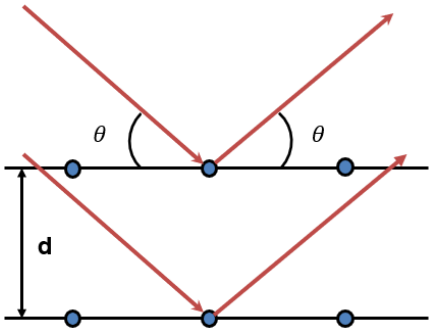


Figure 2.3. Scattering of X-rays from the 1st and 2nd rows of atoms in a crystal lattice. This figure was drawn on basis of ref. 6.

Miller indices are used for denoting a specific set of planes in a crystal. Calculation of the interplanar spacing for individual Miller indices can offer some information in the preliminary investigation. In this thesis, variation in the interplanar spacing is used to verify the formation of Pd-^{int}B/C, Pd-^{int}Li/C and Pt-^{sub}Li/C. Since Pd and Pt are cubic structure, the interplanar spacing d_{hkl} between parallel planes (*h,k,l*) of a unit cell with lengths, *a* for a cubic system can be calculated by the Equation 2.2.

$$\frac{1}{d_{hkl}^2} = \frac{h^2 + k^2 + l^2}{a^2} \qquad \text{(Equation 2.2)}$$

XRD diffraction patterns can not only provide interplanar spacing but also provide other vulnerable information, such as information of particle size. The Scherrer equation[7] is used to estimate the size of the crystal, as presented in Equation 2.3.

$$B_{hkl} = \frac{(K \times \lambda)}{(L \times cos\Theta)} \qquad \text{(Equation 2.3)}$$

Where B_{hkl} is the full width half maximum (FWHM) of the X-ray diffraction peak, λ is the wavelength of the incident X-ray; *K* is the crystallite-shape factor; *L* is the crystallite size.[8] In the case of the NPs, the presence of defects and particle size distribution may affect the peak profile, leading to peak diffusing. To confirm the particle size of the NP samples, other complementary analytical techniques, such as TEM, are often used.

2.4 Neutron Diffraction

X-ray diffraction measurements mainly rely upon the interaction between the incident X-ray and the electron cloud surrounding each atom, and hence, the diffracted X-ray intensity is highly dependent on the atomic number. As a result, it is challenging to utilise X-ray diffraction to probe materials containing light elements. Neutron diffraction is a type of elastic neutron scattering where incident neutron serves as diffraction source. It can provide complementary structure information to X-ray diffraction. A schematic of a neutron diffraction experiment is

shown in Figure 2.4. Neutrons can be produced by either steady-state reactors or pulsed, accelerator-driven spallation neutron sources. In a reactor source, enriched U-235 isotopes undergo fission by striking with a high flux of thermal neutrons. While in a spallation source, the production of the neutrons is by striking a target of heavy elements (W, U) with protons accelerated to 500−1000 eV. The high energy neutrons are slowed down by passing then through a moderator, which contains light or heavy water in the case of reactor source, and a hydrogenous material, (typical polyethylene) in the case of spallation sources.[9] The neutrons produced pass through a collimator, which can define their trajectory. An energy filter produces a monochromatic and collimated beam. The sample is packed in a volume of 1 to 5 cm^3 container since such preparation can ensure a sufficient number of grains are in the right position to reflect from any set of crystal planes. The beam hits and is diffracted from the sample at a certain angle, which with then passes to an analyser and detector.[10] The aforementioned Bragg equation can also describe the elastic scattering at crystal lattices.

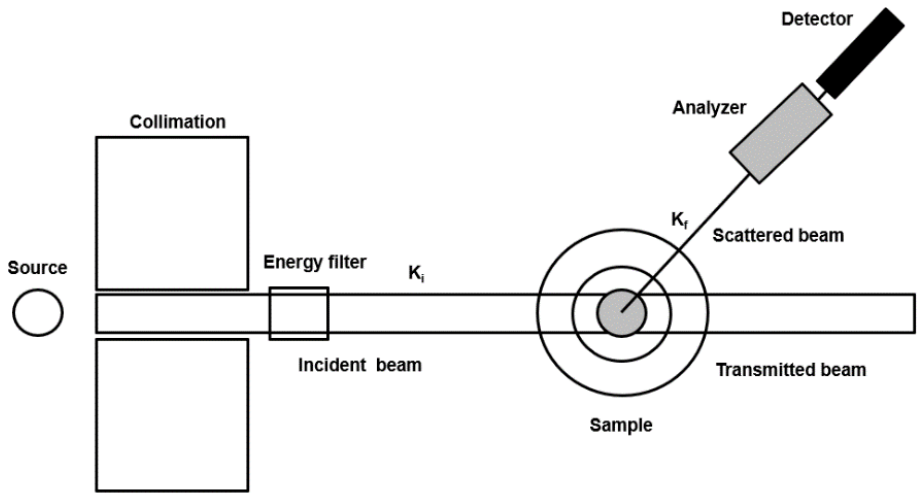


Figure 2.4. A schematic of a neutron diffraction experiment. This figure was drawn on basis of ref. 10.

It should be pointed out that the neutron diffraction mechanism is different from the X-ray diffraction mechanism. Neutrons interact primarily with the nucleus, instead of the electron cloud. The diffraction signal is highly dependent on the scattering cross-section, $\sigma = 4\pi b^2$. The scattering length, b, is used to determine the scattering strength of X-rays and neutrons by an

atom.[11] The scattering length of the X-ray scattering is dependent on the atomic number of the element, whereas that of the neutron scattering varies between elements and even varies between different isotopes of the same element. In particular, the scattering length for some light elements is similar to those for heavy elements. As such, in this thesis, neutron diffraction is an appropriate technique to determine the location of light elements in the presence of heavy elements,[12] and it is expected to resolve the Li location of the Pd-^{int}Li/C and Pt-^{sub}Li/C.

2.5 Pair Distribution Function (PDF)

Diffraction is a powerful technique but sometimes is unable to solve structural arrangement of low crystallinity materials, particular for the amorphous materials. In the case of the nano-scaled sample, the features of low crystallinity, such as the presence of lattice distortion, lattice mismatch or even amorphous components can result in very broad and diffuse peaks, which is known as Scherrer broadening.[13] PDF is a promising technique which can analyse the information of broad diffuse patterns to obtain nearest atomic distances and the coordination number. This is because the PDF experiment collects not only Braggs scattering information, but also the diffuse scattering information, measuring total scattering signals over a wide-angular range of reciprocal space. The configuration of the experiment is shown in Figure 2.5.

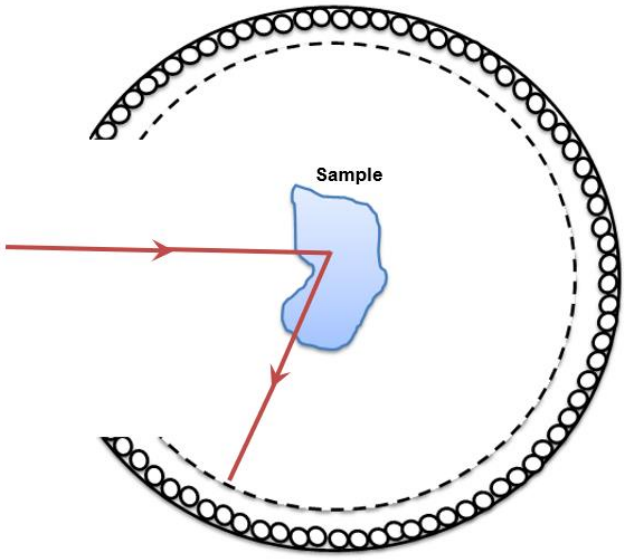


Figure 2.5. A schematic representation of the process for collecting PDF scattering information. This figure was drawn on basis of ref. 14.

Q is the scattering vector, which is used to measure location in the reciprocal space.[15] The magnitude of scatter vector (Equation 2.4) is defined as:

$$Q = \frac{4\pi \sin\theta}{\lambda} \qquad \text{(Equation 2.4)}$$

Where θ is half of the scattering angle and λ is the wavelength of the incident source. Commonly, a synchrotron X-ray or a spallation neutron source are generally used for high-resolution PDF measurements as their shorter wavelengths can ensure a broad location in the reciprocal space. Ideally, Q is expected to be equal or higher than 30 $Å^{-1}$.[16,14,17] The signal is processed to correct for instrumental artefacts, and normalized, resulting in a reduced structure function, which is expressed by Equation 2.5:

$$F(Q) = Q(S(Q)-1) \qquad \text{(Equation 2.5)}$$

Where the S(Q) is the total scattering structural function. The experimental G(r) can be obtained by a Fourier transformation over a reasonably large Q range:[18]

$$G(r)=(2/\pi) \int_{Q_{min}}^{Q_{max}} Q[s(Q)-1]\sin(Q_r)dQ \qquad \text{(Equation 2.6)}$$

Though in practice, the reduced atomic pair distribution function (Equation 2.7) is more frequently used:

$$G(r)=4\pi r(\rho(r) - \rho_0) \quad \text{(Equation 2.7)}$$

Where r is the distance between two atoms, $\rho(r)$ is the microscopic pair density and ρ_0 is the average number density.[15] In a typical PDF pattern, the peak position reveals the distance of atomic pairs. The peak of the area is correlated with the abundance of the relevant pairs weighted by their scattering power. The width of peaks reveals the degree of disorder inside the material in terms of the structural disorder or/and atomic thermal vibrations. The maximum distance at which peaks are found is related to the size of the particle or coherent domain.[19] In this thesis, this technique was employed to characterise Pd-^{int}B/C and Pd-^{int}Li/C, since the incorporation of the light element can induce meaningful disorder upon the host metal system. PDFgui software was used to retrieve the structural information from the experimental profile.[20]

2.6 Inductively Coupled Plasma Mass Spectroscopy (ICP-MS)

ICP-MS is a powerful analytical technique which can provide the elemental analysis at trace level for wide applications, such as biological fluids, food, materials and chemicals.[21] The configuration of ICP-MS consists of 6 components, as depicted in Figure 2.6,[22] which are the sample introduction system, coupled plasma (ICP), interface, ion optics, mass analyser and detector.

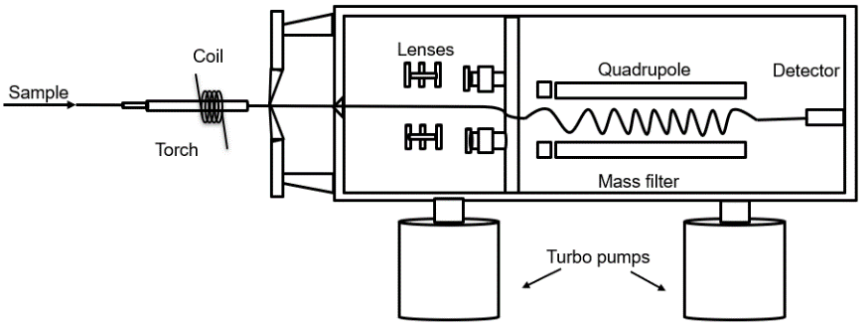


Figure 2.6. A schematic of ICP-MS configuration. This figure was drawn on basis of ref. 22.

Liquid samples are initially nebulised in the sample introduction system, yielding a fine aerosol that is later delivered to the argon plasma. In contrast to the low-temperature ion sources for molecular ions, the high-temperature plasma can break up all of the bonds irrespective of their chemical bonding to atomise and ionise the sample, resulting in the formation of ions. The ions are later extracted through the interface region and transferred into the ion optics (a set of electrostatic lenses). The ion optics focus and emit the ion beam into quardrupole mass analyser. The mass analyser separates ions based on their mass-charge ratio (m/z), then these ions are detected by the detector. In comparison with inductively coupled plasma atomic emission spectrometry (ICP-AES), one major advantage of ICP-MS has lower detection limit. However, the instrumental cost of ICP-MS is very high, which is not cost effective for a low-volume laboratory.[22] In this thesis, ICP-MS was carried out to measure the atomic ratio of Pd-^{int}Li/C and Pt-^{sub}Li/C to estimate the Li content in these two samples.

2.7 X-Ray Photoelectron Spectroscopy (XPS)

XPS is a spectroscopic technique which can determine the chemical state of solid material surfaces to a depth of 2−5 nm. Information about surface chemical composition, oxidation state of individual elements and chemical bonding can be derived from the measured electron energy and energy shifts, respectively.

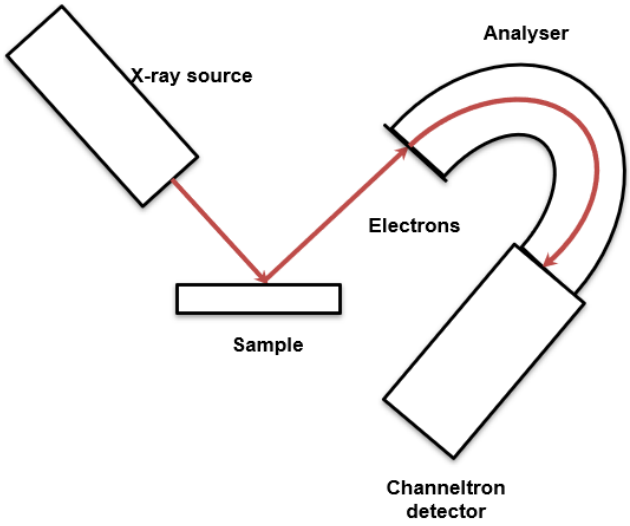


Figure 2.7. The schematic of XPS instrumental configuration. This figure was drawn on basis of ref. 23.

The physical phenomenon behind the XPS is photoelectric effect, which was mathematically explained in the early 20th century. A typical XPS instrumental configuration is shown in Figure 2.7. The most conventional X-ray incident sources are characteristic Kα lines from Al (1253.6 eV) and Mg (1486.6 eV) anodes because of their small natural line width (0.7 eV for Al Kα; 0.56 eV for Mg Kα).[24] Additionally, with the aid of recent development in synchrotron source facilities, other X-ray sources, such as Ag Lα, Si Kα; Ti Kα, can also be employed to acquire a spectrum with a higher resolution.[24] During the XPS measurement, the sample is irradiated by a beam of X-ray photons of a known energy, which induces the photoelectric effect. A fraction of electrons close to the surface are ejected into the vacuum and drift into the channeltron detector which is used to measure the electron current as a function of their kinetic energy.

The key factor of the XPS spectra is the binding energy, which is obtained from the measured kinetic energy E_k of the detected photoelectrons, as depicted in the Equation 2.8 below.

$$E_b = h\nu - E_k \qquad \text{(Equation 2.8)}$$

Where $h\nu$ is the photon energy; E_b is the electron binding energy; E_k is the photoelectron kinetic

energy.

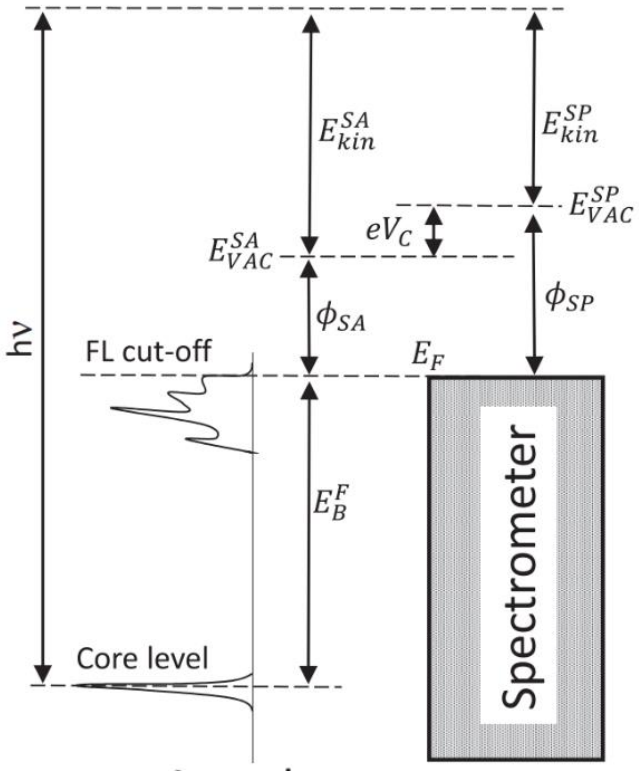


Figure 2.8. Energy level diagram for a sample in good electrical contact. This figure has been reproduced from ref. 24 with permission from Elsevier, copyright 2020.

It is worthwhile to point out that such equation is only applicable for gas-phase measurements. In the case of solid samples, other factors, for instance, sample and spectrometer work functions must be included, since the photoelectrons ejecting from the sample have to overcome the work function ϕ_{sample}, which equals to the energy difference between the Fermi level and the vacuum level. Moreover, a potential difference between the sample to the spectrometer needs to be considered (Figure 2.8), and hence, equation 2.8 should be modified as shown below (Equation 2.9).

$$E_k = h\nu - E_b - \phi_{spec} \qquad \text{(Equation 2.9)}$$

Where the ϕ_{spec} is the work function of the spectrometer and should be established before the experiments.

The resultant intensity vs. energy plots is the so-called XPS spectra. The detection

limitation is dependent on the element. The XPS spectroscopic notations are labelled in the form of "X *nlj*",[25] where X represents as the element; n denotes the principal quantum number (n = 1, 2, 3, …); l is the angular quantum number (s, p , d, f corresponding to l = 0, 1, 2,…, n − 1). j describes as the total angular momentum quantum number, which is sum of the angular and spin (s = ± 1/2) quantum numbers, $j = l + s$. All core-level signals with $l \geq 1$ have a form of spin-split doublets ($p_{3/2}$-$p_{1/2}$, $d_{5/2}$-$d_{3/2}$, $f_{7/2}$-$f_{5/2}$) with a theoretical area ratio of 2:1, 3:2 and 4:3 respectively, that are determined by the degeneracy of each electronic level ($2j$+1).

Based on the location of the binding energy in the spectrum, oxidation states of the sample can be estimated. If the sample is oxidised, withdrawal of the valence electron makes a contribution to increase in binding energy, as the core electrons are held more strongly by the nucleus and is reversed when the sample is in a reduced state. Sometimes, the accumulation of positive charges over the surface, so called sample charge, may also result in shift towards higher binding energy. The predominant method is to correct the binding energy scale, using the C1s peak as the reference. With the aid of the computational programming, compositional quantitative analysis can be performed by fitting and integrating the intensity of XPS peaks. In this thesis, XPS measurement in combination with XPSPEAK 41 software was employed to identify oxidation state of the Pt^{2+} and Pt^{0} from Pt/C and Pt-^{sub}Li/C NPs and quantify the relative ratio of Pt^{2+} and Pt^{0}.

2.8 Solid State Nuclear Magnetic Resonance (ssNMR)

Nuclear magnetic resonance spectroscopy has been popular among the chemists and material scientists for the investigation of molecular structure, electronic structure and overall crystal structure.

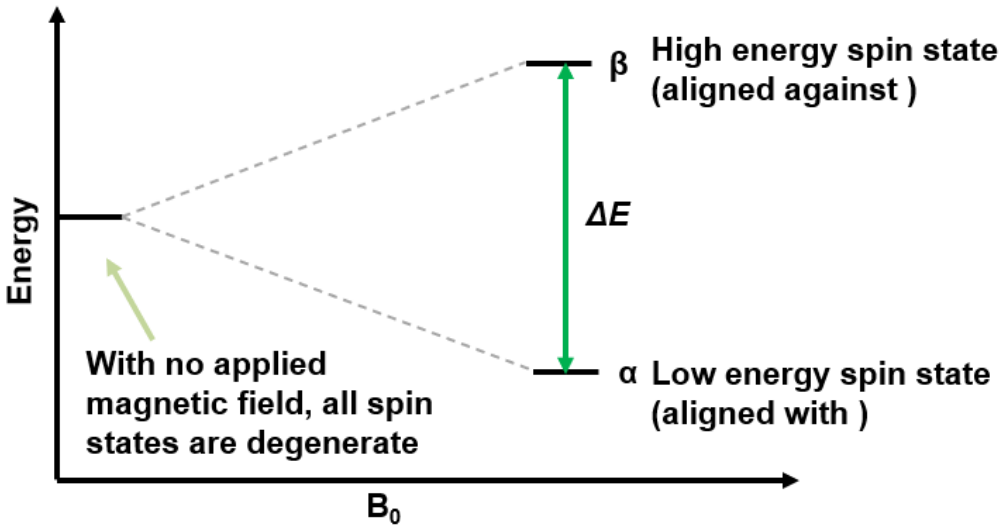


Figure 2.9. The energy difference between the α and β spin state is dependent on the applied magnetic field B_0. This figure was drawn on basis of ref. 6.

Depending on the relative numbers of the protons and neutrons within the nuclei, the categories of the nuclei can be classified as in inactive ($I = 0$), dipolar ($I = \frac{1}{2}$), and quadrupolar ($I > \frac{1}{2}$). Take the example of the ^{13}C or ^{1}H, they behave like bar magnets and align themselves with or against in the presence of an external magnetic field B_0, in light of the rule of "$2nI + 1$ (n = the number of coupling nuclei)". The external magnetic field B_0 can remove the degeneracy of the nuclear spin states and lead to the formation of the α spin state and β spin state, respectively, as depicted in Figure 2.9. The energy separation between α spin state and β spin state is given by equation 2.10:

$$\Delta E = \frac{h\gamma B_0}{2\pi} \qquad \text{(Equation 2.10)}$$

Where h is the Planck's constant; γ is the gyromagnetic ratio and B_0 is the strength of the applied magnetic field.

If the energy of the incident radiation matches with the difference in energy of the spin states, the energy is absorbed to generate resonance, which promotes the nucleus to the higher spin state.[6] When the electromagnetic radiation stops irradiating, the nucleus then relaxes to

the original state, and the released energy is detected by a sensitive radiofrequency receiver. The intensity is dependent on a number of factors. Decreasing temperature or increasing applied magnetic field can enhance a stronger intensity in the NMR spectra,[26] which can be justified by the Boltzmann distribution based derivation (Equation 2.11).[27]

$$\text{Intensity} \propto (N\alpha - N\beta)B_0 \qquad \text{(Equation 2.11)}$$

Where $N\alpha - N\beta \approx \frac{N\gamma\hbar B_0}{2kT}$, N is the total number of spins ($N = N_\alpha + N_\beta$).

The presence of the external magnetic field can induce an electron circulation, thus generating a local magnetic field. Dependent on the electron clouds near the magnetic nucleus of interest, nuclei in different chemical environments have different shielding constants, so coming into resonance at different frequencies. The difference between its resonance frequency and that of a reference standard is called the chemical shift of the nucleus. The area under the peaks located at individual chemical shifts is integrated to resolve the number of atoms in each chemical environment.

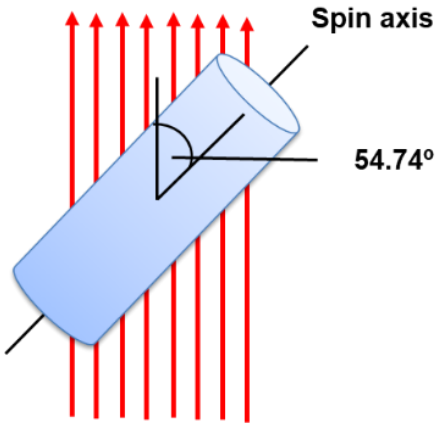


Figure 2.10. In magic angle spinning, the sample rotates at 54.74° with respect to the external magnetic field. This figure was drawn on basis of ref. 27.

However, it is worthwhile to note that, in comparison with the liquid or solution-based sample, characterisation of the solid-state NMR has a broader linewidth, because of the direct magnetic dipolar interaction between nuclear spins, anisotropy of the chemical shifts and

electric quadrupole interaction. To reduce the linewidths of solid samples, magic-angle spinning (MAS) is a powerful strategy which is employed to average the effect of dipole-dipole interactions and chemical shift anisotropy to zero by spinning the sample at 54.74º ($1-3\cos^2\theta = 0$) to the applied magnetic field, shown in Figure 2.10. However, the effect of extremely large anisotropic interaction cannot be averaged to zero by conventional techniques such as MAS. The pattern is much wider than the bandwidth of the probe and hence is it impractical to excite an entire spectrum in a single experiment. Variable-offset cumulative spectroscopy (VOCS) has been used frequently to address this problem.[28] The principle of the method is to record a series of spectra in multiple pieces, with individual sub-spectra acquired at different transmitter frequencies. The total spectrum is subsequently reconstructed by summing up each individual sub-spectra. In this thesis, ssNMR was utilised to investigate the chemical environments of the host metal system in the presence of the dopants, which can give strong evidence in addition to the scattering techniques.

2.9 Electron Microscopy

Despite the fact that scattering-based techniques have already provided valuable structural information about the solid catalyst, it is also essential to gain insight into nanocrystal structure at the atomic level. This is because macro-analysis only provides average information, and so might miss some critical chemical /structural information in the local environment. Transmission Electron Microscopy (TEM) and Scanning Transmission Electron Microscopy (STEM) are used to investigate the chemical composition and structure at the atomic scale. This resolution cannot be provided by other methods. This is because utilisation of the acceleration voltage in (S)TEM can achieve a higher spatial resolution than other X-ray or optical served instruments, the resolution can be expressed by Equation 2.12:

$$r_{min} \sim a(C_S\lambda^3)^{1/4} + b\lambda^{1/2}\left(\frac{C_C\Delta E}{E_0}\right)^{1/2} + \text{parasitic aberrations}^{29} \qquad \text{(Equation 2.12)}$$

Where λ is the wavelength of the radiation; C_s is the spherical aberration coefficients; C_c is the chromatic aberration coefficients; a and b are numbers that depend on the image mode; ΔE is the spread of the energy. Parasitic aberration points to misalignment of the electron-optical column or the effect of stray magnetic fields, which might result in mechanical and electrical instabilities.

Due to wave-particle duality, electrons possess wave-like properties, where the De Broglie wavelength is given by:

$$\lambda = \frac{h}{p} \qquad \text{(Equation 2.13)}$$

λ is the wavelength; p is the momentum and h is Planck's constant.

The electron is accelerated by an electrostatic potential V; the wavelength can be expressed as:

$$\lambda = \frac{h}{\sqrt{2m_0 eV(1+\frac{eV}{2m_0c^2})}} \qquad \text{(Equation 2.14)}$$

Where m_0 is the electron mass; e is the elementary charge; c is the speed of light; h is Planck's constant. As can be seen in Equation 2.14 a higher electrostatic potential can lead to a higher resolution. Note this equation can be simplified into $\lambda = \frac{h}{\sqrt{2m_0 eV}}$, if the applied voltage is below 100 kV. This is because relativistic effects are negligible below 100 kV operating voltage.[30] However, the magnetic lens in electron microscopy is not perfect so aberrations will exist. For instance, astigmatisms, coma, spherical aberration and chromatic aberrations. The appearance of aberrations can limit the resolution and blur the image contrast. Even though the increase in operating voltage can improve the resolution and relieve the influence of the aberration, excessively high accelerating voltage can easily damage the specimen. Spherical aberration is the most dominant factor which limits the resolution of the imaging, as shown in Figure 2.11a.

Rays from a point on the optical axis passing through the lens are not focused on this same position in the optical axis. As a result, a circular blurred image is generated on the image plane. Formation of chromatic aberration is when the electron beam with a big energy spread are incorrectly bent by the magnetic lens, leading to mismatch at the focal plane, depicted in Figure 2.11c.

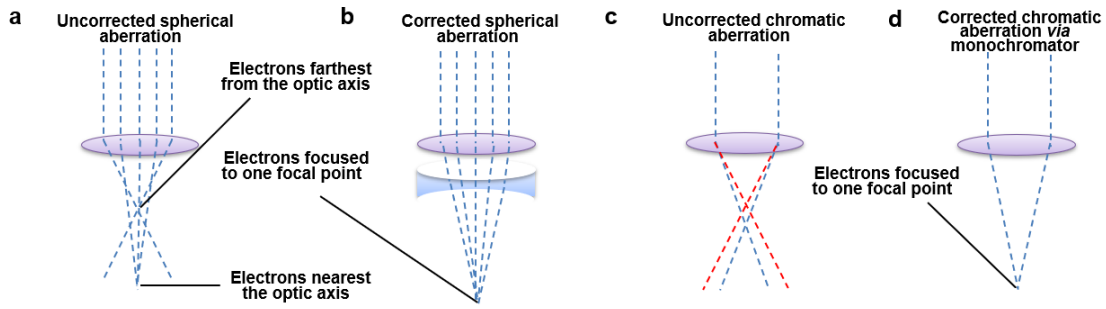


Figure 2.11. (a) Ray schematic without aberration corrector. (b) Ray schematic with an aberration corrector. (c) Ray schematic of chromatic aberration. (d) Ray schematic after correction of chromatic aberration. This figure was drawn on basis of ref. 31, 32.

Benefitting from the recent development in microscopy devices and technique, the advent of advanced aberration correctors offer the opportunity to correct the spherical aberration and obtain the images with a sub-angstrom spatial resolution (Figure 2.11b).[33] The arrival of the cold field-emission electron gun[34] and monochromator[35] have made it possible to electron beams with narrow energy spread, and help to reduce chromatic aberrations (Figure 2.11d). Depending on what information investigators are looking for, in the image mode, (S)TEM can provide images of solid catalyst, from which size distribution and morphology studies of the catalyst can be made. The image mode can also be converted to diffraction mode, indicating the symmetry and space group of a specimen.[36] Additionally, electron microscopes (EM) are often equipped with spectroscopic instruments for experiments such as energy-dispersive X-ray spectroscopy (EDS) or electron energy loss spectroscopy (EELS), which allows images and the corresponding spectroscopic information to be acquired simultaneously.

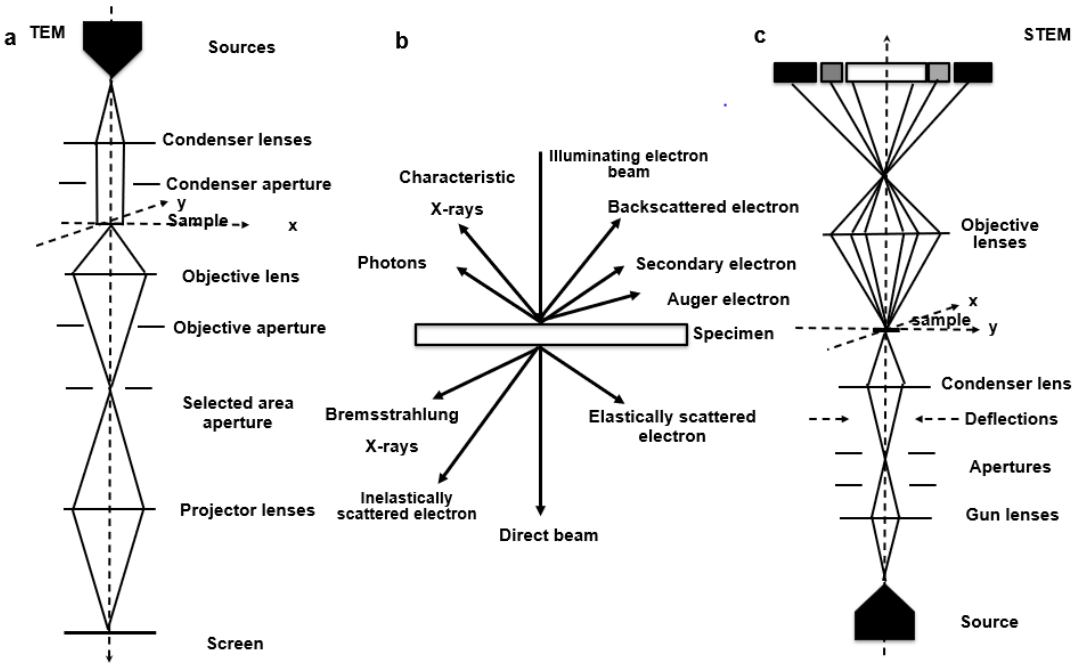


Figure 2.12. (a) The schematic optical configuration of TEM imaging mode. (b) The type of signals generated when electron beam interacts with a specimen. (c) The Schematic optical configuration of STEM imaging mode. This figure was drawn on basis of ref. 37.

Depending on the lens configuration, the operation mode of TEM can be further classified as TEM and STEM mode. Figure 2.12a demonstrates a lens configuration of a simplified TEM model.[38] The electron gun at the top of the electron microscope emits a beam of electrons, which is subsequently focused into a small beam by condenser lens. The condenser lens aperture sometimes is brought into the ray pathway to eliminate high angle electrons. The beam interacts with the sample loaded on the specimen stage to generate a different type of electron beam, as shown in Figure 2.12b. A part of the electron beam is scattered, and a part of it is transmitted. The transmitted portion is focused again by the objective lens and then enlarged by the projector lens into an image on a charge-coupled (CCD) camera. This is known as the bright field (BF) image. In contrast, if scattered electrons are selected, the corresponding image is known as the dark field (DF) image.

The other commonly used operation mode is STEM (Figure 2.12c), where the electron beam is converged to a probe. The probe is scanned over the specimen in a raster fashion by a set of scanning coils. One of the key advantages of the STEM mode is that multiple detectors

can work simultaneously and collect the many types of signal simultaneously, giving complementary views of the specimen. The conventional detectors are BF and ADF detectors respectively. The BF detector collects the forward-scatter on-axis electrons; the ADF collects electrons scattered out to higher angles. The adjusting post specimen lenses can change the camera length, which can further control the inner and outer semi-angles of the detector. Low-angle annular dark-field (LAADF), medium-angle annular dark-field (MAADF), high angle annular dark-field (HAADF) images can be obtained respectively, by choosing corresponding ADF detector and camera length.

In LAADF mode, the ADF detector collects low angle scattered electrons which contain both Z-contrast and diffraction contrast information,[39] which is suitable for visualising the strained or defected features. In the case of JEOL ARM-200 located in Department of Materials-University of Oxford,[40] the typical inner semi-angle of the detector is approximately 22.85 mrad and the outer semi-angle of the detector is 36.0 mrad, if the semi-convergence angle is 22.3 mrad. Although using LAADF mode to investigate Pd or Pt based NPs can boost the signal to noise ratio of the image, the mixture of strain contrast and thickness contrast make it hard to interpret structural information of the sample in LAADF mode. In MAADF mode, the ADF detectors collect electrons scattered through intermediate angles, which can provide information containing some of the characteristics of the HAADF and LAADF.[41] The typical inner semi-angle of the detector is approximately 28.13 mrad, and the outer semi-angle of the detector is approximately 104.36 mrad. In HAADF mode, the ADF detector collects high angle scattered electrons, which at the appropriate angle, enhances the atomic number of the image contrast, which is also known as Z-contrast image (where Z is the atomic number). The typical inner semi-angle of the detector is approximately 50.39 mrad, and the outer semi-angle of the detector is approximately 199.89 mrad. The Z-contrast relationship in STEM -HAADF makes the interpretation of the images straightforward. In this thesis, STEM-HAADF was utilised in

combination with the ptychography to identify the locations of interstitial dopants since STEM-HAADF can enhance the contrast and help to interpret the NP orientation.

2.10 Electron Energy Loss Spectroscopy (EELS)

EELS often accompanies the electron microscopy system.[42] This characterisation technique can reveal the elemental distribution[43], oxidation state[44] and even magnetic measurements[45] at a local environment. Even though Energy Dispersive Spectroscopy (EDX) can also provide spectroscopic information, it is challenging to probe the light elements (boron is typically the lightest element measurable) because of low fluorescence yield. In comparison with the EDX, EELS analytical technique is more sensitive to the light elements. Therefore, in this thesis, EELS was selected to identify the local elemental composition of the Pd-^{int}Li/C, Pd-^{int}B/C and Pt-^{sub}Li/C.

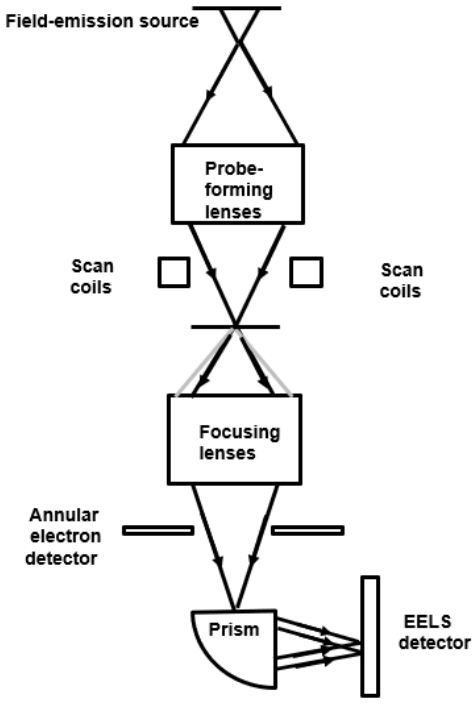


Figure 2.13. Schematic of EELS configuration in STEM mode. This figure was drawn on basis of ref. 42.

As presented in Figure 2.13, the electron beam interacts with the specimen and loses energy due to inelastic collisions. The transmitted electron beam with a variable energy distribution will pass through the entrance aperture of the spectrometer. The function of the

entrance aperture is to control the collection angle, β. A large collection angle can allow for high-intensity signals collection but leads to a poor energy resolution. In contrast, a small aperture can enhance high-energy-resolution spectrum but lose some intensity. The key component of EELS instrumentation is the magnetic prism, which can generate a static magnetic field. Due to the presence of the magnetic field, the rest of the electrons are deflected into a different trajectory because the bending radius is dependent upon the electron speed and hence on the electron energy. A slit located in the exit of the spectrometer allows for an EELS acquisition.

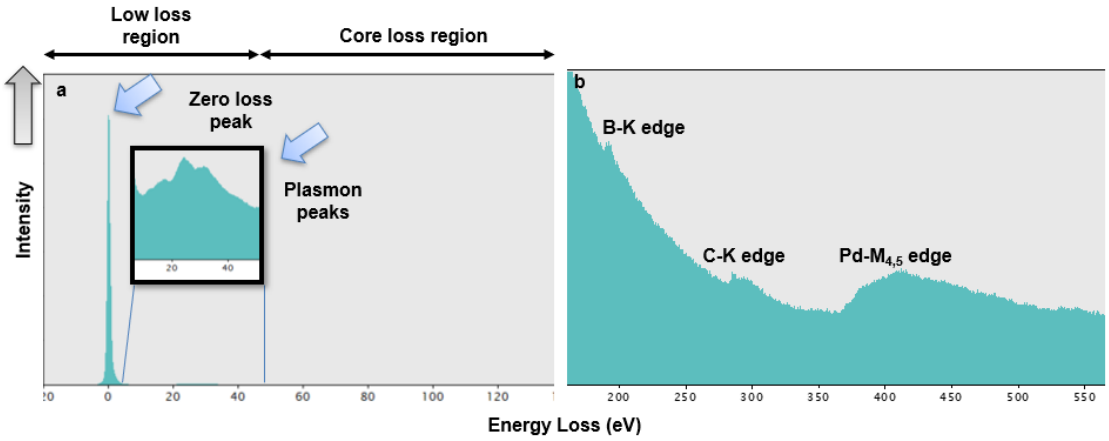


Figure 2.14. (a) A typical example of Pd-^{int}Li/C EELS spectrum. (b) A typical example of Pd-^{int}B/C EELS spectrum.

Figure 2.14a shows a typical EELS spectrum of Pd-^{int}Li/C, which consists of two regions.[46] One is low-loss region (< 50 eV), the other one is core-loss region (> 50 eV). In the low-loss region, the most intense peak, existing at 0 eV, is known as the zero-loss peak (ZLP). The energy resolution of the spectrum can be obtained through measuring the full width at half maximum (FWHM) of the ZLP. This peak mainly contains elastic, forward-scattered electrons, but also contains electrons which have lost a small amount of energy. The peak adjacent to the ZLP is the plasmon peak, which gives meaningful information such as the band structure and dielectric properties of a material. The peak is formed from electrons which have interacted with the weakly bound, outer-shell electrons of the atoms. The core-loss region of the spectrum

shows the peak known as ‘‘ionization edges’’. Figure 2.14b shows a typical EELS spectrum of Pd-^{int}B/C in the core-loss region. When an electron transfers enough energy to a core-shell electron, it will result in an electron in the K, L, M, N or O shells being ejected into the vacuum. With the aid of the digital programming, an EELS spectrum and the corresponding spectral image can be further processed to obtain EELS mapping and atomic ratio, which can provide the relevant structure information at the local environment level.

2.11 Electron Ptychography

STEM has been selected as a priority instrument for the characterisation of materials, because it allows for simultaneous atomic-resolution imaging and spectroscopy. Furthermore, one of the most commonly used STEM imaging techniques, STEM-HAADF, is incoherent and hence produces images that are easily interpretable. However, it is very challenging to image light elements which are adjacent to heavy elements using common STEM imaging modes. This is because the scattering of light elements is significantly weaker than that of heavy elements. Even though annular bright-field STEM (STEM-ABF) can provide atomically resolved contrast of both light and heavy elements, it is sensitive to aberrations and sample tilting.[47] Recently, it has been demonstrated that electron ptychography is capable of solving these difficulties, because it can probe the phase shifts of the electron wave, which can provide contrast for light elements.[48]

The principle of electron ptychography is that a camera records the resultant diffraction patterns formed by transmitted electrons in the far field. The phase information can be retrieved with respect to the interference of direct and diffracted beams.[49] Additionally, ptychography in typical mode can be used simultaneously with conventional ADF and EDX for a single scan,[50] which enables the light element to be observed in the restored phase image in comparison with the ADF image.

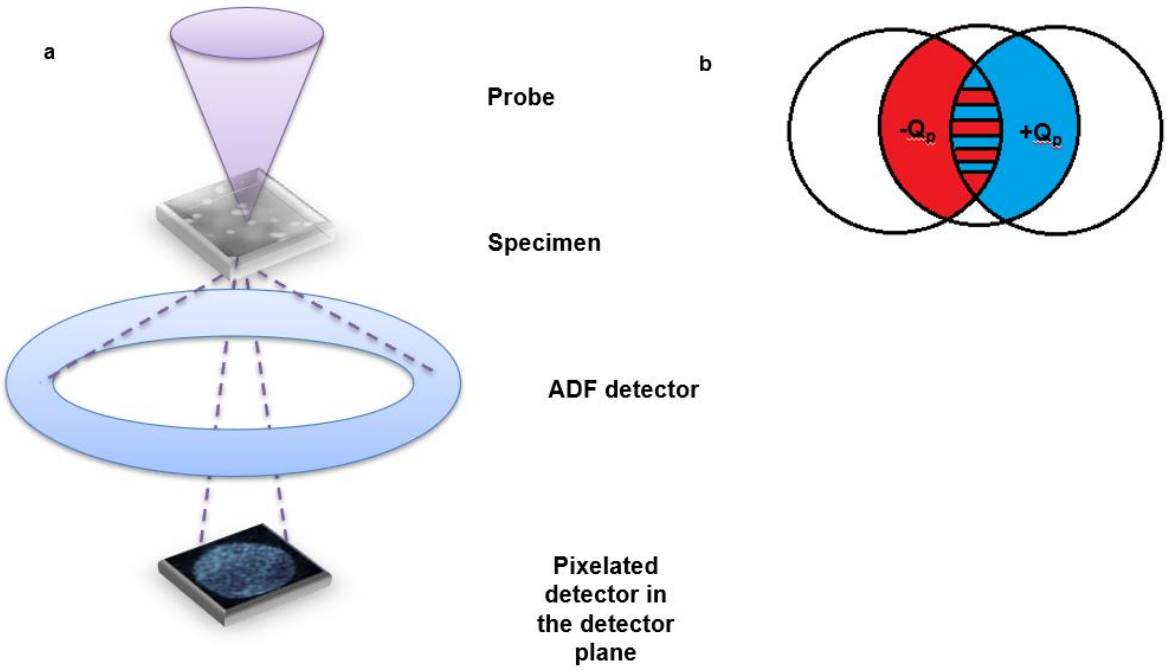


Figure 2.15. (a) An instrumental configuration of STEM ptychography. When the probe is scanned across the specimen, the intensity of the electrons scattered to high angles is collected by the ADF detector, while the pixelated detector records a 2D diffraction pattern. (b) An schematic representation of 4-dimentional dataset $G(K_f, Q_p)$ for a typical Q_p (spatial frequency), where two diffracted beams ($\pm Q_p$) overlap with the direct beam. This figure was drawn on basis of ref. 49.

A schematic of the ptychography experiments that were performed throughout this research project is shown in Figure 2.15a. The experimental procedure is as follows:

The fast-pixelated detector can record the intensity of the convergence beam diffraction patterns at each probe position $\mathbf{R_p}$ in a 2D scan over the specimen. This results in a four-dimensional dataset, denoted $|M(\mathbf{K_f}, \mathbf{R_p})|^2$, where $\mathbf{K_f}$ corresponds to the scattering vector in the detector plane. By performing a Fourier transform with respect to $\mathbf{R_p}$, one can obtain a complex (the combination of real & imaginary number) 4-dimensional dataset, $G(\mathbf{K_f}, \mathbf{Q_p})$ which contains information about the interferences between the direct and diffracted beams (Figure 2.15b). This can be expressed mathematically (Equation 2.15) as below.[51]

$$G(\mathbf{K_f}, \mathbf{Q_p}) = \mathscr{F}_{RP}[|M(\mathbf{K_f}, \mathbf{R_p})|^2]$$

$$= A(\mathbf{K_f})A^*(\mathbf{K_f}+\mathbf{Q_p}) \otimes_{K_f} \psi(\mathbf{K_f})\, \psi^*(\mathbf{K_f}-\mathbf{Q_p}) \qquad \text{(Equation 2.15)}$$

Where M($\mathbf{K_f}$, $\mathbf{R_p}$) is the electron wave in the detector plane; $\mathbf{K_f}$ is the scattering vector; $\mathbf{Q_p}$ is the spatial frequency; $\psi(\mathbf{K_f})\ \psi^*(\mathbf{K_f}-\mathbf{Q_p})$ is the product of two specimen transmission functions separated by $\mathbf{Q_p}$; $\otimes_{Kf}$ is representative of a convolution with respect to the scattering angle, and $A(\mathbf{K_f})\ A^*(\mathbf{K_f}+\mathbf{Q_p})$ denotes the product of two aperture functions separated by $\mathbf{Q_p}$.

Several algorithms can be used to retrieve the phase information from the 4D datasets. In the Nellist research group, the single side band (SSB) and Wigner distribution deconvolution (WDD) methods are the most common algorithms used to reconstruct the phase images from the 4D datasets. SSB is based on the weak phase approximation,[52,53] which is suitable for very thin specimens, such as 2D materials. The Wigner distribution deconvolution (WDD) method involves a construction algorithm that takes into account the non-linear terms through a deconvolution approach. In comparison to the SSB method, the WDD method is suitable for a broader range of materials, including thin Li-rich battery cathodes,[50] nanotubes[49] and NPs.[54] In this thesis, the WDD method was utilised to reconstruct the phase image of the Pd-^{int}B/C, Pd-^{int}Li/C, and Pt-Li/C NPs, in order to identify the location of the foreign dopants.

2.12 Gas Chromatography-Mass Spectroscopy (GC-MS)

GC-MS has become an essential analytical instrument in the chemical laboratory. Its main purpose is to separate, identify and quantify the volatile or semi-volatile chemical components in complex mixtures.[55]

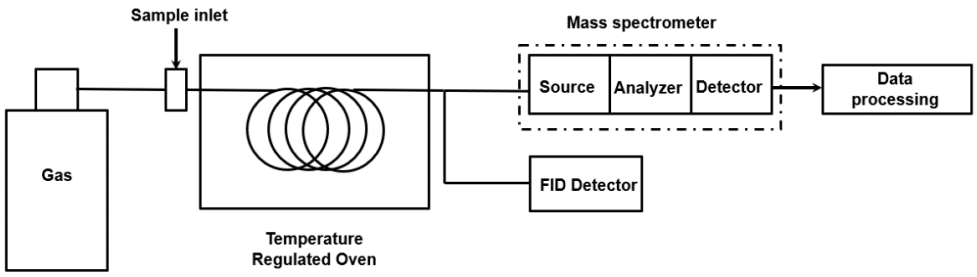


Figure 2.16. A schematic diagram of the GC-MS/GC set-up used in this work. This figure is drawn on the basis of ref. 56.

The principles of GC-MS (Figure 2.16) mainly involve four steps which described below.

1. A liquid sample is injected into a heated system, where it is vaporised.
2. The vapourised sample travels through a column, packed with a stationary (solid) phase, by an inert carrier gas (such as He, N_2 or Ar). Different components of the sample are separated based on a combination of molecular mass and polarity and they elute from the column at different times, which are referred to as "retention times".
3. Once the components of the sample leave the GC column, they pass through a heated transfer region and enter an ion source, where the sample is positively ionised and fragmented by electron bombardment. The generated charged particles are then accelerated through the mass analyser of the instrument generally via a quadrupole or ion trap, separated based on their different mass-to-charge (*m/z*) ratios and detected in proportion to their abundance. A mass spectrum of a molecule displays the result in the form of a plot of ion abundance versus mass-to-charge ratio. Because almost every fragment generated by electron ionisation (EI) had a charge of +1, the highest value of m/z represents the molecular weight of the compound.
4. A computer which controls the GC-MS system contains a library of spectra for the identification of molecular structure. The mass spectrums obtained from the sample analysis is then compared with the data inside the library where a list of potential identifications are made according to the statistical probability of the match. It is worthy to note that the relative area integrated under the peaks of mass spectrum cannot be used for quantitative composition analysis since the ionisation process is random. Therefore, the GC-MS used in this thesis has been reformed. The outlet of the GC column is split into two terminals which are connected to a GC detector and a mass spectrometer. The choice of the GC detector is highly dependent on the physical properties of the target characteristic compounds. For example, a flame ionisation detector (FID) specialises in sensing almost

all combustible organic compounds,[57] while thermal conductivity detector (TCD) can detect all compounds.[58] In this thesis, a GC-MS equipped with FID detector and TCD detector was used to identify and quantify each chemical fragment after hydrogenation of HMF.

2.13 References

1 J. A. Dumesic, G. W. Huber and M. Boudart, in *Handbook of Heterogeneous Catalysis*, Wiley-VCH Verlag GmbH & Co. KGaA, Weinheim, Germany, 2008, pp. 1–15.

2 S. Vyazovkin, in *Characterization of Materials*, John Wiley & Sons, Inc., Hoboken, NJ, USA, 2012, pp. 344–362.

3 J. S. J. Hargreaves, *Crystallogr. Rev.*, 2005, **11**, 21–34.

4 A. A. Bunaciu, E. Gabriela Udriştioiu and H. Y. Aboul-Enein, *Crit. Rev. Anal. Chem.*, 2015, **45**, 289–299.

5 H. Cheng, C. Lu, J. Liu, Y. Yan, X. Han, H. Jin, Y. Wang, Y. Liu and C. Wu, *Prog. Nat. Sci. Mater. Int.*, 2017, **27**, 66–73.

6 S. Duckett and B. Gilbert, *Foundations of spectroscopy*, Oxford University Press, Oxford, 1st edn., 2000.

7 F. T. L. Muniz, M. A. R. Miranda, C. Morilla dos Santos and J. M. Sasaki, *Acta Crystallogr. Sect. A Found. Adv.*, 2016, **72**, 385–390.

8 U. Holzwarth and N. Gibson, *Nat. Nanotechnol.*, 2011, **6**, 534–534.

9 E. Prince, *Appl. Spectrosc. Rev.*, 2004, **34**, 159–172.

10 H. Schober, *J. Neutron Res.*, 2014, **17**, 109–357.

11 Y. Ren and X. Zuo, *Small Methods*, 2018, **2**, 1800064.

12 B. S. F. Parker and P. Collier, *Johnson Matthey Technol. Rev.*, 2016, **60**, 132–144.

13 K. He, N. Chen, C. Wang, L. Wei and J. Chen, *Cryst. Res. Technol.*, 2018, **53**, 1700157.

14 S. J. L. Billinge, *Philos. Trans. R. Soc. A Math. Phys. Eng. Sci.*, 2019, **377**, 20180413.

15 A. Mancini and L. Malavasi, *Chem. Commun.*, 2015, **51**, 16592–16604.

16 P. F. Peterson, E. S. Božin, T. Proffen and S. J. L. Billinge, *J. Appl. Crystallogr.*, 2003, **36**, 53–64.

17 V. Petkov, in *Characterization of Materials*, John Wiley & Sons, Inc., Hoboken, NJ, USA, 2012, pp. 1361–1372.

18 V. Petkov, *Mater. Today*, 2008, **11**, 28–38.

19 K. W. Chapman, *MRS Bull.*, 2016, **41**, 231–240.

20 C. L. Farrow, P. Juhas, J. W. Liu, D. Bryndin, E. S. Božin, J. Bloch, T. Proffen and S. J. L. Billinge, *J. Phys. Condens. Matter*, 2007, **19**, 335219.

21 A. A. Ammann, *J. Mass Spectrom.*, 2007, **42**, 419–427.

22 S. Wilschefski and M. Baxter, *Clin. Biochem. Rev.*, 2019, **40**, 115–133.

23 P. Zimmermann, S. Peredkov, P. M. Abdala, S. DeBeer, M. Tromp, C. Müller and J. A. van Bokhoven, *Coord. Chem. Rev.*, 2020, **423**, 213466.

24 S. Oswald, in *Encyclopedia of Analytical Chemistry*, John Wiley & Sons, Ltd, Chichester, UK, 2013.

25 G. Greczynski and L. Hultman, *Prog. Mater. Sci.*, 2020, **107**, 100591.

26 G. P. A. Burrows, J. Holman, A. Parsons, G. Pilling, *Chemistry^3: Introducing inorganic, organic and physical chemistry*, Oxford University Press, New York, 2nd edn., 2013.

27 J. D. Paula. and P. Atkins, *Atkins' Physical Chemistry*, OUP Oxford, Oxford, 9th edn., 2009.

28 O. Pecher, D. M. Halat, J. Lee, Z. Liu, K. J. Griffith, M. Braun and C. P. Grey, *J. Magn. Reson.*, 2017, **275**, 127–136.

29 R. F. Egerton, *Ultramicroscopy*, 2014, **145**, 85–93.

30 D. B. Williams and C. B. Carter, *Transmission Electron Microscopy*, Springer US, Boston, MA, 2009.

31 S. I. Sanchez, M. W. Small, S. Sivaramakrishnan, J. Wen, J.-M. Zuo and R. G. Nuzzo, *Anal. Chem.*, 2010, **82**, 2599–2607.

32 R. Leary and R. Brydson, *Advances in Imaging and Electron Physics*, 1st edn., Elsevier Inc., 2011, vol. 165, pp. 73–130.

33 O. L. Krivanek, N. Dellby and A. R. Lupini, *Ultramicroscopy*, 1999, **78**, 1–11.

34 Y. Kohno, E. Okunishi, T. Tomita, I. Ishikawa, T. Kaneyama, Y. Ohkura, Y. Kondo and T. Isabell, *Microsc. Anal.*, 2010, **24**, S9.

35 O. L. Krivanek, J. P. Ursin, N. J. Bacon, G. J. Corbin, N. Dellby, P. Hrncirik, M. F. Murfitt, C. S. Own and Z. S. Szilagyi, *Philos. Trans. R. Soc. A Math. Phys. Eng. Sci.*, 2009, **367**, 3683–3697.

36 D. S. Su, B. Zhang and R. Schlögl, *Chem. Rev.*, 2015, **115**, 2818–2882.

37 J. C. Meyer, in *Graphene*, Elsevier, 2014, pp. 101–123.

38 P. J. Goodhew and J. Humphreys, *Electron Microscopy and Analysis*, CRC Press, London, 3rd edn., 2000.

39 D. A. Basha, J. M. Rosalie, H. Somekawa, T. Miyawaki, A. Singh and K. Tsuchiya, *Sci. Technol. Adv. Mater.*, 2016, **17**, 115–127.

40 L. Jones, A. Varambhia, H. Sawada and P. D. Nellist, *J. Microsc.*, 2018, **270**, 176–187.

41 I. Maclaren and Q. M. Ramasse, *Int. Mater. Rev.*, 2014, **59**, 115–131.

42 R. F. Egerton, *Reports Prog. Phys.*, 2009, 72, 016502.

43 P. Trebbia and N. Bonnet, *Ultramicroscopy*, 1990, **34**, 165–178.

44 J.-L. Maurice, G. Herranz, C. Colliex, I. Devos, C. Carrétéro, A. Barthélémy, K. Bouzehouane, S. Fusil, D. Imhoff, É. Jacquet, F. Jomard, D. Ballutaud and M. Basletic, *Europhysics Lett.*, 2008, **82**, 17003.

45 P. Schattschneider, S. Rubino, M. Stoeger-Pollach, C. Hébert, J. Rusz, L. Calmels and E. Snoeck, *J. Appl. Phys.*, 2008, **103**, 07D931.

46 F. Hofer, F. P. Schmidt, W. Grogger and G. Kothleitner, *IOP Conf. Ser. Mater. Sci. Eng.*, 2016, **109**, 012007.

47 D. Zhou, K. Müller-Caspary, W. Sigle, F. F. Krause, A. Rosenauer and P. A. Van Aken, *Ultramicroscopy*, 2016, **160**, 110–117.

48 J. G. Lozano, G. T. Martinez, L. Jin, P. D. Nellist and P. G. Bruce, *Nano Lett.*, 2018, **18**, 6850–6855.

49 H. Yang, R. N. Rutte, L. Jones, M. Simson, R. Sagawa, H. Ryll, M. Huth, T. J. Pennycook, M. L. H. Green, H. Soltau, Y. Kondo, B. G. Davis and P. D. Nellist, *Nat. Commun.*, 2016, **7**, 12532.

50 P. D. Nellist, G. T. Martinez, C. O'Leary and L. Jones, *Microsc. Microanal.*, 2018, **24**, 190–191.

51 H. Yang, I. MacLaren, L. Jones, G. T. Martinez, M. Simson, M. Huth, H. Ryll, H. Soltau, R. Sagawa, Y. Kondo, C. Ophus, P. Ercius, L. Jin, A. Kovács and P. D. Nellist, *Ultramicroscopy*, 2017, **180**, 173–179.

52 J. M. Rodenburg, B. C. McCallum and P. D. Nellist, *Ultramicroscopy*, 1993, **48**, 304–314.

53 T. J. Pennycook, A. R. Lupini, H. Yang, M. F. Murfitt, L. Jones and P. D. Nellist, *Ultramicroscopy*, 2015, **151**, 160–167.

54 T. Chen, I. Ellis, T. J. N. Hooper, E. Liberti, L. Ye, B. T. W. Lo, C. O'Leary, A. A. Sheader, G. T. Martinez, L. Jones, P.-L. Ho, P. Zhao, J. Cookson, P. T. Bishop, P. Chater, J. V. Hanna, P. Nellist and S. C. E. Tsang, *J. Am. Chem. Soc.*, 2019, **141**, 19616–19624.

55 J. Sneddon, S. Masuram and J. C. Richert, *Anal. Lett.*, 2007, **40**, 1003–1012.

56 M. A. Sephton, *Mass Spectrom. Rev.*, 2012, **31**, 560–569.

57 Y. Wan, D. Yan, J. Xiao, D. Chu and Y. Zhang, *J. Phys. Conf. Ser.*, 2019, **1347**, 012106.

58 P. Patnaik, B. B. Kebbekus and S. Mitra, *Enviromental Chemical Analysis*, Routledge, 1st edn., 1997.

Chapter 3 Experimental Procedures

3.1 General information

Unless stated otherwise, synthesis of NPs was carried out under a N_2 atmosphere in the furnace. The reduction of NPs was performed under 5%H_2/N_2 in the furnace. Pd-^{int}B/C synthesis was performed under N_2 and H_2 in oven-dried glassware on a Schlenk line. Although samples were prepared from different batches, to ensure the reproducibility of the synthesis, the samples were characterised by the Lab-source XRD to confirm successful doping of B or Li into Pd and Pt metal framework before carrying out catalytic reactions or other characteristic measurements.

3.2 Materials and Methods

Chemical precursors were purchased from commercial suppliers (Sigma-Aldrich or Alfa Aesar) unless stated otherwise.

3.2.1 X-Ray Diffraction (XRD)

XRD was performed on Bruker D8 ECO or Panalytical X'Pert Pro diffractometer, equipped with an X-ray source Cu anode at 40 kW and 40 mA, of which the corresponding wavelength was 1.5406 Å. Samples were placed onto glass or plastic slides and then pressed by a glass slide before placing onto a sample stage. The XRD profile range was between 5 and 90°.

3.2.2 X-Ray Photoelectron Spectroscopy (XPS)

XPS measurements were carried out using an Omicron sphera II photoelectron spectrometer equipped with an Al-Kα X-ray emitter (hv = 1486.6 eV). All measurements were calibrated using C 1s peak (284.5 eV).

3.2.3 Thermogravimetric Analysis (TGA)

Measurement of TGA was carried out using a TGA Q50 instrument. Samples (10 to 20 mg in weight) were added to a tared platinum pan and were stabilised under a flow of inert gas (N_2 or Ar). All samples were subsequently heated to 800 ^oC at a ramping rate of 10 ^oC per min.

3.2.4 Transmission Electron Microscopy-Bright Field Imaging (TEM-BF)

TEM-BF images were acquired at 300 kV by using the JEOL-3000 microscope (equipped with field emission gun) and/or the JEOL JEM-2100 microscope (equipped with LaB_6 source), both of which were located at Department of Materials-University of Oxford (United Kingdom). Samples (3 mg in weight) were sonicated in either 10 mL of isopropanol or ethanol for 30 minutes. Specimens were prepared by dipping holey-carbon films located on Cu TEM grids into the NPs suspension (made by ultra-sonicating powdered NPs in ethanol). The TEM grids were subsequently dried or baked by Fishione 1020 Plasma Cleaner under vacuum before characterisation.

3.2.5 Scanning Transmission Electron Microscopy-Annular Dark Field Imaging (STEM-ADF)

STEM-ADF images were acquired using the JEOL ARM-200F microscope (equipped with cold field emission source (CFEG) at 80 kV or 200 kV and Cs probe aberration corrector) Department of Materials-University of Oxford or the JEOL ARM-300F (S)TEM (equipped with two aberration correctors at 80 kV) located at the Electron Physical Science Imaging Centre (ePSIC). The convergence semi-angle for imaging was set as 24.8 mrad.

3.2.6 Electron Energy Loss Spectroscopy (EELS)

3.2.6.1 5 wt% Pd-^{int}B/C

EELS acquisition of 5 wt% Pd-^{int}B/C was conducted using the JEOL ARM-200F microscope (equipped with a cold field emission source (CFEG) at 200 kV) located at

Department of Materials-University of Oxford. The CL2-3 aperture was inserted in the beam path to give a semi-convergence angle of 14.25 mrad. Camera length was adjusted to 4 cm, which gave rise to a collection angle of 37.94 mrad with an entrance aperture of 5 cm. EELS spectra were de-noised with Hyperspy (an open source Python library) using the theory of principle component analysis as the basis of the analyses.

3.2.6.2 5 wt% Pd-^{int}Li/C

EELS acquisition of 5 wt% Pd-^{int}Li/C was carried out using the JEOL ARM-200F microscope (which was equipped with a cold field emission source (CFEG) at 200 kV) at Department of Materials-University of Oxford. The CL2-3 aperture was inserted into the pathway, which yielded a semi-convergence angle of 14.25 mrad. The camera length was adjusted to 4 cm, which gave a collection angle of 37.94 mrad with an entrance aperture of 5 cm. Additionally, the sample was also sent to the SuperSTEM facility for EELS experiment at 60 kV to be carried out. The EELS acquisition of Pd-^{int}Li/C was carried out using the Nion UltraSTEM 100MC (which was equipped with high-energy-resolution monochromator for ultimate 15meV energy resolution) at the SuperSTEM facility. The semi-convergence angle is 30 mrad and the collection angle is 44 mrad.

3.2.6.3 20 wt% Pt-^{sub}Li/C

EELS acquisition for 20 wt% Pt-^{sub}Li/C was conducted using the JEOL ARM-200F microscope (which was equipped with a cold field emission source (CFEG) at 200 kV) located at Department of Materials-University of Oxford. The CL2-2 aperture was inserted into the pathway to yield a semi-convergence angle of 22.3 mrad. Camera length was adjusted to 4 cm, which gave a collection angle of 37.94 mrad with an entrance aperture of 5 cm.

3.2.7 Ptychography

Atomic-resolution STEM imaging was performed at 200 kV using a probe-corrected JEOL ARM200CF microscope. The probe-forming aperture was set to be 30 μm in diameter, which gave a convergence angle of 22.3 mrad. Ptychographic datasets were collected using the JEOL 4DCanvas, which is a hard-pixelated, direct electron-radiated detector installed on the JEOL ARM200CF microscope. This camera was capable of delivering full-frame images of 264×264 pixels in resolution at a readout speed of 1,150 frames per second (fps). Across all ptychography experiments, convergent beam electron diffraction (CBED) patterns were acquired under the 4-fold binning mode (66×264 pixels), which increased the readout speed to 4,000 fps. Probes were positioned in either a 512 × 512 or 256 × 256 pixels configuration and images were collected in approximately 90 seconds. The bright-field (BF) disc was set to cover almost the entire detector area (achieved by adjusting the camera length) and dark-field signals were collected using an annular dark-field (ADF) detector. The ADF images and ptychographic datasets were acquired simultaneously. Electron ptychography was subsequently performed on datasets that were acquired with the JEOL 4D Canvas. The purpose was to obtain an electron-phased reconstruction of the object. The phase was retrieved with an in-house ptychography code by leveraging the Wigner distribution deconvolution (WDD)[1] algorithm. Specimens were prepared by dipping holey-carbon films located on Cu TEM grids into the NPs suspension (made by ultra-sonicating powdered NPs in ethanol).

3.2.8 Synchrotron X-Ray Diffraction (SXRD)

SXRD data of 5 wt% Pd/C, 5 wt% Pd-^{int}B/C, 5 wt% Pd-^{int}Li/C and 20 wt% Pd-^{sub}Li/C were collected using the Diamond Light Source science facility located at the Harwell Science and Innovation Campus in Oxfordshire, United Kingdom. The wavelength was set at 0.97920 Å and corresponding energy of the synchrotron X-ray beams were at 12.6 keV. SXRD samples were prepared by filling up glass capillary tubes with NPs. Using the TOPAS software, the

diffraction patterns were analysed by Le Bail or Rietveld refinement methods to obtain components. Works described in the preceding paragraphs of this sub-section were carried out by Dr. Lin Ye and Mr. Chris Foo, and their effort has been duly acknowledged on the front-page of this thesis.

3.2.9 in-situ X-Ray Pair Distribution Function (XPDF)

In-situ XPDF data of 50 wt% Pd/C, 50 wt% Pd-^{int}B/C and 50 wt% Pd-^{int}Li/C were collected with the Beamline l14 instrument located at the aforementioned Diamond Light Source science facility. Wavelength was set at 0.16190 Å and corresponding energy of the synchrotron X-ray beams were at 76.6 keV. Data were collected over the range of $0.5 < Q < 27$ Å^{-1}. In these measurements, the synchrotron X-ray beams were monochromated by Bent-Laue monochromator and had an energy level of 76.6 keV. Samples were prepared by filling up capillary tubes with NPs and sealing up the tubes with glue sol. Horizontal focusing was set at 700 μm. Samples were packed on borosilicate capillaries of 1-mm in diameter and scattered X-ray images were collected by a Perkin Elmer XRD 1611 CP3 area pixel detector once the X-ray beams had reached the spinning samples. The detector had an active surface area of 409.6 × 409.6 mm. Pixel size was set at 100 μm and the sample-to-detector distance was 240.72 mm. Samples were heated using a hot-air blower. The PDFgui refinement was carried out by Dr. Ben Lo. His effort has been duly acknowledged on the front-page of this thesis.

3.2.10 Solid State Nuclear Magnetic Resonance (ssNMR)

^{7}Li MAS Solid state NMR spectra of 20 wt% Pt-^{sub}Li/C were obtained for the ^{7}Li samples at 155.4 MHz (9.4 T) on a Bruker Avance IIIHD spectrometer. In order to obtain quantitative MAS spectra, a single pulse excitation was applied by setting a short pulse length of 0.26 μs. 10000 scans were acquired at a MAS rate of 10 kHz with 0.1 s delay using a 4 mm O.D zirconia rotor. The chemical shift of ^{7}Li was externally referenced against an aqueous solution of Li(NO_3) (0 ppm). ^{105}Pd NMR measurements of 50 wt% Pt-^{sub}Li/C were performed (^{105}Pd

Larmor frequencyυ_0 (^{105}Pd) = 26.58 – 26.64 MHz) under static conditions. Variable-offset cumulative spectroscopy (VOCS) was deployed at a step-size ($\Delta\upsilon 0$) of 20 kHz to provide the required frequency range for excitation, to enable full visualisation of the broad ^{105}Pd NMR lineshapes.[2,3] The experiments were conducted using a Varian 9.5 mm MAS probe (with low-gamma attachment) and all measurements were referenced with respect to the H_2PdCl_6 solution (δ_{iso} = 0.0 ppm)[4]. A solid echo $\pi/2$–τ–$\pi/2$–τ sequence was utilised to avoid ringing effects that were present at low frequencies – the $\pi/2$ pulse length, τ period and recycle delays were set at 10 μs. 30 μs and 0.01 second respectively. Work described within this sub-section (3.2.10) of the thesis were performed by Dr. Thomas Hooper of Warwick University and Dr. Nick Rees of ICL, University of Oxford and their efforts have been thoroughly acknowledged as outlined on the front-page of this thesis.

3.2.11 Neutron Diffraction

Neutron (powder) diffraction experiments of 50 wt% Pd-^{int}Li/C and 20 wt% Pt-^{sub}Li/C were carried out on a time-of-flight diffractometer. Specifically, the general-purpose powder diffractometer (GPPD) at the China Spallation Neutron Source (CSNS) facility in Dongguan, China was utilised. Samples were loaded onto 9.1mm vanadium cans and diffraction patterns were collected at a wavelength range of 0.1~ 4.9 Å.

3.2.12 Analysis of Product Distribution

The reactor was cooled down to room temperature before releasing any residual H_2 Gas. Mesitylene (0.1 mL, internal standard) was added into the reactor and the resulting mixture was stirred for at least 30 minutes. Solid catalysts were removed by filtering the mixture through celite and collecting the remaining aqueous portion in the GC vials to enable characterisation by GC analysis. Response factors were calculated to estimate selectivity of the target product. Conversion of the substrate and selectivity of the target product are calculated by using the following formulas:

(a)

$$\text{Conversion} = \frac{N_T - N_a}{N_T}$$

N_T: amount of input substrates (in moles)

N_a: amount of the remaining substrates after quenching the reaction (in moles)

(b) $$\text{Selectivity} = \frac{N_i}{\sum_i^j N_x}$$

Ni: amount of each individual compound yielded from the reaction (in moles)

$\sum_i^j N_x$: All products found from the GC (in moles)

3.3 Experimental Procedures

3.3.1 5 wt% Pd/C Synthesis

$Pd(OAc)_2$ (106.4 mg) and Vulcan ® XC72R (950 mg) were both added to 50 mL of acetone. The mixture was sonicated for 30 minutes and then heated to 80 ^oC. The resulting powder was placed in calcination for 2 hours under N_2 atmosphere at 250 ^oC, with a ramp rate of 2.5 ^oC/min. Depending on the purity of procured $Pd(OAc)_2$ precursor, calcination temperature may need to be increased to 500 ^oC to eliminate side product formation.

3.3.2 Pd-^{int}B/C Synthesis

150 mg of 5 wt% Pd/C was heated at 40 ℃ to evaporate any residual water content under the N_2 atmosphere. This was followed by increasing the heating temperature to 100 ℃ and maintaining this for 15 minutes under H_2 atmosphere. The resultant powder was wetted with 2 mL of tetrahydrofuran (THF) before adding 3 mL of 1M BH_3·THF in dropwise portions. The resulting mixture was stirred for 15 minutes and then heated at 40 ℃ under N_2 atmosphere to evaporate the THF content. The powder was then heated at 200 ℃ for 1 hour and cooled to

room temperature. And the product was subsequently washed with 150 mL of deionised water and 150 mL of ethanol.

3.3.3 Pd-^{nt}Li/C Synthesis

100 mg of 5 wt% Pd/C was ground together with $Li(OAc)\cdot 2H_2O$ (73 mg) using pestle and mortar until yielding a homogeneous phase. The resulting powder was then heated at 250 ^oC for 2 hours and subsequently washed with 150 mL of deionised water and 150 mL of ethanol.

3.3.4 Pt-^{sub}Li/C Synthesis

20 wt% Pt/C catalyst (procured from Sigma Aldrich) was undergone thermal treatment under 750 ^oC for 2 hours at a ramp rate of 15 ^oC/min in N_2 atmosphere. Then, 100 mg of 20 wt% Pt/C was wet-impregnated with water and ethanol, followed by grinding with 0.262 g of $Li(OAc)\cdot 2H_2O$ by pestle and mortar until obtaining a homogeneous phase. The powdered mixture was then heated in a furnace at 750 ^oC for 2 hours at a ramp rate of 15 ^oC/min. The sample was subsequently washed with 150 mL of deionised water and 150 mL of ethanol.

3.3.5 Hydrogenation of 5-(hydroxymethyl)furfural (HMF)

Hydrogenation of HMF was conducted in a 50 mL sealed autoclave reactor (Parr 4792, pressure vessel) with an inner glass container. Specifically, 0.128 mg of HMF (procured from Sigma Aldrich, $\geq$ 99%) and 40 mg of powdered catalyst were dispersed in 12 mL of isopropanol. The autoclave was purged with H_2 three times and then pressured to 30 bar and heated to the various temperatures and times as summarised in Table 3.1. The autoclave was subsequently cooled to room temperature using an ice bath and 0.1 mL of mesitylene (prepared as internal standard) was added into the resulting mixture. 1 mL of the black suspension was filtered by micro-filter into a GC vial for subsequent GC or GC/MS analysis.

Table 3.1. The summary of reaction temperature and time used in hydrogenation of HMF reaction.

Reaction Time (hour)	Reaction Temperature (°C)
1, 2, 4	100
1,2,4	120

3.4 Computational Programme

3.4.1 ADF Imaging Simulation

3.4.1.1 Pd-^{int}B/C

The ADF-STEM images were simulated using the multi-slice frozen phonon approach as prescribed in the MULTEM[5] software package. The Pd-^{int}B/C unit cell structure (FCC: *Fm-3m*, a = 3.98 Å) was established in accordance with the macro-analytical technique, XPDF. A super cell was projected onto a [010] plane of 2.8143 nm × 2.7860 nm in size. Thickness of the crystal structure aligned in the same as the beam direction were gradually increased to 6.1914 nm. To account for B occupancy, vacancies at interstitial sites were randomly distributed in the super cell cavity to ensure consistency with the EELS mapping. A numerical real space grid of 61 × 86 probe positions was utilised with a sampling resolution of 0.14 Å /pixel for the real space region. Imaging parameters (Table 3.2, which includes acceleration voltage, probe convergence semi-angle and ADF inner and outer collection semi-angles) were set to be the same as those implemented in the experiments. Thermal vibrations were included using a frozen phonon approach[6,7], following an Einstein model with 30 phonon configurations. Debye-Waller factors of Pd and B were obtained from external sources.[8] Gaussian broadening was also implemented to the simulated ADF images with full width at half maximum (FWHM) set to be 0.45 Å. Works described in the preceding paragraphs of this sub-section were carried out by Dr. Emanuela Liberti of Diamond Light Source and her effort has been duly acknowledged on the front-page of this thesis.

Table 3.2. Parameters of ADF imaging simulation.

Accelerating voltage (kV)	200
Phonon configuration	30
Potential Parameterization	Lobato et al.[9]
Slice thickness	2 nm
Probe convergence semi-angle (mrad)	22.3
ADF inner and outer collection semi-angles (mard)	50−242
Scan grid (reciprocal space)	1024 × 1024
Scan grid (real space)	61 × 86
Pixel size	0.14, 0.14

3.4.1.2 Pd-^{int}Li/C

In consideration of the unit cell structure of Pd-^{int}Li (FCC: *Fm-3m*, a = 3.99 Å), a super cell of the size 5.0785 nm × 5.1870 nm was prepared and projected in the direction of the [010] plane. Thickness of the crystals in the beam direction were gradually increased to 6.20708 nm. ADF-STEM images were simulated using the multi-slice frozen phonon approach as prescribed in the MULTEM[5] software package. Imaging parameters (Table 3.3, which includes acceleration voltage, probe convergence semi-angle and ADF inner and outer collection semi-angles) were set to be the same as those used in the experiments. A numerical real space grid of 256 × 256 position was used to scan a region of 8.464 × 7.9800 Å with a sampling resolution of 0.033 Å × 0.031 Å /pixel^2 across the scanning region. Thermal vibrations were included using the frozen phonon approach[6,7] following an Einstein model with 30 phonon configurations. Debye-Waller factors of Pd and Li were obtained from an external source.[8]

Table 3.3. Parameters of ADF imaging simulation**.**

Accelerating voltage (kV)	200
Phonon configuration	30
Potential Parameterization	Lobato et al.[9]
Slice thickness (Å)	1.4107
Probe convergence semi-angle (mrad)	22.3
ADF inner and outer collection semi-angles (mard)	50−242
Scan grid (reciprocal space)	1024 × 1024
Scan grid (real space)	256 × 256
Pixel size (Å)	0.044 × 0.078

3.4.1.3 Pt_7Li

In consideration of the unit cell structure of Pt_7Li (FCC: *Fm-3m*, a = 7.758 Å), a super cell of the size 4.6548 nm × 4.6528 nm was prepared and projected in the direction of the [010] plane. Thickness of the crystals in the beam direction were gradually increased to 6.2336 nm. The simulated ADF-STEM images for the Pt_7Li samples were computed using the multi-slice frozen phonon approach that were prescribed in the MULTEM[5] software package. Imaging parameters (Table 3.4, which includes the acceleration voltage, probe convergence semi-angle and ADF inner and outer collection semi-angles used) were set to be the same as those used in the experiments. The scan view was set to be 1.9375 nm × 1.9375 nm and probes were positioned in a numerical real space grid of the size 512 × 512 in configuration. Sampling resolution was set at 0.038 Å × 0.038 Å /pixel^2. Thermal vibrations were included using the frozen phonon approach,[6,7] following an Einstein model with 30 phonon configurations. Debye-Waller factors of Pt and Li were obtained from an external source.[8]

Table 3.4. Parameters of ADF imaging simulation.

Accelerating voltage (kV)	200
Phonon configuration	30
Potential Parameterization	Lobato et al.[9]
Slice thickness (Å)	1.4107
Probe convergence semi-angle (mrad)	22.3
ADF inner and outer collection semi-angles (mard)	50−199
Scan grid (reciprocal space)	1024 × 1024
Scan grid (real space)	512 × 512
Pixel size (Å)	0.038 × 0.038

3.4.2 Ptychographic Imaging Simulation

3.4.2.1 Pd-^{int}B/C

Coherent electron diffraction patterns (CBEDs) were simulated by using the multi-slice method[10,11] as prescribed in the MULTEM software package.[12] In consideration of the unit cell structure of Pd-^{int}B/C crystals (FCC: *Fm-3m*, a = 3.98 Å), a super cell of size 2.8143 nm × 2.7860 nm was prepared and projected in the [010] plane. Thickness of the crystals in parallel to the beam direction was gradually increased to 6.1914 nm. To account for B occupancy, vacancies at interstitial sites were randomly distributed across the super cell to ensure consistency with EELS mapping. a numerical real space grid of 61 × 86 probes was used, and sampling resolution was set to be 0.14 Å /pixel.

Table 3.5. Parameters of phase imaging simulation.

Accelerating voltage (kV)	200
Phonon configuration	30
Potential Parameterisation	Lobato et al.[9]
Slice thickness	5.7 nm
Probe convergence semi-angle (mrad)	22.3
Scan grid (reciprocal space)	1024 × 1024
Scan grid (real space)	61 × 86
Pixel size	0.14, 0.14

In relation to Pd (FCC: *Fm-3m*, a = 3.88 Å), a super cell of the size 2.7453 nm × 2.7177 nm was constructed in a [010] projection, and the thickness of the crystal was prepared to be 6.0396 nm. A numerical real space grid of 59 × 84 scan positions was set (a sampling resolution of 0.14 Å /pixel) to scan across the region. Thermal vibrations were included using the frozen phonon approach[6,7] under the 30 phonon configuration of the Einstein model. Debye-Waller factors of the elements were obtained from an external source[13]. Details of the key parameters used in performing the simulations have been summarised in Table 3.5 above. A Wigner Deconvolution Distribution algorithm was used to retrieve the samples' wave functions from calculated 4D STEM datasets, in line with approach described in the main manuscript.

3.4.2.2 Pd-^{int}Li/C

Coherent electron diffraction patterns (CBEDs) were simulated using the multi-slice method[10,11] from MULTEM software[12] package. In consideration of the unit cell structure for Pd-^{int}Li/C (FCC: *Fm-3m*, a = 3.98 Å), a super cell of the size 2.814 nm × 2.7860 nm was

prepared and projected in a [010] plane. Thickness of the crystals in parallel to the beam direction was gradually increased to 2, 4 and 6 nm respectively. A numerical real space grid of 61 × 86 scan positions was used as the scanning area. Sampling resolution was set to be 0.14 Å /pixel for scanning across the real space region. Thermal vibrations were included using the frozen phonon approach[6,7], following an Einstein model with 30 phonon configurations. Debye-Waller factors of the elements were obtained from external sources[8].

Details of the key parameters used in setting the simulations are provided in Table 3.6 below. A Wigner Deconvolution Distribution algorithm was used to retrieve the samples' phase information from the calculated 4D STEM datasets, consistent with approach described in the main manuscript.

Table 3.6. Parameters of phase imaging simulation at the 60, 80 and 200 kV.

Accelerating voltage (kV)	200	80	60
Phonon configuration	30	30	30
Potential Parameterization	Lobato et al.[9]	Lobato et al.[9]	Lobato et al.[9]
Slice thickness	2, 4, 6 nm	2, 4, 6 nm	2, 4, 6 nm
Probe convergence semi-angle (mrad)	22.3	24.8 and 31.0	30.6 and 39.1
Scan grid (reciprocal space)	1024 × 1024	1024 × 1024	1024 × 1024
Scan grid (real space)	58 × 81	58 × 81	58 × 81
Pixel size	0.14, 0.14	0.14, 0.14	0.14, 0.14

3.5 References

1 H. Yang, I. MacLaren, L. Jones, G. T. Martinez, M. Simson, M. Huth, H. Ryll, H. Soltau, R. Sagawa, Y. Kondo, C. Ophus, P. Ercius, L. Jin, A. Kovács and P. D. Nellist, *Ultramicroscopy*, 2017, **180**, 173–179.

2 D. Massiot, I. Farnan, N. Gautier, D. Trumeau, A. Trokiner and J. P. Coutures, *Solid State Nucl. Magn. Reson.*, 1995, **4**, 241–248.

3 J. V. Hanna, K. J. Pike, T. Charpentier, T. F. Kemp, M. E. Smith, B. E. G. Lucier, R. W. Schurko and L. S. Cahill, *Chem. - A Eur. J.*, 2010, **16**, 3222–3239.

4 T. J. N. Hooper, T. A. Partridge, G. J. Rees, D. S. Keeble, N. A. Powell, M. E. Smith, I. P. Mikheenko, L. E. Macaskie, P. T. Bishop and J. V. Hanna, *Phys. Chem. Chem. Phys.*, 2018, **20**, 26734–26743.

5 I. Lobato and D. Van Dyck, *Ultramicroscopy*, 2015, **156**, 9–17.

6 R. F. Loane, P. Xu and J. Silcox, *Acta Crystallogr. Sect. A Found. Crystallogr.*, 1991, **47**, 267–278.

7 D. A. Muller, B. Edwards, E. J. Kirkland and J. Silcox, *Ultramicroscopy*, 2001, **86**, 371–380.

8 L.M. Peng, G. Ren, S. L. Dudarev and M. J. Whelan, *Acta Crystallogr. Sect. A Found. Crystallogr.*, 1996, **52**, 456–470.

9 I. Lobato and D. Van Dyck, *Acta Crystallogr. Sect. A Found. Adv.*, 2014, **70**, 636–649.

10 J. M. Cowley and A. F. Moodie, *Acta Crystallogr.*, 1957, **10**, 609–619.

11 P. Goodman and A. F. Moodie, *Acta Crystallogr. Sect. A*, 1974, **30**, 280–290.

12 I. Lobato and D. Van Dyck, *Ultramicroscopy*, 2015, **156**, 9–17.

13 T. G. Berger, Universität Stuttgart, 2005.

14 A. De Backer, K. H. W. van den Bos, W. Van den Broek, J. Sijbers and S. Van Aert, *Ultramicroscopy*, 2016, **171**, 104–116.

15 P. L. Galindo, S. Kret, A. M. Sanchez, J. Y. Laval, A. Yáñez, J. Pizarro, E. Guerrero, T. Ben and S. I. Molina, *Ultramicroscopy*, 2007, **107**, 1186–1193.

Chapter 4 In-Depth Characterisation of Pd-^{int}B/C NPs

4.1 Introduction

It is well known that small atomic species such as boron (B), carbon (C) and nitrogen (N) can diffuse into interstitial sites of transition metal framework, which can modify the catalytic properties, tune the product selectivity or extend the stability of catalysts. For example in the Fischer-Tropsch reaction, inclusion of B or C in Co or Fe during the catalyst preparation stage can enhance the catalytic activities and extend stability.[1] Recently, Takanabe *et al.* experimentally demonstrated that the presence of the B dopants in Co NPs can enhance CH_4 and CO_2 activation. In DFT calculations reported by Takanabe *et al.*,[2] boron atoms are energetically favored to be located at the Co (100) facet of the NP, leading to a significant structural reorganisation.[2]

Selective hydrogenation of alkynes to alkenes is an important area of heterogeneous catalysis. For instance, conversion of acetylene to ethylene is a crucial step to remove trace amounts of acetylene from ethylene streams for production of commercially valuable stocks of the ethylene for polymerisation.[3] The conventional metal catalyst used in this reaction is Pd. To suppress the formation of β-PdH_x which can accelerate the conversion but results in over-hydrogenation,[4] Pd metal catalysts are often alloyed with other foreign elements. Recently, light elements have emerged as a popular choice to alloy into a Pd metal system for selective hydrogenation of alkynes to alkenes.[5] Table 4.1 demonstrates several typical examples of foreign elements that have been used to modify Pd catalysts. Armbrüster *et.al* reported that an outstanding ethylene selectivity of more than 90% over 20 hours on stream can be achieved by the highly ordered intermetallic compound, $Cu_{60}Pd_{40}$ (Table 4.1, entry 1).[6] As suggested by the in-situ prompt gamma activation analysis (PGAA), β-PdH_x formation was excluded after alloying the Cu into the Pd metal system. Addition of other non-precious transition metals,

such as Ag, to the Pd host metal system can also enhance the selectivity for ethylene, but resulted in a lower conversion rate (Table 4.1, entry 2). It is anticipated that β-PdH_x species can be effectively blocked by the Ag shell, and hence promoting the ethylene selectivity. It has also been reported that modification upon the sub-layer of Pd metals by incorporating B or Li can enhance the selectivity for ethylene (Table 4.1, entry 3, 4). It is anticipated that the presence of B can downshift the d-band centre of the metal owing to the movement of electrons from the boron's, p orbital to the palladium's d orbital, which weakens the strength of adsorption for the alkene products.[8] Additionally, the accommodation of the B at the octahedral sites can block the formation of the β-PdH_x species.[5]

Table 4.1. Catalytic performance of Pd-based catalysts for hydrogenation of acetylene to ethylene.

Entry	Catalyst	Reaction system	Conv %	Selec %	Ref
1	$Cu_{60}Pd_{40}$	Catalyst (5 mg), continuous flow (C_2H_2: H_2:C_2H_4 = 1:10:100), 200 °C, 20 hours	90	92%	[6]
2	Pd(0.95)@Ag(0.97)/TiO_2	Catalyst (50 mg), continuous flow (60 mL min^{-1}; C_2H_2: H_2:C_2H_4 vol% = 0.73:1.46: 52.6), 60 °C	82.0	79.0	[7]
3	Pd-^{int}B/C	Catalyst (5 mg), continuous flow (C_2H_2: H_2 = 1:1), 75 °C, 6.7 hours	95	90	[5]
4	Pd-^{int}Li/C	Catalyst (5 mg), continuous flow (C_2H_2: H_2 = 1:1), 75 °C, 6.7 hours	97	85	[5]

It should be emphasised that any explanation of the potential catalytic mechanism is heavily reliant on the characterisation results obtained from various analytical techniques. Currently, the conventional techniques utilised for the interstitial modified system are lab-source XRD[9], HR-TEM[10], XPS[11] and DFT calculations[12]. Although these analytical techniques give general structural information, such as surface composition and local structure, they fail to answer two key questions.

1. How do the B dopants influence the nearby parent structure?

2. Is it possible to visualise the B dopants on the powder-based catalyst sample at the atomic level?

Herein, we introduce a novel combination of characterisation methodology beyond conventional analytical techniques: SXRD,[13] aberration-corrected STEM-ADF image,[14] XPDF,[15] EELS,[16] and ptychography,[17] to investigate the B atom positions any structural modifications to the palladium lattice and the properties of an industrial-type interstitial boron palladium nanoparticle catalyst system (Pd-^{int}B/C NPs).

4.2 Objectives and Methodology

In this chapter, a novel combination of advanced techniques was used to study the Pd-^{int}B/C system, in addition to the conventional techniques. The structural model resulting from the refinement of high-quality SXRD was compared with the results obtained from XPDF and STEM-ADF imaging, establishing a convincing structural model. The presence of B at octahedral sites was, for the first time, further confirmed by ^{105}Pd NMR. Moreover, EELS not only allowed the presence of B distribution to be probed, but also allowed quantification of the local B concentration. The use of ptychography to probe the light element at octahedral sites at the atomic level was also investigated.

4.3 X-Ray Diffraction (XRD)

5 wt% Pd-^{int}B/C powder was made according to a previously reported synthetic procedure involving the thermal decomposition of borane hydride THF complex in the presence of 5 wt% Pd/C at 200 °C.[5] The 5 wt% Pd-^{int}B NPs with an average size/diameter of 6.69 nm were obtained and homogeneously dispersed across the carbon support (See Chapter 8 Appendix Figure 8.1). 5 wt% Pd-^{int}B/C was initially characterised and compared to the pure 5 wt% Pd material, by using XRD (Figure 4.1).

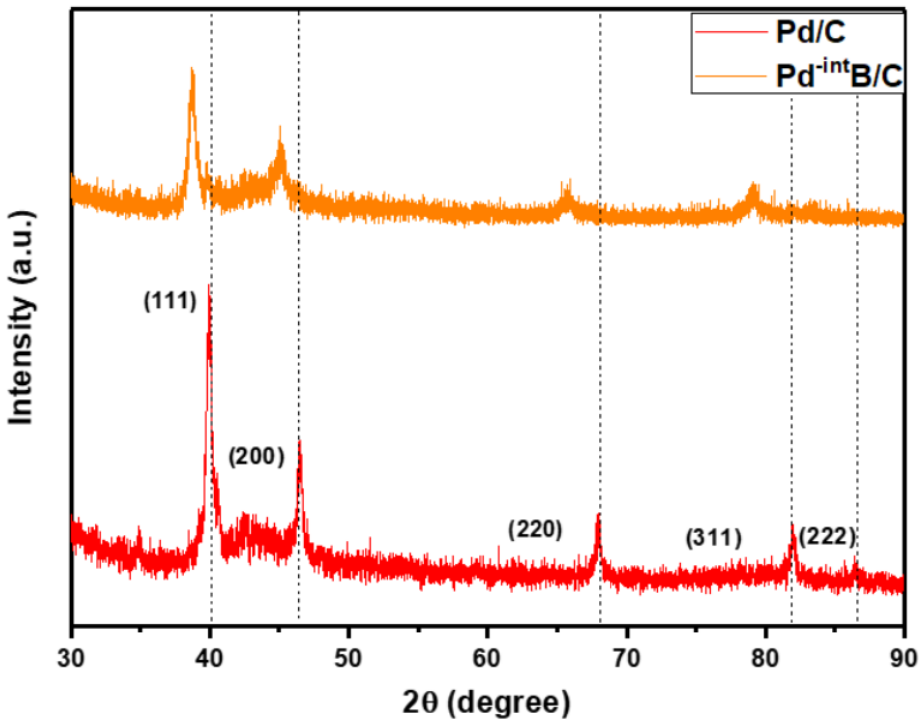


Figure 4.1. Lab source XRD patterns of 5 wt% Pd/C (red), 5 wt% Pd-^{int}B/C (orange). The peaks labelled with dash lines corresponding to Pd (111), (200), (220), (311) and (222) are characteristic of the Pd face-centred cubic (FCC) structure.[18]

As expected, the 5 wt% Pd/C exhibits reflections that match the FCC structure of Pd metal. Five Bragg diffraction peaks of Pd NPs are observable at 2θ = 39.97°, 46.51°, 68.08°, 81.92° and 86.42°, corresponding to the (111), (200), (220), (311) and (222) indices of the FCC structure, respectively, which are illustrated in Table 4.2. 5 wt% Pd-^{int}B/C was subsequently characterised and then compared to pure Pd. The diffraction patterns look similar but differ in

their positions. The reflections are shifted towards lower 2θ values by a shift of ~1 - 3°. The diffraction peak located at (111) shifts from 2θ = 39.97° to 38.71°; the diffraction peak located at (200) shifts from 2θ = 46.51° to 44.99°; the diffraction peak located at (220) shifts from 2θ = 68.08° to 65.65°; the diffraction peak located at (311) shifts from 2θ = 81.92° to 79.06° and the diffraction peak located at (222) shifts from 2θ = 86.42° to 83.62°, leading to average expanded d-spacing (d_{111}= 2.33 Å ; d_{200} = 2.01 Å ; d_{220} = 1.42 Å ; d_{311} = 1.21 Å ; d_{222} = 1.16 Å), in comparison with d_{111} = 2.25 Å; d_{200} = 1.95 Å; d_{220} =1.38 Å; d_{311} = 1.17 Å; d_{222} =1.12 Å for pure Pd metal NPs (Table 4.2). The lattice parameter of Pd−Pd after B modification is now 4.04 Å, representing an increase of ~3.9%. This systematic shift to lower 2θ values by the lattice expansion of the Pd-^{int}B/C system indicates that B is successfully alloyed into the Pd metal.

Table 4.2. Data of XRD patterns of Pd before/after B doping.

Pd diffraction angle 2θ (°) before B doping	***h k l***	**d-spacing (Å)**	**Pd diffraction angle 2θ (°) after B doping**	**d-spacing (Å)**
39.97	111	2.25	38.71	2.33
46.51	200	1.95	44.99	2.01
68.08	220	1.38	65.65	1.42
81.92	311	1.17	79.06	1.21
86.42	222	1.12	83.62	1.16

4.4 Synchrotron X-Ray Diffraction (SXRD)

Although XRD reveals that the bulk phase of supported Pd-^{int}B NPs matches well with an expanded Pd FCC structure, it cannot show whether the incorporation of B can result in other Pd−B based species, such as orthorhombic Pd_2B[19] and Pd_3B[20], monoclinic Pd_5B_2[21] and hexagonal Pd_2B[22].To determine confidently the potential structural phases in the sample and the corresponding lattice parameter, high-resolution SXRD data (Figure 4.2) was collected and analysed.

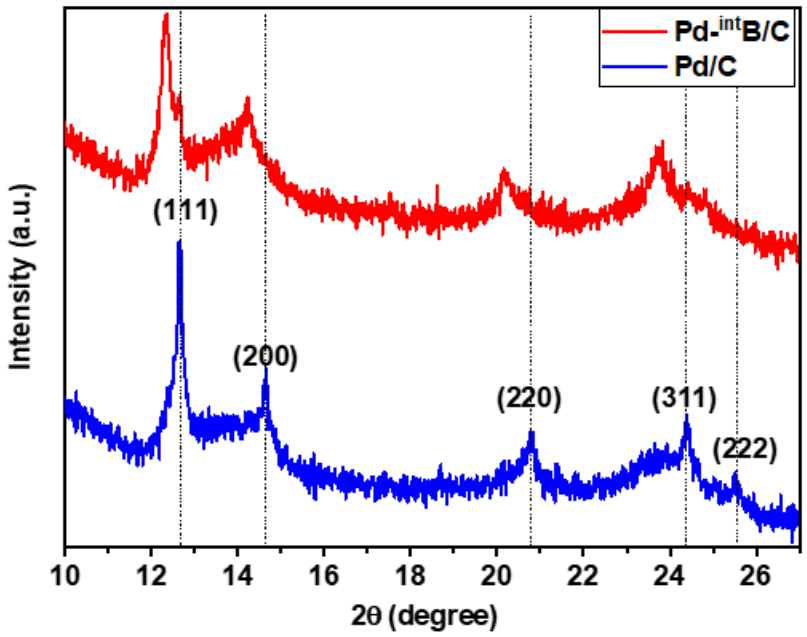


Figure 4.2. SXRD diffraction patterns of the 5 wt% Pd/C and 5 wt% Pd-^{int}B/C.

Le Bail fitting was carried out in TOPAS academic 5.0.[23] Because the synthetic strategy of 5 wt% Pd-^{int}B/C NPs preparation is analogous to that of the HCP Pd_2B nanocrystal preparation,[22] phase, Pd-^{int}B/C (HCP: *P6mm*), was introduced in addition to the other phases, (Pd/C, Pd-^{int}B/C (FCC: *Fm-3m*). R-factors (R_{wp} / R_p / R_{exp} / χ^2) were utilised to evaluate the quality of the fitting. The R-factors decreased continuously as the number of structures was introduced progressively. As depicted in Table 4.3, the R-factor suggests that the combination

of the Pd/C, Pd-^{int}B/C (*Fm-3m*), and Pd-^{int}B/C (*P6mm*) phases reproduced the observed patterns well.

Table 4.3. R-factors of 5 wt% Pd-^{int}B/C samples by Le Bail fitting.

Samples	**Le Bail** R_{wp} / R_p / R_{exp} / $\chi 2$	**Cell parameters (Å)**
Pd/C	3.32/2.65/2.85/1.16	Cubic 3.8954(8)
+ Pd-^{int}B/C (*Fm-3m*)	3.22/2.56/2.84/1.13	Cubic 3.9886(9)
+ Pd-^{int}B/C (*P6mm*)	2.95/2.33/2.83/1.04	Hexagonal 2.8724(3); 3.6253(8)

As presented in Table 4.4, the Le Bail fitting suggests that the lattice parameter of the FCC structure is a = 3.9886(9) Å, an increase of 2.4% compared with the lattice parameter of the pure Pd/C. The lattice parameters of the HCP structure suggested by the Le Bail fitting are a = 2.8724(3) Å and c = 3.6253(8) Å. The obtained refinement result for the HCP structure is further confirmed by the ADF image (Figure 4.3).

Table 4.4. Summary of Space group and lattice parameters for the structure of 5 wt% Pd-^{int}B/C retrieved by TOPAS refinement.

Crystal Structure	**Point Group**	**Structural Information**
FCC	*Fm-3m*	$a = b = c$ = 3.9886(9) Å
HCP	*P6mm*	a = 2.8724(3) Å, c = 3.6253(8) Å

To date, the combination of SXRD refinement and ADF image reveals that the presence of B additives can lead to phase transformation from a FCC to a HCP structure. This phenomenon coincides with the observation by Kobayashi *et al.* that the excess concentration of B additives can lead to the phase transformation of FCC to HCP in Pd,[22] which reveals the presence of dopants can result in structural changes in the host metal system.

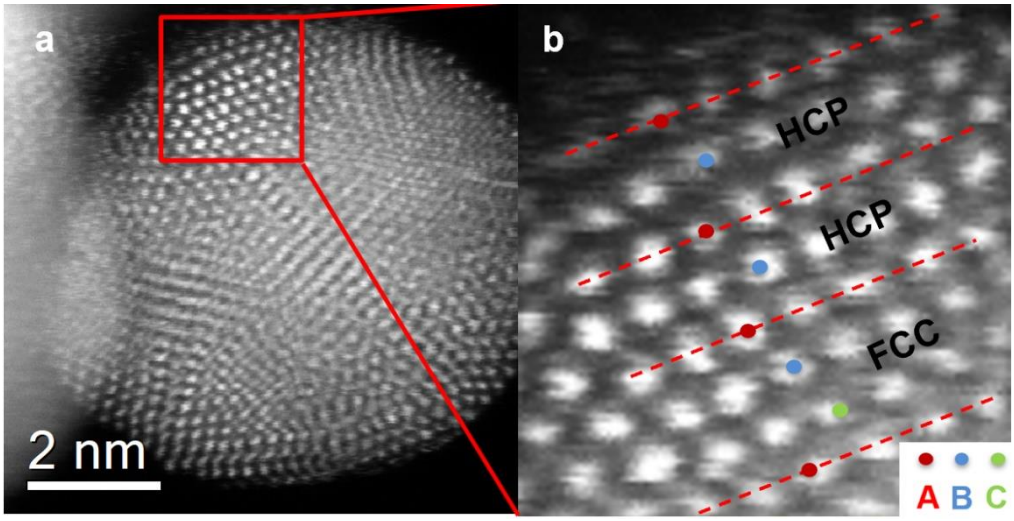


Figure 4.3. (a) A typical example of 5 wt% Pd-^{int}B/C NP contains FCC and HCP phase, which are demonstrated in inset (b). FCC (ABCA) and HCP (ABA) stacking have been annotated by red, blue and green dots. These dots represent different atomic layers.

Although STEM-ADF images and SXRD refinements prove the presence of a minor HCP phase and a dominant FCC structure, Le Bail fitting is unable to provide a phase composition ratio of FCC and HCP structure because Le Bail algorithm only can provide unit cell structure and corresponding space group on the basis of the diffraction peak positions, but excludes scaling factor which is used for quantitative calculations.[24] Moreover, the other relevant refinement methodologies are not appropriate owing to the excessive peak broadening and the inadequate number of diffraction peaks obtained from this powder-based sample.

4.5 In-situ X-Ray Pair Distribution Function (XPDF)

To estimate the phase ratio of FCC and HCP structure, the (X)PDF technique (utilising a synchrotron source) was used to investigate a more detailed characterisation of the Pd/C before and after B interstitial modification. Due to the limitation of current PDF techniques, the scattering intensity collected by the detector was inadequate if the catalyst loading of Pd-^{int}B/C was 5 wt%. This problem is also applicable to the measurement of the neutron diffraction and ^{105}Pd static ssNMR. As suggested by the beam scientist in Diamond Light source Beamline I15-1, Pd loading of the sample has to increase at least 50 wt% or more. Lab-source XRD was carried out and illustrates that diffraction patterns of 50 wt% Pd-^{int}B/C (See Chapter 8, Figure

8.2) still resembles to that of 5 wt% one (Figure 4.2). Even though the peak width gets narrower, revealing the particle size of NPs is bigger, similar XRD profile suggests that replacement of 5 wt% Pd loading based sample with 50 wt% one is still acceptable.

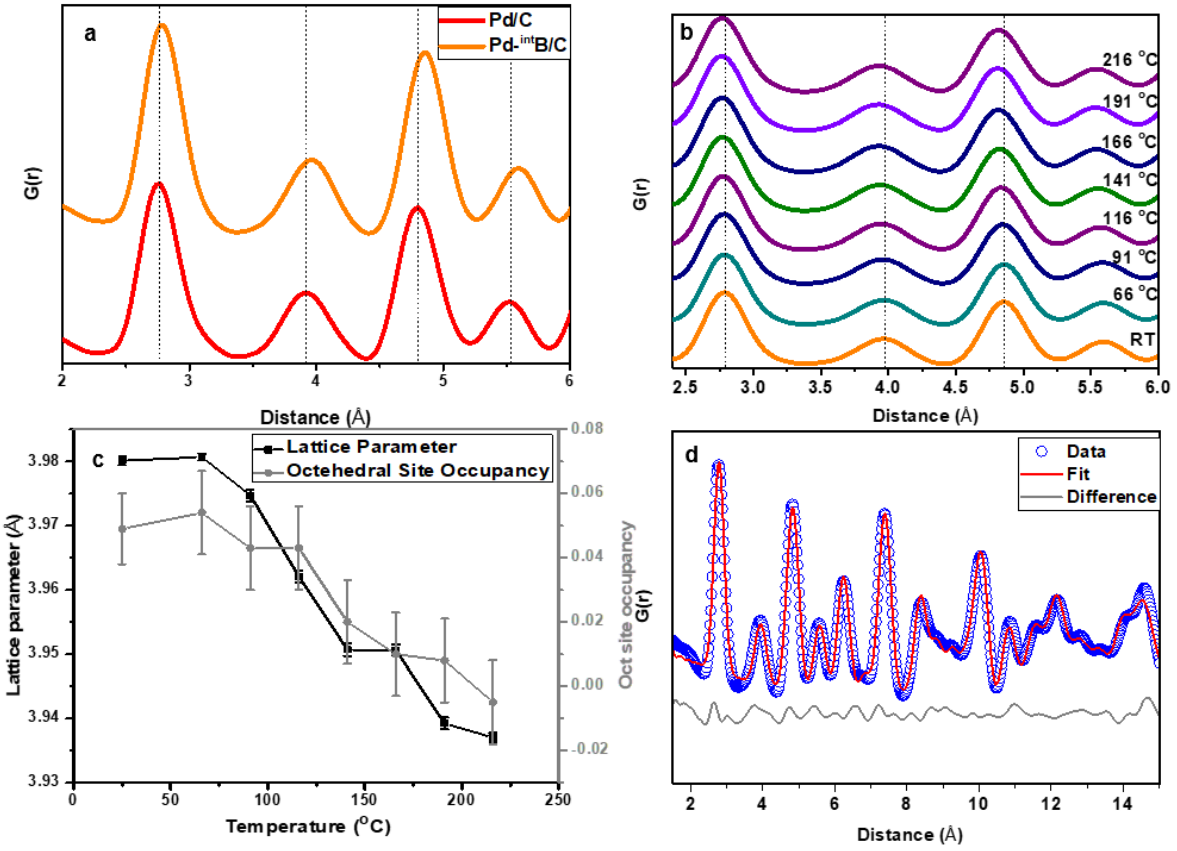


Figure 4.4. Probe average structural distortion by using *in-situ* XPDF and PDFgui. (a) XPDF profile of 50 wt% Pd/C and 50 wt% Pd-^{int}B/C at room temperature provides information on Pd−Pd bond distance at the range of 2 to 6 Å. (b) *in-situ* XPDF of Pd-^{int}B/C. The temperature is rising up from room temperature to the elevated temperature, at the range of 2 to 6 Å. (c) The relationship between the Pd–Pd lattice parameter and corresponding B occupancy possibility in the octahedral sites under different temperature. (d) A typical fit – fitting range = 1.5 – 15 Å. R_w = 12.5%; other fittings parameters can be found in Table 4.6.

As depicted in Figure 4.4a, a clear set of the FCC peaks are distributed across the x-axis of 2 to 6 Å, which is indicative of the Pd FCC structure. The second peak located at 3.9027(7) Å is assigned to the Pd lattice parameter, which matches well with the literature value.[25] The FCC structure pattern is also found in the G(r) of Pd-^{int}B/C, with an expanded lattice (a = 3.9801(7) Å), which is coincident with the structural information of the Pd FCC phase retrieved from the TOPAS refinement. The accommodation of the dopant atoms at the interstitial sites can weaken the metallic bonding interaction, due to the reduce in overlapping of the d-orbital.

However, no reliable set of peaks correspond to the structure of the Pd-B HCP phase, indicating the absence of the HCP phase. These results suggest the major structure of the NP is FCC whereas the HCP phase is only minor or even trace component.

The thermal stability of 50 wt% Pd-^{int}B/C phases has also been investigated by the *in-situ* XPDF (Figure 4.4b). While increasing the temperature from room temperature to 216 °C, the lattice parameter, a, gradually decreases from 3.9801(7) Å to 3.9370(7) Å (Figure 4.4c). This observation suggests that the distorted Pd FCC structure contracts to the pristine structure because of the interstitial B atoms thermally leaching out from the Pd lattice. The PDFgui software was utilised to probe the location of B atoms in the bulk Pd lattice. FCC remains the major structure of the Pd-^{int}B for all of the temperature-programmed G(r) XPDF, and hence there are only two possible interstitial sites in which B can reside, namely the octahedral sites (0.5, 0.5, 0.5) and tetrahedral sites (0.25, 0.25, 0.25).

Table 4.5. The list of the maximum radius of a dopant that may be accommodated in a tetrahedral or octahedral hole in a close-packed solid composed of spheres of radius r.

Limiting ratio	**Structural arrangement**
0.225r	Tetrahedral
0.414r	Octahedral

The work of King has suggested that the maximum radius of a spherical solute which can diffuse into an interstice in metal structures for interstitial solid solutions, assuming that the atoms are hard spheres in contact with each other.[26] In reference to this literature, this methodology was employed to determine the position of B. As shown in Table 4.5, the limiting value of tetrahedral structural arrangement is 0.225r and the limiting value of octahedral structural arrangement is 0.414r. The derivation progress of these numbers is demonstrated in

Chapter 8 Appendix, Figure 8.3. The atomic radius of Pd is 169 pm,[27] and the calculation process is as follows:

Max. atomic radius at tetrahedral sites:169 pm × 0.225 = 38.03 pm

Min. atomic radius at octahedral sites: 169 pm × 0.414 = 69.97 pm

Although the atomic radius of B (87 pm) is too large to be accommodated at tetrahedral sites and octahedral sites,[27] these values are subject to keeping the close-packed spheres in contact. As shown in the XPDF result, the lattice parameter of the unit cell after doping has increased from 3.9027(7) Å to 3.9801(7) Å, which suggests that the atoms in the unit cell may not be close-packed. This means that the permitted maximum atomic radius may be larger than 0.414r. Additionally, DFT calculation work reported by Studt *et.al* demonstrated that B is highly favorable to adsorb at the octahedral sites of (111) plane.[28] Therefore, XPDF fitting was conducted using a Pd FCC model where B was fixed at the octahedral sites.

Table 4.6. Lattice parameter and occupancy versus temperature of 50 wt% Pd-^{int}B/C.

Temperature (°C)	Lattice parameter (Å)	Occupancy	R_w (%)
25	3.9801(7)	0.049(11)	16.1
66	3.9807(5)	0.054(13)	15.3
91	3.9747(9)	0.043(13)	14.3
116	3.9621(9)	0.043(13)	13.6
141	3.9507(10)	0.020(13)	12.5
166	3.9506(9)	0.010(13)	12.5
191	3.9392(9)	0.008(13)	12.3
216	3.9370(7)	-0.005(13)	20.6

A typical example is shown in Figure 4.4d. All the refined atomic parameters are displayed in Table 4.6. The residual function (R_w) is a factor used to evaluate the agreement between the calculated PDF (G_{calc}) from the refined model and the experimental PDF data (G_{obs}).[29] Since this factor falls within the acceptable range, 10-20 %. From room temperature to 66 °C, the Pd lattice parameter remains at approximately 3.9801(7) Å, and the corresponding B site occupancy is around 5%. When the temperature rises further, both the lattice parameter and B site occupancy start to decrease. The refinement results highlight that the B site occupancy almost approaches zero at 191 °C. The exclusion of B at such low temperature suggests that B is perhaps only kinetically stable at room temperature, and most of the B leaches out from the interstitial sites of the NPs presumably with sufficient kinetic energy to relax the strained sites at elevated temperatures.

4.6 ^{105}Pd VOCS Static Solid State Nuclear Magnetic Resonance (ssNMR)

The presence of B in the interstitial octahedral sites is also supported by the high-resolution ssNMR, a technique that is sensitive to changes in short-range chemical environments. In previous work,[30,31] Dr. Ellis and Dr. Hooper had attempted to identify the chemical shift of the interstitial B (12.6 ppm) before and after acid wash by using ^{11}B MAS ssNMR. To further confirm the validity of interstitial B occupation, ^{105}Pd VOCS static NMR characterisation was employed to characterise both the Pd-^{int}B/C system and fresh Pd/C precursor.

To obtain enough signal from the ^{105}Pd ssNMR, 50 wt% Pd-^{int}B/C was prepared, and the corresponding particle size was 13 ± 9 nm, which was determined by TEM. Figure 4.5 shows the ^{105}Pd static NMR data of the 50 wt% Pd-^{int}B/C and 50 wt% Pd/C system in comparison with two previous established Pd metal systems (44-149 μm sized bulk metal, and monodisperse 16 ± 3 nm sized poly(N-vinyl-2-pyrrolidone) (PVP) stabilised Pd NPs.

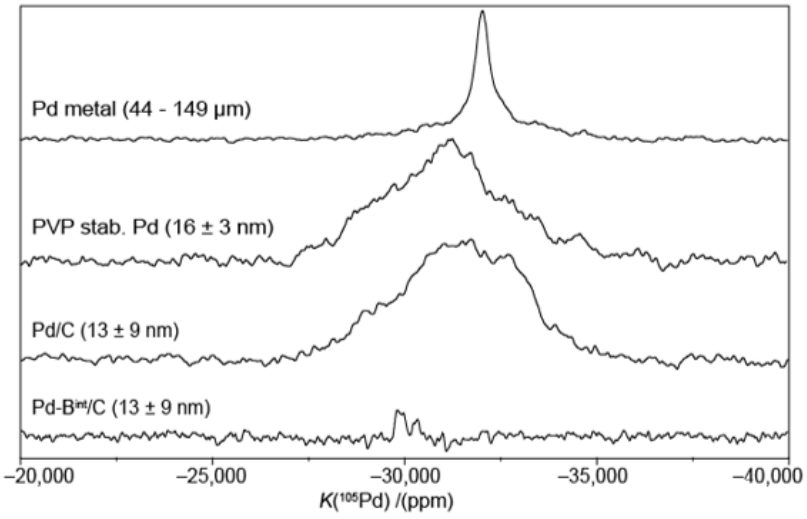


Figure 4.5. ^{105}Pd VOCS static NMR comparing 50 wt% Pd-^{int}B/C to Pd metal, PVP stabilised NPs and the 50 wt% Pd/C precursor labelled with their respective particle size distributions.[30]

The bulk Pd metal is characterised by a well-defined resonance at a Knight shift of -32050 ±60 ppm. Nevertheless, the resonance linewidth of the 50 wt% Pd/C and 50 wt% Pd/PVP is approximately 50 times broader. The very large ^{105}Pd quadrupole moment (Q) allows the quadrupole interaction at each Pd position to be a very sensitive probe of structural distortion and deviation from rigid FCC symmetry. This result suggests that the 50 wt% Pd/C and 50 wt% Pd/PVP are slightly perturbed from pure FCC symmetry due to the high surface-to-bulk atomic ratio. Despite the scattering technique providing a long-range structure that suggests retained FCC symmetry, the ^{105}Pd NMR suggests the symmetry is disrupted by the presence of strain and disorder induced by the particle size effect. It was found that the additional disorder induced by the interstitial incorporation of the B enhances the disorder broadening of the ^{105}Pd resonance, so that it is unobservable. The absence of the ^{105}Pd signal upon B incorporation gives another solid confirmation of the interstitial modification. If the B species stayed only on the surface of the Pd/C NPs, the ssNMR spectrum would be analogous to that of the Pd/C.

To date, the combined suite of characterisation toolboxes has demonstrated that the proposed structure for Pd-^{int}B/C retains an overall FCC character, whereas the irregular B

occupancy in the octahedral sites introduces a short-range disorder which is accompanied by the disorder induced by the particle size phenomena.

4.7 Electron Energy Loss Spectroscopy (EELS)

Previously, PDFgui has suggested B site occupancy, however, it struggles to reveal the B site occupancy in the local environment. In order to carry out more local analysis of the elemental composition, simultaneous STEM-EELS was carried out. In STEM-EELS, a high energy electron beam interacts with the specimen, resulting in energy loss by the inelastic scattered electron, also called the ionisation edge, which is then utilised to probe the presence of the element in the specimen.

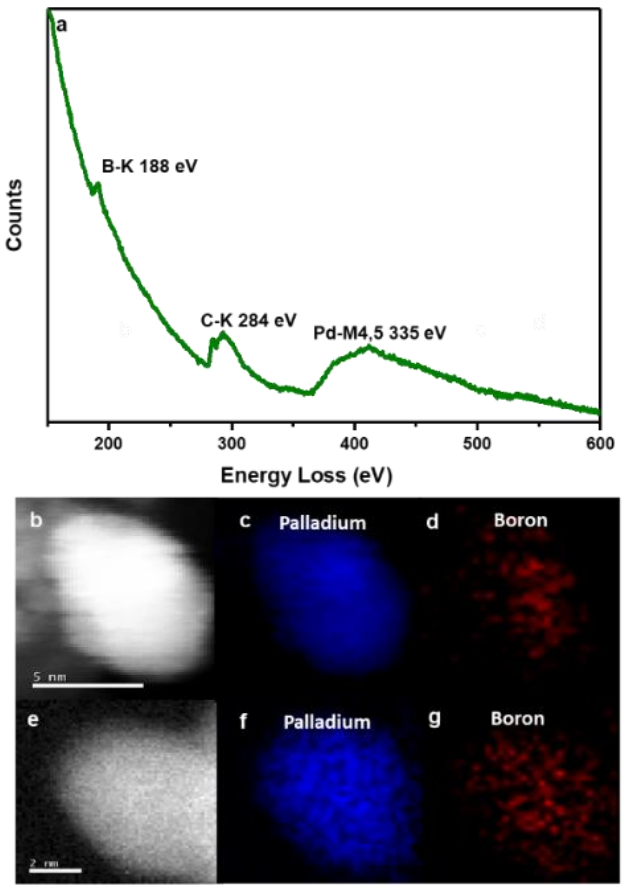


Figure 4.6. Typical EELS elemental analysis of the 5 wt% Pd-^{int}B NP on the carbon support. (a) EELS spectrum extracted from the EELS spectrum image recorded from a Pd-^{int}B NP. The three edges are starting at 188 eV, 284 eV and 334 eV. (b) and (e) are the spectrum images of Pd-^{int}B NPs. Elemental maps of the Pd-^{int}B NPs are presented in the (c), (d), (f) and (g), where the Pd-$M_{4,5}$ is annotated with blue and the B-K edge is annotated with red, respectively. The B elemental distribution in (d) is different from that in (g), highlighting that the B doping source distributes inhomogeneously for each NP.

A typical EELS spectrum extracted from a spectrum image of a NP is depicted in Figure 4.6a. Three reliable edges at 188 eV, 284 eV and 335 eV are found, which are coincident with the literature values of the B-K edge,[32] C-K edge[33] and Pd-M4,5 edge respectively.[34] No evidence of oxygen was presented, which would manifest in an extra signal located at 532 eV.[35] Moreover, edges located at 195 eV and 202.5 eV, which would indicate the presence of B_2O_3, were not found.[36] This indicates the surface of the NP in the local environment is not covered with boron-based oxides, and these NPs are stable at room temperature.

Table 4.7. EELS quantification analysis results of four 5 wt% Pd-^{int}B/C NPs.

Entry	Element	Background removal parameters	Signal quantification parameters			Relative quantification
		Fitting range (eV)	Signal (Counts)	Edge Type	Integration range (eV)	Atomic ratio
1	B	167.0-183.0	3.19e+006 ± 7881	K	188.0-211.0	0.25 ± 0.034
	Pd	311.0-324.8	1.92e+006 ± 5021	M	335.0-358.0	1.00 ± 0.000
2	B	167.0- 183.0	9.10+006 ±14007	K	188.0-211.0	0.19 ± 0.070
	Pd	299.0- 328.0	7.32+006 ±8204	M	335.0-358.0	1.00 ± 0.000
3	B	156.0-182.0	1.71e+006 ± 6321	K	188.0-211.0	0.18 ± 0.026
	Pd	301.3-330.3	1.44e+006 ± 3723	M	335.0-358.0	1.00 ± 0.000
4	B	167.0- 183.0	1.02e+006 ± 5490	K	188.0-211.0	0.22 ± 0.031
	Pd	308.5- 327.0	7.05+005 ± 4138	M	335.0-358.0	1.00 ± 0.000

EELS elemental mappings of different NPs (Figure 4.6c, d, f, g) also show that the foreign sources of B did not distribute homogeneously across the volume of the NPs. STEM-EELS and its complementary GMS analytical program can be used to compute local elemental analysis of individual NP *via* spectra quantification. Despite the fact that XPDF has suggested that the site occupancy of B is approximately 5%, it should be noted that 5% is an average value for the entire batch of NPs. Additionally, the x-ray scattering is directly proportional to the atomic number of the element. Because the scattering generated from B is much weaker than the Pd,

quantification of B content by using PDFgui is less reliable. The results of individual five nanoparticle are summarised in Table 4.7. The average atomic ratio of Pd : B was about 1 : 0.2, similar to that of the FCC $Pd_{0.82}B_{0.18}$ phase.[37] Due to the absence of the B-K edge in boron oxide, it is reasonable to assume that all B dopants reside at the interstitial sites and thus the corresponding B site occupancy for a NP was about 0.2.

4.8 Annular Dark Field (ADF)-Ptychography Imaging

In order to visualise B atoms in the octahedral sites of the Pd-^{int}B/C NPs, electron ptychography was performed in conjunction with ADF imaging. The risk of electron-beam damage needs to be considered during the experiment, because beam damage can affect the structure and/or the chemistry of the specimen. The dominant form of beam damage upon the B contained sample might be knock-on damage which is the displacement of atoms from the crystal lattice and leads to the formation of point defects.[38,39] If the atoms are ejected from the specimen, it is termed sputtering. To lower the risk of knock-on damage, total electron dose used for imaging acquisition was reduced during the experiment.

The total electron dose used for data acquisition was 0.9×10^6 $e^-Å^{-2}$ at 200 kV with a camera length of 12 cm. This value is similar to the electron dose used by Peng *et al.* for ptychographic imaging of B in a LaB_6 nanocrystal at 300 kV, and hence, it is reasonable to assume that the B atoms will remain in the octahedral sites during data acquisition.[40] As depicted in Figure 4.3a, the Pd-^{int}B/C NP contains a high density of stacking faults and phase transformations which might hinder contrast interpretation and the direct image of B during the experiment. If the defects are distributed on the planes that are parallel to the direction of viewing, it is possible to see their presence. However, if the defects are inclined to the direction of viewing, the projected lattice might result in atomic-column peaks between those from the expected FCC structure. A set of crystals containing atomic twins, extrinsic and intrinsic faults parallel along Pd {110} planes that are inclined to the electron beam were established to

determine the positions where additional peaks may emerge. As shown in Chapter 8 Appendix Figure 8.4 to 8.8, these atomic models do not show the presence of atomic columns at positions of the octahedral sites but can induce additional peaks rising up at the positions that correspond to the tetrahedral sites.

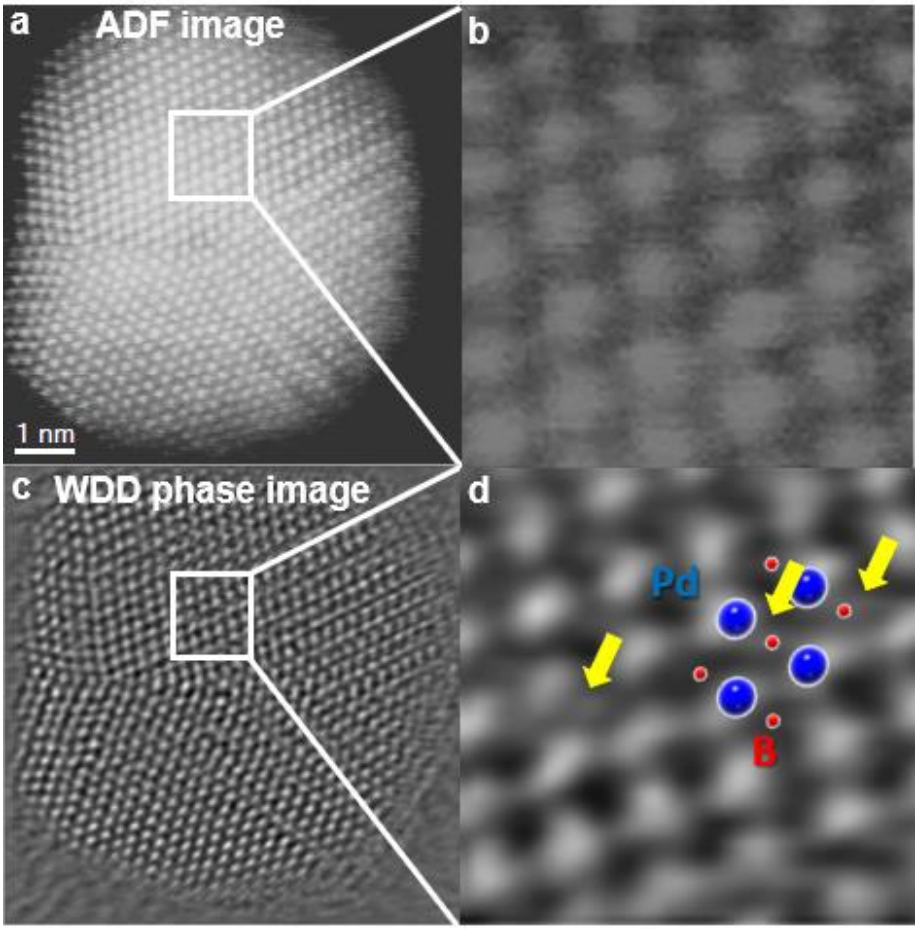


Figure 4.7. Simultaneously acquired Z-contrast STEM-ADF and phases images (reconstructed by Wigner Distribution Deconvolution (WDD)) of a 5 wt% Pd-^{int}B dispersed on the carbon support, where is oriented in the [110] zone axis. (a) ADF-image of Pd-^{int}B NP. Inset (b) from (a) highlights an enlarged area. Inset (d) from (c) phase image reconstructed by using a WDD method. New atomic columns arise after aberration correction between the Pd atomic columns, which matches well with the general crystal model proposed by XPDF. This experiment was performed at an emission current of 6.0 µA, pixel dwell time of 0.25 ms and a total dose of 0.9×10^{6} $e^{-}Å^{-2}$.

Figure 4.7a shows a typical STEM-ADF image that shows a NP with fewer defects. Owing to the strong atomic number dependence of the STEM-ADF ($Z_{Pd} = 46$, $Z_C = 6$ and $Z_B = 5$), only Pd atomic columns are clearly visible in the image. In order to analyse the ADF contrast quantitatively, ADF image simulation of the Pd-^{int}B with local concentration yielded from

STEM-EELS was compared to that of the pure Pd over different thicknesses. As seen in Figure 4.8, the ADF images at the top row and the bottom row are indistinguishable. In contrast to the ADF image in Figure 4.7b, the phase image reconstructed by the WDD algorithm[41] after aberration correction (Figure 4.7c) highlights some intensities which rise up in the interstitial octahedral sites intercalated between the Pd atomic columns. When the unit cell of Pd-^{int}B projected in the [110] direction is superimposed to the zone-up image in Figure 4.7d, the model matches well with the octahedral sites.

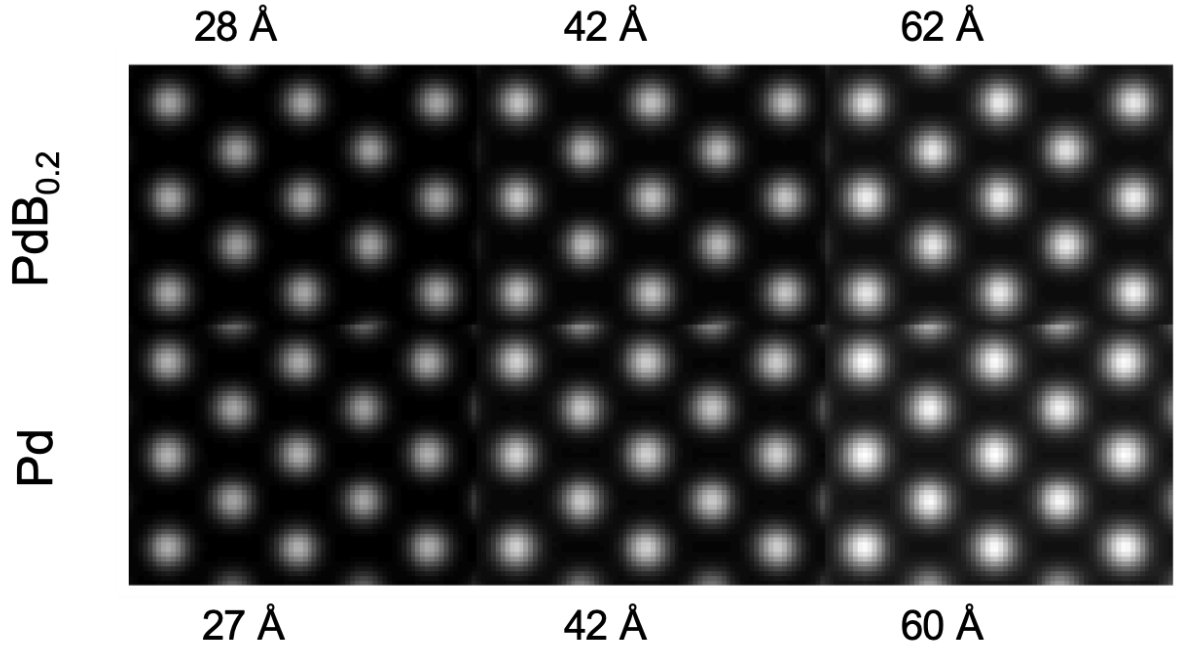


Figure 4.8. Simulated ADF images of $PdB_{0.2}$ single crystal and Pd over different thicknesses. The simulated ADF images have the same number of repeating unit cells. Owing to the difference in the Pd−Pd lattice parameter for Pd and Pd-^{int}B specimen, the thickness is slightly different. B atomic columns are not visible in the ADF image because of the Z-contrast rule.

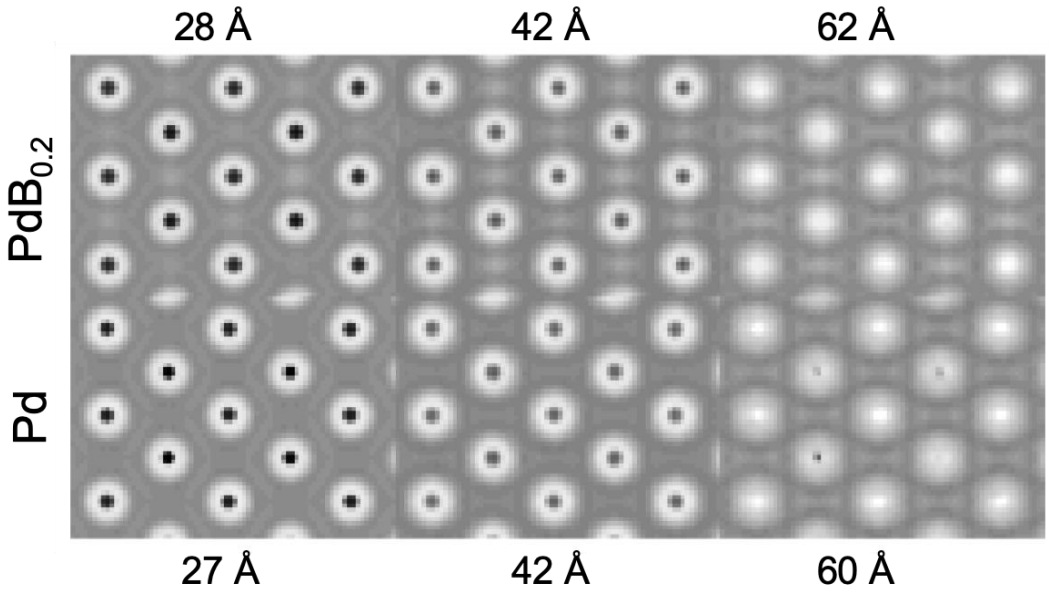


Figure 4.9. Simulated phase image of Pd and $PdB_{0.2}$ over different thickness. Multislice frozen phonon methods implemented in the MULTEM was used for the simulation. B atoms can be observed at the interstitial sites. Pd atomic columns demonstrate phase contrast reversal and wrapping, which is attributed to the dynamical scattering of electrons, so that affects the multiplicative approximation. This phenomenon partially leads to the well-known contrast mismatch between experimental phase images and simulations, named as the Stobbs factor.[43]

Additionally, the ptychographic phase contrast was analysed quantitively *via* a comparison with simulation by using multislice methods implemented in the MULTEM.[42] A number of phase images were calculated at various thicknesses up to 6 nm, as shown in Figure 4.9. for both Pd and Pd-^{int}B/C. These results show that in all cases, B atomic columns can be clearly visualised at the octahedral sites. However, Pd atomic columns demonstrate phase contrast reversal and wrapping (i.e "doughnut shape"), which is attributed to the dynamic scattering of electrons, which affects the multiplicative approximation. This phenomenon partially leads to the well-known contrast mismatch between experimental phase images and simulations, termed the Stobbs factor,[43] which is a long-term challenge in the electron microscopy field. To date, the weaker intensity between the Pd atomic columns can be ascribed to the interstitial B in accordance with the quantitative simulation and EELS result. Extra evidence can also be found in Chapter 8 Appendix Figure 8.9.

4.9 Conclusion

Overall, a novel combination of analytical techniques beyond conventional characterisation tools allows for local and global assessments when light elements such as B atoms inhomogeneously distribute at interstitial sites of supported noble metal NPs in industrial-type powder-based catalysts. The macro-analytical techniques can allow us to establish the average crystal model, while the micro-analytical techniques can provide information about elemental distributions, structural distortion behaviour and local phase transformations. According to the EELS quantification, the atomic ratio of Pd to B is about 1 : 0.2, which resembles the FCC phase Pd-B solid solution. Such a broad range of analytical techniques can pave a path for in-depth investigation of light element alloyed catalyst systems which can give quantitative information to establish their catalytic performance and give guidance for novel catalyst design. Here, in light of characterisation results of multi-quantitative techniques, the atomic columns probed by the fast pixelated technique can be assigned to B with confidence for the first time, which can be shown to lead to significant local expansion of the metal lattice giving rise to severe local lattice strain or even phase transformation.

4.10 References

1 K. F. Tan, J. Chang, A. Borgna and M. Saeys, *J. Catal.*, 2011, **280**, 50–59.

2 A. J. Al Abdulghani, J. H. Park, S. M. Kozlov, D. C. Kang, B. AlSabban, S. Pedireddy, A. Aguilar-Tapia, S. Ould-Chikh, J. L. Hazemann, J. M. Basset, L. Cavallo and K. Takanabe, *J. Catal.*, 2020, **392**, 126–134.

3 S. A. Nikolaev, L. N. Zanaveskin, V. V Smirnov, V. A. Averyanov and K. L. Zanaveskin, *Russ. Chem. Rev.*, 2009, **78**, 231–247.

4 A. Borodziński and G. C. Bond, *Catal. Rev. - Sci. Eng.*, 2006, **48**, 91–144.

5 I. T. Ellis, E. H. Wolf, G. Jones, B. Lo, M. Meng-Jung Li, A. P. E. York and S. C. Edman Tsang, *Chem. Commun.*, 2017, **53**, 601–604.

6 M. Friedrich, S. Villaseca, L. Szentmiklósi, D. Teschner and M. Armbrüster, *Materials (Basel).*, 2013, **6**, 2958–2977.

7 Y. Han, D. Peng, Z. Xu, H. Wan, S. Zheng and D. Zhu, *Chem. Commun.*, 2013, **49**, 8350.

8 B. Hammer and J. K. Norskov, *Nature*, 1995, **376**, 238–240.

9 K. Okitsu, Y. Mizukoshi, H. Bandow, T. A. Yamamoto, Y. Nagata and Y. Maeda, *J. Phys. Chem. B*, 1997, **101**, 5470–5472.

10 D. S. Su, B. Zhang and R. Schlögl, *Chem. Rev.*, 2015, **115**, 2818–2882.

11 J. Lynch, C. Giannini, J. K. Cooper, A. Loiudice, I. D. Sharp and R. Buonsanti, *J. Phys. Chem. C*, 2015, **119**, 7443–7452.

12 B. Yang, R. Burch, C. Hardacre, P. Hu and P. Hughes, *J. Phys. Chem. C*, 2014, **118**, 3664–3671.

13 F. Lin, Y. Liu, X. Yu, L. Cheng, A. Singer, O. G. Shpyrko, H. L. Xin, N. Tamura, C. Tian, T. C. Weng, X.-Q. Yang, Y. S. Meng, D. Nordlund, W. Yang and M. M. Doeff, *Chem. Rev.*, 2017, **117**, 13123–13186.

14 S. J. Pennycook, M. F. Chisholm, A. R. Lupini, M. Varela, A. Y. Borisevich, M. P. Oxley, W. D. Luo, K. van Benthem, S.-H. Oh, D. L. Sales, S. I. Molina, J. García-Barriocanal, C. Leon, J. Santamaría, S. N. Rashkeev and S. T. Pantelides, *Philos. Trans. R. Soc. A Math. Phys. Eng. Sci.*, 2009, **367**, 3709–3733.

15 C. I. Hiley, H. Y. Playford, J. M. Fisher, N. C. Felix, D. Thompsett, R. J. Kashtiban and R. I. Walton, *J. Am. Chem. Soc.*, 2018, **140**, 1588–1591.

16 R. F. Egerton, *Electron Energy-Loss Spectroscopy in the Electron Microscope*, Springer US, Boston, MA, 3rd edn., 2011.

17 H. Yang, R. N. Rutte, L. Jones, M. Simson, R. Sagawa, H. Ryll, M. Huth, T. J. Pennycook, M. L. H. Green, H. Soltau, Y. Kondo, B. G. Davis and P. D. Nellist, *Nat. Commun.*, 2016, **7**, 12532.

18 S. Navaladian, B. Viswanathan, T. K. Varadarajan and R. P. Viswanath, *Nanoscale Res. Lett.*, 2009, **4**, 181–186.

19 L. E. Tergenius and T. Lundström, *J. Solid State Chem.*, 1980, **31**, 361–367.

20 R. Gumeniuk, H. Borrmann and A. Leithe-Jasper, *Zeitschrift für Krist. - New Cryst. Struct.*, 2006, **221**, 425–426.

21 G. Akopov, M. T. Yeung and R. B. Kaner, *Adv. Mater.*, 2017, **29**, 1604506.

22 K. Kobayashi, H. Kobayashi, M. Maesato, M. Hayashi, T. Yamamoto, S. Yoshioka, S. Matsumura, T. Sugiyama, S. Kawaguchi, Y. Kubota, H. Nakanishi and H. Kitagawa, *Angew. Chemie Int. Ed.*, 2017, **56**, 6578–6582.

23 A. A. Coelho, *J. Appl. Crystallogr.*, 2018, **51**, 210–218.

24 A. Le Bail, H. Duroy and J. L. Fourquet, *Mater. Res. Bull.*, 1988, **23**, 447–452.

25 B. N. Dutta and B. Dayal, *Phys. status solidi*, 1964, **5**, 73–75.

26 H. W. King, *J. Mater. Sci.*, 1971, **6**, 1157–1167.

27 E. Clementi, D. L. Raimondi and W. P. Reinhardt, *J. Chem. Phys.*, 1967, **47**, 1300–1307.

28 J. S. Yoo, Z.-J. Zhao, J. K. Nørskov and F. Studt, *ACS Catal.*, 2015, **5**, 6579–6586.

29 A. S. Masadeh, *J. Exp. Nanosci.*, 2016, **11**, 951–974.

30 T. Chen, I. Ellis, T. J. N. Hooper, E. Liberti, L. Ye, B. T. W. Lo, C. O'Leary, A. A. Sheader, G. T. Martinez, L. Jones, P.-L. Ho, P. Zhao, J. Cookson, P. T. Bishop, P. Chater, J. V. Hanna, P. Nellist and S. C. E. Tsang, *J. Am. Chem. Soc.*, 2019, **141**, 19616–19624.

31 L. T. Ellis, PhD thesis, University of Oxford, 2016.

32 K. Sato, N. Fukata and K. Hirakuri, *Appl. Phys. Lett.*, 2009, **94**, 161902.

33 G. Lieser, S. Mittler-Neher, J. Spinke and W. Knoll, *Biochim. Biophys. Acta - Biomembr.*, 1994, **1192**, 14–20.

34 P. Longo, R. D. Twesten and G. Kothleitner, *Microsc. Microanal.*, 2013, **19**, 1612–1613.

35 C. C. Ann, O. L. Krivanek, *EELS atlas: a reference collection of electron energy loss spectra covering all stable elements.*, Arizona State University, New York, 1983.

36 R. J. Nicholls, Z. Aslam, M. C. Sarahan, A. Koós, J. R. Yates, P. D. Nellist and N. Grobert, *ACS Nano*, 2012, **6**, 7800–7805.

37 M. Beck, M. Ellner and E. J. Mittemeijer, *Mater. Sci. Forum*, 2000, **321**–**324**, 604–609.

38 J. Kotakoski, C. H. Jin, O. Lehtinen, K. Suenaga and A. V. Krasheninnikov, *Phys. Rev. B*, 2010, **82**, 113404.

39 D. B. Williams and C. B. Carter, *Transmission Electron Microscopy*, Springer US, Boston, MA, 2009.

40 P. Wang, F. Zhang, S. Gao, M. Zhang and A. I. Kirkland, *Sci. Rep.*, 2017, **7**, 2857.

41 H. Yang, I. MacLaren, L. Jones, G. T. Martinez, M. Simson, M. Huth, H. Ryll, H. Soltau, R. Sagawa, Y. Kondo, C. Ophus, P. Ercius, L. Jin, A. Kovács and P. D. Nellist, *Ultramicroscopy*, 2017, **180**, 173–179.

42 I. Lobato and D. Van Dyck, *Ultramicroscopy*, 2015, **156**, 9–17.

43 M. J. Hÿtch and W. M. Stobbs, *Ultramicroscopy*, 1994, **53**, 191–203.

Chapter 5 In-Depth Characterisation of Pd-^{int}Li/C NPs

5.1 Introduction

The combination of the state-of-the-art techniques described in Chapter 4 can offer complementary information to elucidate structural variations and physicochemical properties of an industrial type of noble metal NP when interstitial B is incorporated, thus guiding our understanding of catalysis. Similarly, in this chapter, an in-depth characterisation of Pd-^{int}Li/C system will be presented using the integrative state-of-the-art techniques.

Li, as the lightest alkali element, is often used as a catalytic promoter or modifier to improve the activity of heterogeneous catalysts,[1] or to enhance catalyst's stability.[2] Additionally, owing to its stronger oxidising effect and higher gravimetric capacity in comparison to Na, Mg and Al, intense research has been centered upon the field of Li-ion rechargeable batteries.[3] However, limited structural studies have been reported with respect to the characterisation of the Li-containing solid-state catalysts,[2,4] due to the more challenging physicochemical properties of Li than B or C. For instance,

1) The intensity of XRD patterns is directly proportional to the electron cloud density of the element which is dependent on the atomic number. Since the atomic number of Li is only 3, XRD is unable to identify the Li phase directly. This rule is also applicable to the intensity of electron diffraction and the contrast of STEM-ADF imaging.

2) The electron configuration of Li is $1s^2 2s^1$; therefore, Li has only one characteristic peak, 1s at 55 eV in XPS. However, XPS sometimes fails to measure the chemical state of the Li if other elemental signals are present next to the Li 1s binding energy peak. In addition, unlike the high crystallinity specimen, the powder-like sample is highly distorted and contains point/line defects or grain boundaries. Inhomogeneous distribution of dopants also adds to the difficulties of Li involved in industrial catalyst characterisation. Therefore, it is essential to address these

challenges in order to guide the synthesis of novel heterogeneous catalysts and establish the structure-activity relationship of the catalytic reactions.

Previously, Dr. Leuan Ellis, former Tsang group member, attempted to alloy Li interstitially into the host system of Palladium NPs (Pd-^{int}Li/C NPs) for selective hydrogenation of acetylene. The modified catalyst gave ethylene selectivity of over 80%, while the fresh Pd alone gave ethylene selectivity of only 50%. The origin of the premium catalytic selectivity is attributed to the occupation of Li at Pd octahedral sites.[5] However, there is no direct visualisation of the Li in the Pd interstices. To date, the structure of Pd-^{int}Li/C NPs remains unclear with regards to the crystal structural distortion induced by the foreign element, and the exact location of Li is ambiguous. Hence, Pd-^{int}Li/C NPs merits further investigation. In parallel to the in-depth structural characterisation of the Pd-^{int}Li/C, strain effect induced by Li was also explored. It is expected that this research will open a new window to directly probe the local dopant effects of a distorted structure in powder-like nanoparticles from bulk characterisation methods to atomic resolution ones.

5.2 Objectives and Methodology

The aim of this chapter is to employ the state-of-the-art characterisation techniques in order to identify the crystal structure and strain effect, induced by the Li dopant, on the Pd-^{int}Li/C NPs. For this purpose, the Pd-^{int}Li/C NPs were prepared in accordance with the previously reported synthetic strategy.[5] The sample was initially characterised by Lab-source XRD and ^{105}Pd (Variable offset Cumulative Spectroscopy) VOCS static ssNMR to ensure the sample preparation was successful. After that, SXRD, neutron diffraction and *in-situ* X-ray pair distribution function (XPDF) techniques were employed for in-depth characterisation.

After gaining general information from these collaborative macro-techniques, the focus turned to the field of the electron microscope. STEM-EELS, STEM-ADF and ptychography were used to characterise samples at the atomic level. The TEM-related algorithm program, Statstem,[6] was used to map the straining distribution of an individual Pd-^{int}Li NP. The ptychography technique was also attempted to probe the Li intercalated between the Pd atomic columns. Overall, with this methodology, one aims to pave a new path for in-depth investigation of light element alloyed nanocatalysts as well as understand the strain effect induced by the light element in more detail.

5.3 Initial Characterisation with ICP, XRD and STEM-ADF

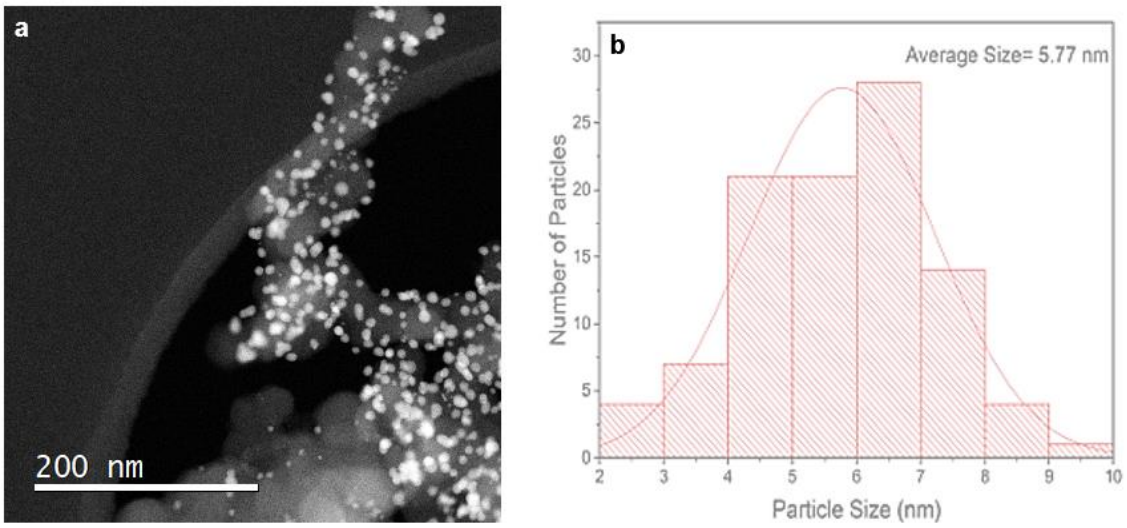


Figure 5.1. Particle size analysis by STEM-ADF imaging. (a) Overview STEM-ADF image of 5 wt% Pd-^{int}Li/C NPs. (b) Histogram from size analysis of catalyst particles. Average particle size 5.77 nm.

5w t% Pd-^{int}Li/C NPs (5% Pd loading) was synthesised by heating a mixture of Pd/C and Li(OAc)·2H_2O at 250 ℃ for two hours, according to the previous reported synthetic strategy.[5] The ICP suggests that the atomic ratio of the Pd and Li is approximately 1:0.1. The corresponding average particle size(diameter) was determined by conventional STEM-ADF imaging, as shown in Figure 5.1a. The size histogram was built from measuring the diameter of at least 100 NPs manually which is depicted in Figure 5.1b. Based on that, the average size of the NPs was calculated as 5.77 nm which is smaller in comparison with the average NP size reported in the previous study.

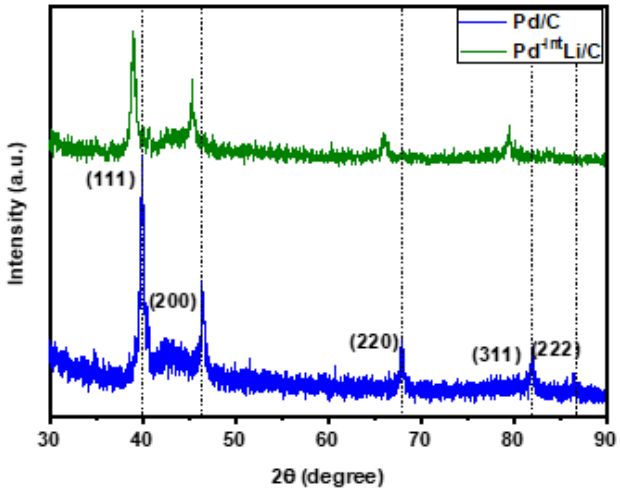


Figure 5.2. XRD patterns of 5 wt% Pd/C (blue), 5 wt% Pd-^{int}Li/C (green). The peaks labelled with dash lines corresponding to the Pd (111), (200), (220), (311) and (222) are characteristics of the Pd face-centred cubic (FCC) structure.

The successful preparation of NPs was also confirmed by the XRD (Figure 5.2). The diffraction peaks located at 39.98°, 46.53°, 67.95°, 82.00° corresponding to the (111), (200), (220), (311) planes, are shifted to lower angles by 0.93°, 1.21°, 2.05°, 2.50°, respectively. Owing to the background noise, it is hard to identify the location of the (222) index plane after lithiation. Based on the Bragg equation, the Pd d-spacing expands from 2.252 $Å_{(111)}$ to 2.308 $Å_{(111)}$; 1.949 $Å_{(200)}$ to 1.999 $Å_{(200)}$; 1.378 $Å_{(220)}$ to 1.416 $Å_{(220)}$; and 1.174 $Å_{(311)}$ to 1.204 $Å_{(311)}$ (See Table 5.1).

Table 5.1. Data of XRD patterns of Pd before/after Li doping.

Pt diffraction angle 2θ (°) before Li doping	***h k l***	**d-spacing (Å)**	**Pt diffraction angle 2θ (°) after Li doping**	**d-spacing (Å)**
39.98	111	2.252	39.05	2.308
46.53	200	1.949	45.32	1.999
67.95	220	1.378	65.90	1.416
82.00	311	1.174	79.50.	1.204

In light of the obtained d-spacing, the lattice parameter of the Pd increases from 3.8907 Å to 3.997 Å, which is similar to the lattice expansion of the Pd induced by the B dopants. This result indicates that the entire diffraction pattern shifts to the left by a different degree in the presence of Li dopants, thus expands the d-spacing and lattice parameters of the Pd as expected from previous studies.

5.4 ^{105}Pd Static VOC Solid State Nuclear Magnetic Resonance (ssNMR)

Spectroscopic techniques, such as ssNMR, may also be used to confirm the formation of Pd-^{int}Li/C. In the previous work, XPS and ^{7}Li MAS ssNMR were attempted for the structural investigation of the Pd-^{int}Li/C. However, the Li 1s (55 eV) signal could not be detected in the XPS experiment, due to either a low amount of Li or the presence of Pd 3p located at 55 eV. ^{7}Li MAS ssNMR was thus employed to determine the chemical environments of the Li nuclei in the Pd-^{int}Li/C. A saturation recovery experiment was carried out to assign the chemical environment and confirmed the chemical shift of the interstitial Li at -0.7 ± 0.2 ppm.[7] To further confirm the validity of the Pd-^{int}Li/C NPs formation, in this work, ^{105}Pd VOCs static ssNMR was performed in collaboration with Dr. Thomas Hooper, from the University of Warwick.[8]

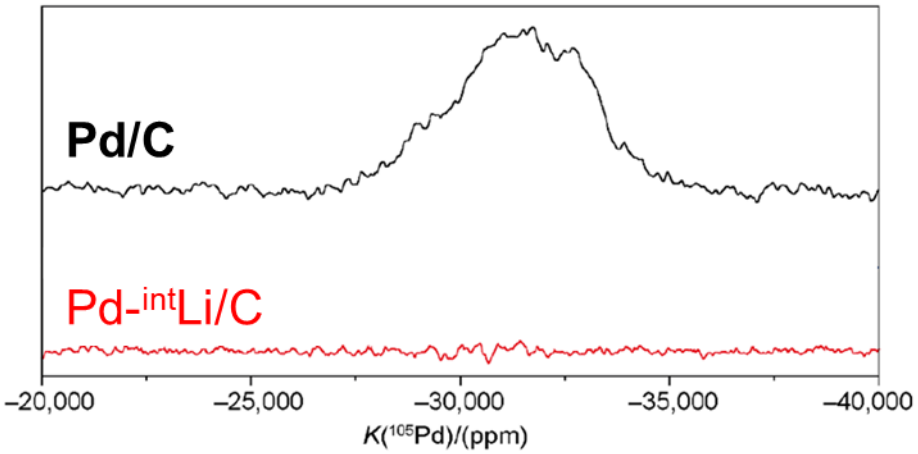


Figure 5.3. The ^{105}Pd static VOCS NMR of 50 wt% Pd/C, 50 wt% Pd-^{int}Li/C at 14.1 T.[9]

As depicted in Figure 5.3, the ^{105}Pd VOCs static NMR technique was implemented on the Pd-^{int}Li/C system and on Pd/C for investigation of the presence of interstitial Li and the

structural distortion induced by the Li. In order to aid the acquisition of ^{105}Pd NMR, Pd-^{int}Li/C was synthesised from a Pd/C precursor with 50 wt% Pd loading. These higher Pd loaded samples exhibited particle sizes of 13 ± 9 nm, The centre-of-gravity K_{tot} of Pd/C has shifted downfield to a 'less metallic'/reduced Knight shifted environment; and the resonance linewidth is ~50 times broader, the same as described in Chapter 4.[9] This result provides evidence that the NPs are slightly disordered from pure FCC symmetry due to the size effect (high-surface-to-bulk atomic ratio). Although diffraction provides an average structure that suggests FCC symmetry is maintained, the short-range information from ^{105}Pd NMR suggests that particle size effects can result in strain and disorder that introduce short-range departure from this symmetry. No Pd resonance was detected for the 50 wt% Pd-^{int}Li/C species even when sweeping a wide K range (see the bottom of Figure 5.3). It can be explained by the concept that the additional disorder generated after interstitial incorporation of the Li increases the strain and disorder broadening of the ^{105}Pd resonance to the extent that the resonance was lost. If the Li remained only on the surface of the Pd/C NPs, the NMR spectrum would be analogous to that of the Pd/C. Therefore, the absence of the ^{105}Pd signal provides further confirmation of successful interstitial modification.

To this point, the combined suite of analytical techniques from our studies has clearly demonstrated that the proposed crystal structure for Pd-^{int}Li/C NPs exhibits overall FCC character, and the irregular Li incorporation in the interstitial sites introduces short-range disorder in addition to that induced by particle size phenomena.

5.5 Synchrotron X-Ray Diffraction (SXRD)

Although the lab source XRD suggests that incorporation of Li into the Pd host system retains the FCC structure, it is hard to identify other potential crystal structures, due to the resolution limit of the lab incident x-ray source. In order to understand the nanostructure in more detail, SXRD was employed and XRD patterns are depicted in Figure 5.4. Despite both

the Pd/C and Pd-^{int}Li/C diffraction peaks being subject to relative broadening due to the small particle size effect, they still reveal that the presence of Li can shift diffraction peaks to a lower degree.

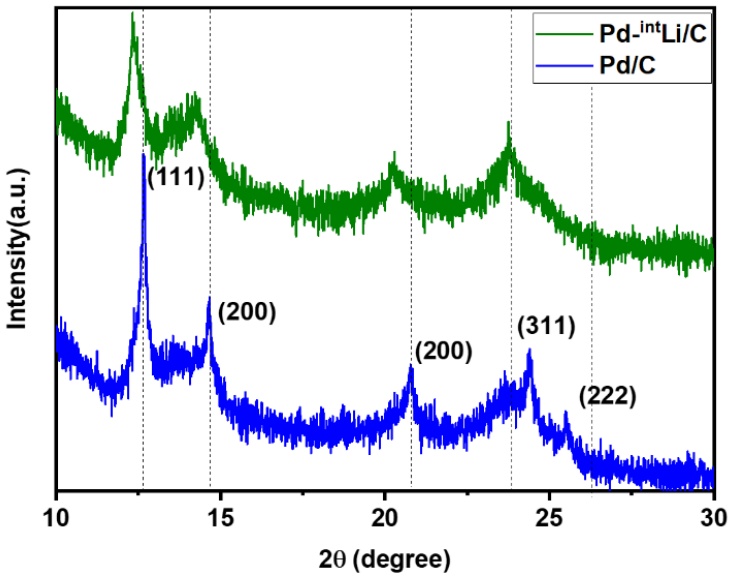


Figure 5.4. SXRD patterns of the 5 wt% Pd/C and 5 wt% Pd-^{int}Li/C samples. Diffraction patterns of Pd/C are annotated with blue and diffraction patterns of the Pd-^{int}Li/C are annotated with green. The peaks labelled with dash lines corresponding to the Pd (111), (200), (220), (311) and (222) were characteristics of the Pd face-centred cubic (FCC) structure.

The SXRD data was subsequently analysed to propose the potential phase through utilisation of the parallel analysis programming, TOPAS-Academic V5.0 software.[10] In light of the Pd-Li phase diagram reported by Pelton *et.al*,[11] the structure of Pd_7Li is FCC, which has a lattice parameter of 7.7134 Å, approximately twice that of the Pd. However, bulk Pd_7Li is prepared by annealing at 600 °C, which is much harsher than the reaction conditions of Pd-^{int}Li/C sample preparation (250 °C). Because the diffraction pattern profile of the Pd-^{int}Li/C NPs resembles to that of the Pd, the sample refinement was initiated with the model, pure Pd.[12] Employment of the Le Bail method provided an acceptable fit, which accounts for all the diffraction peak positions. A low R-weighted pattern (R) was utilised to evaluate the quality of the retrieved refinement results, as presented in Table 5.2.

Table 5.2. R-factors of 5 wt% Pd-^{int}Li/C samples by Le Bail.

Samples	Le Bail R_{wp} / R_p / R_{exp} / $\chi 2$	Cell parameters (Å)
Pd	3.32/2.65/2.85/1.16	Cubic 3.8954(8)
+ Pd-^{int}Li/C (*Fm-3m*)	3.01/2.85/2.39/1.055	Cubic 3.9707(6)

Summary of the space group and lattice parameters for 5 wt% Pd-^{int}Li/C retrieved by TOPAS refinement can be found in Table 5.3. The space group of 5 wt% Pd-^{int}Li/C is *Fm-3m* and the lattice parameter is $a = b = c = 3.9707(6)$ Å, which is consistent with the lattice parameter obtained from the conventional XRD.

Table 5.3. Summary of the space group and lattice parameters for the structure of 5 wt% Pd-^{int}Li/C retrieved by TOPAS refinement.

Crystal Structure	Space Group	Structural Information
FCC	*Fm-3m*	$a = b = c = 3.9707(6)$ Å

As described in Chapter 4, the Pd-^{int}B/C system also contains a HCP structure based on SXRD refinement results. Herein, a single HCP structure or combination of FCC and HCP structures were also adapted to fit the diffraction patterns simultaneously. However, as depicted in Table 5.4, the goodness of fit (GOF; given by the ratio of $\frac{R_{wp}}{R_{exp}}$) was found to be more than 1, evidencing that is unlike the Pd-^{int}B/C. A HCP structure is not likely to exist in Pd-^{int}Li/C. Even though SXRD does not suggest the presence of the HCP structure, the TEM images of individual NPs, presented in Section 5.9, show minor HCP regions at the edge of the NP. However, it is expected that the total amount of the HCP crystalline phase might be so minor that it is under the detection limit of the SXRD measurement. More details about this aspect will discussed in Section 5.9.

Table 5.4. Summary of GOF for the structure of 5 wt% Pd-^{int}Li/C retrieved by TOPAS refinement.

Crystal Structure	Space Group	GOF
HCP	*P6mm*	1.0697

Apart from the space group of the unit cell that can be extracted from the SXRD profile, other information such as the particle size or microstrain of the sample can be extracted as well. As described in literature, microstrain is caused by the non-uniform displacements of the atoms with respect to their reference-lattice positions,[13,14] arising from the origin of defects (point/line/grain boundary). The combination of particle size and microstrain, in additional to the instrumental geometry and aberrations, can cause the line broadening. The line profile broadening caused by particle size can be described by a Lorentzian function while the line profile broadening caused by microstrain can be described by a Gaussian function. By deconvolution of the diffraction pattern profile depicted in Figure 5.4, it was suggested that the microstrain of Pd/C is 0.00154, and that of the Pd-^{int}Li/C is 0.00795 (Table 5.5).

Table 5.5. Microstrain measurement of the 5 wt% Pd/C and 5 wt% Pd-^{int}Li/C.

Sample	microstrain	Error
5 wt% Pd/C	0.00154	0.23680
5 wt% Pd-^{int}Li/C	0.00795	0.00567

As given in Table 5.5, the microstrain of the 5 wt% Pd-^{int}Li/C is approximately 5 times larger than that of the 5 wt% Pd/C, which suggests that the inclusion of Li can cause some degree of microstrain towards the Pd/C host system but the system still maintains the FCC structure at a global level. The increase in formation of defect sites and microstrains in Pd NPs upon inclusion of Li was evident by the STEM-ADF images, presented in Chapter 8, Appendix

Figure 8.10, which supports the results obtained by deconvolution of diffraction pattern profiles. However, it is clear that the error, which is a parameter used to evaluate the validity of the result, is very high (about 136% and 71.3% for 5 wt% Pd/C and 5 wt% Pd-^{int}Li/C respectively). We envisage that these results still involve some artifacts which could be attributed to over broad diffraction pattern profile or lack of typical instrumental parameters (i.e zero error parameter) to perform accurate devolution analysis of the diffraction pattern profiles. Therefore, the results presented herein are not viable to draw a definitive quantitative conclusion. A design of new experimental setup is required to increase the signal quality from SXRD and to obtain more viable error factor.

5.6 Neutron Diffraction

The former synchrotron source scattering technique has outlined the general structure profile of the Pd-^{int}Li/C sample. However, the intensity of X-ray diffraction patterns is highly dependent on the electron cloud of the element, so the X-ray diffraction technique is insensitive to the light element because of its low electron density. Neutron diffraction is similar to X-ray diffraction but can provide complementary information, owing to the different scattering mechanism. The neutron diffraction intensity is mainly attributed to the interaction between the neutrons with the nucleus of the atom. Furthermore, the light (low atomic number) atoms can contribute strong diffraction intensity even in the presence of heavy elements.[15] Therefore, this technique is anticipated to identify the presence of Li.

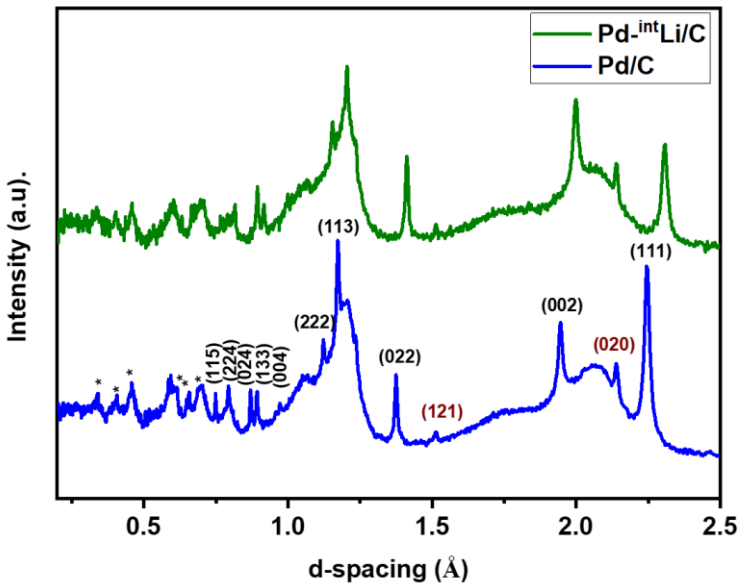


Figure 5.5. Neutron diffraction for the time-of-flight neutron profiles measured for 50 wt% Pd/C and 50 wt% Pd-^{int}Li/C. The Pd phases corresponding to the individual spacing are annotated with black. * means unknown phases. The peaks at 2.1390 and 1.5108 Å are anticipated as the phase of BCT carbon, based on ref. 16.

Figure 5.5 shows the neutron diffraction patterns for the time-of-flight neutron profiles measured for Pd/C and Pd-^{int}Li/C. The diffraction profile is analogous to the result obtained from the XRD. The d-spacings of the Pd expand after incorporation of Li, but the presence of the diffuse scattering limits the resolution, which reveals the poly-crystallinity feature of the NPs. The feature can be confirmed by the STEM-ADF images depicted in Appendix Figure 8.10. The other peaks at 2.1390 and 1.5108 Å are assigned to the carbon phases.[16] No reliable peaks could be assigned to the Li or Pd-Li phases, for which there are two main reasons, other than the scattering cross-section and scattering length. First of all, in contrast to the case of absorption of X-rays, neutron absorption has the unusual property that it is restricted only to some elements, such as B *etc*.[17] The absorption cross-section for neutron absorption of Li (70.5 barn) is much smaller than that of B (767.8 barn), but is larger than that of Pd (6.9) and C (0.0035). Such a high absorption cross-section is due to the isotope ^{6}Li, of which the absorption cross-section is 940.0 barn even though the natural abundance is about 7.5%. The other reason why Li could not be identified in our case may be attributed to the low Li content in Pd-^{int}Li/C as determined by ICP analysis (the atomic ratio of Li to Pd is 0.1 to 1).

5.7 In-situ X-Ray Pair Distribution Function (XPDF)

Even if the synchrotron XRD can provide relatively high-quality scattering results and the complementary refinements can retrieve the general structural information of the NPs, peak boardening also occurred. This is due to the small size and low crystallinity of the NPs, leading to a decrease in the accuracy of the refinement results. The neutron diffraction characterisation of the Pd/C and Pd-^{int}Li/C were attempted but failed to probe the presence of the Li-related phases. Therefore, another scattering technique is sought after, namely pair distribution function (PDF). This technique collects not only the Bragg scattering but also the diffuse scattering from which we can reveal the local environment of Pd, i.e. the position and occupancy of interstitial Li.

In order to obtain enough intensity counts, 50 wt% Pd/C and 50 wt% Pd-^{int}Li/C were prepared. Figure 5.6a shows a comparison of the XPDF information between Pd/C and Pd-^{int}Li/C at room temperature. A scattering peak at around 3.9027(7) Å is assigned as Pd−Pd in Pd/C in agreement with the literature value of the pure Pd lattice parameter. Compared with Pd/C, peaks of the Pd-^{int}Li/C slightly shift in upwards, standing at around 3.9888(3) Å, which is close to the structural information retrieved by the TOPAS refinement. To avoid any uncertainties, this sample was continuously heated to 216 ℃ to remove the Li atoms from the interstitial sites. As depicted in Figure 5.6b, the lattice parameter progressively returns to the lower value, which results in local structure distortion of the Pd host system. Overall, this measurement is consistent with the analysis from the TOPAS refinement and confirms that the presence of the Li atoms can enlarge the lattice parameter, which is similar to the effect caused by the B dopant. However, peaks corresponding to the Li lattice parameter were not found in Figure 5.6a because of the weak scattering.

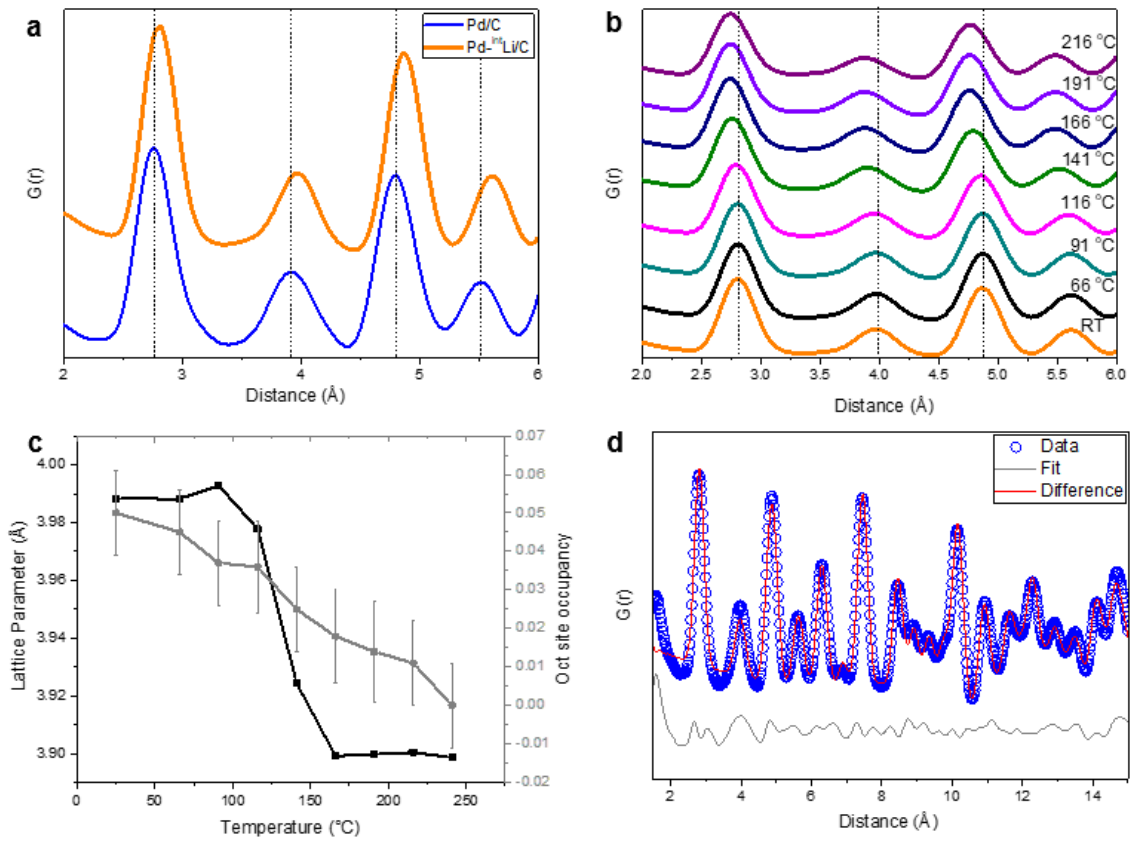


Figure 5.6. Local structural distortion probed by using in-situ XPDF and PDFgui. (a) XPDF analysis of 50 wt% Pd/C and 50 wt% Pd-^{int}Li/C at room temperature providing data on Pd−Pd bond distance at the range of 2 to 6 Å. (b) in-situ XPDF of 50 wt% Pd-^{int}Li/C from room temperature to the elevated temperature at the range of 2 to 6 Å. (c) The Pd–Pd lattice parameter and corresponding Li occupancy in the octahedral sites against temperature. (d) A typical fit – fitting range = 1.5 – 15 Å. R_w = 20.6%; other fittings parameters can be found in Table 5.7.

Even though Li is a light element, its atomic radius is 167 pm.[18] Obviously, its atomic size is too large to be accommodated at the octahedral or tetrahedral interstitial sites of Pd host system. In light of the previous DFT calculations reported by Ellis *et.al*,[5] charge transfer from Li to the Pd host can happen, which means that the Li dopants could be treated as Li^+ and Pd host system could be treated as Pd^-. Radius ratio rule is a conventional way to estimate structure type in binary compounds. Victor Goldschmidt was first to use the concept of ionic-radius ratio rule to solid state lattices in accordance with the literature reported by Jensen *et.al*.[19] The radius ratio describes the ratio of the radius of the smaller ion (r_{small}) to that of the larger (r_{large}), which is illustrated as below (Equation 5.1):

$$\gamma = \frac{r_{small}}{r_{large}} \qquad \text{(Equation 5.1)}$$

The r_{small} is the cation radius and the r_{large} is the anion radius, which is used to address the geometrical problem of ionic based model. To the best of my knowledge, ionic radius ratio rule so far has not been applicable for other systems, such as covalent or metallic system. As aforementioned above, there is charge transfer from the Li to Pd, and hence, the interstitial solid solution system, Pd-Li, can be considered as an analogue to the ionic component system. Therefore, the ionic radius ratio rule was adapted to propose a possible location of the Li.

Table 5.6. The relationship between radius ratio and coordination number.

Limiting ratio	Coordination number	Structural arrangement	Size range (pm)
0. 225−0.414	4	tetrahedral	38.025 to 69.966
0. 414−0.732	6	Octahedral	69.966 to 123.708

Since the ionic radius of Pd anion has not reported yet, the atomic radius of elementary Pd is used for calculation. The limiting ratio range of tetrahedral sites (coordination number 4) and octahedral sites (coordination number 6), and the size range are listed in Table 5.6. The Pd atomic radius is 169 pm. The size range for the tetrahedral site is from 38.025 to 69.966 pm, while the size range for the octahedral site is from 69.966 to 123.708 pm. Because the atomic radius of Li^+ is 76 pm, which is at the range of 0.432r−0.732r, it can occupy a octahedral hole in a close-packed or slightly expanded close-packed array of Pd.

The PDFgui software further supports this conclusive statement. A typical PDFgui fitting from 1.5 to 15 Å is depicted in Figure 5.6d. The R_w is 20%, which is in the acceptable range, according to the literature review of PDFgui refinement for NPs.[20] We furthermore used PDFgui to correlate the relationship between the lattice parameter and site occupancy at different temperatures, as depicted in Table 5.7. From room temperature to 66 ℃, the lattice parameter remains at 3.9888(3) Å and the corresponding Li occupancy at around 5.0%. When

the temperature increases step by step, the Pd lattice parameter and occupancy of Li start to decrease continuously. At 141 ℃, the lattice parameter is 3.9245(9) Å and the Li occupancy further decreases to 2.5%. This indicates that Li can stably reside in the interstitial sites at room temperature, but starts to leach out at an elevated temperature.

Table 5.7. Lattice parameter and occupancy versus temperature of 50 wt% Pd-^{int}Li/C.

Temperature (°C)	Lattice parameter (Å)	Occupancy	R_w (%)
25	3.9883(8)	0.050(11)	20.6
66	3.9882(7)	0.045(11)	20.6
91	3.9928(6)	0.037(11)	17.2
116	3.9778(9)	0.036(12)	12.8
141	3.9245(9)	0.025(11)	13.0
166	3.8992(9)	0.018(12)	13.2
191	3.8998(9)	0.014(13)	13.1
216	3.9004(9)	0.011(11)	13.5

5.8 Electron Energy Loss Spectroscopy (EELS)

In Chapter 4, EELS was demonstrated which is a powerful technique to determine the amount of B and its spatial distribution in the Pd-^{int}B/C NPs. EELS is sensitive to the Li, where the excitation of low energy loss occurs around the Li-K edge. To estimate the site occupancy in the local environment, Li-K edge measurements were carried out using a JEOL-ARM 200 equipped with a Gatan GIF Quantum 965 ER featuring Dual EELS and EFTEM capabilities at 80, 200 kV and Nion UltraSTEM at 60 kV.

5.8.1 200 kV

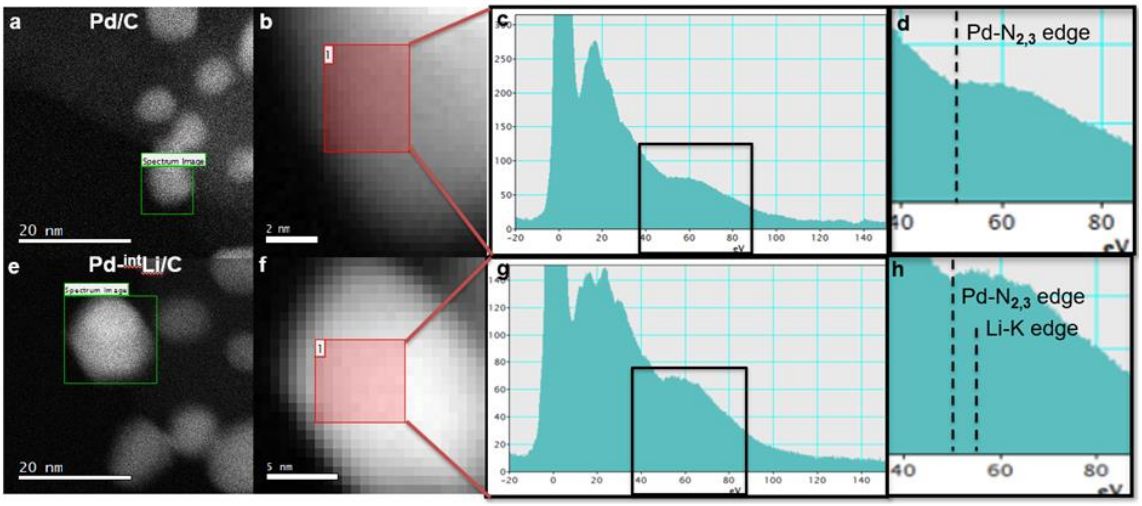


Figure 5.7. EELS of 5 wt% Pd-^{int}Li/C and 5 wt% Pd/C at 200 kV. (a) and (e) are SI survey images of 5 wt% Pd/C and 5 wt% Pd-^{int}Li/C, respectively, which indicate the locations of the NPs to be characterised. (b) and (f) are spectrum images of 5 wt% Pd/C and 5 wt% Pd-^{int}Li/C, where EELS spectra were taken along each pixel of the selected red square. (c) is the EELS spectrum of 5 wt% Pd/C and (g) is the EELS spectrum of 5 wt% Pd-^{int}Li/C. (d) is the inset of EELS spectrum (c), which shows the Pd-$N_{2,3}$ edge starting from the 51 eV. (h) is the inset of EELS spectrum (g), which shows the Pd-$N_{2,3}$ edge starting from 51 eV. Additionally, the Li-K edge is absent in the spectrum. The literature location of the Pd-$N_{2,3}$ edge and Li-K edge are annotated with black dotted lines respectively. The resolution of the EELS is 0.8 eV in accordance with the full width at half maximum (FWHM) of the ZLP (see Appendix Figure 8.11).

Since the Pd-$N_{2,3}$ edge starts from 51 eV and the Li-K edge starts from 55 eV, both Pd/C and Pd-^{int}Li/C were measured for comparison. Figure 5.7c and 7g are typical EELS spectra in the low-loss region of 5 wt% Pd/C and 5 wt% Pd-^{int}Li/C, including zero-loss peaks. The location of the Pd-$N_{2,3}$ edge and the Li-K edge are annotated with black dotted lines. As depicted in Figure 5.7h, it is hard to identify the presence of the Li-K edge, because of the delayed Pd-$N_{2,3}$ edge. Moreover, it is well known that Li, as the lightest metallic element, is challenging to detect because of smaller scattering power and higher knock-on probability.[21]

5.8.2 80 kV

Since Pd-^{int}Li/C is an interstitial alloy NP, which is a metallic based material, the dominant beam-induced damage mechanism may be the "knock-on".[21] This suggests that lowering the accelerating voltage to 80 kV might help to reduce beam damage, which in turn would aid in Li detection. Resulting spectra collected at 80 kV are shown in Figure 5.8, which are similar to

the spectra obtained at 200 kV. The Pd-$N_{2,3}$ edge (51 eV) is rather close to the Li-K edge (55 eV), so it is very challenging to separate these two completely in the spectrum and confirm the presence of Li unambiguously. Moreover, the resolution of EELS is also 0.8 eV at 80 kV, which makes the separation of the Li and Pd signals difficult.

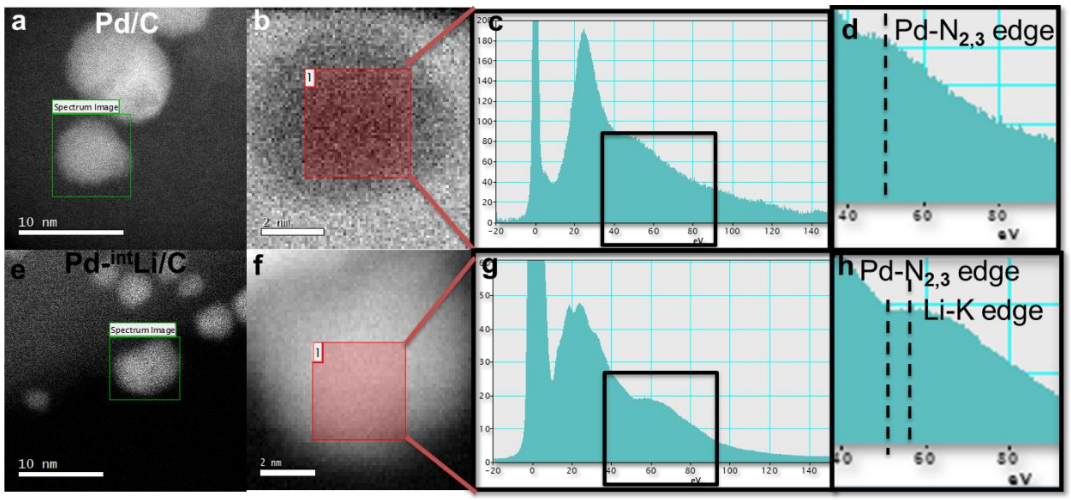


Figure 5.8. EELS of 5 wt% Pd-^{int}Li/C and 5 wt% Pd/C at 80 kV. (a) and (e) are SI survey images of 5 wt% Pd/C and 5 wt% Pd-^{int}Li/C, respectively, which indicate the location of the NPs to be characterised. (b) and (f) are spectrum images of 5 wt% Pd/C and 5 wt% Pd-^{int}Li/C, where EELS spectra were taken along each pixel of the selected red square. (c) is the EELS spectrum of 5 wt% Pd/C and (g) is the EELS spectrum of 5 wt% Pd-^{int}Li/C. (d) is the inset of EELS spectrum (c), which shows the Pd $N_{2,3}$ edge starting from 51 eV. (h) is the inset of EELS spectrum (g), which shows the Pd-$N_{2,3}$ edge starting from 51 eV. Additionally, the Li-K edge is absent in the spectrum. The literature location of the Pd-$N_{2,3}$ edge and the Li-K edge are annotated with black dotted lines respectively. The resolution of the EELS is 0.8 eV in accordance with the full width at half maximum (FWHM) of the ZLP (see Appendix Figure 8.12).

5.8.3 60 kV

Moreover, to directly probe the Li signal, it is advised that the unique capabilities of monochromated electron microscopy will be used. The combined high spatial and energy resolution of this instrument should allow for the acquisition of information regarding local electronic structure and elemental distribution of the individual particles and their surrounding matrix at a higher level of detail than the Oxford-based instrumentation. It is expected that the increased energy resolution will make the sharp Li-K edge more visible above the broad Pd-$N_{2,3}$ edge. Reducing the accelerating voltage to 60 kV can also decrease the probability of "knock-on" damage. However, even though the electron microscopy equipped with a

monochromator was used to probe the Li signal, as depicted in Figure 5.9d and h, we have found that the EELS spectrum of the Pd-^{int}Li/C is still indistinguishable to that of the Pd/C. This result indicates that the use of the monochromator cannot allow identification of the Pd and Li edges directly.

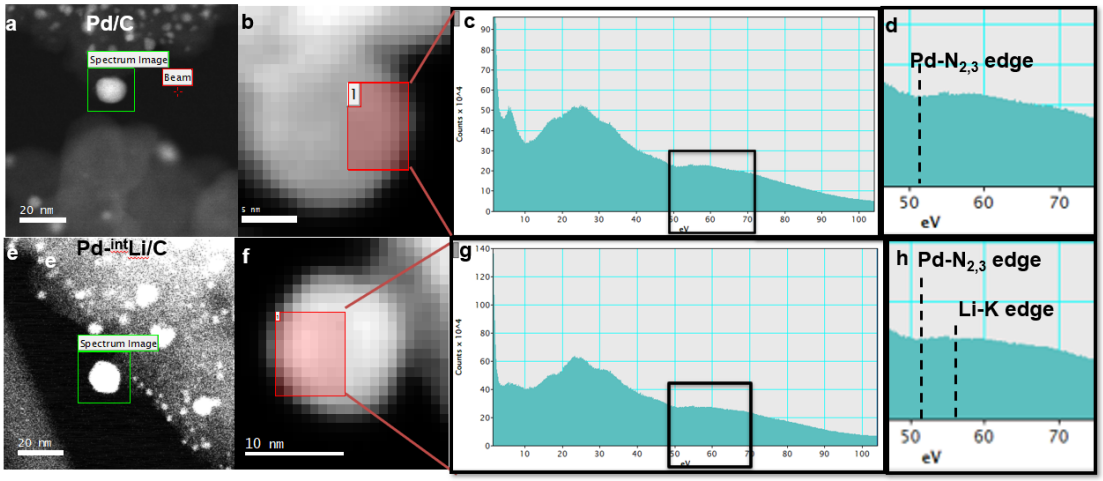


Figure 5.9. EELS of 5 wt% Pd-^{int}Li/C and 5 wt% Pd/C at 60 kV. (a) and (e) are SI survey images of 5 wt% Pd/C and 5 wt% Pd-^{int}Li/C, respectively, which indicate the location of the NPs to be characterised. (b) and (f) are spectrum images of 5 wt% Pd/C and 5 wt% Pd-^{int}Li/C, where EELS spectra were taken along each pixel of the selected red square. (c) is the EELS spectrum of 5 wt% Pd/C and (g) is the EELS spectrum of 5 wt% Pd-^{int}Li/C. (d) is the inset of EELS spectrum (c), which shows the Pd $N_{2,3}$ edge starting from 51 eV. (h) is the inset of EELS spectrum (g), which shows the Pd-$N_{2,3}$ edge starting from 51 eV. Additionally, the Li-K edge is absent in the spectrum. The literature location of the Pd-$N_{2,3}$ edge and the Li-K edge are annotated with black dotted lines respectively. The resolution of EELS is 0.2 eV in accordance with full width at half maximum (FWHM) of the ZLP (see Appendix Figure 8.13).

It has been reported that the plasmon energy of the NPs is very sensitive to the Li concentration because the presence of Li changes the number of carrier electrons.[22] In the plasmon region, it was found that the plasmon profile of Pd/C (Figure 5.7c, 5.8c and 5.9c) differs from that of the Pd-^{int}Li/C (Figure 5.7g, 5.8g and 5.9g). Although the change in the origin of the modification of the plasmon response is intriguing, this does not prove the presence of Li in the structure outright. Additionally, the presence of carbon also affects the plasmon profile, which cannot be deconvoluted from the EELS spectrum linearly. To date, the EELS technique is unable to probe and quantify the Li concentration at local environment.

5.9 Annular Dark Field (ADF) Imaging

In light of the lattice expansion of the lithiated Pd system, ideally, the system tolerates an expanded type of strain with respect to the fresh Pd system. However, it is the consensus that NPs are not simply analogous to the bulk metal. Various contributions can result in unusual forms of structural disorder and thus induce surface strain (i.e compression or stretch of surface atoms). Therefore, we then moved to the micro-level for visualisation of the surface strain variation at the atomic level.

200 kV was initially adopted to acquire the ADF and ptychography simultaneously. To avoid saturation of the fast-pixelated detector and reduce the knock-on damage,[23] the emission current was reduced to the 6 μA, and the corresponding electron dose was about 0.92×10^6 $e^-/Å^2$. As indicated in section 5.3 Figure 5.1b, the histogram shows that the particle size is at the range of 2-10 nm. It must be pointed out that particle size itself can result in strain on the catalytic surface. Such a size-dependent strain in the NPs is due to the high percentage of surface atoms which tend to undergo compression to lower the surface energy, according to the Gibbs−Thomson relationship (Equation 5.2):

$$\mu(R) - \mu(\infty) = \frac{4\gamma v}{R} \qquad \text{(Equation 5.2)}$$

Where μ(R) is the molar free energy of a particle of radius, R, μ(∞) is the free energy in bulk, γ is the surface tension, and v is the molar volume. Smaller particle size can therefore increase the surface energy. To compensate for the resulting increase in free energy, the NP tends to undergo a volumetric compression.[24] Hence, to ensure the consistency of each of the measurements, it will be ideal to find a high-crystallinity NP of which particle size is close to the average particle size of 5 wt% Pd-^{int}Li/C. The particle size of this NP depicted in Figure 5.10 is measured to be ca. 5.6 nm, based on the line profile depicted in Chapter 8 Appendix

Figure 8.15, which is close to the average particle size (5.77 nm) calculated from the histogram (Figure 5.1b). Therefore, this NP was selected for further investigation.

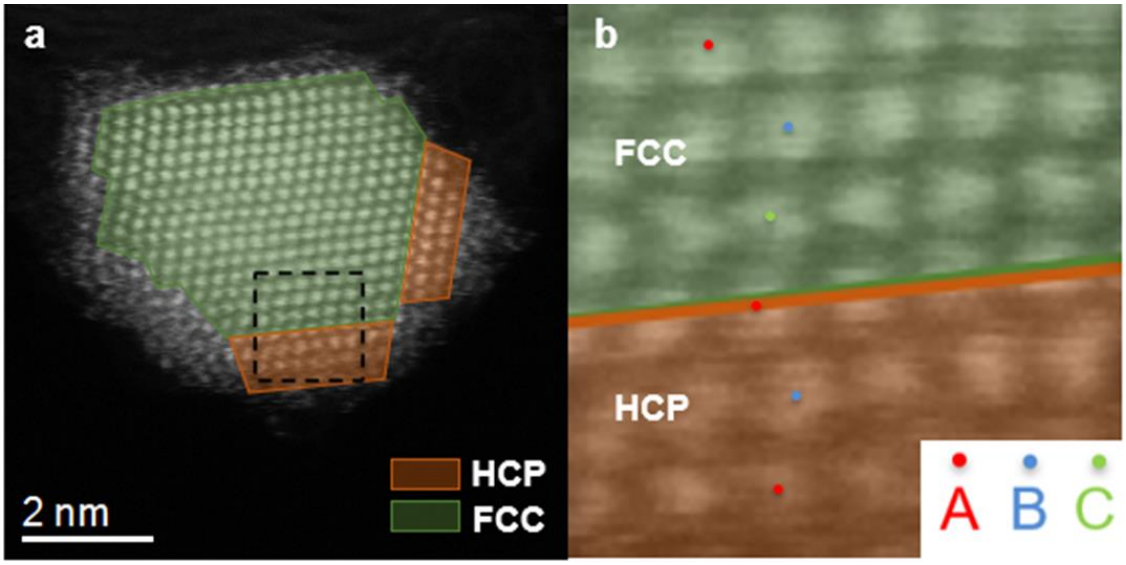


Figure 5.10. Z-contrast STEM-ADF imaging of 5 wt% Pd-^{int}Li/C NP. (a) is a typical Z-contrast STEM-ADF of a 5 wt% Pd-^{int}Li/C NP, which is well-orientated in the zone axis <110> direction. Two phases are found in (a) and has been further demonstrated in (b). Region annotated with green shows FCC structure; region annotated with orange shows HCP structure. FCC (ABCA) and HCP (ABA) stacking have been annotated by red, blue and green dots. These dots represent different atomic layers.

Indeed, strain induced by smaller particle size would compress the volume, leading to the change in the lattice parameter, but retaining the overall structure. However, two different phases are found across this NP. The region annotated with green has an FCC structure, while the region annotated with orange has an HCP structure. Whilst neither of the bulk material characterisations through SXRD and PDF (in subchapter 5.5 and 5.7) substantiate the existence of the HCP structure over their corresponding refinements, the atomic resolution STEM-ADF imaging shows the existence of small region of the HCP structure. It should be pinpointed that Pd possessing an HCP structural arrangement is particularly uncommon, and only can be achieved by templating the growth of a Pd NP on an HCP support, such as graphite.[25] Therefore, the presence of an HCP structure might be due to two reasons:

1. Effect of extrinsic strain

Due to the presence of foreign additives, atoms staying at the edges or corners can dislocate easier, resulting in nanoscale phase transitions.[26]

2. Formation of Li-rich phase

As explained in Chapter 4, the foreign Boron (B) additives are randomly distributed throughout the volume of the NPs. Some regions are rich with B additives, other regions are not. Similar to the B distribution of Pd-^{int}B/C, it is reasonable to assume that a typical region of the Pd-^{int}Li/C NP has a large amount of Li incorporated, leading to the formation of Li-rich species, such as Li_2Pd and LiPd, which have an HCP structure.[11]

Additionally, an attempt has been made to study the effect of extrinsic strain variation with respect to the centre of the NP by using Statstem which is a Matlab-based program developed by the University of Antwerp for quantitative electron microscopy analysis.[6] A model-based estimation algorithm is implemented to quantify the atomic column positions and intensities from atomic resolution TEM or STEM images, and particularly for the STEM-ADF images.

The overall strain distribution is a sum of the contribution of individual effects (particle size, shape, presence of the dopants, support and phase transformation), and therefore it is essential to deconvolute and evaluate each effect individually. A STEM-ADF of a Pd/C NP with the same particle size should be acquired at the same experimental conditions (number of pixels and magnification) for reference. However, it is a great challenge to find a defect free Pd/C NP with the same particle size and atomic configuration to the Pd-^{int}Li/C shown in Figure 5.10, and acquire data from the particle at the same experimental conditions without any scan distortion. Current results involve an artefact (See Chapter 8 Appendix Figure 8.14 for details); thus, further effort is still required.

5.10 Ptychographic Imaging at 200 kV

In parallel to attempt to determine the impact of Li dopants on the local strain contribution, availability of the Li visualisation in the Pd host system was investigated. It is well known that ADF-STEM imaging is used for the determination of the atomic location because of the difference in atomic number. The atomic number of Pd is 46, and the atomic number of Li is 3, which means that the intensity of Pd is much higher than that of Li. Li atomic columns are invisible in the ADF image due to low scattering power at higher angles scattering. ADF imaging simulations of Pd and Pd-^{int}Li over different thicknesses were performed, as shown in Figure 5.11. This indicates that Li atomic columns are not visible even with thickness up to 6 nm.

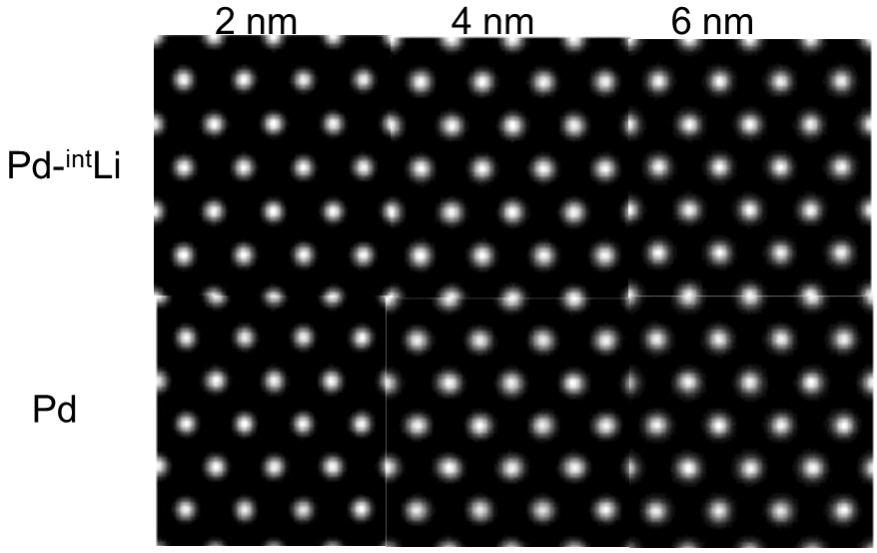


Figure 5.11. Simulated Z-contrast ADF-STEM image of Pd-^{int}Li/C and Pd/C over the different thickness of 2 nm, 4 nm and 6 nm respectively.

After implementation of the Wigner distribution deconvolution (WDD) reconstruction method,[27] this ambiguity was resolved by phase imaging as demonstrated in Figure 5.12c and d, which shows a lower relative image contrast (see the blue arrow, Figure 5.12d) that can be attributed to additional atomic columns residing between the higher contrast Pd atomic columns. If the projected Pd-^{int}Li structure model is superimposed to the enlarged image in Figure 5.12d, a good match is found in the octahedral sites.

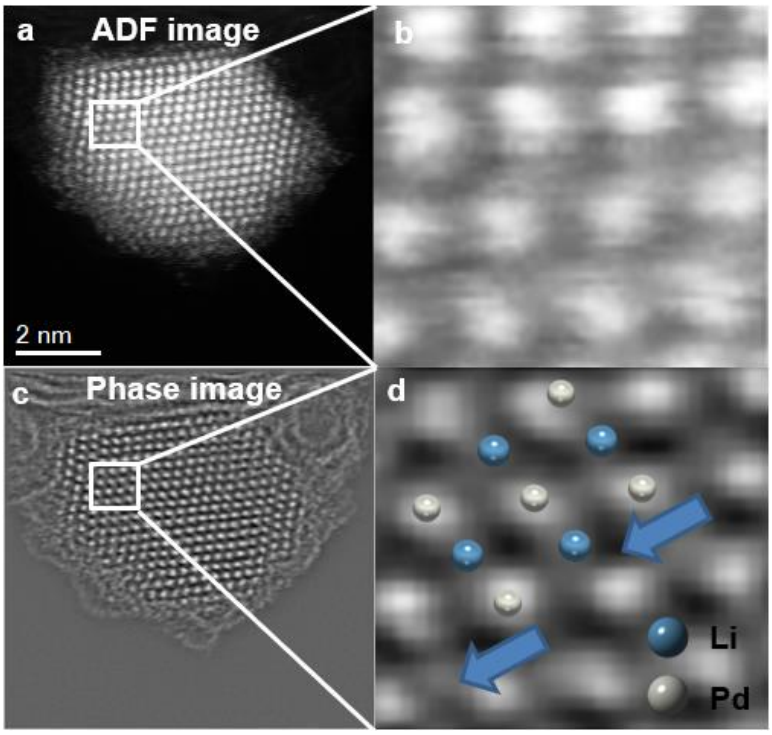


Figure 5.12. Simultaneous Z-contrast ADF-STEM image and phase image of 5 wt% Pd-^{int}Li/C. (a) is the ADF imaging of the NP. The inset (b) shows enlarged images with an atomic configuration orientated in <110> direction. The Li atomic columns are invisible because of low atomic number. (c) is the phase image reconstructed via the WDD method. (d) is the inset of phase image (c), which shows that contrast resolves and new atomic columns labelled with blue arrows emerge at octahedral sites.

Corresponding image simulations at the experimental optical condition over different thicknesses and Li site occupancy were calculated, as shown in Figure 5.13, respectively. The phase of the relatively heavy Pd is wrapped, which is attributed to the dynamical scattering behaviour, and hence violates the multiplicative approximation.[28] Hence, the contrast reversal is observed in Figure 5.13a to f. However, in this case, Figure 5.13c shows Li atomic columns intercalated with the Pd metal framework. As shown in Figure 5.13g to l, site occupancy of Li above a certain degree allows for availability of Li visualisation *via* ptychography, although the contrast of Pd mismatches with experimental data. Thus, on the basis of the other analytical techniques, the ptychography is supportive of Li in octahedral sites.

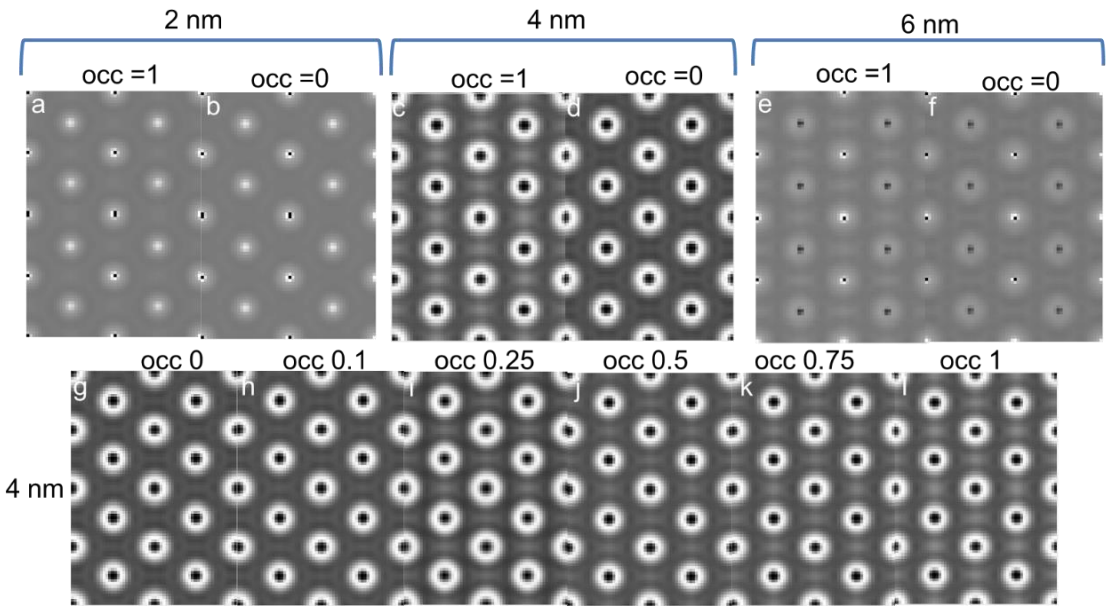


Figure 5.13. Ptychographic imaging simulation of Pd-^{int}Li over different thicknesses and Li octahedral site occupancy (occ) at 200 kV (semi-convergence angle: 22.3 mrad).

5.11 Ptychographic Investigation at Low Voltage

In parallel to visualising the Li atomic columns at the high accelerating voltage, the investigation of Li atomic columns at the lower accelerating voltage has also been explored. This is because the predominant beam damage mechanism of the interstitial alloy-based material is the "knock-on damage",[21] instead of the radiation decomposition damage.[29] In order to reduce the possibility of "knock-on damage", ptychographic experiments were also carried out at 60 kV and 80 kV, respectively.

5.11.1 Ptychographic Imaging at 80 kV

Experiments were carried out on an aberration-corrected JEOL ARM300F operating at 80 kV. A 30-μm aperture was brought into the lens and can yield a semi-convergence angle of 24.8 mrad.

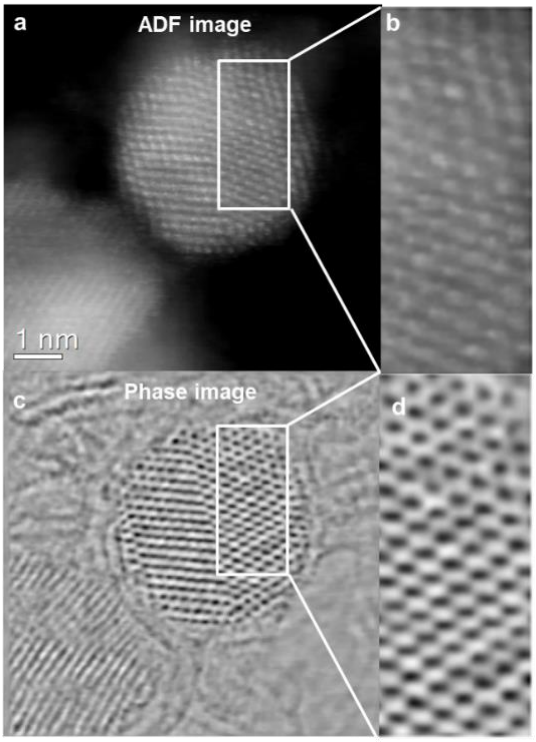


Figure 5.14. Simultaneous Z-contrast ADF-STEM image and phase image of 5 wt% Pd-^{int}Li/C at 80 kV. (a) is the ADF imaging of the NP. The inset (b) shows enlarged images with an atomic configuration orientated in <110> direction. The Li atomic columns are invisible because of low atomic number. (c) is the phase images reconstructed via WDD method. (d) is the inset of phase image (c).

Figure 5.14a is a typical Pd-^{int}Li/C NP with a thickness of 4.5 nm (See Chapter 8 Appendix Figure 8.16), orientated in the <110> zone axis. With regards to the rule of the Z-contrast, Li atomic columns are invisible because of the low scattering power. After the reconstruction of the phase image via the WDD algorithm, despite the contrast of the phase image (Figure 5.14c) being boosted, it was unfortunate that no reliable contrast for the Li atomic columns was found at the interstitial sites. This is because lowering the accelerating voltage can reduce the resolution, as shown in the following equation (Equation 5.3),[30,31]

$$d = \frac{0.753}{\alpha\sqrt{V}} \qquad \text{(Equation 5.3)}$$

where d is the resolution in nm, α is the half-opening angle of objective, and V is the accelerating voltage. For a better in-depth investigation of the ptychographic phase contrast, the image simulation of Pd-^{int}Li with specimen thickness up to 6 nm at the experimental condition was computed and shown in Figure 5.15. It can be seen that the phase of the relatively

heavy Pd is wrapped owing to the dynamic scattering. Even if the Li site occupancy is up to 1, only residual intensity can be found at the interstitial sites over different thickness. It means that the semi-convergence angle of 24.8 mrad may not be large enough to resolve the Li atomic columns.

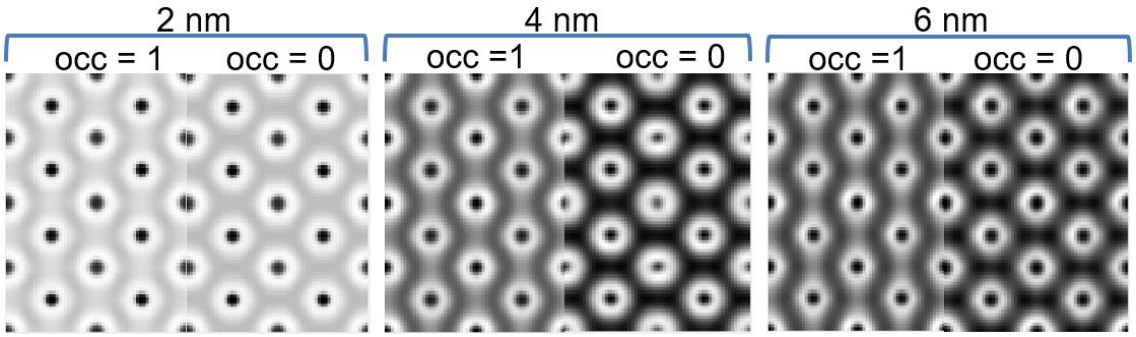


Figure 5.15. Ptychographic imaging simulation of Pd-^{int}Li over different thickness at 80 kV (semi-convergence angle: 24.8 mrad). Image contrast was compared at Li octahedral site occupancy occ = 0 and occ = 1, respectively. These results reveal that residue intensity can be found in the interstitial sites, but the aperture is not big enough to fully resolve the Li atomic columns.

To further pave a pathway for the future work, the image simulation of Pd-^{int}Li with a thickness of 2 nm was computed (Figure 5.16), using a 31.74 mrad STEM probe (ARM300, aperture size: 40-μm) at 80 kV. Li atomic columns at the interstitial sites can be fully resolved even if the phase of the heavy Pd becomes wrapped owing to the dynamic scattering. It is therefore expected that a larger aperture could be used to attempt direct visualisation of Li at 80 kV in future work.

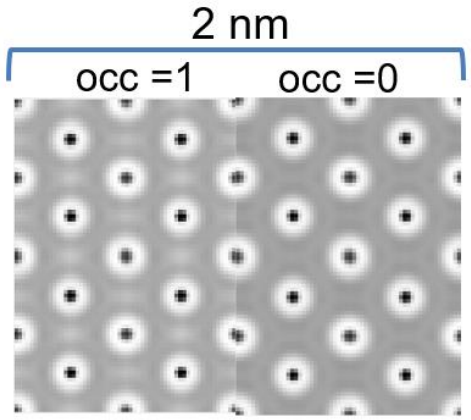


Figure 5.16. Ptychographic imaging simulation of Pd-^{int}Li with the thickness of 2 nm at 80 kV (semi-convergence angle 31.74 mrad). Image contrast was compared at octahedral site occupancies (occ) of 0 and 1, respectively.

5.11.2 Ptychographic Imaging at 60kV

Additionally, the experiments were also carried out at the same microscope at an even lower accelerating voltage, 60 kV. An aperture of size 30-μm was brought into the ray pathway and can yield a convergence semi-angle of 30.6 mrad. However, after lowering the accelerating voltage, the microscope was unstable, resulting in 3-fold astigmatism and coma. Therefore, the convergence semi-angle could not be tuned to a higher degree for the acquisition of high-quality datasets.

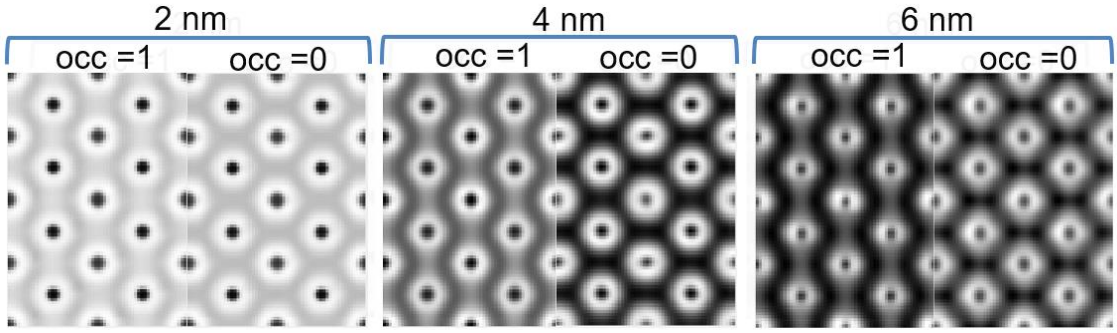


Figure 5.17. Ptychographic imaging simulation of Pd-^{int}Li over the different thicknesses at 60 kV (semi-convergence angle: 30.6 mrad). Image contrast was compared at Li site occupancies of (occ = 0) and (occ = 1), respectively. These results reveal that residue intensity can be found in the interstitial sites, but the aperture is not big enough to fully resolve the Li atomic columns.

Although acceptable images were not obtained because of the instrumental problem, for a better understanding of the ptychographic phase contrast, ptychographic imaging simulations *via* the WDD algorithm were performed over different thicknesses in accordance with the experimental conditions. As depicted in Figure 5.17, ptychographic imaging simulations over various thicknesses were conducted and compared at Li octahedral site occupancies of occ = 0 and occ = 1, respectively. The results resemble the simulation work computed under the condition of 80 kV accelerating voltage. Despite the fact that the ptychographic experiments were carried out using a larger semi-convergence angle, the resolution is limited by the accelerating voltage leading to contrast blurring at the interstitial sites.

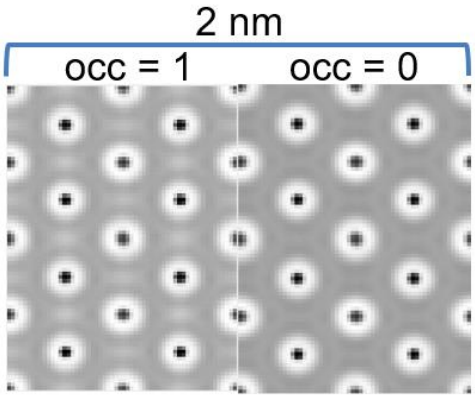


Figure 5.18. Ptychographic imaging simulation of Pd-^{int}Li with a thickness of 2 nm at 60 kV (semi-convergence angle 39.1 mrad). Image contrast was compared at Li site occupancies of occ = 0 and occ = 1, respectively.

Based on the previous theoretical relationship between the resolution with the convergence semi-angle, a larger convergence angle leads to phase image sensitivity to the lighter elements. Calculated phase images (Figure 5.18) of Pd-^{int}Li NPs with 2 nm specimen thickness, considering a semi-convergence angle of 39.1 mrad (corresponding aperture size: 40-μm), can show up clearly visible Li atomic sites, even if the phase of the heavy Pd becomes wrapped. This simulation result suggests Li atomic sites may only be fully visible, using a STEM probe of 39.1 mrad, if the microscopic stability allows.

5.12 Conclusion

In conclusion, we have introduced a combination of characterisation tools, from macro- to micro- analysis, to evaluate the structural disorder resulting from the Li dopants. The lattice expansion, phase transformation and loss of symmetry is the consequence of the structural distortion. The associated strain effect was also evaluated by global analysis, showing that the incooperation of Li can induce meaningful strain, but the validity of the result still needs extra experiments to prove this. Moreover, ptychography probed the Lithium-like atomic columns intercalated with Pd atomic columns, which can at least partially rationalise the structure-distortion phenomenon. However, this resolved contrast would require direct identification of the Li signal to assign to Li fully. Probing the Li spectroscopic signal was primarily investigated at 200 kV, 80 kV and 60 kV. Due to the limitation of the EELS resolution and the

potential knock-on damage, the Li-K edge was not detected outright. However, it is also worth noting that the plasmon region of Pd-^{int}Li/C EELS was different from that of pure Pd. In this respect, a more advanced instrument would be required to identify the Li edge and quantify the local concentration accurately. Using ptychography and implementation of the Wigner distribution deconvolution (WDD) reconstruction method can potentially show the additional atomic columns residing between the higher contrast Pd atomic columns to be Li atoms in octahedral sites at 200 kV. However, the electron beam damage of the materials is anticipated to be a serious issue. Modelling showed that if ptychography was carried out over the Pd-^{int}Li NPs with 2 nm specimen thickness, using a convergence semi-angle of 39.1 mrad (corresponding aperture size: 40-µm), a good image to visualise Li columns without severe beam damage at 60 kV can be collected. Nevertheless, it is believed that the current results can open a window towards the in-depth investigation of the light element such as Li modified Pd structure analysis by means of structural distortion.

5.13 References

1 C. Zhang, F. Liu, Y. Zhai, H. Ariga, N. Yi, Y. Liu, K. Asakura, M. Flytzani-Stephanopoulos and H. He, *Angew. Chem. Int. Ed.*, 2012, **51**, 9628–9632.

2 T. W. Elkins, B. Neumann, M. Bäumer and H. E. Hagelin-Weaver, *ACS Catal.*, 2014, **4**, 1972–1990.

3 C. Liu, Z. G. Neale and G. Cao, *Mater. Today*, 2016, **19**, 109–123.

4 S. Arndt, G. Laugel, S. Levchenko, R. Horn, M. Baerns, M. Scheffler, R. Schlögl and R. Schomäcker, *Catal. Rev.*, 2011, **53**, 424–514.

5 I. T. Ellis, E. H. Wolf, G. Jones, B. Lo, M. Meng-Jung Li, A. P. E. York and S. C. Edman Tsang, *Chem. Commun.*, 2017, **53**, 601–604.

6 A. De Backer, K. H. W. van den Bos, W. Van den Broek, J. Sijbers and S. Van Aert, *Ultramicroscopy*, 2016, **171**, 104–116.

7 Ieuan T. Ellis, PhD Thesis, University of Oxford, 2016.

8 T. J. N. Hooper, T. A. Partridge, G. J. Rees, D. S. Keeble, N. A. Powell, M. E. Smith, I. P. Mikheenko, L. E. Macaskie, P. T. Bishop and J. V. Hanna, *Phys. Chem. Chem. Phys.*, 2018, **20**, 26734–26743.

9 T. J. N. Hooper, PhD Thesis, University of Warwick, 2018.

10 A. A. Coelho, *J. Appl. Crystallogr.*, 2018, **51**, 210–218.

11 J. Sangster and A. Pelton, *J. Phase Equilibria*, 1992, **13**, 63–66.

12 J. W. Arblaster, *Platin. Met. Rev.*, 2013, **57**, 177–185.

13 A. R. Bushroa, R. G. Rahbari, H. H. Masjuki and M. R. Muhamad, *Vacuum*, 2012, **86**, 1107–1112.

14 M. Birkholz, *Thin Film Analysis by X‐Ray Scattering*, Wiley, 2005, vol. 58.

15 B. Song, G. M. Veith, J. Park, M. Yoon, P. S. Whitfield, M. J. Kirkham, J. Liu and A. Huq, *Chem. Mater.*, 2019, **31**, 124–134.

16 X. F. Zhou, G. R. Qian, X. Dong, L. Zhang, Y. Tian and H. T. Wang, *Phys. Rev. B*, 2010, **82**, 134126.

17 V. F. Sears, *Neutron News*, 1992, **3**, 26–37.

18 E. Clementi, D. L. Raimondi and W. P. Reinhardt, *J. Chem. Phys.*, 1967, **47**, 1300–1307.

19 W. B. Jensen and W. B. Jensen, *J. Chem. Educ.*, 2010, **87**, 587–588.

20 A. S. Masadeh, E. S. Božin, C. L. Farrow, G. Paglia, P. Juhas, S. J. L. Billinge, A. Karkamkar and M. G. Kanatzidis, *Phys. Rev. B*, 2007, **76**, 115413.

21 F. Wang, J. Graetz, M. S. Moreno, C. Ma, L. Wu, V. Volkov and Y. Zhu, *ACS Nano*, 2011, **5**, 1190–1197.

22 C. S. Granerød, S. R. Bilden, T. Aarholt, Y. F. Yao, C. C. Yang, D. C. Look, L. Vines, K. M. Johansen and Ø. Prytz, *Phys. Rev. B*, 2018, **98**, 115301.

23 B. D. Levin and D. A. Muller, *Microsc. Microanal.*, 2013, **19**, 1228–1229.

24 B. T. Sneed, A. P. Young and C. K. Tsung, *Nanoscale*, 2015, **7**, 12248–12265.

25 J. Walter, J. Heiermann, G. Dyker, S. Hara and H. Shioyama, *J. Catal.*, 2000, **189**, 449–455.

26 K. Appavoo, D. Y. Lei, Y. Sonnefraud, B. Wang, S. T. Pantelides, S. A. Maier and R. F. Haglund, *Nano Lett.*, 2012, **12**, 780–786.

27 H. Yang, I. MacLaren, L. Jones, G. T. Martinez, M. Simson, M. Huth, H. Ryll, H. Soltau,

R. Sagawa, Y. Kondo, C. Ophus, P. Ercius, L. Jin, A. Kovács and P. D. Nellist, *Ultramicroscopy*, 2017, **180**, 173–179.

28 S. Gao, P. Wang, F. Zhang, G. T. Martinez, P. D. Nellist, X. Pan and A. I. Kirkland, *Nat. Commun.*, 2017, **8**, 163.

29 C. Zhang, Y. Feng, Z. Han, S. Gao, M. Wang and P. Wang, *Adv. Mater.*, 2019, **32**, 1903747.

30 G. F. Rempfer, *Ultramicroscopy*, 1992, **47**, 241–255.

31 K. Andres, *Introduction To Electron Microscopy Instrumentation*, Center for Microscopy and Image Analysis, University of Zürich, 2014.

Chapter 6 Design of Platinum Lithium Binary NPs

6.1 Introduction

The structure of the Pd-^{int}B/C and Pd-^{int}Li/C materials have been investigated in-depth in Chapters 4 and 5, showing the foreign dopants' location and structural distortion towards the host system. The presence of Li and B residing at the interstitial sites of the Pd host system hindered the over-hydrogenation reaction *via* inhibition of β-hydride formation.[1] Inspired by their novel structures and corresponding synthesis strategy, alloying Li to other transition metal systems for construction of a new binary NP system has been further explored in this chapter.

Pt is considered as an alternative host metal system for the synthesis of Li alloyed solid-state material. Accordingly, investigation of Pt-Li bulk binary systems can be dated back to the early 20th century. Molten Li and metallic Pt were found to undergo an exothermic reaction under Argon atmosphere at an ignition temperature of about 540 ℃, leading to the formation of an $LiPt_2$ intermetallic compound.[2] Subsequently, intense research had been accumulated, and a binary phase diagram of the Pt-Li system was established by Sangster *et al.*,[3,4] as depicted in Figure 6.1. In the late 1980s, Muller *et al.*[5] had characterised the structure of $LiPt_7$, in which Li is proposed to reside in the interstitial sites of the Pt metal system. In the early 21st century, Köhler *et al.* analysed the bonding picture of $LiPt_2$, LiPt and Li_2Pt that captured the essence of their electronic structures using DFT calculations.[6] In 2013, Ohsaka *et al.* reported that electro-deposition of Li on a Pt electrode in propylene carbonate could result in the formation of a Pt-Li alloy, which exhibited enhanced activity in formic acid oxidation, in comparison with pure Pt electrodes.[7] Recently, Howies *et al.* have just reported a novel intermetallic compound $Li_{11}Pt_2$ which can be obtained under harsh conditions.[8] To date, this substance contains the highest Li content among reported intermetallic compounds.

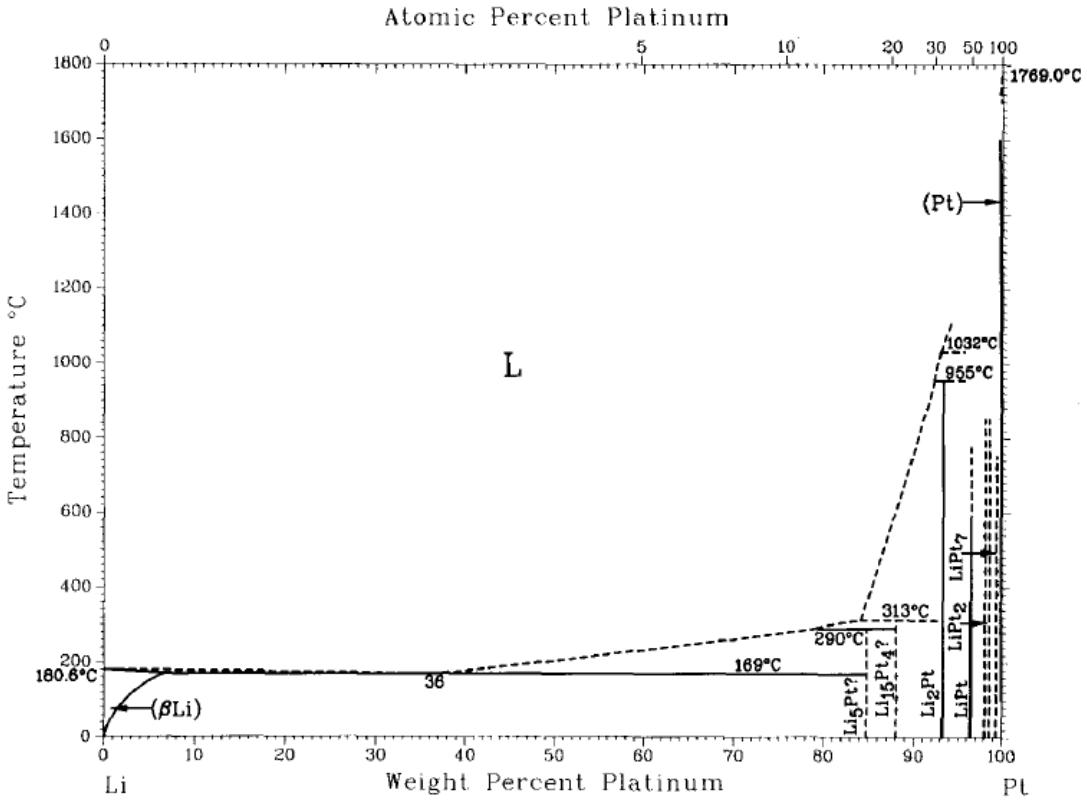


Figure 6.1. Suggested partial phase diagram of Pt-Li based on differential thermal analysis. This figure has been reproduced from ref. [4] with permission from Springer Nature, copyright 1991.

However, except for some bulk alloy investigations, the field of Pt-Li binary NPs investigation remains barely explored. The most relevant work was reported by Lu *et al.*, who stated that supported Pt NPs can be yielded from Pt-Li solid solution, which suggested Pt-Li solid solution might exist in the form of NPs during the reaction.[9] However, the work did not include the synthesis method of Pt-Li binary NPs or a proper structural analysis. Thus, it is valuable to design and synthesise Pt-Li binary NPs to broaden the library of nano binary systems with novel structures and properties. Ideally, this should be synthesised by a simple experimental procedure, coupled with an easy method of tuning Li concentration using low toxicity precursors.

Considering the catalytic property of Pt NPs, they have been frequently utilised in hydrogenation processes to convert biomass to useful fine chemicals.[10] Hydrogenation of HMF to BHMF is a promising process for upgrading biomass. Intensive research has contributed to

designing novel catalysts by alloying promotors or additives, optimising the support and controlling the particle size and shape. However, as described in Chapter 1, few examples were reported about the utilisation of Pt-based metal catalysts for the HMF to BHMF conversion. To explore the application and study the properties of the Pt-Li NPs, this catalyst was therefore employed in this reaction.

6.2 Objectives and Methodology

Previously reported synthetic methods were employed to synthesise novel Pt-Li NPs. Ex-situ XRD and TGA were initially utilised to determine the feasibility of the experiment. After gaining primary evidence, the structure of the novel material was identified step by step by using a set of characterisation techniques, such as SXRD, neutron diffraction, XPS, ^{7}Li MAS ssNMR, STEM-EELS, STEM-ADF and ptychography. After determination of the structure of the Pt-Li bimetallic NPs, this catalyst was tested in the selective hydrogenation of HMF reaction to determine the catalytic effect induced by the Li.

6.3 Thermogravimetric Analysis (TGA)

TGA is a method of thermal analysis in which the mass of a sample is measured over time as the temperature changes. It can be used to determine the chemical composition and thermal stability of the sample, since the chemical composition is reflected by the weight difference over different temperatures.

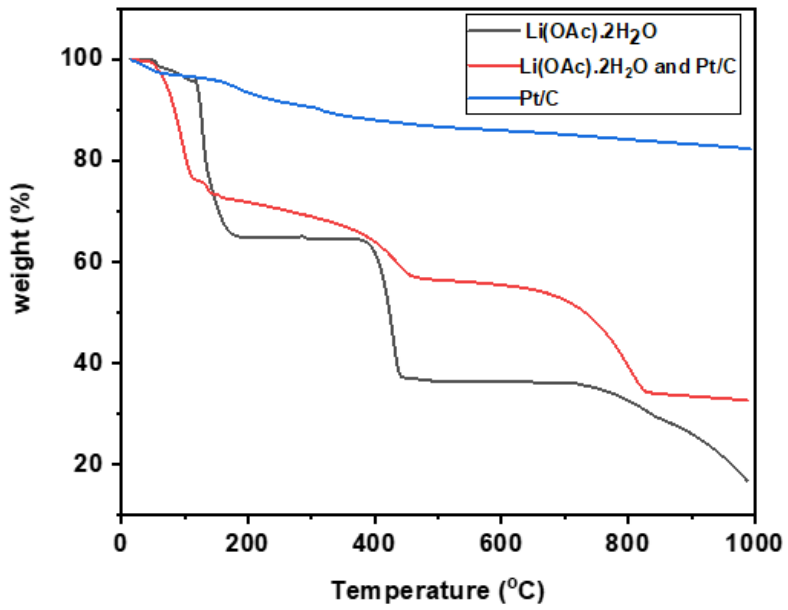


Figure 6.2. TGA of 20 wt% Pt/C, Li(OAc)·2H$_2$O and the mixture of Li(OAc)·2H$_2$O with 20 wt% Pt/C from 0 to 1000 °C. The weight loss in each stage is further displayed in Table 6.1.

Table 6.1. Measurement of weight loss during the TGA of Li(OAc)·2H$_2$O, Pt/C and Li(OAc)·2H$_2$O and 20 wt% Pt/C.

Compound	Temperature (°C)	Weight loss (%)
20 wt% Pt/C	1000	18
Li(OAc)·2H$_2$O	177	35
	423	28
	1000	17
20 wt %Pt/C+Li(OAc)·2H$_2$O	111	27
	457	16
	823	23

As indicated in Figure 6.2 and Table 6.1, when 20 wt% Pt/C is heated from room temperature to 1000 °C, the total weight loss is about 18%, which can be attributed to thermal

vaporisation of the moisture or hydrocarbon impurities on the carbon-based material. In contrast, three significant weight loss events in different temperature ranges were observed over investigation of the commercial $Li(OAc)\cdot 2H_2O$. $Li(OAc)\cdot 2H_2O$ starts to dehydrate at ~118 ℃ and is completed at ~177 ℃ with a ~35% weight loss which is equal to the weight percentage of the two water molecules.[11] The percentage of weight retained (WR) remains the same after the dehydration process. When the temperature increases to 423 ℃, another 28% weight loss occurs owing to the thermal decomposition of the Li(OAc). Previous literature reported that Li(OAc) can decompose to Li_2CO_3 at elevated temperatures, in the presence of air.[12] The gas supply in this experiment was replaced with inert gas, N_2, but the TGA profile still resembled that of the literature, in air. It can be explained that the nitrogen supply may contain trace amount of air, resulting in the formation of the Li_2CO_3. The third thermal decomposition event starts at 723 ℃ and ends up at 1000 ℃, accompanied by a weight loss of 17%. This phenomenon is coincident with the thermal decomposition of Li_2CO_3, involving multiple steps such as melting of Li_2CO_3, dissolution of Li_2O and CO_2 in Li_2CO_3, and adsorption of the CO_2 in Li_2O, respectively.[13] The WR profile of $Li(OAc)\cdot 2H_2O$ in the presence of Pt/C is similar to that of the $Li(OAc)\cdot 2H_2O$ but the trend of the weight loss behaves slightly differently. The weight loss of the mixture is 27% during the dehydration process. The second decomposition process appears at approximately 423 ℃, with a weight loss of 16%. The WR remains at 57% until the temperature increases to 723 ℃. 23% of the sample weight is lost when the sample is further heated up to 823 ℃. Finally, the WR remains constant until the end of the temperature programme. If the Li(OAc) did not react with Pt/C, the trend of weight loss would be similar to that of the $Li(OAc)\cdot 2H_2O$, excluding the dehydration process.

The difference between the TGA profiles of $Li(OAc)\cdot 2H_2O$ and the $Li(OAc)\cdot 2H_2O$-Pt/C mixture can be explained by reaction of the Li species with Pt/C. Nevertheless, despite the fact that the TGA suggests that a chemical reaction might take place between the $Li(OAc)\cdot 2H_2O$

and the Pt/C at elevated temperatures, it is limited in its ability to elucidate how the Pt structure changes in terms of d-spacing and phase shift in the presence of the Li species. Therefore, utilisation of an X-ray scattering technique is the key to answering this question.

6.4 X-Ray Diffraction (XRD)

XRD is one of the most conventional analytical techniques which provides primary crystallography information in terms of the d-spacing, unit cell dimensions and phase identification. 20 wt% Pt/C with $Li(OAc)\cdot 2H_2O$ was ground by mortar and pestle, and the obtained mixture was heated at a range of temperatures under a N_2 environment, with a ramping rate of 15 ℃/min. After cooling down, the mixture was immediately transferred to the sample holder and then characterised with XRD.

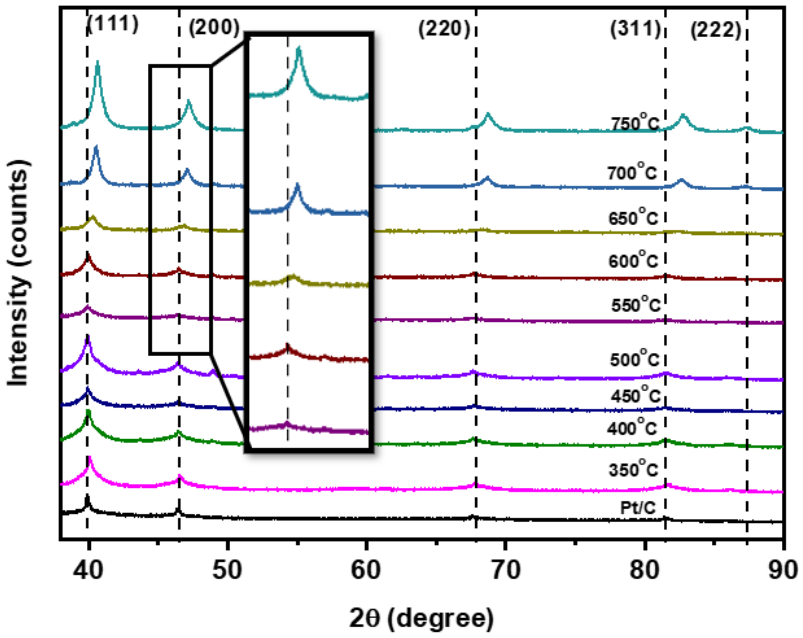


Figure 6.3. Ex-situ XRD profiles of heating 20 wt% Pt/C + $Li(OAc)\cdot 2H_2O$ at different temperatures for two hours under a N_2 atmosphere. Mixtures were characterised with XRD after heating at 350, 400, 450, 500, 550, 600, 650, 700, 750 ℃, without vacuum filtration treatment. The inset shows an example that diffraction peaks of Pt shift to a higher angle when the temperature is at 650 ℃. The peaks labelled with dash lines corresponding to the Pt (111), (200), (220), (311) and (222) are characteristics of the Pt face-centred cubic (FCC) structure.

As presented in Figure 6.3, the Pt diffraction peaks located at (111), (200), (220), (311) and (222) index do not shift between 350 and 600 ℃. When the temperature rises to 650 ℃, the diffraction peaks (111), (200), (220), (311) and (222) shift to higher angles, which can be

demonstrated in Table 6.2. The diffraction peak (111) shifts from 39.88° to 40.50°; the diffraction peak (200) shifts from 46.42° to 47.06°; the diffraction peak (220) shifts from 67.56° to 68.57°; the diffraction peak (311) shifts from 81.33° to 82.53°; and the diffraction peak (222) shifts from 86.20° to 87.08°. According to Bragg equation, the d-spacing corresponding to each diffraction index contracts from $2.258_{(111)}$ to $2.224_{(111)}$ Å; $1.9538_{(200)}$ to $1.928_{(200)}$ Å; $1.385_{(220)}$ to $1.367_{(220)}$ Å;$1.182_{(311)}$ to $1.167_{(311)}$ Å and $1.127_{(222)}$ to $1.117_{(222)}$ Å.

Table 6.2. Data of XRD patterns of Pt before/after thermal calcination at 650 ℃ after 2 hours, in the presence of the $Li(OAc)\cdot 2H_2O$.

Pt diffraction angle 2θ (°) before thermal calcination	***h k l***	**d-spacing (Å)**	**Pt diffraction angle 2θ (°) after thermal calcination**	**d-spacing (Å)**
39.88	111	2.258	40.50	2.224
46.42	200	1.9538	47.06	1.9280
67.56	220	1.385	68.57	1.367
81.33	311	1.182	82.53	1.167
86.20	222	1.127	87.08	1.117

However, various effects can result in the movement of the diffraction peaks, such as instrumental artifacts,[14] variations in the crystalline phase/structure,[15] thermal annealing *etc*.[16] The instrumental artefacts effect can be excluded because the diffraction peaks do not shift by the same amount to the higher angle. Literature shows that CeO_2 after thermal annealing treatment can crystallise so that the diffraction peaks shift slightly to a higher degree.[16] Therefore, it is essential to perform a control experiment for further comparisons.

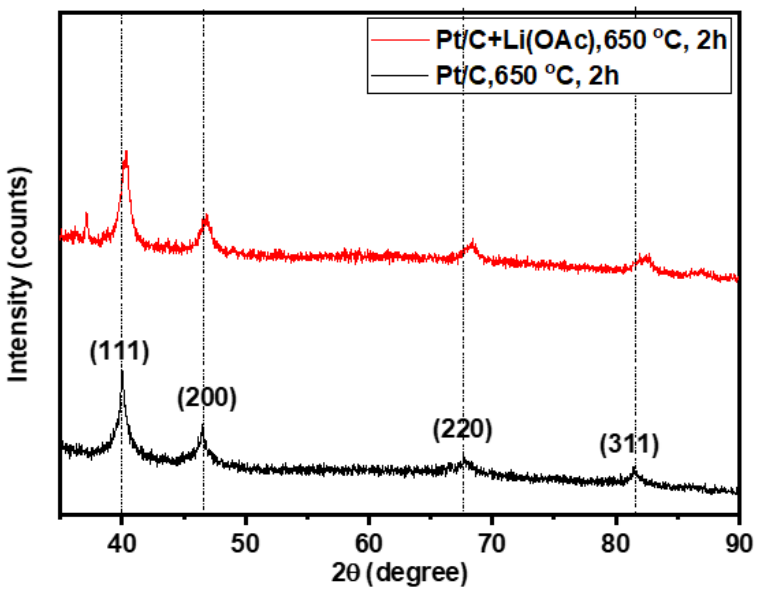


Figure 6.4. Ex-situ XRD profiles of 20 wt% Pt/C and 20 wt% Pt/C + Li(OAc)·2H_2O after thermal treatment at 650 °C for 2 hours under a N_2 environment. The collected sample was characterised by XRD without vacuum filtration treatment. The peaks labelled with dash lines corresponding to the Pt (111), (200), (220), (311) and (222) are characteristic of the Pt face-centred cubic (FCC) structure.

Commercial 20 wt% Pt/C and the mixture of the 20 wt% Pt/C + Li(OAc)·2H_2O were calcined at 650 °C for two hours respectively and then analysed by XRD. As illustrated in Figure 6.4, the diffraction peaks of Pt (111), (200), (220), (311) and (222) also shift in the right direction but to different degrees, in comparison with Pt. Hence, the reason for the diffraction peaks movement is not attributed to the thermal annealing. In parallel to the XRD characterisation, an ICP-MS measurement was carried out, and the atomic ratio of Pt:Li was approximately 1:1. Therefore, it can suggest that Li can be alloyed to the Pt NPs host system and give rise to the formation of a new phase. However, even though ICP technique can provide the atomic ratio of Pt:Li, it cannot further distinguish the ratio of individual Li-containing species. This means the presence of the unreacted Li precursors, such as Li_2O or $L_{i2}CO_3$ can also contribute to the atomic ratio of Pt:Li, resulting in an overestimation of Li content. Moreover, contraction of the d-spacing is contradictory to the observation of Pd-^{int}Li/C and Pd-^{int}B/C XRD in Chapters 4 and 5, which means that the structure might differ to that of the Pd-^{int}Li/C and Pd-^{int}B/C. Due to the resolution limitation of the lab source X-ray, it is challenging

to retrieve structures accurately from the XRD profile. In order to identify the potential crystal structure, an advanced X-ray scattering technique is required for the next step.

6.5 Synchrotron X-Ray Diffraction (SXRD)

With the advent of the synchrotron incident X-ray source, high resolution and high-quality diffraction data can be generated. In a combination of the complementary TOPAS refinement software,[17] quantitative structure information can be retrieved from the synchrotron X-ray powder diffraction (SXRD) datasets.[18] In Chapters 4 and 5, the use of SXRD and its complementary retrieved refinement elucidated the average structure of Pd-^{int}B/C and Pd-^{int}Li/C. Herein, such methodology was utilised again to propose the general crystal structure of the Pt-Li/C NPs system.

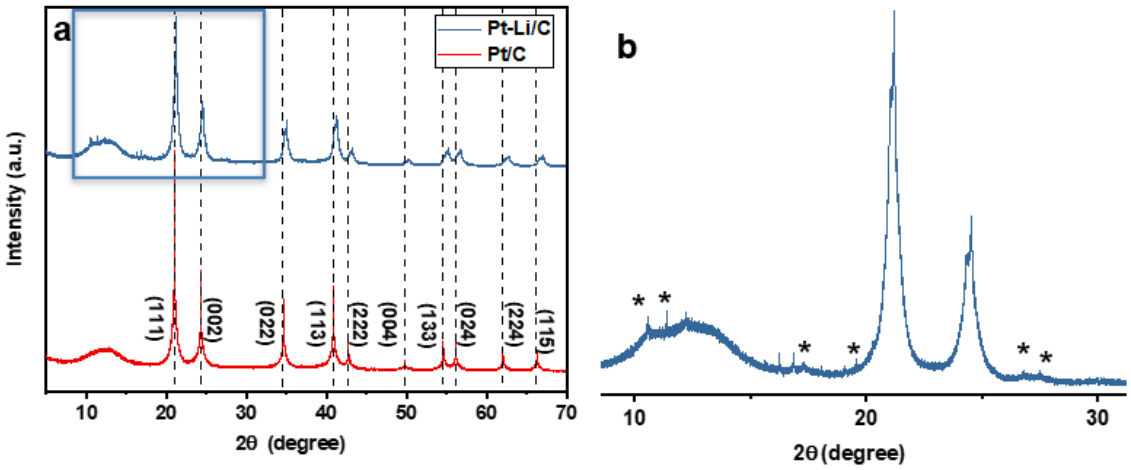


Figure 6.5. (a) SXRD profiles of 20 wt% Pt/C and 20 wt% Pt-Li/C. (b) shows the enlarged diffraction patterns at the range of 8 to 32° enlarged from the inset annotated with blue square. * is used to label the peaks locating at 10.5º, 12.2°, 17. 2°, 20.23°, 26.7° and 27.3°, which are corresponding to the index of (111), (002), (022), (113), (133), (024) of the Pt_7Li, respectively.

Figure 6.5 is the SXRD profile of 20 wt% Pt-Li/C and 20 wt% Pt/C. Utilisation of the TOPAS-Academic V5.0 refinement, the Pt/C diffraction patterns were analysed by the Rietveld method to understand how crystal structure influences these diffraction patterns. The R-factors ($R_{wp}/R_p/R_{exp}/\ \chi 2$) were utilised to gauge the quality of the refinement.

Table 6.3. R-factors of Pt/C sample by Rietveld method.

Phase	Rietveld R_{wp} / R_p / R_{exp} / $\chi 2$ (%)
Pt/C_{single}(*Fm-3m*)	11.22/2.65/2.85/15.4
Pt/C′ (*Fm-3m*); Pt/C″ (*Fm-3m*)	7.66/5.22/5.960/1.65

As illustrated in Table 6.3, the pure Pt model (crystal structure: FCC; space group: *Fm-3m*) with lattice parameter $a = b = c = 3.92390$ Å) was introduced to fit the observed patterns of Pt/C. However, no single phase fits the peak well in accordance with the large R-factors even if the lattice parameter is adjusted to 3.9213(3) Å. Therefore, two phases (packing structure: FCC; space group: *Fm-3m* with lattice parameter $a = b = c = 3.9208(7)$ Å and lattice parameter $a = b = c = 3.9229(9)$ Å) were introduced to fit the experimental profile progressively (Table 6.4). The R_w value reduced to 7.66%, which indicates that the number of phases approaches the real structure.

Table 6.4. Summary of space group and lattice parameters for the structure of the 20 wt% Pt/C retrieved by TOPAS refinement.

Phase	Crystal structure	Space group	Structural information	Composition/wt%
Pt/C′	FCC	*Fm-3m*	$a' = b' = c' = 3.9208(7)$ Å	81.135
Pt/C″	FCC	*Fm-3m*	$a'' = b'' = c'' = 3.9229(9)$ Å	18.865

As depicted in Table 6.4, the Pt lattice parameter of the metallic NPs in both phases contracts in comparison with the literature value of bulk Pt (3.9242 Å), which is the consequence of the particle size effect.[19,20] The Rietveld method can also provide the relative composition ratio of these two phases with a slight difference in lattice parameter (Table 6.4). The Pt/C′ (lattice parameter $a' = b' = c' = 3.9208(7)$ Å) phase dominates 81wt% of the sample, while the Pt/C″ phase ($a'' = b'' = c'' = 3.9229(9)$ Å) occupies the remaining 18%. Pt NPs with smaller particle size could result in a smaller lattice parameter, in accordance with work by

Dmitrev *et al.* on X-ray diffraction analysis and theoretical considerations.[20] These refinement results reveal that particle size distribution is relatively broad, but smaller particles dominate.

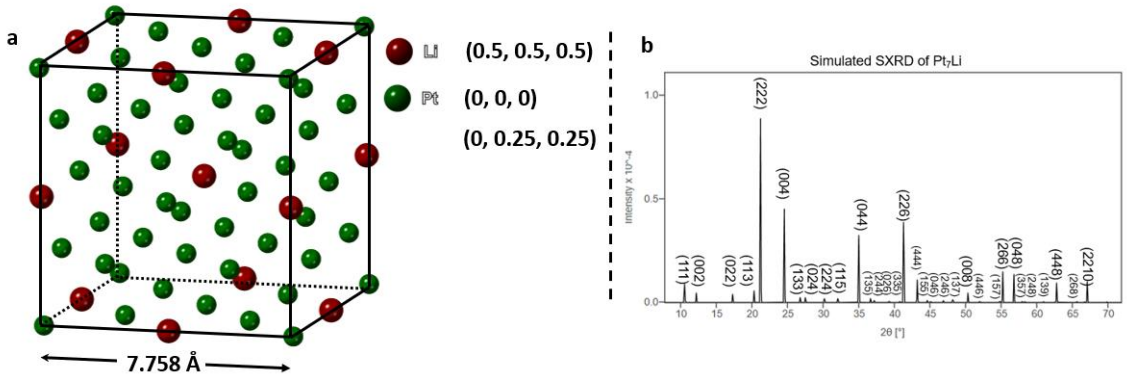


Figure 6.6. (a) Structure of Pt_7Li in which the atomic arrangement of Pt is (0, 0, 0) and (0, 0.25, 0.25), and the atomic arrangement of Li is (0.5, 0.5, 0.5).[3,4] (b) Simulated SXRD of Pt_7Li based on the experimental setting in the Diamond Light Source I11 beamline with the incident wavelength of 0.825300 Å.

In comparison with pure Pt diffraction patterns, diffraction peaks of the Pt-Li sample exhibit broadening and shift to a higher degree by different amounts. Additionally, some small peaks are located at the 10.5°, 12.2°, 17.2°, 20.23°, 26.7° and 27.3° in the low angle region (the range of 0 to 35º), as depicted in Figure 6.5b. To identify the origin of the diffraction patterns, the unit cell of various Pt-Li based compounds was established and then the corresponding SXRD simulations were attempted using 'Crystal Maker' powder diffraction software, and the instrumental parameter was applied based on the experimental setting in the Diamond Light Source I11 beamline with the incident wavelength of 0.825300 Å. It was found that the simulated SXRD of the Pt_7Li (see Pt_7Li structure in Figure 6.6a) depicted in Figure 6.6b contains low-intensity indexes located at $10.5°_{(111)}$, $12.2°_{(002)}$, $17.2°_{(022)}$, $20.23°_{(113)}$, $26.7°_{(133)}$ and $27.3°_{(024)}$, which is consistent with the experimental SXRD profile. This result suggests that this samples contained the phase of Pt_7Li. With the confidence of the simulated results on hand, the structure of the Pt-Li/C sample was then retrieved by the Rietveld method. Two phases (Pt-Li/C: *Fm-3m*, lattice parameter $a = b = c = 3.88964(3)$ Å; Pt_7Li: *Fm-3m*, lattice parameter $a = b = c = 7.76018(8)$ Å, seen in the structure of Pt_7Li in Figure 6.6a) were

introduced to the program. The input of the Pt_7Li model can fit the major diffraction patterns at 21.2°, 24.5°, 35.0°, 41.3°, 43.2°, 50.398°, 55.2°, 56.6°, 62.5° and 67.1° which are the characteristic index of (222), (004), (044), (226), (444), (008), (266), (048), (448) and (2210) respectively, in addition to establishing a good fit for the aforementioned indexes of (111), (002), (022), (113), (133) and (024).

Table 6.5. R-factors of 20 wt% Pt-Li/C sample by Rietveld method.

Phase	**Rietveld** R_{wp} / R_p / R_{exp} / $\chi 2$ **(%)**
Pt-Li/C (*Fm-3m*); Pt_7Li (*Fm-3m*)	7.67/5.49/5.96/1.64

As shown in Table 6.5, Once two phases are introduced, the fitting result approaches the real structure, as assessed by the R_{wp} / R_p / R_{exp} / $\chi 2$ **(%)** value. The summary of space groups and lattice parameters for the structure of the Pt-Li system retrieved by the TOPAS refinement is demonstrated in Table 6.6. The lattice parameter of the Pt_7Li phase is analogous to that of bulk Pt_7Li (7.758 Å) reported in the literature.[5] It is also worth noting that the structure of Pt_7Li is very similar to pure Pt. The space group remains unchanged from *Fm-3m* and the packing can be recognised as typically FCC. The lithiation of pure Pt to Pt_7Li can be described as a topotactic phase transition, in which one in eight Pt atoms are substituted by Li atoms as they have very similar atomic radii (lithium 176 pm and platinum 177 pm), and are expected to result in the favourable substitution.[21,22] From the fitting, the lattice parameter of the Pt-Li phase in the 20 wt% Pt-Li/C is 3.8896(4) Å, which is slightly smaller than the conventional Pt lattice parameter (3.9208(7) Å). Additionally, it can be found that lattice parameter of the Pt-Li phase in the 20 wt% Pt-Li/C is approximately half (a_{Pt_7Li} = 7.76 Å vs. $2\times a_{Pt\text{-}Li}$ = 7.85 Å) the lattice parameter of Pt_7Li. It is anticipated that the change in lattice parameters is the direct result of the incorporation of lithium into these nanoparticles and the Pt-Li phase is actually the sub-structure of the Pt_7Li supercell (Figure 6.7). On the other hand, since the structure of

other Li-rich Pt species were not found in accordance with the result of SXRD refinement, it clearly reveals that the former atomic ratio of Pt : Li (1:1) obtained from ICP analysis is not accurate enough, since this is a bit larger than that from the SXRD fitting. The sample contained unreacted Li_2CO_3 and/or Li_2O compounds, as confirmed by the ^7Li ssNMR (see section 6.8).

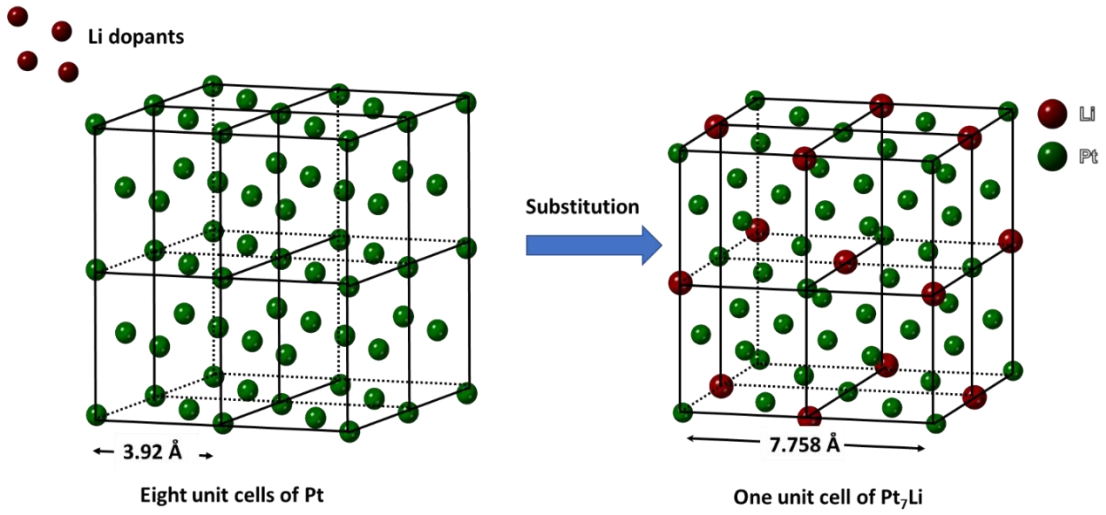


Figure 6.7. A schematic shows the Pt/C is substituted by foreign Li dopants to generate Pt_7Li, despite this is an interstitial intermetallic compound on the basis of the Li location.

Table 6.6. Summary of space group and lattice parameters for the structure of the 20 wt% Pt-Li/C retrieved by TOPAS refinement.

Crystal structure	Space group	Structural information	Composition/wt%
Pt-Li/C	*Fm-3m*	$a = b = c = 3.8896(4)$ Å	96.533
Pt_7Li	*Fm-3m*	$a = b = c = 7.7601(9)$ Å	3.467

By working out the total scattering generated from the unit cells of the individual phases, the composition ratio (mass percentage) of the Pt-Li/C and Pt_7Li phases can be estimated (Table 6.6). The Pt-Li/C is the dominant phase, which accounts of 96.533%, while the rest of the composition is Pt_7Li, which is about 3.467%. To date, the SXRD refinement suggests that most of the Pt_7Li NPs are highly distorted and hence break up the high symmetry of the crystal structure. This could be a consequence of inhomogeneous lithiation or a certain degree of

amorphization in NPs, leading to a loss of long-range order as observed in SXRD for Pt_7Li NPs.

6.6 Neutron Diffraction

Despite the fact that SXRD in combination with the TOPAS refinement can help to suggest the presence of Li, it is essential to obtain further verification by using other techniques. Since neutron diffraction is sensitive to light elements, it is expected that carrying out a neutron diffraction measurement can probe the Li or Li-containing phases. The neutron diffraction for the time-of-flight (TOF) neutron profiles measured for the 20 wt% Pt/C and 20 wt% Pt-Li/C are presented in Figure 6.8. The indexes, (115), (224), (024), (133), (222), (113), (022), (002) and (111), labelled in black correspond to the Pt phase and the indexes (121), (002), (020), labelled in brown correspond to the C phase.

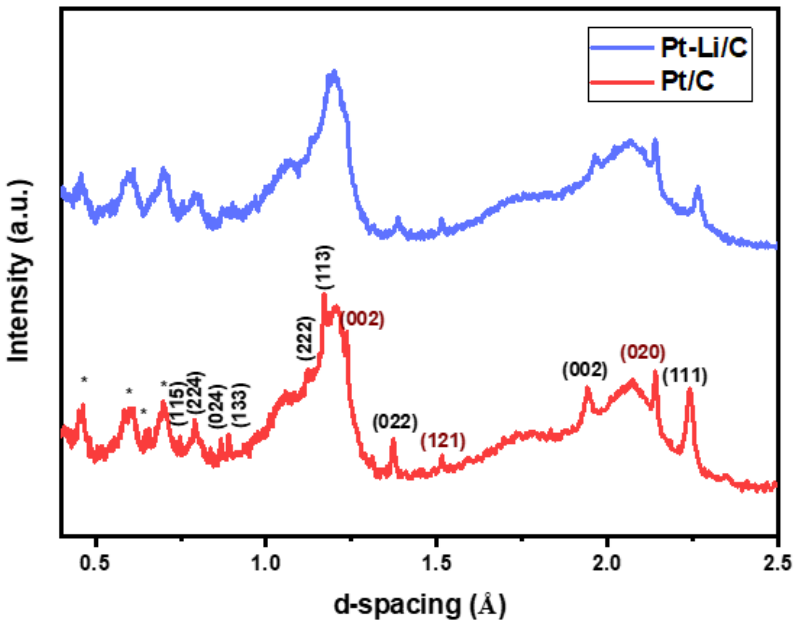


Figure 6.8. Neutron diffraction for the TOF neutron profiles over the 20 wt% Pt/C (red) and 20 wt% Pt-Li/C (blue). The Pt phases corresponding to the individual spacing are annotated in black. * means unknown diffraction phases. The peaks at 2.1390, 1.5108 and 1.2190 Å area anticipated as the phases of the BCT carbon, based on ref. 23.

In comparison to the TOF neutron profile of the 20 wt% Pt/C, no reliable new phases are found in this spectrum (Figure 6.8). This observation may be explained by the fact that the

absorption cross-section of Li (70.3 barn) is approximately seven times larger than Pt (10.3 barn),[24] which means that the nucleus of Li has a higher probability to absorb a neutron as it travels through the material. Therefore, it is reasonable to suggest low accuracy of phase segregation is due to the higher degree of adsorption of neutrons on Li.[25] Also, the resolution of the diffraction peaks is affected by diffuse scattering, so the Pt diffraction patterns after lithiation shift in opposite directions. Therefore, other spectroscopic techniques are needed to further confirm the presence of the Li.

6.7 X-Ray Photoelectron Spectroscopy (XPS)

So far, the X-ray scattering technique has proposed some basic structural information about the Pt-Li system but still requires additional solid evidence to confirm. XPS is one of the most conventional spectroscopic techniques which can offer the surface information of the sample in terms of surface compositions, and chemical/electronic states. XPS survey spectra are displayed in Figure 6.9a, and show signals of Pt 4f, 4d, C1s and O1s.

The area annotated with a green square shows an enlarged spectrum in the range of 45 to 67 eV. As illustrated in Figure 6.9b, a weak signal located at 52 eV is detected from the Pt/C sample, which is ascribed to the Pt-5p species. In contrast, the 20 wt% Pt-Li/C sample displays a much more intense signal. This is presumably due to high dispersion of the Pt-Li NPs on the carbon support, as illustrated by the TEM-BF image in the appendix (Figure 8.17), which can make a contribution to enhance the signal to noise ratio.[26] The binding energy peak of pure metallic Li is located at 55.6 eV,[27] but the signal profile starts from 50 eV, which is adjacent to the Pt 5p signal. However, the ICP-MS measurement, as mentioned above, has already shown the presence of the Li species with an identified atomic ratio of Pt to Li. Therefore, it can be concluded that the Li 1s signal is superimposed on that of Pt 5p, leading to a broad signal profile.

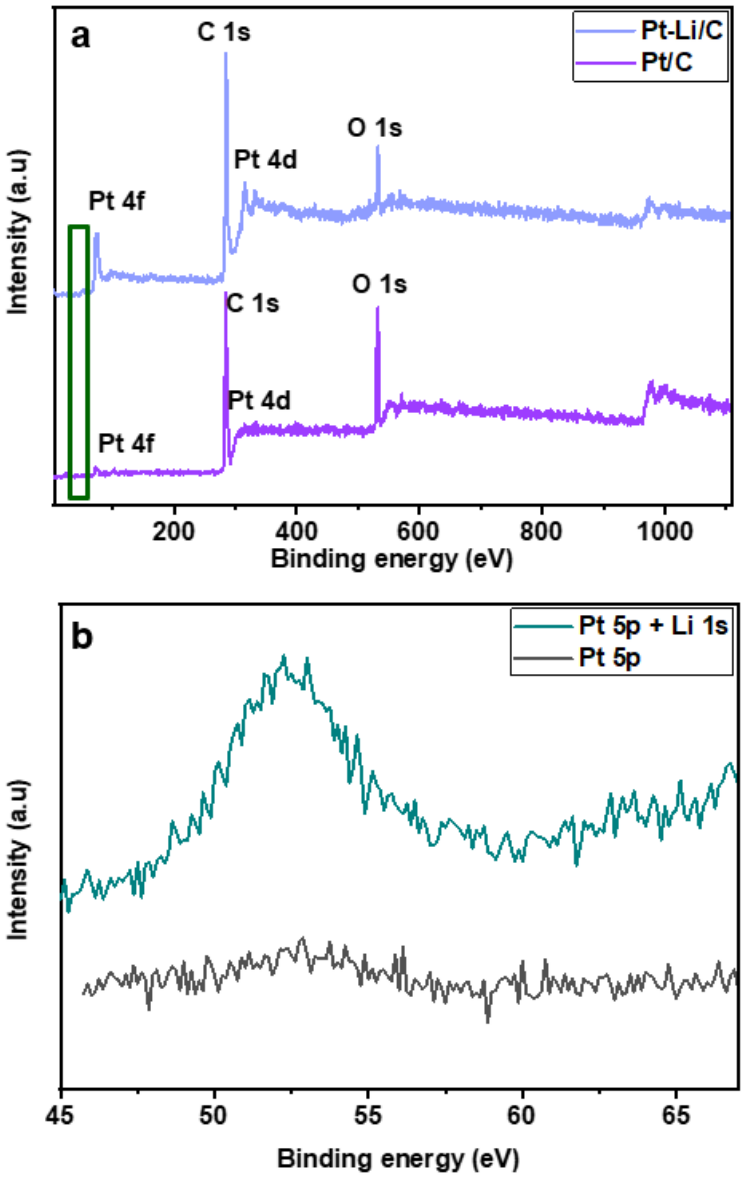


Figure 6.9. XPS profile of 20 wt% Pt/C and 20 wt% Pt-Li/C. (a) A survey spectrum from the surface of the 20 wt% Pt/C and 20 wt% Pt-Li/C. (b) inset from (a) shows the enlarged spectrum at the range of 45 to 67 eV (annotated with green square). Peaks have been corrected based on the measurement of C1s.

Figure 6.10 demonstrates the XPS profiles of Pt $4f_{7/2}$,$_{5/2}$ over the 20 wt% Pt/C and 20 wt% Pt-Li/C samples. The Pt 4f XPS pattern of 20 wt% Pt/C has two convoluted peaks located in 72.1 eV and 75.3 eV, respectively; the 20 wt% Pt-Li/C has similar peaks where the positions shift to the higher binding energies.

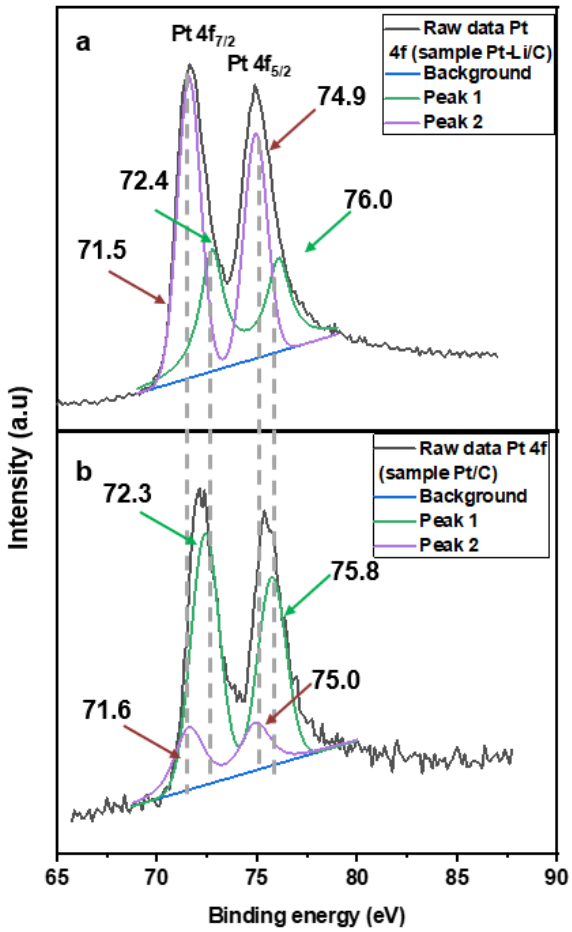


Figure 6.10. Pt 4f XPS profiles for (a) 20 wt% Pt-Li/C and (b) 20 wt% Pt/C.

To further identify the states of the Pt species, both spectra were deconvoluted into smaller doublets by using XPSpeak41 software. Data on XPS curve fitting and the relative integrated area are summarised in Table 6.7. For 20 wt% Pt/C, the deconvoluted spin-orbital doublet peaks at 71.6 eV, 75.0 eV and 72.3 eV and 75.8 eV can be ascribed to the Pt^0 and Pt^{2+} species, respectively.[28,29] PtO was formed during the preparation of the sample for XPS (exposure to the air). The relative integrated areas of Pt^0 and Pt^{2+} are 21.7% and 78.3%. The deconvoluted peaks of the 20 wt% Pt-Li/C 4f spectra are located in similar positions, 71.5 eV and 74.9 eV, and 72.4 and 76.0 eV. The peak shifting by 0.1 to 0.2 eV is too small to indicate the oxidation state variation of the Pt, and hence the deconvoluted peaks are ascribed to Pt^0 and Pt^{2+}. Nevertheless, the relative integrated area of Pt^0 and Pt^{2+} of the 20 wt% Pt-Li/C sample changes significantly in comparison to that of 20 wt% Pt/C. The relative integrated area of the Pt^0

species rises to 65.2% while that of the Pt^{2+} species rises to 34.8%. The composition ratio of PtO/Pt in 20 wt% Pt/C is 3.60, whereas that in 20 wt% Pt-Li/C is 0.53. This reveals that the major component of Pt-Li exists in the form of Pt^0 rather than Pt^{2+}. This result suggests that some of the Pt surface had been lithiated to passivate the Pt, or to protect the Pt surface from the formation of platinum oxide.

Table 6.7. Curve-fitting results of 20 wt% Pt/C and 20 wt% Pt-Li/C.

Catalyst	Pt Species			
	Species	$BF_{Pt}\,4f_{7/2}$(eV)	$BF_{Pt}\,4f_{5/2}$ (eV)	Relative integrated area%
20 wt% Pt/C	Pt^0	71.6	75.0	21.7
	Pt^{2+}	72.3	75.8	78.3
20 wt% Pt-Li/C	Pt^0	71.5	74.9	65.2
	Pt^{2+}	72.4	76.0	34.8

6.8 ^{7}Li MAS Solid State Nuclear Magnetic Resonance (ssNMR)

Results of the XPS analytical technique suggest that the Pt-Li/C sample contains either surface-covering Li species, or the Pt-Li alloy or both. ^{7}Li MAS ssNMR is a powerful technique to demonstrate Li chemical environments from short-range to long-range. In order to identify the chemical environment, the mixture of 20 wt% Pt/C and $Li(OAc)\cdot 2H_2O$ before/after thermal treatment was studied by ^{7}Li MAS ssNMR, as displayed in Figure 6.11.

Figure 6.11a depicts the ^{7}Li MAS ssNMR of $Li(OAc)\cdot 2H_2O$–Pt/C mixture before thermal treatment. There is a narrow peak located at -1.39 ppm, which coincides with the chemical shift of the commercial $Li(OAc)\cdot 2H_2O$. After thermal treatment at 650 °C for two hours, followed with vacuum filtration, a doublet starting from 10.0 ppm to -30.0 ppm is seen, which can be further deconvoluted into two peaks located at -0.1 and -9.9 ppm, respectively (Figure 6.11b).

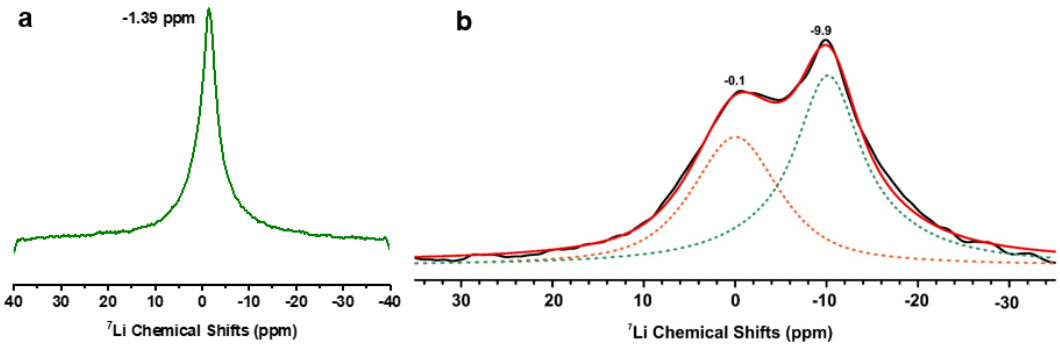


Figure 6.11. ^{7}Li MAS ssNMR chemical shifts of 20 wt% Pt/C and Li(OAc)·2H_2O before and after thermal treatment. (a) 20 wt% Pt/C and Li(OAc)·2H_2O before thermal treatment. The peak located at -1.39 ppm is attributed to the Li(OAc)·2H_2O. (b) 20 wt% Pt/C and Li(OAc)·2H_2O after thermal treatment. The obtained sample was washed with EtOH and water to remove the unreacted Li species and Li based side products before measurement. The signal can be deconvoluted into two peaks. One is located at -0.1 ppm, and the other is located at -9.9 ppm.

From reference to the literature, the chemical shift of conventional lithium sources is displayed in Table 6.8,[30,31] in which peaks at -0.1 ppm can be assigned to Li_2CO_3, which is reasonable to assign as the Li surface species. On the basis of the SXRD refinement, it is reasonable to assume that the signal at -9.9 ppm could be attributed to the Li in the Pt phase. However, due to the limitation of the 1D-NMR resolution, it is essential to use ^{195}Pt MAS ssNMR,[32] 2D-NMR or other techniques for further verification.

Table 6.8. ^{7}Li MAS ssNMR of conventional lithium species.

Conventional Li Chemical species	Chemical shifts (ppm)
Li_2O	2.8
$LiOH{\cdot}H_2O$	0.4
Li_2CO_3	0.0

6.9 Electron Energy Loss Spectroscopy (EELS)

EELS characterisation was also performed to detect the Li species and their chemical states. The EELS study of the 20 wt% Pt/C and 20 wt% Pt-Li/C is displayed in Figure 6.12. The

resolution is 0.95 eV, according to the FWHM of the ZLP peak (Chapter 8 Appendix Figure 8.18). However, the EELS spectrum, as depicted in Figure 6.12c and f looks similar. Both of the EELS spectra show a convincing Pt-$O_{2,3}$ edge (starting from 52 eV) and Pt-$N_{6,7}$ edge (starting from 71 eV), but the Li-K edge (starting up from 55 eV) is not visible. Because of the absence of the monochromator, the adjacent Pt-$O_{2,3}$ edge might have swamped the abrupt Li-K edge, rendering it invisible.

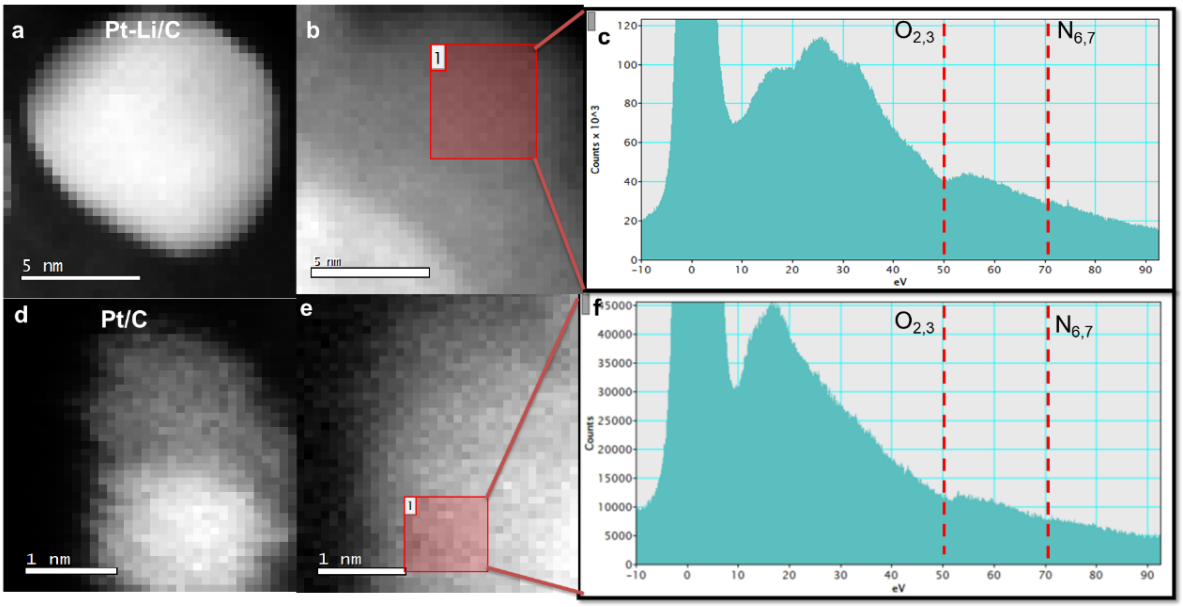


Figure 6.12. EELS study of 20 wt% Pt/C and 20 wt% Pt-Li/C. (a) ADF image of 20 wt% Pt-Li/C NP, where EELS spectra were taken along each pixel of the selected area. (b) EELS spectra image of the 20 wt% Pt-Li/C NP. (c) EELS spectra of the selected square in EELS spectra image (b). (d) ADF image of 20 wt% Pt/C NP, where EELS spectra were taken along each pixel of the selected area. (e) EELS spectra of the 20 wt% Pt/C. (f) EELS spectra of the selected square. The locations of the Pt low loss edge, $O_{2,3}$ and $N_{6,7}$, are annotated with the red dash line.[33]

Although direct visualisation of the Li signal was not possible, it was found that the plasmon region of the 20 wt% Pt-Li/C EELS spectrum differs to that of the pure 20 wt% Pt/C. This could be ascribed to the fact that the presence of the Li changes the overall electronic structure of the Pt, giving rise to a different plasmon profile.[34] However, an intensive investigation is still required to exclude other contributions since composition,[35] strain,[35,36] shape[37] and particle size[38] can also result in customisation of the plasmon profile.

6.10 Simultaneous Annular Dark Field (ADF) and Ptychographic Imaging

Aberration-corrected electron microscopy was for the first time employed to directly visualise the structure of the NPs at the atomic level. Additionally, it is a benefit of the fast pixelated ptychographic technique that the ADF imaging and ptychographic datasets at the atomic level could be acquired simultaneously.

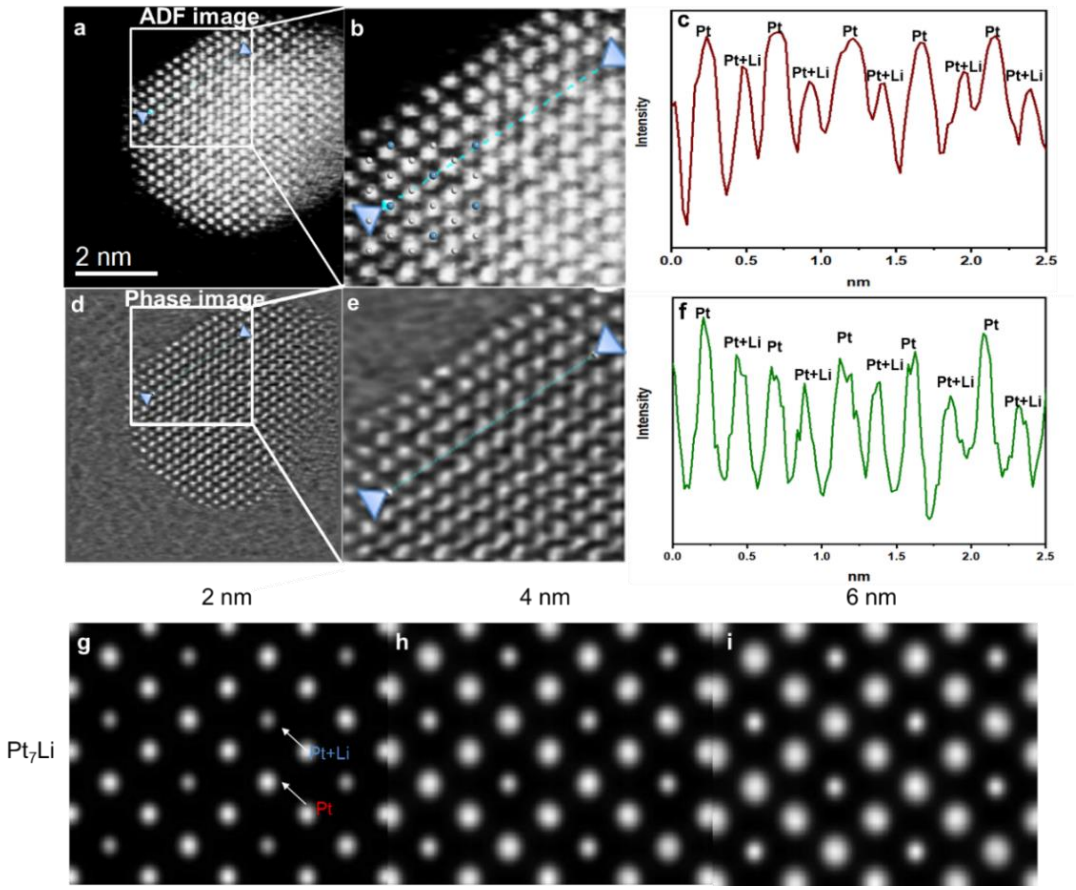


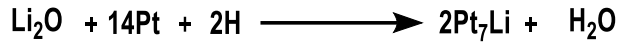
Figure 6.13. Simultaneously acquired Z-contrast STEM-ADF, ptychographic phase images of 20 wt% Pt-Li/C NPs without miss-tilt. (a) Z-contrast STEM-ADF image of 20 wt% Pt-Li/C NP orientated in the <110> zone axis. (b) Inset from (a) highlights an enlarged area of the NP. Pt_7Li orientated in the <110> direction is superimposed with the inset, demonstrating a good match between the Pt_7Li model and the NP structure. Mixed Pt and Li atoms are annotated with blue dots and Pt atoms are annotated with gray dots. (c) ADF intensity line profile taken along the line is indicated in (a). (d**)** Ptychographic phase image was reconstructed by using a Wigner Distribution Deconvolution (WDD) method.[39] (e) Inset from (d) does not show any new contrast between the Pt atomic columns. (f) Ptychography phase image intensity line profile taken along the line is indicated in (e). (h), (i) and (j) are the ADF image simulations of the Pt_7Li over different thicknesses. Pt columns are annotated with red and Pt-Li columns are annotated with blue.

Figure 6.13a shows a typical Z-contrast STEM-ADF image of the 20 wt% Pt-Li/C NP with a thickness of 5.85 nm (see Chapter 8 Appendix Figure 8.19), orientated in the <110> direction.

Owing to the rule of the Z-contrast, only heavy element (Pt) atomic columns can be visible in the ADF image because of the much stronger scattering. However, it can be found that some of the Pt atomic columns are less bright than others. Initially, the ADF image was compared with Pt_7Li to resolve the structure of the NP. When the image is superimposed to the crystal structure of the Pt_7Li orientated in the <110> direction, a good match was found between the model and the NP structure. Owing to the rule of the ‘‘Z-contrast’’, the intensity of the ADF image is highly dependent on the atomic number. The presence of the Li gives much weaker scattering, which can be supported by the intensity profile analysis of the ADF image (Figure 6.13c) taken from the indicated line (Figure 6.13b). The restored phase image does not show any unusual contrast in accordance with the line profile (Figure 6.13e and f), which is indistinguishable from the ADF image.

To confirm the validity of the STEM-ADF result, simulated STEM-ADF image of the Pt_7Li was computed over different thicknesses, as depicted in Figure 6.13g, h, i. These simulated images show that the total integrated intensity of the Pt columns is much higher than the adjacent Pt columns which contain Li atoms. Therefore, there is the compelling evidence for Li being substituted into the original position of the Pt, leading to the formation of the Pt_7Li. Pt_7Li can be classified as an interstitial alloy, as the location of the Li is at (0.5, 0.5, 0.5) between the lattice sites of Pt. However, as indicated in section 6.5, the Pt atom located at the vertex of the Pt unit cell is replaced with the foreign Li atom after reaction. Therefore, the Li is clearly in the substitution site. Additionally, on the basis of the above results and previous description in TGA session, a reaction mechanism can be proposed for the formation of the Pt_7Li. The thermal decomposition of the $Li(OAc)\cdot 2H_2O$ can give intermediate Li_2CO_3 which might further decompose to a finely divided oxide, Li_2O, when temperature increases. Elevated temperatures can promote this process to accelerate the slow diffusion of ions in the solids and to overcome the strong coulombic attractions between the ions. Subsequently, Li_2O could exchange with Pt,

in the presence of the hydrogen source, which is expressed in Scheme 6.1.[5] The origin of the hydrogen source is expected to come from the wet impregnated solvent, EtOH and/or crystal water of $Li(OAc)\cdot 2H_2O$.



Scheme 6.1. Proposed reaction scheme for the formation of Pt_7Li.

As stated in Chapter 1, the principle of categorizing mixed alloys into intermetallic compounds or solid solution alloys is dependent on whether the space group remains the same or not. In light of the SXRD refinement result, the major composition is Pt-Li, and the space group of Pt after lithiation remains the same despite contraction of the lattice parameter. Overall, with the ADF image in combination with the SXRD refinement and spectroscopic result in hand, it can be concluded that the mixture of the Pt/C NPs and $Li(OAc)\cdot 2H_2O$ after thermal treatment at elevated temperature can yield a Li-substituted Pt solid solution nanoalloy (Pt-^{sub}Li).

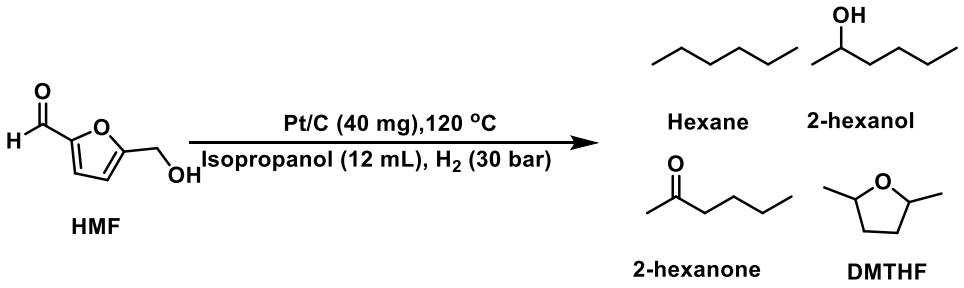
6.11 Catalytic Testing in the Hydrogenation of HMF

HMF, the main compound extracted from cellulosic biomass, is a promising alternative to the traditional petroleum-based feedstock. The furan ring contains a hydroxyl and a carbonyl group, making it reactive to further catalytic processes such as hydrogenation,[40] oxidation,[41] decarbonylation[42] and etherification.[43] Nevertheless, HMF can undergo aldol addition and self-condensation reactions to generate side products, humins, under acidic condition.[44,45] The direct use of HMF is still restricted by several issues. For example, large scale production of HMF is limited by the isolation and purification from the reaction mixture.[46,47] Despite the selective hydrogenation of HMF can yield various useful commercial products, such as BHMF,[47] DMF[48] *etc*, undesired side reactions can happen as well.[49]

As demonstrated in Chapter 8 Table 8.1, catalytic performances of 5 wt% Pd/C, 5 wt% Pd-

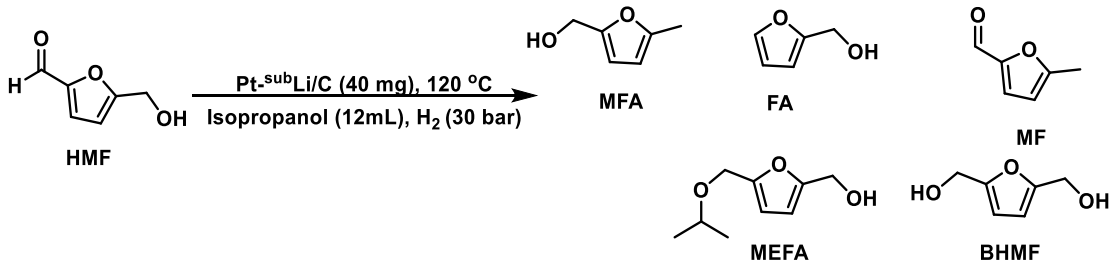
^{int}Li/C, 5 wt% Pd-^{int}B/C are compared in hydrogenation of HMF at 120 °C and in 30 bar of H_2 for two hours. A full conversion of HMF can be achieved by 5 wt% Pd/C, accompanied with 62% selectivity of 2,5-dimethylfuran (DMF), 35% selectivity of 2,5-dimethyltetrahydrofuran (DMTHF) and a trace amount of hexanone (<1%). Yet the Pd NPs after incooperation of B or Li dopants deaccelerated the conversion of the HMF, leaving a board distribution of intermediates. Despite the conversion slowed down in the presence of 5 wt% Pd-^{int}B/C, the selectivity for value-added chemicals, DMF or BHMF was retained. In contrast, 5 wt% Pd-^{int}Li/C can achieve the product selectivity of BHMF with 68%, but the conversion of HMF was much slower in comparison with catalytic result of 5 wt% Pd-^{int}B/C. Hence, it is expected that the Li-alloyed Pt catalyst can inhibit the reaction pathways that form side products and enhance the target product selectivity. Isopropanol (IPA) was used as the solvent, due to its hydrogen donating properties.[50,51,52,53]

Primary catalytic testing on the hydrogenation of HMF with 20 wt% Pt-^{sub}Li/C (Pt:Li(OAc)·2H_2O = 1:1 molar equiv.) and 20 wt% Pt/C were performed at 120 ℃ and in 30 bar of H_2 for two hours. The results are displayed in Table 6.9. Pt/C mainly promoted hydrodeoxygenation (HDO) and ring opening of the HMF, leading to a range of products. GC-MS analysis of the reaction mixture (Scheme 6.2) showed the typical product distribution consists of hexane, 2-hexanol, 2-hexanone and a DMTHF. In addition to these products, there were still some unknown byproducts formed.



Scheme 6.2. Products obtained after hydrogenation of HMF with 20 wt% Pt/C after 2 hours in IPA (isopropanol). Typical products are hexane, 2-hexanol, 2-hexanone and DMTHF.

In contrast, 20 wt% Pt-^{sub}Li/C NPs (Pt: Li(OAc)·2H_2O = 1:1 molar equiv.) can achieve nearly full conversion and result in higher selectivity despite the broader product distribution. GC-MS analysis of the reaction mixture (Scheme 6.3) showed the typical production distribution consists of 5-methyl furfuryl alcohol (MFA); furfuryl alcohol (FA); 5-[(1-methylethoxy)methyl]-2-furanmethanol (MEFA); 2,5-Bis(hydroxymethyl)furan (BHMF); 5-methyl furfural (MF). MFA and MEFA were found as the major side products. What is more, the selectivity toward BHMF was significantly enhanced, standing at around 60%.



Scheme 6.3. Products obtained after hydrogenation of HMF with 20 wt% Pt-^{sub}Li/C after 2 hours in IPA. Compounds: 5-methyl furfuryl alcohol (MFA); furfuryl alcohol (FA); 5-[(1-methylethoxy)methyl]-2-furanmethanol (MEFA); 2,5-Bis(hydroxymethyl)furan (BHMF); 5-methyl furfural (MF).

In order to optimise the selectivity of the BHMF and understand the catalytic role of Li, 20 wt% Pt/C was lithiated with Li(OAc)·2H_2O with different loadings at 650 ℃ for two hours and then was tested in the hydrogenation of HMF. The introduction of 0.5 molar equiv. of Li additives resulted in the selectivity of BHMF increasing to approximately 99%. The 20 wt% Pt/C loaded with 0.25 molar equiv. of Li additives achieved similar selectivity to BHMF, but the conversion decreased to 84%. Apparently, as compared to the fresh Pt commercial catalyst, the Li-alloyed Pt/C NPs displayed a much lower tendency to undergo the hydrodeoxygenation (HDO) reaction pathway, leading to almost-exclusive selectivity toward BHMF. As suggested by the literature,[54] the hydrogenation catalytic activity and selectivity of the NPs is critically governed by the location of the d band centroid of the metallic structure, ε_c, and the degree of electron filling with respect to the Fermi level. The upshift of the d-band centroid will increase the adsorption strength of the substrate whereas the degree of electron filling will reduce the

binding of the substrate. Viewed from the small change in lattice parameter, the anticipated effect of d-band shifting is weak. In contrast, being an electropositive element, Li can enhance the electron filling of the Pt d-band, resulting in weaker adsorption of HMF. This would result in lower catalytic activity but higher selectivity to the partially hydrogenated product, BHMF. Therefore, the observation matches with the theoretical prediction.

Table 6.9. Catalytic performances of 20 wt% Pt/C and 20 wt% Pt-^{sub}Li/C in the hydrogenation of HMF in IPA. Reaction conditions: [HMF] =0.126 g, T =120 °C; P = 30 bar; t = 2 hours.

Catalyst	Molar equiv. Pt:Li	HMF Conversion (mol%)	BHMF Selectivity (mol%)	MEFA Selectivity (mol %)	MFA Selectivity (mol %)	Other side product selectivity (%)
20 wt% Pt/C[a]	n/a	>99	<1	<1	<1	99[a]
20 wt% Pt-^{sub}Li/C	1:1	>99	60	9	30	<1[b]
20 wt% Pt-^{sub}Li/C	1:0.5	>99	99	<1	<1	<1
20 wt% Pt-^{sub}Li/C	1:0.25	84%	98	<1	<1	<1

[a] The main products of HMF hydrogenation in the presence of Pt/C are hexane, hexanol, 2-hexanone and DMTHF.

[b] Other side products includes FA and MF.

To date, it can be found that the presence of Li in the Pt metal lattice can significantly enhance the product selectivity of BHMF, which is comparable to the results presented in Table 1.2. Even though the reaction time spent in this experiment is same as the reaction time reported in entry 2 (2 hours) and shorter than the reaction time reported (3 hours) in entry 3, the temperature and pressure reported in entry 2 (T = 35 °C; P = 8 bar) and entry 3 (T = 20 °C; P = 1 bar) are much milder. In entry 3, the temperature and pressure used for the reaction are harsher than that of the entry 2 and entry 4, but the full conversion can be achieved after half an hour. Overall, in comparison with the operating condition reported by literature, reaction conditions in terms of temperature and pressure used in this experiment are harsher, and hence,

reaction conditions are required to be optimised for future work.

To gain more insights into the effect of Li, the reaction was carried out at a range of reaction times to investigate the product distribution at 100 ºC. The conversion of HMF and the selectivity toward BHMF were investigated after one, two and four hours, respectively. The time-course of HMF hydrogenation over 20 wt% Pt/C and 20 wt% Pt-^{sub}Li/C with regards to the conversion and the selectivity toward BHMF is displayed in Table 6.10.

Table 6.10. Time-course of hydrogenation HMF with 20 wt% Pt/C and 20 wt% Pt-^{sub}Li/C with regards to the conversion and the selectivity toward BHMF in IPA.

Catalyst	Reaction Time (hour)	HMF Conversion (mol %)	BHMF Selectivity (mol %)	MEFA Selectivity (mol %)	MFA Selectivity (mol %)	side products selectivity (%)
20 wt% Pt/C	1	94	11	30	4	55
20 wt% Pt/C	2	>99	9	32	trace	59
20 wt% Pt/C	4	>99	7	18	trace	75
20 wt% Pt-^{sub}Li/C	1	86	87	1	9	3
20 wt% Pt-^{sub}Li/C	2	98	93	1	6	trace
20 wt% Pt-^{sub}Li/C	4	99	93	trace	5	2

At 100 ℃, 20 wt% Pt/C exhibited only 11% selectivity towards BHMF even though 94% of HMF had been converted after one hour. The major side product was MEFA, in addition to by-products such as liquid alkane, ring-opening products and intermediate fragments. In comparison with the results at 120 ℃, it can be found that temperature is an important factor to tune chemoselectivity of the HMF hydrogenation and it is favourable to undergo etherification of IPA and BHMF or MFA at low temperatures. When the reaction time reached two hours, the HMF conversion and target product selectivity remained mostly unchanged. After prolonging the reaction time to four hours, it was found that selectivity toward MEFA dropped to 18%. This result indicates that the residual HMF and MEFA have undergone

hydrogenation or a HDO reaction to form other side products. In contrast, 20 wt% Pt/C after introduction of 0.5 molar equiv. of $Li(OAc)\cdot 2H_2O$ can indeed lead to lower activity with a 86% conversion of HMF but 87% selectivity toward BHMF. Conventional reaction intermediates, such as furfural and 5-[(1-methylethoxy)methyl]-2-furan-2-carbaldehyde (MEFCA), were not found according to the GC/MS results. Prolonging the reaction time to two hours resulted in a nearly full conversion of HMF, and the selectivity toward BHMF slightly increased to around 93%. When the reaction time was extended to four hours, 93% selectivity toward BHMF was still achieved, accompanied by a trace amount of the HDO products, MFA (5%) and FA (2%).

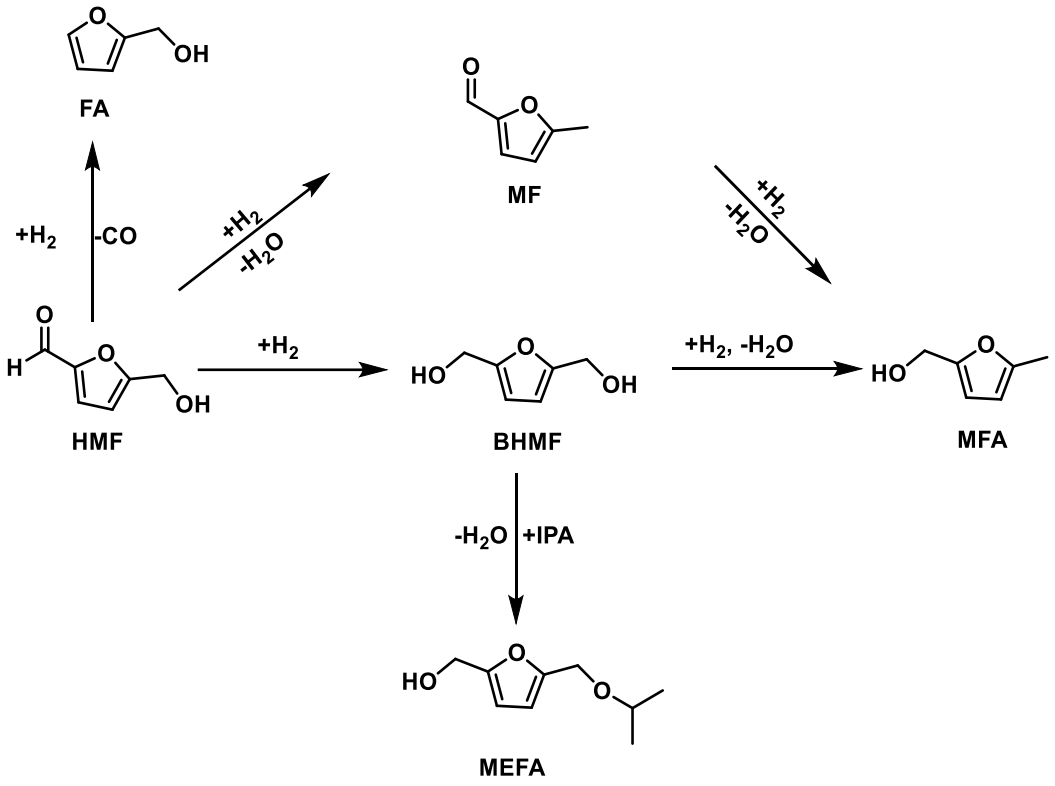


Figure 6.14. Proposed catalytic reaction pathway of HMF reaction.

Based on the aforementioned results, the proposed reaction pathway for the conversion of HMF catalysed by Pd-^{sub}Li/C is shown in Figure 6.14. With the Pd-^{sub}Li/C catalyst, the hydrogenation of HMF to BHMF is the major reaction pathway. A trace amount of BHMF may either undergo further HDO reaction to form MFA or undergo etherification to generate MEFA. In parallel to the HMF hydrogenation pathway, a trace amount of HMF can also undergo

decarbonylation and hydrogenolysis to form FA and MF, respectively. The MF can also be further hydrogenated to form MFA.

6.12 Conclusion

Pt NPs alloying with Li dopants substitutionally can be prepared at high temperature. The presence of a Li signal can be confirmed by the XPS and ^{7}Li MAS ssNMR, while the indication of the unusual Pt lattice contraction and the presence of the Pt_7Li phase were verified by the SXRD and its complementary refinements. Additionally, STEM-ADF imaging directly revealed the appearance of the NPs at the atomic level, which suggested that Li atoms have been substituted into Pt sites instead of occupying interstitial sites. To the best of our knowledge, it is the first time Pt-^{sub}Li has been established in the form of nanoparticles. Their catalytic performance was tested in the hydrogenation of biomass-derived HMF to produce BHMF. The catalytic testing result indicated that the presence of the Li dopant can suppress the formation of side products by inhibition of the extensive HDO reaction pathways. It is anticipated that the electron filling of the d-band centre of the Pt after lithiated modification can weaken the adsorption of HMF molecules, leading to higher selectivity toward the partially hydrogenated product, BHMF. Future work aims to optimise the reaction conditions, use DFT to rationalise the electronic effect of Li on the Pt system and identify the selective sites using chemical kinetics.

6.13 References

1 I. T. Ellis, E. H. Wolf, G. Jones, B. Lo, M. Meng-Jung Li, A. P. E. York and S. C. Edman Tsang, *Chem. Commun.*, 2017, **53**, 601–604.

2 C. P. Nash, F. M. Boyden and L. D. Whittig, *J. Am. Chem. Soc.*, 1960, **82**, 6203–6204.

3 O. Loebich and C. J. Raub, *Platin. Met. Rev.*, 1981, **25**, 113–120.

4 J. Sangster and A. . Pelton, *J. Phase Equilibria*, 1991, **12**, 678–681.

5 W. Bronger, G. Klessen and P. Müller, *J. Less Common Met.*, 1985, **109**, L1–L2.

6 C. Lee, M.-H. Whangbo and J. Köhler, *J. Comput. Chem.*, 2008, **29**, 2154–2160.

7 Z. Awaludin, T. Okajima and T. Ohsaka, *Electrochem. commun.*, 2013, **31**, 100–103.

8 J. Binns, M. Marqués, P. Dalladay-Simpson, R. Turnbull, M. Frost, E. Gregoryanz and R. T. Howie, *Phys. Rev. B*, 2019, **99**, 220101.

9 T. Xu, C. Lin, C. Wang, D. L. Brewe, Y. Ito and J. Lu, *J. Am. Chem. Soc.*, 2010, **132**, 2151–2153.

10 M. Jeyaraj, S. Gurunathan, M. Qasim, M.-H. Kang and J. H. Kim, *Nanomaterials*, 2019, **9**, 1719.

11 S. Sunaina, M. Sreekanth, S. Ghosh, S. K. Mehta, A. K. Ganguli and M. Jha, *CrystEngComm*, 2017, **19**, 2264–2270.

12 G. E. Tobôn-Zapata, E. G. Ferrer, S. B. Etcheverry and E. J. Baran, *J. Therm. Anal. Calorim.*, 2000, **61**, 29–35.

13 L. Shi, T. Qu, D. Liu, Y. Deng, B. Yang and Y. Dai, in *Materials Processing Fundamentals 2020*, Springer, Cham, 2020, pp. 107–116.

14 S. A. Speakman, *Introduction to X-Ray Powder Diffraction Data Analysis*, Centre for Materials Science and Engineering, Massachusetts, USA, 2013.

15 K. Okitsu, Y. Mizukoshi, H. Bandow, T. A. Yamamoto, Y. Nagata and Y. Maeda, *J. Phys. Chem. B*, 1997, **101**, 5470–5472.

16 H. F. Lopez and H. Mendoza, *ISRN Nanomater.*, 2013, **2013**, 1–7.

17 A. A. Coelho, *J. Appl. Crystallogr.*, 2018, **51**, 210–218.

18 B. T. W. Lo, L. Ye and S. C. E. Tsang, *Chem*, 2018, **4**, 1778–1808.

19 W. H. Qi, M. P. Wang and G. Y. Xu, *J. Mater. Sci. Lett.*, 2002, **22**, 1333–1334.

20 I. N. Leontyev, A. B. Kuriganova, N. G. Leontyev, L. Hennet, A. Rakhmatullin, N. V. Smirnova and V. Dmitriev, *RSC Adv.*, 2014, **4**, 35959–35965.

21 F. A. Peter Atkins, Tina Overton, Jonathan Rourke, Mark Weller, *Inorganic Chemistry*, OUP Oxford, 5th edn., 2009.

22 E. Clementi, D. L. Raimondi and W. P. Reinhardt, *J. Chem. Phys.*, 1967, **47**, 1300–1307.

23 X. F. Zhou, G. R. Qian, X. Dong, L. Zhang, Y. Tian and H.-T. Wang, *Phys. Rev. B*, 2010, **82**, 134126.

24 V. F. Sears, *Neutron News*, 1992, **3**, 26–37.

25 J. A. Shusterman, N. D. Scielzo, K. J. Thomas, E. B. Norman, S. E. Lapi, C. S. Loveless, N. J. Peters, J. D. Robertson, D. A. Shaughnessy and A. P. Tonchev, *Nature*, 2019, **565**, 328–330.

26 J. W. Niemantsverdriet, *Spectroscopy in Catalysis: An Introduction*, Wiley-VCH Verlag GmbH & Co. KGaA, Weinheim, Germany, 2007.

27 K. D. B. John F. Moulder, William F. Stickle, Peter E. Sobol, *Handbook of X-ray Photoelectron Spectroscopy*, Physical Electronics Division, Perkin-Elmer Corporation, Chichester, UK, 1992.

28 J. H. Kim, J. Y. Cheon, T. J. Shin, J. Y. Park and S. H. Joo, *Carbon N. Y.*, 2016, **101**, 449–457.

29 L. M. Martínez-Prieto, L. Rakers, A. M. López-Vinasco, I. Cano, Y. Coppel, K. Philippot, F. Glorius, B. Chaudret and P. W. N. M. van Leeuwen, *Chem. - A Eur. J.*, 2017, **23**, 12779–12786.

30 S. E. Hayes, R. A. Guidotti, W. R. Even, P. J. Hughes and H. Eckert, *J. Phys. Chem. A*, 2003, **107**, 3866–3876.

31 N. Dupre, M. Cuisinier and D. Guyomard, *Interface Mag.*, 2011, **20**, 61–67.

32 S. Todisco, G. Saielli, V. Gallo, M. Latronico, A. Rizzuti and P. Mastrorilli, *Dalt. Trans.*, 2018, **47**, 8884–8891.

33 C. C. Ahn and O. L. Krivanek, *A reference guide of electron energy loss spectra covering all stable elements*, Gatan Inc, Warrendale, 1983.

34 F. S. Hage, T. P. Hardcastle, M. N. Gjerding, D. M. Kepaptsoglou, C. R. Seabourne, K. T. Winther, R. Zan, J. A. Amani, H. C. Hofsaess, U. Bangert, K. S. Thygesen and Q. M. Ramasse, *ACS Nano*, 2018, **12**, 1837–1848.

35 J. Palisaitis, C. L. Hsiao, M. Junaid, J. Birch, L. Hultman and P. O. Å. Persson, *Phys. Rev. B*, 2011, **84**, 245301.

36 M. Tinoco, L. Maduro, M. Masaki, E. Okunishi and S. Conesa-Boj, *Nano Lett.*, 2017, **17**, 7021–7026.

37 X. Chen and L. Jensen, *J. Opt.*, 2016, **18**, 074009.

38 S. Mazzucco, O. Stéphan, M. Kociak and C. Colliex, *EMC 2008 14th European Microscopy Congress 1–5 September 2008, Aachen, Germany*, Springer Berlin Heidelberg, Berlin, Heidelberg, 2008, vol. 1.

39 H. Yang, I. MacLaren, L. Jones, G. T. Martinez, M. Simson, M. Huth, H. Ryll, H. Soltau, R. Sagawa, Y. Kondo, C. Ophus, P. Ercius, L. Jin, A. Kovács and P. D. Nellist, *Ultramicroscopy*, 2017, **180**, 173–179.

40 J. J. Wiesfeld, M. Kim, K. Nakajima and E. J. M. Hensen, *Green Chem.*, 2020, **22**, 1229–1238.

41 Q. Li, H. Wang, Z. Tian, Y. Weng, C. Wang, J. Ma, C. Zhu, W. Li, Q. Liu and L. Ma, *Catal. Sci. Technol.*, 2019, **9**, 1570–1580.

42 J. Mitra, X. Zhou and T. Rauchfuss, *Green Chem.*, 2015, **17**, 307–313.

43 J. Luo, J. Yu, R. J. Gorte, E. Mahmoud, D. G. Vlachos and M. A. Smith, *Catal. Sci. Technol.*, 2014, **4**, 3074–3081.

44 S. K. R. Patil and C. R. F. Lund, *Energy & Fuels*, 2011, **25**, 4745–4755.

45 H. Chang, A. H. Motagamwala, G. W. Huber and J. A. Dumesic, *Green Chem.*, 2019, **21**, 5532–5540.

46 B. Saha and M. M. Abu-Omar, *Green Chem.*, 2014, **16**, 24–38.

47 X. Liu, D. C. Y. Leong and Y. Sun, *Green Chem.*, 2020, **22**, 6531–6539.

48 S. Chen, C. Ciotonea, K. De Oliveira Vigier, F. Jérôme, R. Wojcieszak, F. Dumeignil, E. Marceau and S. Royer, *ChemCatChem*, 2020, **12**, 2050–2059.

49 M. J. Climent, A. Corma and S. Iborra, *Green Chem.*, 2011, **13**, 520–540.

50 S. Cattaneo, H. Naslhajian, F. Somodi, C. Evangelisti, A. Villa and L. Prati, *Molecules*, 2018, **23**, 2007.

51 F. Menegazzo, E. Ghedini and M. Signoretto, *Molecules*, 2018, **23**, 2201.

52 T. Wang, J. Zhang, W. Xie, Y. Tang, D. Guo and Y. Ni, *Catalysts*, 2017, **7**, 92.

53 J. Wei, X. Cao, T. Wang, H. Liu, X. Tang, X. Zeng, Y. Sun, T. Lei, S. Liu and L. Lin, *Catal. Sci. Technol.*, 2018, **8**, 4474–4484.

54 B. Hammer and J. K. Nørskov, *Advances in Catalysis*, 2000, vol. 45, pp. 71–129.

Chapter 7 Conclusion & Future Work

7.1 Conclusion

Throughout this thesis, the in-depth investigation of light element modified late transition metal NPs systems has been carried out via interstitial nanoalloy characterisation, novel substitutional nanoalloy synthesis and the catalytic testing of the newly designed catalysts.

The objectives of Chapter 4 were to probe structure information precisely from the Pd-^{int}B/C by using a novel combination of characterisation techniques. These detailed characterisations provided an improved understanding of the Pd-^{int}B/C system in terms of its structural distortion, composition analysis and visibility of the B atomic columns intercalated between the Pd metal framework.

The objectives of Chapter 5 were similar to Chapter 4, where the investigation object was Pd-^{int}Li/C instead. The same combination of analytical techniques, in addition to neutron diffraction was employed to investigate structural information of Pd-^{int}Li/C and attempted to evaluate the strain effect induced by the Li dopants. Despite the physical properties of Li, current EELS and ptychographic results can suggest the presence of Li in the interstitial positions of Pd; however, more evidence is required to prove it beyond any doubt.

In Chapter 6, with the aid of the combination of the characteristic toolsets, the obtained Pt-Li nanoalloy was defined as a substitutional solid-solution nanoalloy. To the best of our knowledge, Pt-^{sub}Li/C powder was synthesised and characterised for the first time, and the minimum temperature for its synthesis from Pt/C and Li(OAc)·2H_2O was shown to be 650 ℃ or above. This catalyst was tested for activity in the hydrogenation of HMF to BHMF. This novel Pt catalyst, not only retained a good activity but also exhibited exceptional selectivity to the partial hydrogenation product, BHMF. The high catalytic selectivity could be attributed to

the presence of Li on these Pt catalysts, because it substituted for Pt in the lattice, altering the adsorption energy of HMF.

The collection of the start-of-the-art techniques which have been used this thesis can provide quantitative information to analyse structural modifications of the industrial type of noble metal nanoparticle, particularly for the platinum group heterogeneous catalyst, and hence their physicochemical properties when light elements such as B or Li are introduced. This can give insight of structure-activity relationship, and further identify the type of light element doping. Indeed, the presence of light dopants in the heavy metal framework can significantly tune the chemisorption of the catalyst so that enhancing the product selectivity for hydrogenation of biomass-derived compounds. It is expected that this work can open up an opportunity for further investigation of interstitial and substitutional light element doped platinum group metal catalyst in future.

7.2 Future Work

7.2.1 Pd-^{int}B/C Project

As mentioned in Chapter 4, ptychography was used with the support of several other techniques, allowing the new atomic columns at octahedral sites to be assigned to boron. A full spectroscopic elucidation at the atomic level, differentiated over different thicknesses of NPs, will be required to distinguish the contrast of each element precisely. However, that will rely on an intensive three-dimensional elemental mapping investigation *via* STEM-EELS optical sectioning; as has been recently done by Pennycook *et al.* for thin-film heterostructures.[1] The EELS spectrum image can still maintain sufficient resolutions if the depth of field is below 11nm. Although this goes beyond the limitation of the present technique, since the fast-pixelated detector and EELS detector lie in the same line of optical configuration, such spectroscopic investigation will be worth investigating in the future.

7.2.2 Pd-^{int}Li/C Project

In Chapter 5, the combination of multi-techniques was employed to elucidate the location of the Li, but extra work is still required to strengthen the argument. 5 wt% Pd and 50 wt% Pd loading-based sample will be prepared for SXRD measurements to identify the origin of the artifact and quantification of microstrain. So far, the EELS spectrum of Pd-^{int}Li/C has revealed plasmon profile changes, relative to the EELS spectrum of Pd/C; however, it is essential to identify other contributions, such as particle size, shape, dopant and support.

Attempts to use ptychography to probe the Li intercalated between the Pd atomic columns at lower accelerating voltages, to avoid electron beam damage to the materials, have been made but met with limited success. Therefore, ptychographic simulations were computed to propose suitable experimental conditions. It is likely worth carrying out ptychographic experiments at lower accelerating voltages, in accordance with the results proposed by the simulation, but whilst using a larger aperture.

An attempt has also been made to map the strain distribution of the Pd-^{int}Li NPs by using StatSTEM programming. However, due to the lack of Pd NPs with similar particle size for use as a reference, absolute strain cannot be obtained. Future work still aims to find a Pd/C with suitable particle size. To ensure a particle containing Li atomic columns, simultaneous ADF-ptychography acquisition is implemented instead of the conventional ADF multi-frame acquisition. Of course, there is still room to improve the accuracy of the results further. Our research group is developing a multi-framework simultaneous ADF-ptychography acquisition technique which is expected to address the issue of scan distortion. Once this technique is well-developed, it can be explored to minimise the effect of the scan distortion.

7.2.3 Pt-^{sub}Li/C Project

In Chapter 6, a series of analytical techniques were used to confirm the formation of a

novel binary nanoalloy, Pt-^{sub}Li/C NPs. To strengthen this claim, more analytical techniques can be considered. Regarding the scattering technique, neutron PDF could be utilised to probe atomic pairs at the local environments. Although ^{7}Li MAS ssNMR has been carried out, it will be valuable to conduct ^{195}Pt ssNMR which allows for verification of the Pt-^{sub}Li formation and for probing the structural distortion induced by the Li. According to our catalytic testing results, this novel catalyst exhibited a high selectivity in the hydrogenation of HMF to BHMF. However, the catalytic testing was performed under harsh reaction conditions in comparison with the literature. In future work, the priority should be given to the experiments concerned with optimisation of the reaction condition and measuring the chemical kinetics of this reaction and with the identification of the active site.

7.3 References

1 T. J. Pennycook, H. Yang, L. Jones, M. Cabero, A. Rivera-Calzada, C. Leon, M. Varela, J. Santamaria and P. D. Nellist, *Ultramicroscopy*, 2017, **174**, 27–34.

Chapter 8 Appendix

8.1 Supporting information of Chapter 4

8.1.1 Particle Size Analysis

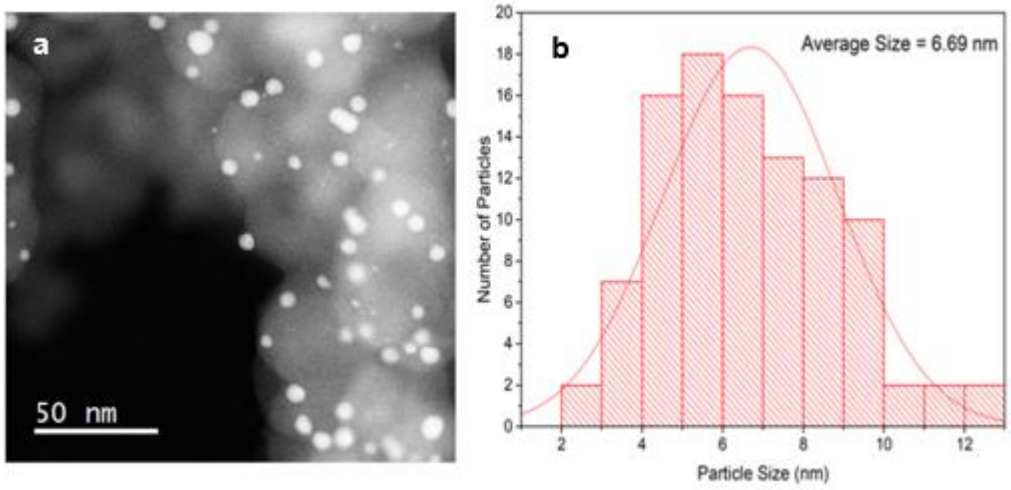


Figure 8.1. Particle size of the 5 wt% Pd-^{int}B/C NPs. (a) ADF-STEM image of 5 wt% Pd-^{int}B NPs dispersed on the carbon support. The average particle size is 6.69 nm, which is obtained from manual particle size analysis depicted in the histogram (b).

8.1.2 Lab-Source XRD of 50 wt% Pd/C, Pd-^{int}B/C and Pd-^{int}Li/C

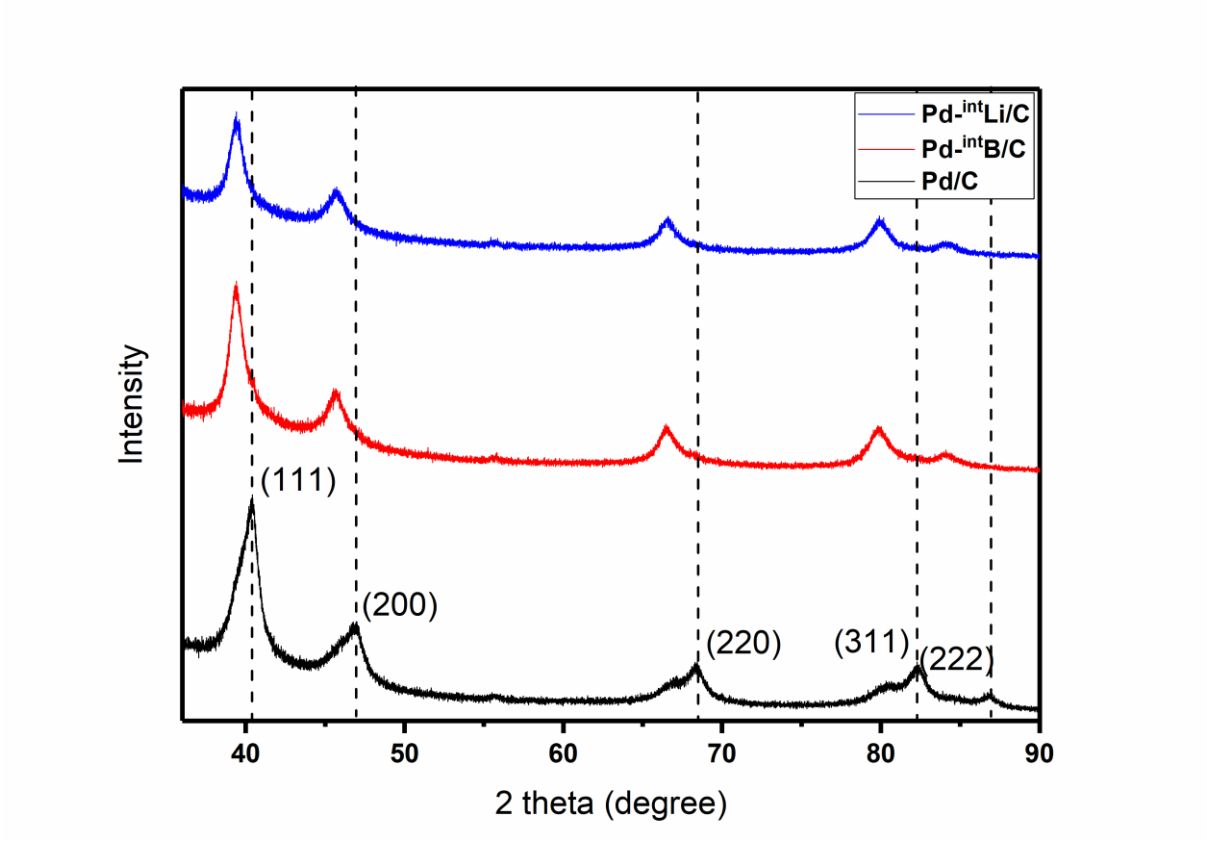


Figure 8.2. Lab source XRD patterns of 50 wt% Pd/C (black), 50 wt% Pd-^{int}B/C (red) and 50 wt% Pd-^{int}Li/C (blue).

8.1.3 The derivation for the minimum and maximum radius ratio for tetrahedral and octahedral interstitial sites.

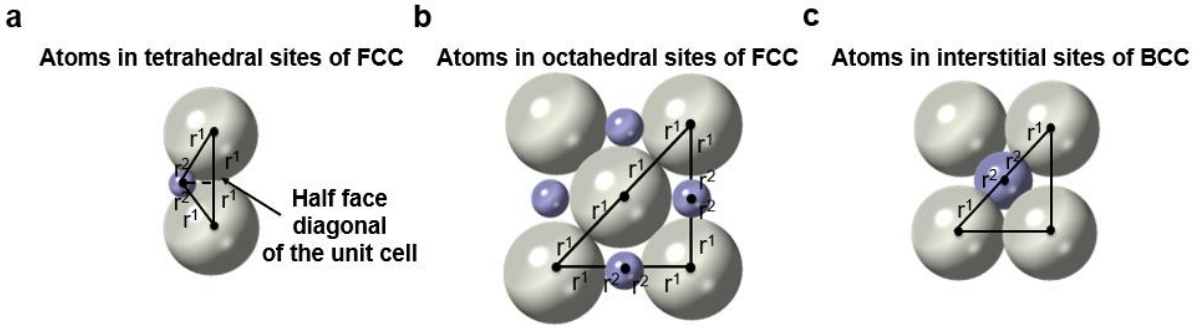


Figure 8.3. A schematic representation of the derivation for the min. and max radius ratio for tetrahedral (a) and octahedral interstitial sites of FCC (b), and cubic interstitial site. The dot line in (a) represents ¼ unit cell edge. The figure is drawn on basis of ref. 1.

a) Derivation for the minimum radius ratio for tetrahedral interstitial sites of FCC.

In a close-packed structure, the distance from the centre of the tetrahedron to the corner, d, is:

$$d = r^1 + r^2$$

The length of side of a FCC unit cell is a, where:

$$4r^1 = \sqrt{2}a$$

The ¼ length of side of a FCC unit cell is ¼ a, where:

$$\frac{1}{4}a = \frac{1}{\sqrt{2}}r^1$$

Therefore:

$$(\frac{1}{\sqrt{2}}r^1)^2 + (r^1)^2 = (r^1+r^2)^2$$

$$\frac{r^2}{r^1} = \frac{\sqrt{6}}{2} - 1 = 0.225$$

b) Derivation for the minimum radius ratio for octahedral interstitial sites of FCC.
The length of side of a FCC unit cell is a, where:
$a = 2r^1 + 2r^2$

The diagonal has length, d, where:

$$d = 4r^1$$

Therefore:

$$(4r^1)^2 = (2r^1+2r^2)^2+(2r^1+2r^2)^2$$

$$\frac{r^2}{r^1} = \frac{2}{\sqrt{2}} - 1 = 0.414$$

c) Derivation for the minimum radius ratio for atoms in interstitial sites of BCC.
The length of side of a BCC unit cell is a, where:
$a = 2r^1$
Along the body diagonal, the atom (r^2) is touching the two atoms (r^1) on either end so its length, d, is:
$d = 2r^1 + 2r^2$
Therefore:
$a^2 + a^2 + a^2 = d^2$
$3a^2 = d^2$
$12r^2 = d^2$
$d = 2\sqrt{3}\, r^1$

$2r^1 + 2r^2 = 2\sqrt{3}\, r^1$

$\frac{r^2}{r^1} = \sqrt{3} - 1 = 0.732$

8.1.4 Typical Examples of Intrinsic Stacking Faults, Extrinsic Stacking Faults and Twinning Models

8.1.4.1 Intrinsic Stacking Fault: ABCABCABCA→ABCACABCA

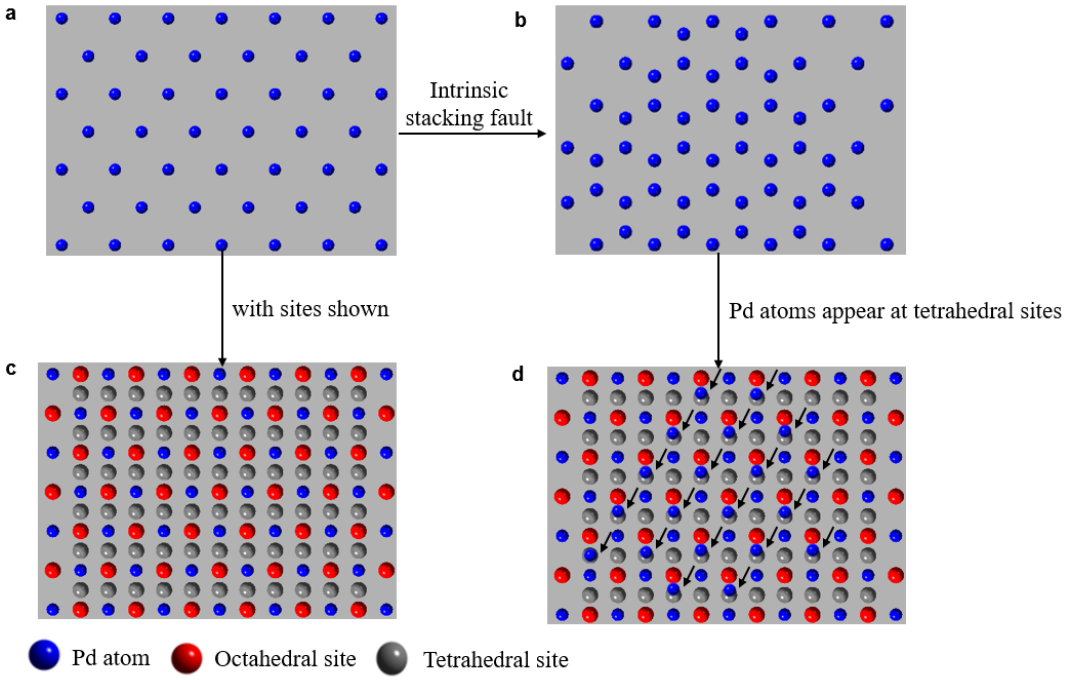


Figure 8.4. Example of a Pd-^{int}B/C intrinsic stacking fault model. Blue dots represent Pd atoms; red dots represent octahedral sites; grey dots represent tetrahedral sites. (a) Pd atomic configuration oriented in a <110> direction. (b) demonstrates an example of Pd atomic configuration projected along a [-1 1 0] direction if an intrinsic stacking fault happens. (c) Pd atomic configuration oriented in a <110> with octahedral sites and tetrahedral sites shown. (d) partially demonstrates the positions where Pd atoms may emerge if an intrinsic stacking fault happens. These models show no atomic occupancy at the observed octahedral site columns, but rather atomic occupancy appearing close to tetrahedral sites.

8.1.4.2 Extrinsic Stacking Fault: ABCABCABCA→ABCACBCABC

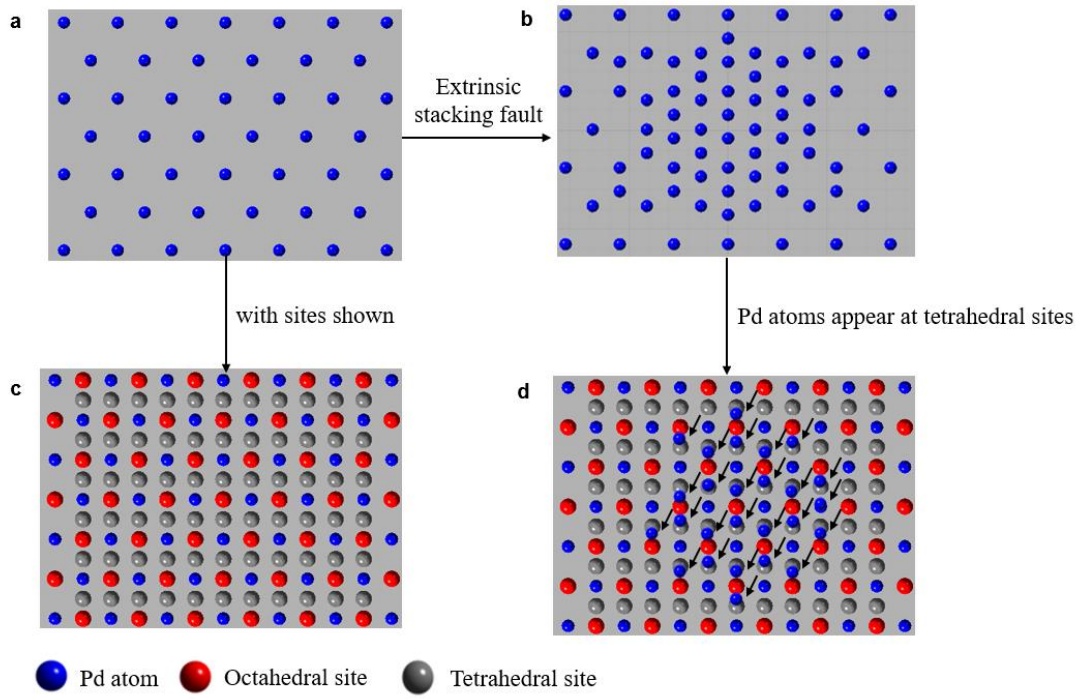


Figure 8.5. Example of a Pd-^{int}B/C extrinsic stacking fault model. Blue dots represent Pd atoms; red dots represent octahedral sites; grey dots represent tetrahedral sites. (a) Pd atomic configuration oriented in a <110> direction. (b) demonstrates an example of Pd atomic configuration projected along a [-1 1 0] direction if an extrinsic stacking fault happens. (c) Pd atomic configuration oriented in a <110> with octahedral sites and tetrahedral sites shown. (d) partially demonstrates the positions where Pd atoms may emerge if an extrinsic stacking fault happens. These models show no atomic occupancy at the observed octahedral site columns, but rather atomic occupancy appearing close to tetrahedral sites.

8.1.4.3 Twinning: ABCABCABCA→ABCACBA; twinning plane is A plane

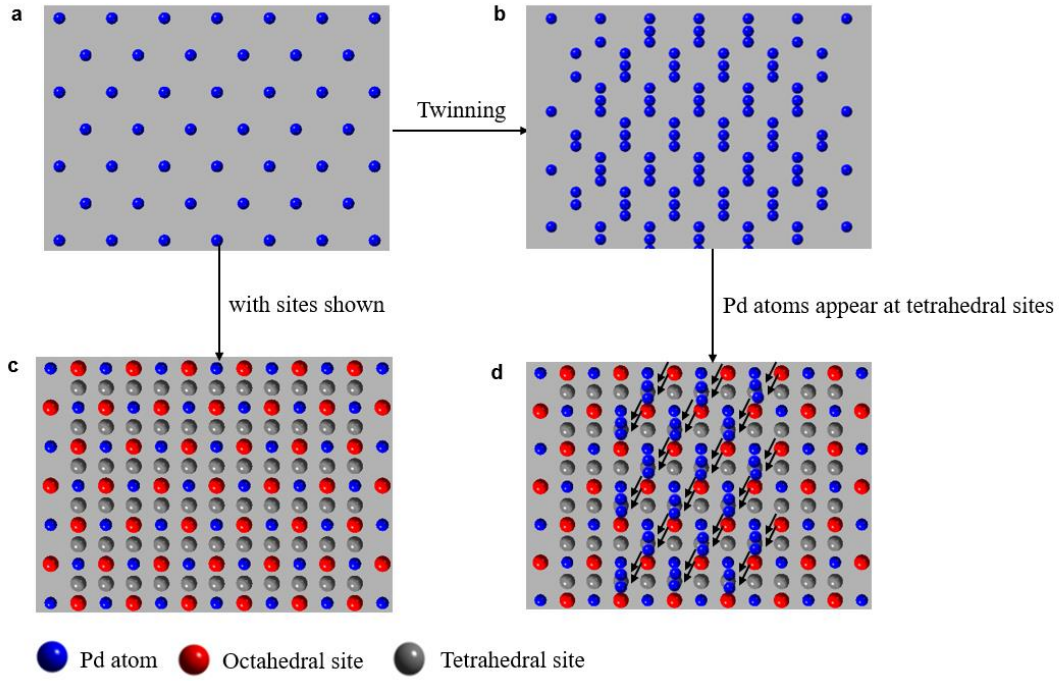


Figure 8.6. Example of a Pd-^{int}B/C twinning fault model, where plane A is a twinning line. Blue dots represent Pd atoms; red dots represent octahedral sites; grey dots represent tetrahedral sites. (a) Pd atomic configuration oriented in a <110> direction. (b) demonstrates an example of Pd atomic configuration projected along a [-1 1 0] direction if a twinning fault happens. (c) Pd atomic configuration oriented in a <110> with octahedral sites and tetrahedral sites shown. (d) partially demonstrates the positions where Pd atoms may emerge if a twinning fault happens. These models show no atomic occupancy at the observed octahedral site columns, but rather atomic occupancy appearing close to tetrahedral sites.

8.1.4.4 Twinning: ABCABCABCA→BCABACB; twinning plane is B plane

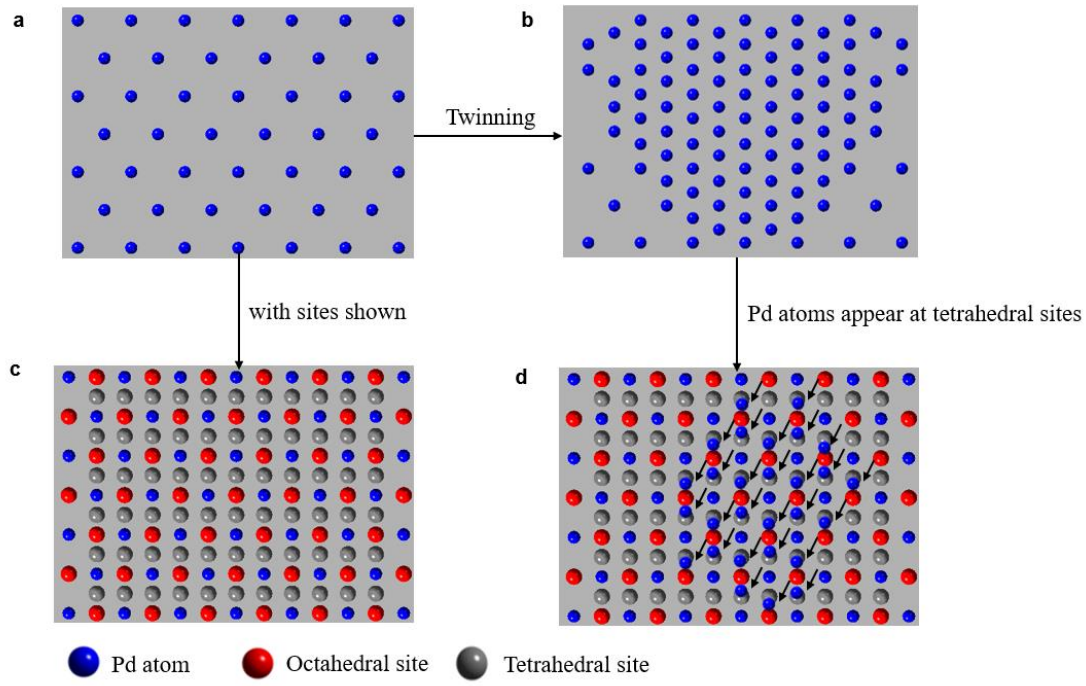


Figure 8.7. Example of a Pd-^{int}B/C twinning fault model, where plane B is a twinning line. Blue dots represent Pd atoms; red dots represent octahedral sites; grey dot represent tetrahedral sites. (a) Pd atomic configuration oriented in a <110> direction. (b) demonstrates an example of Pd atomic configuration projected along a [-1 1 0] direction if a twinning fault happens. (c) Pd atomic configuration oriented in a <110> with octahedral sites and tetrahedral sites shown. (d) partially demonstrates the positions where Pd atoms may emerge if a twinning fault happens. These models show no atomic occupancy at the observed octahedral site columns, but rather atomic occupancy appearing close to tetrahedral sites.

8.1.4.5 Twinning: ABCABCABCA→CABCBAC; twinning plane is C plane

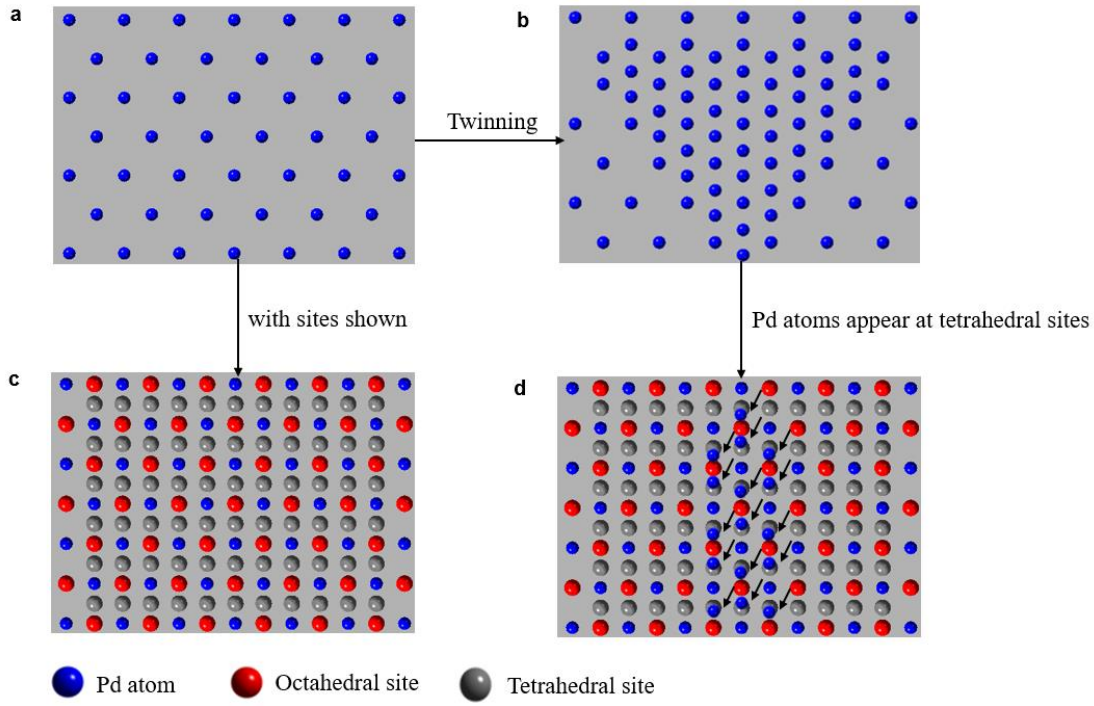


Figure 8.8. Example of a Pd-^{int}B/C twinning fault model, where plane C is a twinning line. Blue dots represent Pd atoms; red dots represent octahedral sites; grey dots represent tetrahedral site. (a) Pd atomic configuration oriented in a <110> direction. (b) demonstrates an example of Pd atomic configuration projected along a [-1 1 0] direction if a twinning fault happens. (c) Pd atomic configuration oriented in a <110> with octahedral sites and tetrahedral sites shown. (d) partially demonstrates the positions where Pd atoms may emerge if a twinning fault happens. These models show no atomic occupancy at the observed octahedral site columns, but rather atomic occupancy appearing close to tetrahedral sites.

8.1.5 Additional Ptychographic Dataset of Pd-^{int}B/C NP

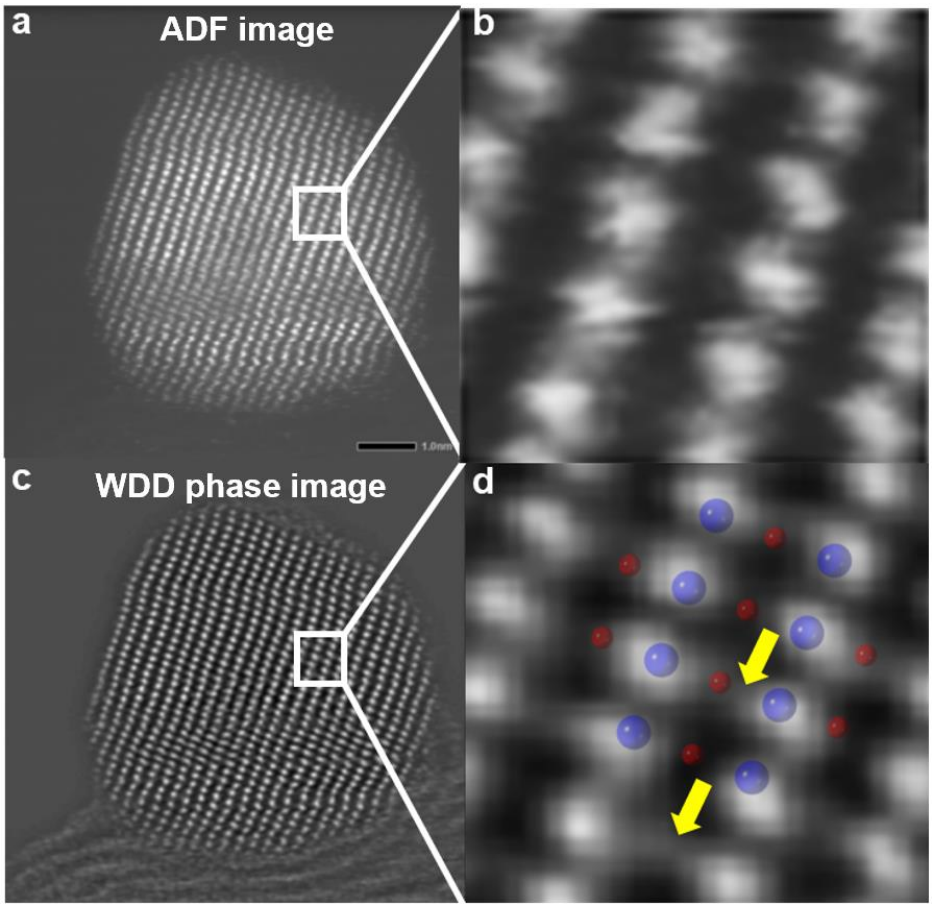


Figure 8.9. Simultaneously acquired Z-contrast STEM-ADF and ptychographic phase image of a 5 wt% Pd-^{int}B/C NP oriented in the relatively defect free [211] zone axis. (a) Z-contrast STEM-ADF image of a Pd-^{int}B/C NP. (b) inset from (a) shows an enlarged area of the NP. (c) Ptychographic phase image reconstructed using the Wigner Distribution Deconvolution (WDD) method. (d) inset from (c) shows an enlarged area of the NP. The enlarged ptychography phase image shows intensity in some, but not all, of the octahedral sites suggesting that these are not artefacts due to aberrations. The ADF image does not show corresponding intensity suggesting the presence of B in the octahedral site. This matches well with the model predicted by XPDF (overlaid).

8.2 Supporting information of Chapter 5

8.2.1 Polycrystalline NPs

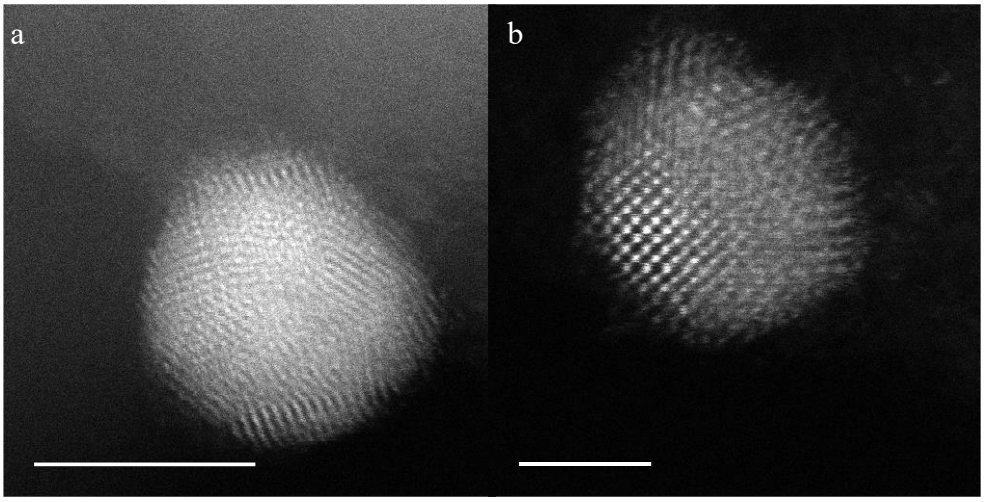


Figure 8.10. Examples of the polycrystalline 5 wt% Pd-^{int}Li/C NPs, which are demonstrated in (a) and (b).

8.2.2 ZLP of EELS

8.2.2.1 200 kV

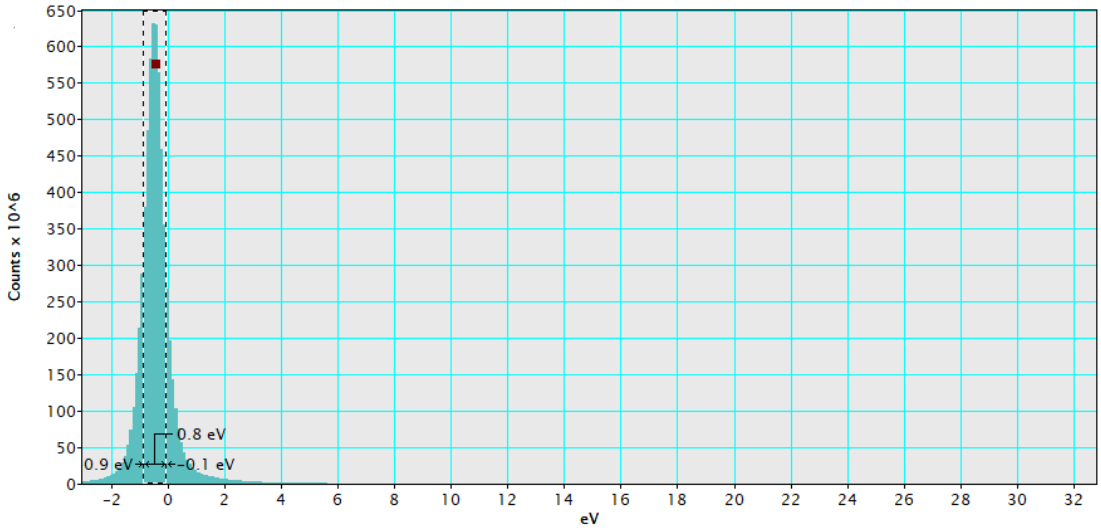


Figure 8.11. ZLP of EELS at 200 kV. The full width at half maximum (FWHM) of the ZLP is 0.8 eV.

8.2.2.2 80 kV

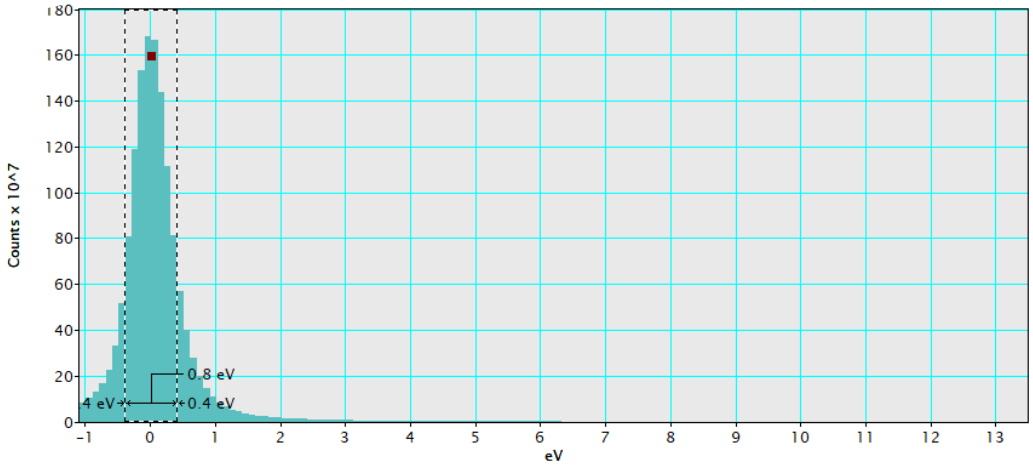


Figure 8.12. ZLP of EELS at 80 kV. The full width at half maximum (FWHM) of the ZLP is 0.8 eV.

8.2.2.3 60 kV

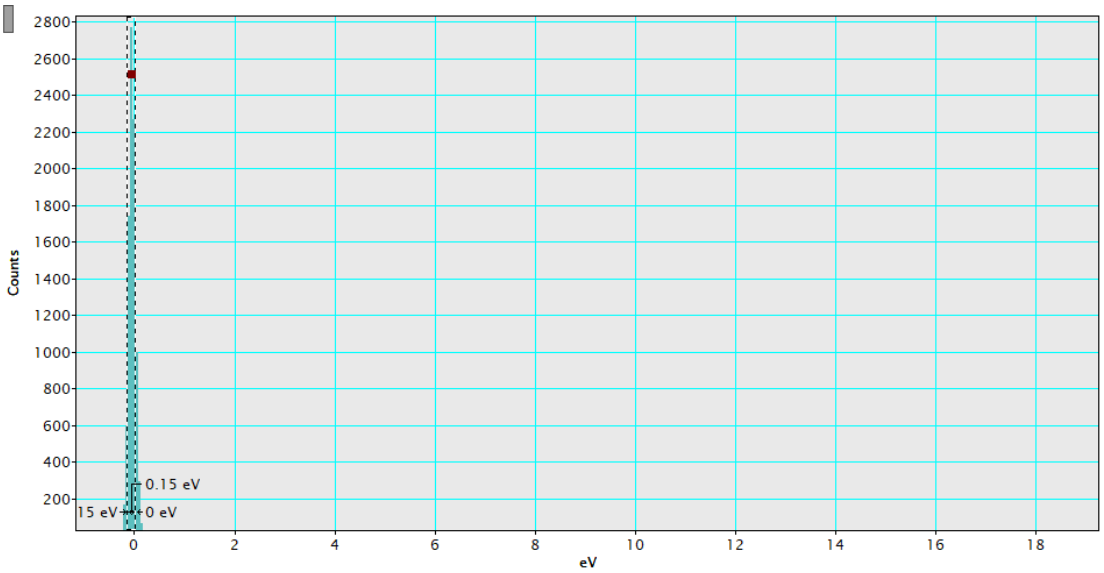


Figure 8.13. ZLP of EELS at 80 kV. The full width at half maximum (FWHM) of the ZLP is 0.15 eV.

Note: In Figure 5.9d, there is a weak peak adjacent to the Pd $N_{2,3}$ edge. This weak peak is assigned to background noise by a means of shifting setting in energy channels.

8.2.3 Strain Mapping

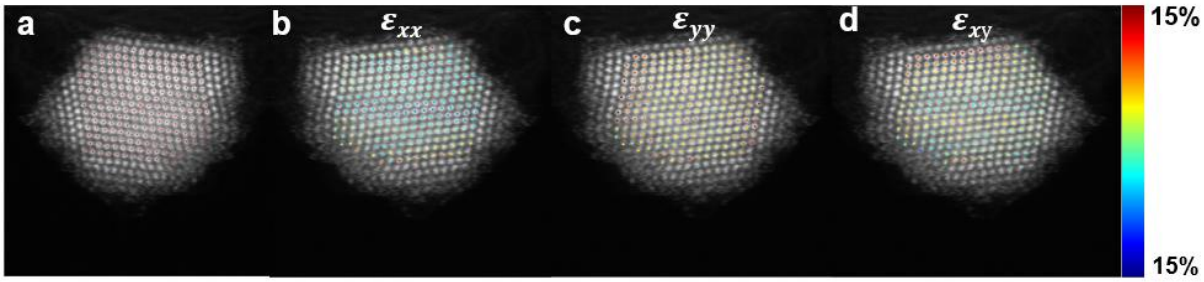


Figure 8.14. Strain variation relative to the centre of a Pd-^{int}Li/C NP, computed by StatSTEM[7]. (a) The reference position for the straining mapping. (b) ε_{xx} strain map of the Pd-^{int}Li NP. (c) ε_{yy} strain map of the Pd-^{int}Li NP. (d) ε_{xy} strain map of the Pd-^{int}Li NP. The intensity scale shows relative deformation. To clarify the nomenclature, terms "compressive strain" ($\boldsymbol{\varepsilon} < 0$) and "tensile strain" ($\boldsymbol{\varepsilon} > 0$) refer to the contracted and expanded lattice parameters measured with respect to the reference region (a).[32] With regards to the type of the strain, $\boldsymbol{\varepsilon_{xx}}$ and $\boldsymbol{\varepsilon_{yy}}$ are the normal strain, and the $\boldsymbol{\varepsilon_{xy}}$ is the shear strain. HCP and left lateral FCC facet were excluded for strain mapping computation to improve the accuracy of the result.

8.2.4 Thickness of the NPs

8.2.4.1 200 kV

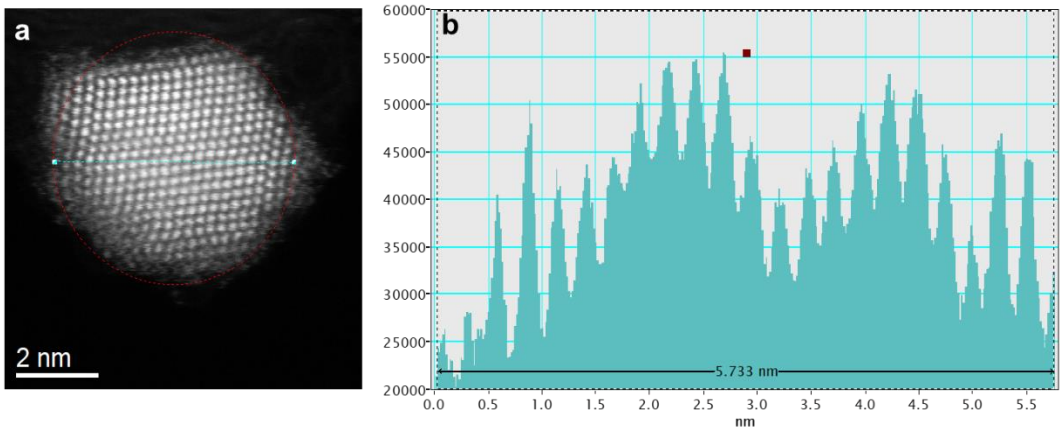


Figure 8.15. Thickness of the NP acquired at 200 kV. Line profile (a) was taken across the NP, the thickness of the NP is about 5.6 nm in accordance with (b).

8.2.4.2 80 kV

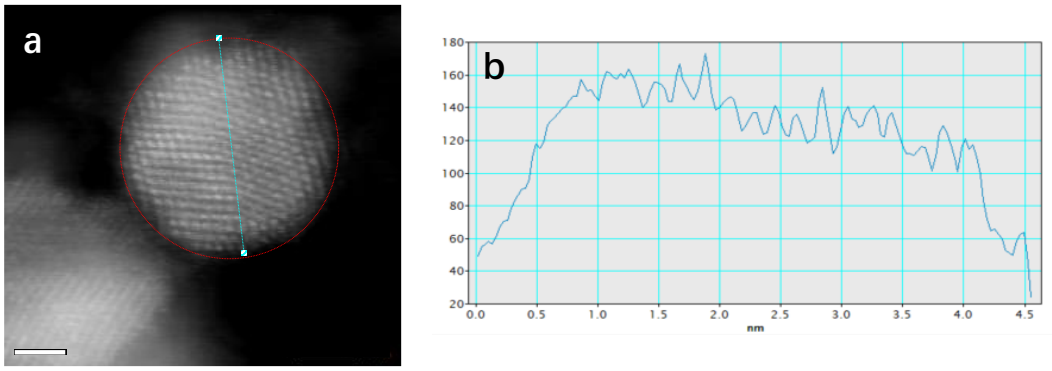


Figure 8.16. Thickness of the NP acquired at 80 kV. Line profile (a) was taken across the NP, the thickness of the NP is about 4.5 nm in accordance with (b).

8.3 Supporting information of Chapter 6

8.3.1 Particle Distribution of the Pt-^{sub}Li/C NPs

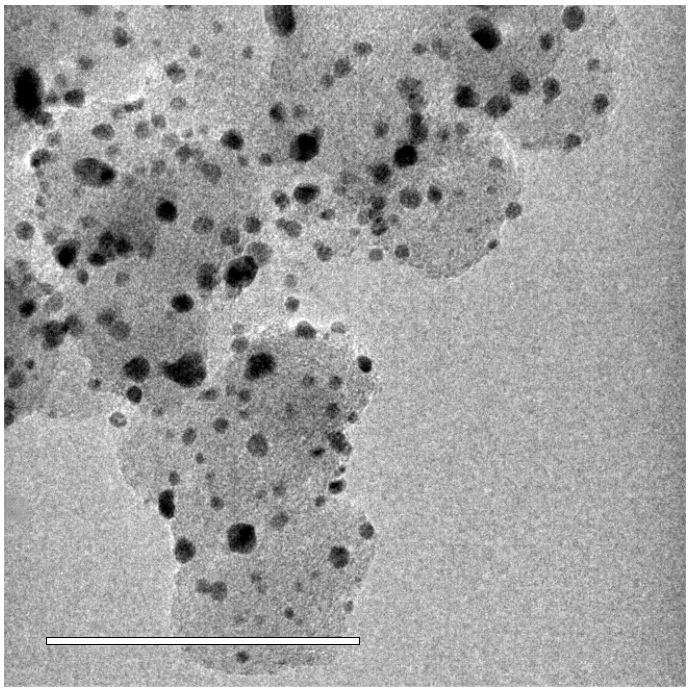


Figure 8.17. BF-TEM of 20 wt% Pt-Li/C NPs.

8.3.2 ZLP of EELS at 200 kV

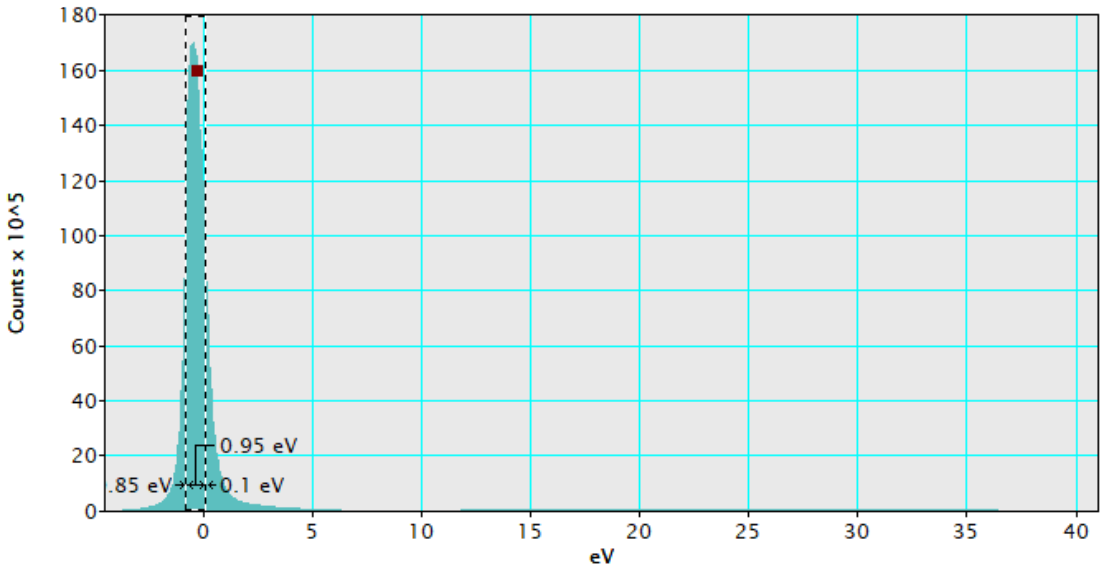


Figure 8.18. ZLP of EELS at 200 kV. The full width at half maximum (FWHM) of the ZLP is 0.95 eV.

8.3.3 Thickness of the NPs

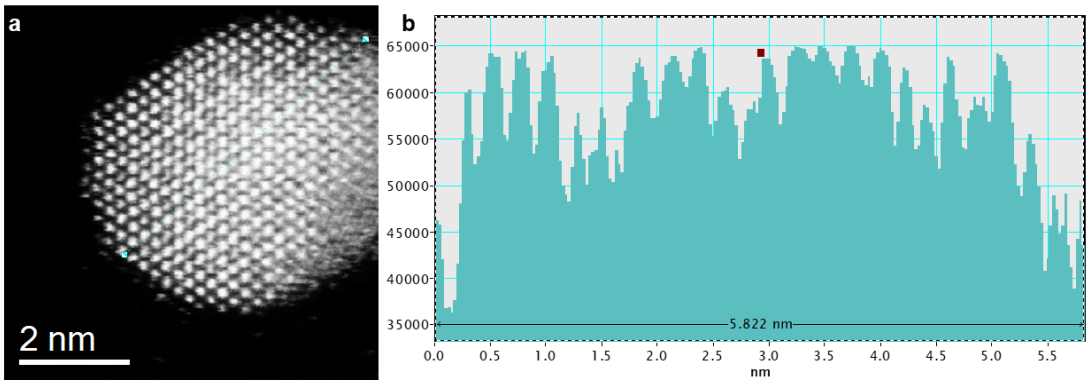


Figure 8.19. Line profile (b) indicates the thickness of the NP in (a) is 5.822 nm.

8.3.4 Hydrogenation of HMF via 5 wt% Pd/C, 5 wt% Pd-^{int}B/C and 5 wt% Pd-^{int}Li/C

Table 8.1. Catalytic performances of 5 wt% Pd/C, 5 wt% Pd-^{int}B/C and 5 wt% Pd-^{int}Li/C in the hydrogenation of HMF in IPA. Reactions: HMF = 0.126 g, T = 120 °C; P = 30 bar; t =2 hour.

Catalyst	HMF Conversion (mol%)	BHMF Selectivity (mol%)	DMF Selectivity (mol%)	DMTHF Selectivity (mol%)	MFA Selectivity (mol%)	Other Side Products selectivity* (mol%)
5 wt% Pd/C	>99	Trace	62	35	Trace	Trace
5 wt% Pd-^{int}B/C	80	6	55	5	Trace	34%
5 wt% Pd- ^{int}Li/C	66	68	10	Trace	12	10%

*: Other side products include 5-methylfurfuryl acetate, 2-hexanone, 2,5-bis(isopropoxymethyl)furan and (5-(isopropoxymethyl)furan-2-yl)methanol.

8.4 References

1 Radius Ratio Rules, http://www.chembio.uoguelph.ca/educmat/chm2060_preuss/L15-2013.pdf, (acessed 10/02/2021)